GIANT MOLECULES BASED ON FUNCTIONALIZED FULLERENES: PRECISE

SYNTHESIS AND DIVERSE ASSEMBLY BEHAVIORS

A Dissertation

Presented to

The Graduate Faculty of The University of Akron

In Partial Fulfillment

of the Requirements for the Degree

Doctor of Philosophy

Zhiwei Lin

August, 2016

GIANT MOLECULES BASED ON FUNCTIONALIZED FULLERENES: PRECISE

SYNTHESIS AND DIVERSE ASSEMBLY BEHAVIORS

Zhiwei Lin

Dissertation

Approved: Accepted:

_____   _____
Advisor   Department Chair
Dr. Stephen Z. D. Cheng   Dr. Coleen Pugh

_____   _____
Committee Member   Dean of the College
Dr. Toshikazu Miyoshi   Dr. Eric J. Amis

_____   _____
Committee Member   Dean of the Graduate School
Dr. Tianbo Liu   Dr. Chand K. Midha

_____   _____
Committee Member   Date
Dr. Abraham Joy

_____
Committee Member
Dr. Chrys Wesdemiotis

ii

ABSTRACT

The emergence of giant molecules built up from molecular nanoparticles (MNP) based nanoatoms has attracted substantial attentions because of their unique molecular design with shape and interaction anisotropy as well as conformation rigidity, leading to intriguing self-assembly behaviors different from traditional building blocks. Numerous hierarchically assembled structures deriving from giant molecules have been theoretically predicted by computer simulation. However, experimental exploration is still in the infancy. In this dissertation, we are aiming to develop several categories of giant molecules based on precisely functionalized fullerene (C_{60}), and study their versatile self-assembly behaviors. To break symmetry, hydrophilic C_{60}-based nanoatoms are designed, bearing multiple carboxyl acid (AC_{60}) or hydroxyl groups (DC_{60}). They are hexa-adducts of C_{60} with precisely defined chemical structures, synthesized by Bingel reaction. Various giant molecules can be achieved through attaching different hydrophobic building blocks onto these hydrophilic C_{60} via "click" chemistry. First of all, two molecular Janus particles with different molecular architectures were obtained by tethering an AC_{60} with one (AC_{60}-C_{60}) or two (AC_{60}-$2C_{60}$) hydrophobic C_{60}. Investigation on the solution self-assembly behavior of these two molecular Janus particles reveals that molecular architectures and solvent polarity are critical parameters in determining the assembled structures. Moreover, the conjugation of AC_{60} with a cyclic polystyrene (CPS)

using sequential click approaches gave rise to a set of novel giant molecules, which are referred to as "nano-diamond-ring-like" giant surfactants. They possess particular molecular structures, and may exhibit completely different self-assembly behaviors from the traditional self-assembly building blocks. We then extend such studies on the assembly of giant molecules in condensed state by synthesizing giant molecules composed of one AC_{60} tethered by PS-b-polyethylene oxide (PEO), as well as one DC_{60} tethered by one to four PS chains. Specifically, several pairs of topological isomers are designed, possessing identical overall molecule masses but with different topologies. Driven by the strong segregation between the hydrophilic C_{60} and hydrophobic PS, a variety of well-ordered structures with feature size below 10 nm are created. It was also demonstrated that the formation of assembled structures is extremely sensitive to their molecular topologies. The formation mechanism of these well-ordered nanostructures is fully discussed.

ACKNOWLEDGEMENTS

TABLE OF CONTENTS

x

LIST OF TABLES

LIST OF FIGURES

LIST OF SCHEMES

CHAPTER I

INTRODUCTION

Inspired by nature such as the lipid bilayers of cell membrane, self-assembly nowadays has become one of the most important approaches in creating new materials across different length scales. Developing new building blocks, directing their assemble into well-established structures, understanding the mechanism in self-assembly processes as well as guiding the fabrication of materials for potential applications have been central themes in the area of chemistry and material science over the past a few decades. The self-assembling building blocks are usually composed of incompatible components. The thermodynamic driving forces for organizing basic building blocks into hierarchically ordered structures are to minimize the overall free energies, in which noncovalent interactions between building blocks play a critical role. One of the representative examples is small-molecule surfactants composed of ionic groups and nonionic alkyl chains. In aqueous solution, they tend to self-organize into various assembled structures such as spheres, cylinders and vesicles with hydrophilic groups aggregating on the outside surface of assembled structures and hydrophobic alkyl chains wrapping within assembled structures. Another classic class of self-assembly building block is diblock

copolymers containing two immiscible segments connected by covalent bonds. To minimize free energy, phase separation occurs between two blocks. Meanwhile, since two blocks are conjugated by chemical bonds, only nanophase separation is feasible, leading to the formation of a variety of nano-ordered structures.

In recent years, the anisotropic interaction and rigidity in shape are recognized as essential parameters in determining the final assembled structures. As a result, numerous novel nanobuilding blocks with diverse surface functionalities, distinct shape, and anisotropic symmetry are proposed. Benefited from the advanced developments in computer science and technologies, theoretical investigation on self-assembly of these new building blocks has been realized. Intriguing assembled structures and rich phase behaviors beyond those from traditional building blocks have been predicted by computer simulation. However, experimental investigations are largely unexplored due to the grand challenges in synthesizing corresponding model self-assembly building blocks with anisotropic interaction and specific shape.

Molecular nanoparticles (MNPs)-based giant molecules have emerged as one of promising candidates for experimentally exploring the assembly of building blocks with anisotropic interactions and shape. MNPs selected to build up giant molecules should capture the important features such as monodisperse molecular weight, well-defined 3D molecular structures, persistent volume and shape, as well as facile surface modification. Typically, they include but are not limited to polyhedral oligomeric silsesquioxane (POSS), [60] fullerene (C_{60}), polyoxometalates (POMs) and folded globular proteins. Based on these MNPs, our group has developed three categories of giant molecules including, giant shape amphiphiles, giant surfactants, and giant polyhedras. Specifically,

a variety of POSS-based giant molecules were synthesized by precise chemistry such as "click" chemistry. The self-assembly behaviors of these giant molecules have also been systematically studied, exhibiting significant differences from traditional self-assembling building blocks such as block copolymers.

Despite the successes in using POSS as basic building block to construct giant molecules, the study on other MNP-based giant molecules is relatively preliminary. C_{60} has attracted tremendous attentions since it was discovered in 1985. It has been regarded as an ideal nano-motif for constructing giant molecules, because it is a monodisperse molecular nanoparticle with persistent volume and shape, which can be readily functionalized by various chemical reactions. More importantly, C_{60} possesses excellent electrical, optical and biological properties. Therefore, C_{60} will be employed as MNPs to construct giant molecules in this dissertation, in which two types of giant molecules, giant shape amphiphiles and giant surfactants, will be focused on. The molecular design, precise synthesis and self-assembly of various C_{60}-based giant shape amphiphiles and giant surfactants will be discussed in details. This dissertation will be organized as follows.

Chapter II provides a background introduction in term of self-assembly of fundamental building blocks and giant molecules. Starting from the concept of self-assembly, the assembly of fundamental building blocks such as atoms, molecules, macromolecules and colloid particles are briefly reviewed, followed by introducing the concept of giant molecules. The general molecular design of giant molecules is described in a relatively detailed manner. Previous studies on synthesis and self-assembly of several typical giant molecules are covered.

Chapter III reports the molecular design, synthesis and self-assembly of two C_{60}-based molecular Janus particles. They are composed of one hydrophilic C_{60} tethered by one or two hydrophobic C_{60}. The conjugation of these two incompatible C_{60} is achieved by "click" chemistry. The self-assembly of these two molecular Janus particles is carried out in different solvents. Various micellar morphologies and corresponding morphological transition are characterized by transmission electronic microscope (TEM), light-scattering and atom force microscope (AFM). The micelles formation and phase transition mechanism is discussed to demonstrate the effect of solvent polarity and molecular architectures on the self-assembly of as-prepared molecular Janus particles.

Chapter IV describes the design and synthesis of a series of giant surfactants consisting of a carboxylic acid functionalized hydrophilic C_{60} (AC_{60}) head and a hydrophobic cyclic polystyrene (CPS). Since the molecular structures of these giant surfactants resemble diamond-ring, they are referred as "nano-diamond-ring-like" giant surfactants. To demonstrate the highly efficient, modular and versatile features of our synthetic approach, various "nano-diamond-ring-like" giant surfactants decorating with different "diamonds", including not only AC_{60} but hydrophilic POSS (such as dihydroxyl-functionalized DPOSS) were synthesized via the modular sequential "click" approaches. These giant surfactants with structural precision represent a novel member in the MNP-based giant surfactant family, which might have distinct self-assembly behaviors compared with their linear analogues.

Chapter V presents the synthesis and assembly of giant surfactants composed of one AC_{60} tethered by a PS-*b*-poly(ethylene oxide) (PEO) block copolymer chain. Three categories of giant surfactants are synthesized by locating the AC_{60} at the end of PS block

25

(AC_{60}-PS-PEO), the end of PEO block (AC_{60}-PEO-PS) or at the junction point between two blocks (PS-(AC_{60})-PEO). The assembly of these giant surfactants in bulk is investigated by small angel X-ray scattering (SAXS), wide angel X-ray diffraction (WAXS), differential scanning calorimetry (DSC), Fourier transform infrared spectroscopy (FTIR) as well as TEM. Various hybrid nano-ordered structures such as lamellae, double gyroids and cylinder with domain size smaller than 10 nm were obtained, which is rarely achieved from block copolymer/nanoparticles blending systems. The topological effects on assembled structures are highlighted by specifically designing two pairs of topological isomers, containing identical molecular weight of polymers but with different topologies.

Chapter VI focuses on the design and synthesis of hydroxyl-functionalized C_{60}-based giant surfactants. Different numbers of PS tails are attached onto one hydrophilic head with varying number of hydroxyl groups. The self-assembly of the single and multi-tailed giant surfactants was studied. The results reveal that the functionalities and architectures are the critical factors determining the assembled structures. Interestingly, the formation of A15 phase was observed from one head with four tails system, which is rarely seen from block copolymer systems.

Finally, Chapter VII gives a summary of the research progress covering in this dissertation and offers a personal perspective on future directions related to this topic.

CHAPTER II

BACKGROUND

2.1 Self-assembly and Self-assembly of Fundamental Building Blocks

Self-assembly is a spontaneous process of organizing either separate or linked components into ordered aggregates.[1] The size of components or building block involved in the process of self-assembly can be ranging from microscopic to macroscopic, giving rise to hierarchical structures with various length scales.[2] The assembled hierarchical structures provide a versatile bridge between microscopic molecular structures and macroscopic properties of materials. Self-assembly is ubiquitous in nature, from the bilayers of cell membrane to the complex compartments of organs. Developing new building blocks and directing their self-assembly to hierarchically ordered structures and further into bulk materials has been one of the most interesting and important issues in material science and engineering over the past several decades.[3] While thousands of types of building blocks with various chemical compositions, architectures and functionalities have been invented, the most well studied fundamental building blocks typically include atoms, small molecules, macromolecules, and colloidal particles.[3] They span length scales from angstrom to micrometer. In the following part, the assembly of these four types of building blocks will be briefly reviewed.

2.1.1 Self-assembly of Atoms

Metal nanocrystals with the dimension between 1 and 100 nm are essential to modern science and technology due to their fascinating properties and potential uses in chemical sensors[4], quantum devices[5], light-emitting diodes[6], lithography,[7] as well as high active and selective catalysts.[8-10] Tremendous efforts have been devoted to the preparation of metal nanocrystals over the past half century, the vast majority of which are synthesized in solution. The first and most important step for the synthesis of metal nanocrystals in solution is the self-nucleation of metal atoms to give seed clusters. The number for construction of the full-shell seed clusters has to fulfill a "magic number", that is, the nth shell of clusters requires $10n^2 + 2$ atoms to incorporate a densest packing. For example, the total number of the full-shell clusters containing 1, 2, 3, 4 and 5 shells possess 13 (1+12), 55 (13+42), 147 (55+92), 309 (147+162) and 561 (309+252) atoms, respectively (Figure 2.1).[11] This is actually consistent with the packing rule that the largest coordination number for hard sphere with equal sizes is twelve for a close packing. These clusters will serve as the nuclei to direct further assembly of metal atoms to form various metal nanocrystals with controllable shapes such as cubes, rods, beams, bipyramids, wires, triangular and hexagonal plates and so on.[12]

Full-Shell "Magic Number" Clusters					
Number of shells	1	2	3	4	5
Number of atoms in cluster	M_{13}	M_{55}	M_{147}	M_{309}	M_{561}
Percentage surface atoms	92%	76%	63%	52%	45%

Figure 2.1. Idealized representation of close sphere packing with "magic numbers" of atoms for building up the full-shell metal clusters.[11] Reproduced with permission from Ref 11.

Compared with above-mentioned single metal atoms, the packing of metal alloy atoms are much more complex, which may result in the formation of many intriguing phases such as Frank-Kasper phases. These phases were first introduced by Frank and Kasper.[13, 14] They are created by the close-packing of two or more metal alloy atoms with periodic structures. Two most well-known examples of Frank-Kasper phases are A15 and sigma (σ) phases. Each repeating unit cell of A15 contains two different types of spheres (sphere A and B). Spheres A are arranged in pairs on each face of the cube, while spheres B locates in the center and eight corners of the cube. Thus, A15 phase is usually consisted of metal alloys with the chemical formula of A_3B. Compared with A15 phase, the packing of σ phase is even more complicated, where 30 spheres with a total of five distinct surrounding environments occupy one tetragonal unit cell. σ phase is usually observed in metal alloys with the chemical formula of AB.
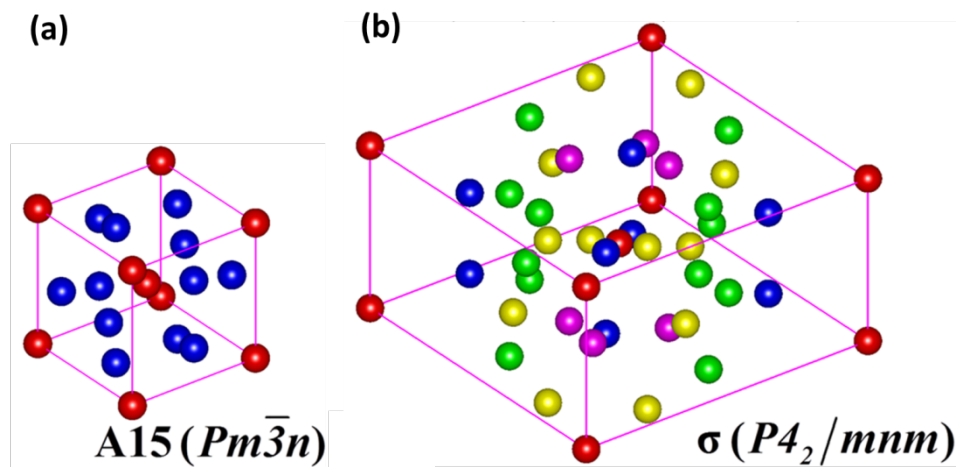
Figure 2.2. Unit cell of (a) A15 phase with a space group of $Pm\bar{3}n$, and (b) σ phase with a space group of $P4_2/mnm$.[15] Reproduced with permission from Ref 15.

2.1.2 Self-assembly of Small-molecule Surfactants

One of the most well studied examples about self-assembly of small molecules is surfactants. The small-molecule surfactants are characteristic of amphiphilic molecules consisting of polar group(s) as head(s) and nonpolar alkyl chain(s) as tail(s). They are compounds that tend to adsorb at interface to lower interfacial free energy.[16] As the concentration of surfactants in aqueous solution reaches their critical micelle concentration (CMC), they start to aggregate to form micellar structures with well-defined order or three-dimensional networks. The major thermodynamic driving forces that govern the aggregation of surfactant in aqueous solution arise from the hydrophobic attraction at the hydrophobic tails-water interfaces, as well as the steric repulsion of hydrophilic or ionic head-groups. The former interaction (attractive hydrophobic interfacial forces) induces the surfactant molecules to associate, while the latter interaction (repulsive head-group forces) assures their contacting with water. These two

opposing interactions compete with each other by decreasing and increasing the interfacial area per molecule exposed to the aqueous phase, giving rise to an optimal head group area (a_0) per headgroup when the average overall interaction energy of each molecule is minimum within an aggregate (Figure 2.3).
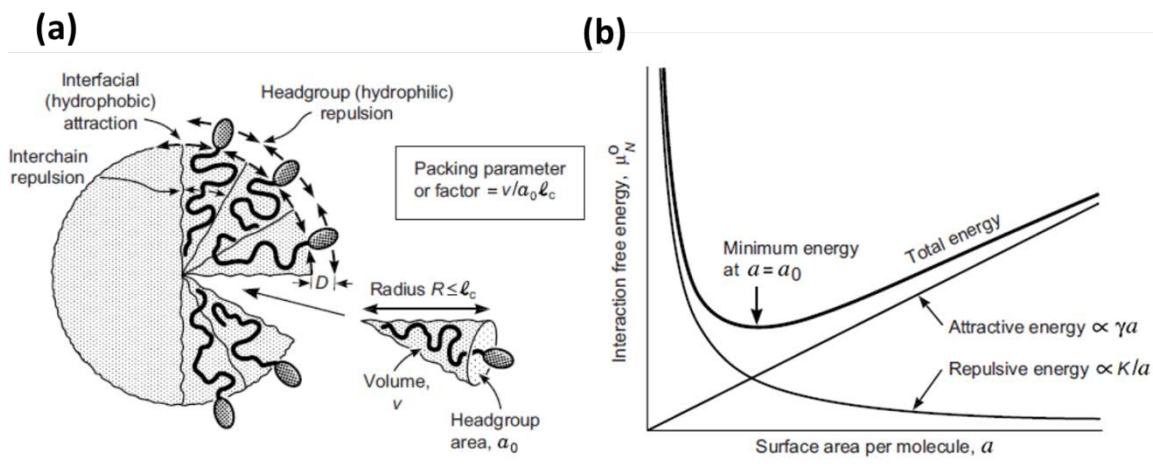
Figure 2.3. (a) Schematic illustration for the aggregation of micelles and various interactions involved within an aggregate; (b) attractive and repulsive energy versus surface area per molecule. Optimal head-group area reaches once the interfacial attraction of hydrophobic tails and the repulsion of head-group are balanced.[17] Reproduced with permission from Ref 17.

After considering above competing interaction and minimum free energy, the geometric packing of surfactants has to be taken into account, since it determines the most favored assembled structures. This geometric consideration is usually established from the packing parameter (P) of surfactants, determined by the optimal surface area (a_0) of hydrophilic part and hydrophobic chain volume (V) and critical length (l_c). Relying on the value of P, the preferred assembled morphologies of aggregation vary from spherical

micelles ($P \leq 1/3$), to cylindrical or rod-like micelles ($1/3 < P \leq 1/2$), to vesicular micelles ($1/2 < P < 1$) to extended bilayers ($P = 1$), and finally to inverted micelles ($P > 1$) (Figure 2.4). Therefore, since the value of a_0, V and l_c are measurable or estimable for a given molecule in aqueous solutions, one may predict which structures will be formed by assembly.[17]

Spherical micelles
($P \leq 1/3$)

Cylindrical micelles
($1/3 < P \leq 1/2$)

Vesicular micelles
($1/2 < P < 1$)

Extend bilayer
($P = 1$)

Inversed micelles
$P > 1$
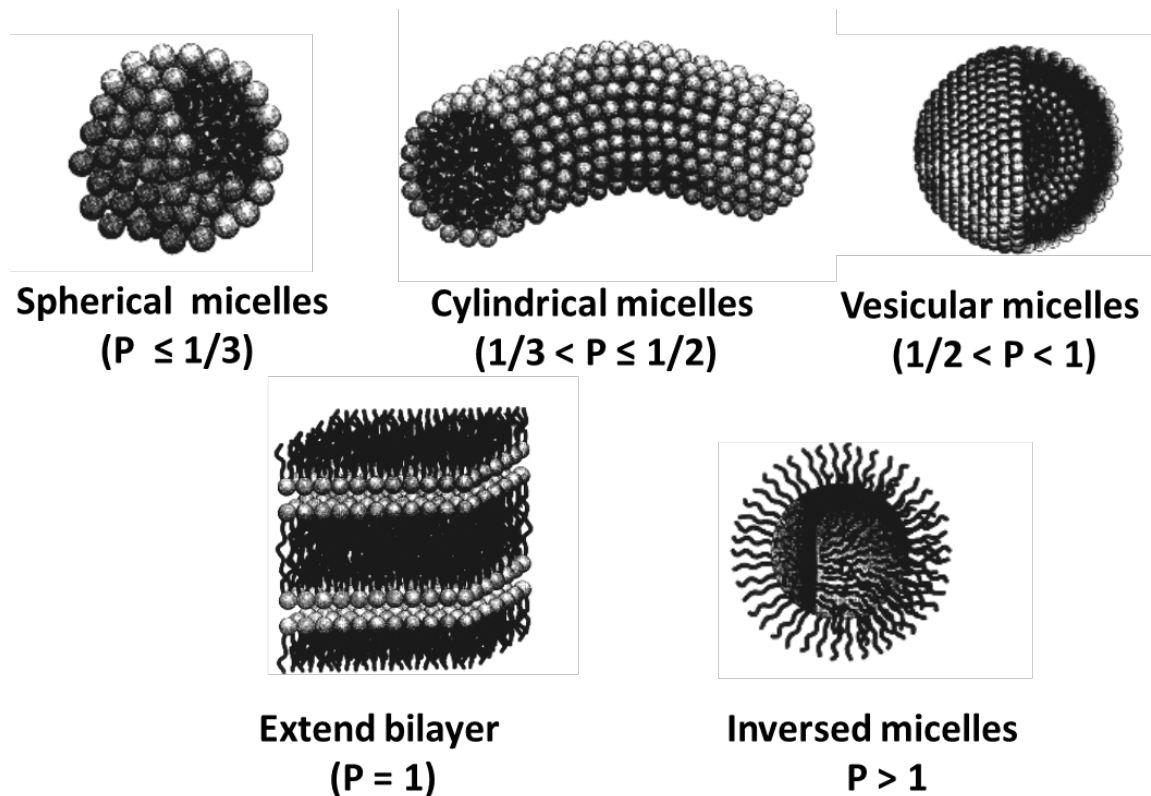
Figure 2.4. Various micellar morphologies and their corresponding packing parameter, where the morphological transition from spheres, to cylinders, to vesicles, to extend bilayer, finally to inverted spheres with increasing packing parameter.[16] Reproduced with permission from Ref 16.

2.1.3 Self-assembly of Macromolecules

Block copolymers, composed of two or more chemically distinct repeating units in sequences or blocks, is one of most important members in the family of macromolecules. The study of block copolymers is a subject of broad research emphasis ranging from macromolecular chemistry of preparing new polymers to macromolecular physics of developing advanced theories and methods.[18] Over the past several decades, the self-assembly of block copolymers is always one of the most active research fields in polymer community, and their self-assembly behaviors in solution, bulk and thin films have been extensively studied in term of theory and experiment.

The amphiphilic di-block copolymers are consisting of one hydrophobic polymer segment connected with one hydrophilic polymer segment via a covalent bond. Similar to small-molecule surfactants, di-block copolymers are able to self-assemble into various thermodynamically stable micellar morphologies in solution, including spheres, cylinders, vesicles and large compound micelles. Different from surfactants where micelles are formed in single solvent, the micelles of amphiphilic copolymers are generally prepared by dissolved in a good solvent for both blocks, followed by adding a poor solvent for one of blocks. There are three prerequisites dominating the formation of micelles. They are the attractive force among insoluble blocks, leading to aggregation, and the repulsive force among soluble blocks, preventing the unlimited growth of aggregates and macro-phase separation, as well as the interaction of soluble blocks and solvent, preventing the precipitation from solution.[19]
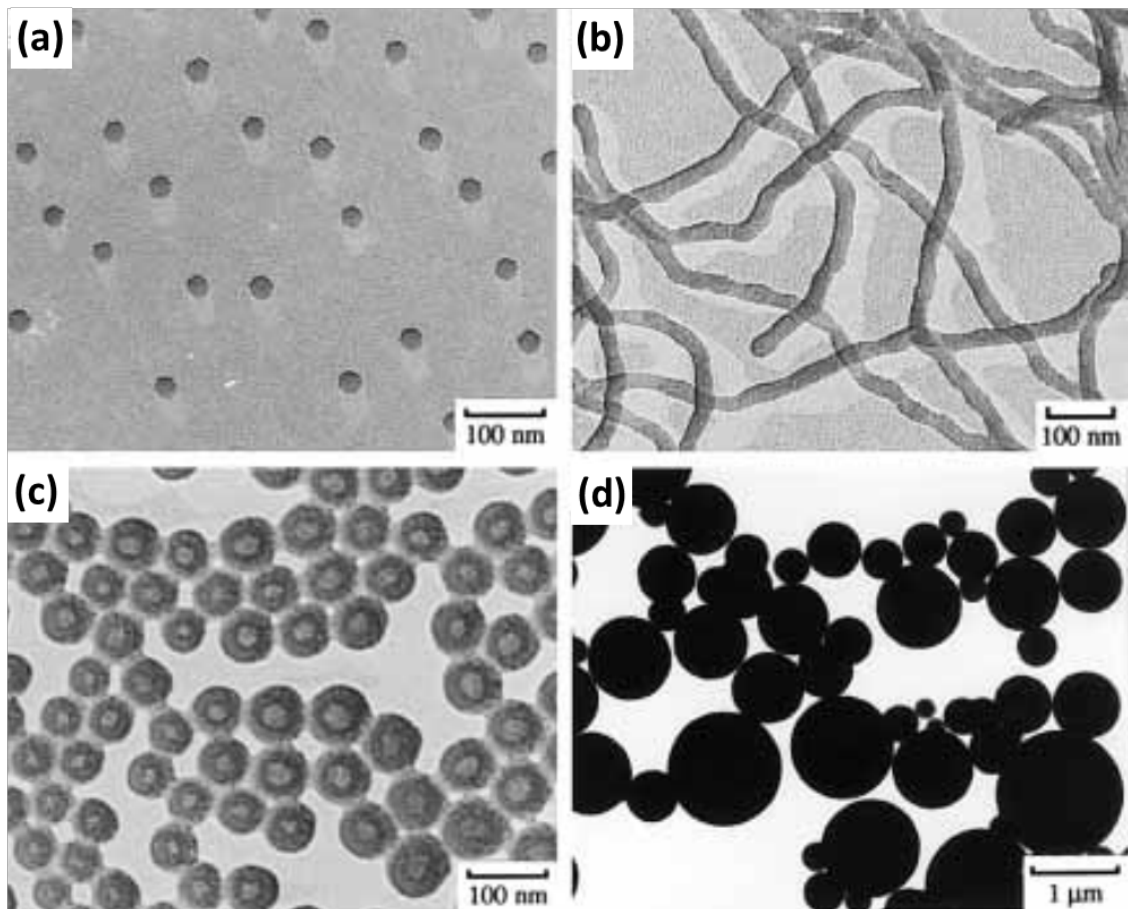
Figure 2.5. Multiple morphologies of micelles prepared from PS_m-b-PAA_n, where m and n represent the number of repeated unit of PS and PAA blocks, respectively. (a) spheres, PS_{200}-b-PAA_{21}, (b) cylinders, PS_{200}-b-PAA_{15} (b) vesicles, PS_{200}-b-PAA_8 and (d) large compound micelles, PS_{200}-b-PAA_4.[20] Reproduced with permission from Ref 20.

The first observation of these four morphologies from one type of block copolymer was reported by Zhang et al.[20] The copolymers they used is polystyrene (PS)-b-poly(acrylic acid) (PAA) with different compositions. When PS-b-PAA were dissolved in N,N-dimethylformamide (DMF) and water were added subsequently, the morphological transitions were observed from spheres to cylinders, to vesicles and finally

34

to large compound micelles with decreasing block length of PAA (Figure 2.5). Accumulated experimental results reveal that the critical factors affecting the resultant assembled morphologies of di-block copolymer are the initial concentration of polymers, the copolymer compositions, the nature of comment solvents and selective solvents, as well as the addition of counterions.[19]

The self-assembly of block copolymer in bulk state has also been theoretically and experimentally explored.[21] It has been revealed that the phase separation of diblock copolymers is determined by three key factors, including Flory-Huggins interaction parameter (χ) of two compositional segments, total degree of polymerization of two blocks (N), and the relative volume fraction (f) of each block. Depending on these three affecting factors, a phase diagram is predicted by self-consistent mean field theory (Figure 2.6 a), where a smallest critical value of χN (10.5) is required to induce the phase separation of diblock copolymers. A series of phase transition from lamellae (L), to double gyroids (G), to hexagonally packed cylinders (C), finally to body centered cubic (S) are revealed with changing the χN and f. The formation of these four phases, which are the most commonly observed and stable phases, and the corresponding phase transitions have been experimentally confirmed. A phase diagram was established by examining the assembly of diblock copolymer of PS-b-polyisoprene (PI) (Figure 2.6 b).[22] It is worth to note that there might appear some metastable phases beyond four classic phases, such as the hexagonal perforated lamellar phase (PL).
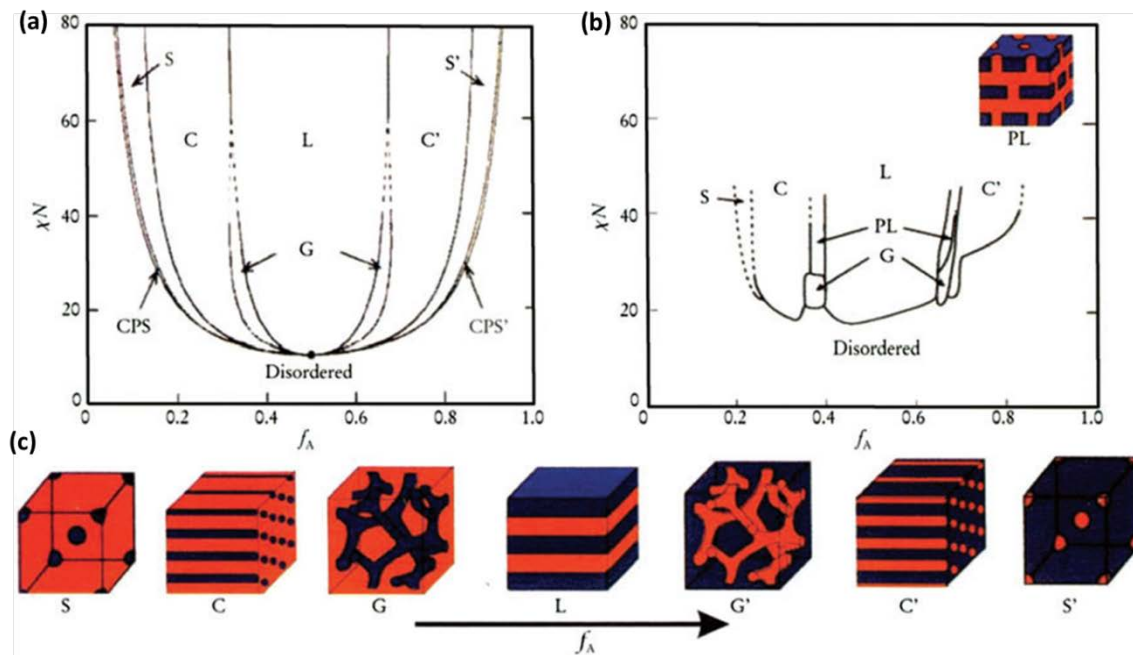
Figure 2.6. (a) The theoretical phase diagram of diblock copolymers predicted by self-consistent mean-field theory; (b) The experimental phase diagram built based on the phase behaviors of PS-b-PI. (c) Schematic illustration of four commonly observed phases formed by diblock copolymer and their phase transition with variation of volume fraction.[23] Reproduced with permission from Ref 23.

2.1.4 Self-assembly of Colloid Particles

Compared with the assembly of atoms, small molecules and macromolecules, which are usually driven by thermal fluctuation, the assembly of colloid particles is difficult to be induced by thermal fluctuation due to their much larger sizes relative to other three building blocks. Additionally, unlike soft amphiphilic building blocks such as surfactants and block copolymers having no definite size or shape but a distribution of some mean value, colloid particles usually possess fixed volume and shape. To direct

36

their assembly, the specific interactions or complementary shapes are designed and introduced into colloid particles.

Sacanna and coworkers developed a "lock and key" technique that leads to the assembly of colloid particles.[24] The "key" and "lock" they employed are spherical colloidal particles and monodisperse colloidal particles bearing a spherical cavity, respectively. The key particles and lock particles are able to bind together spontaneously after introducing polymers in the system, which act as the depletant and result in depletion interaction. The spontaneous binding between lock and key is only determined by their shapes, regardless of the surface chemistry and composition of particles. The free energy (F) variation associated with two particles binding together can be calculated by equation 2.1

$$\Delta F_d \approx k_B T \, n_p \, \Delta V \quad (2.1)$$

where k_B is boltzmann's constant, T is the temperature and n_p is the number density of adding polymers, ΔV is the overlapping exclusion volumes.

Based on the equation 2.1, the interaction or the binding strength between key and lock is proportional to ΔV, where a maximum ΔV is attained as the size and position key particles precisely fit into the cavity of lock particles. A successful lock-key binding can be realized in a configuration demonstrated by the green arrow where the key and lock cavity match perfectly. In contrast, the lock-key fails to bind together in the case shown by red arrows (Figure 2.7 b), where the key either locates out of the cavity or even separate from the lock. The interaction of a pair of lock-key is also dependent on n_p. Thus, a reversible process of binding can be readily controlled by tuning the concentration of adding polymers. Since the formation of lock-key colloidal particles is only associated

with their shape, a multiple binding becomes possible once a key particle can accommodate more than one lock particles (Figure 2.7 c).
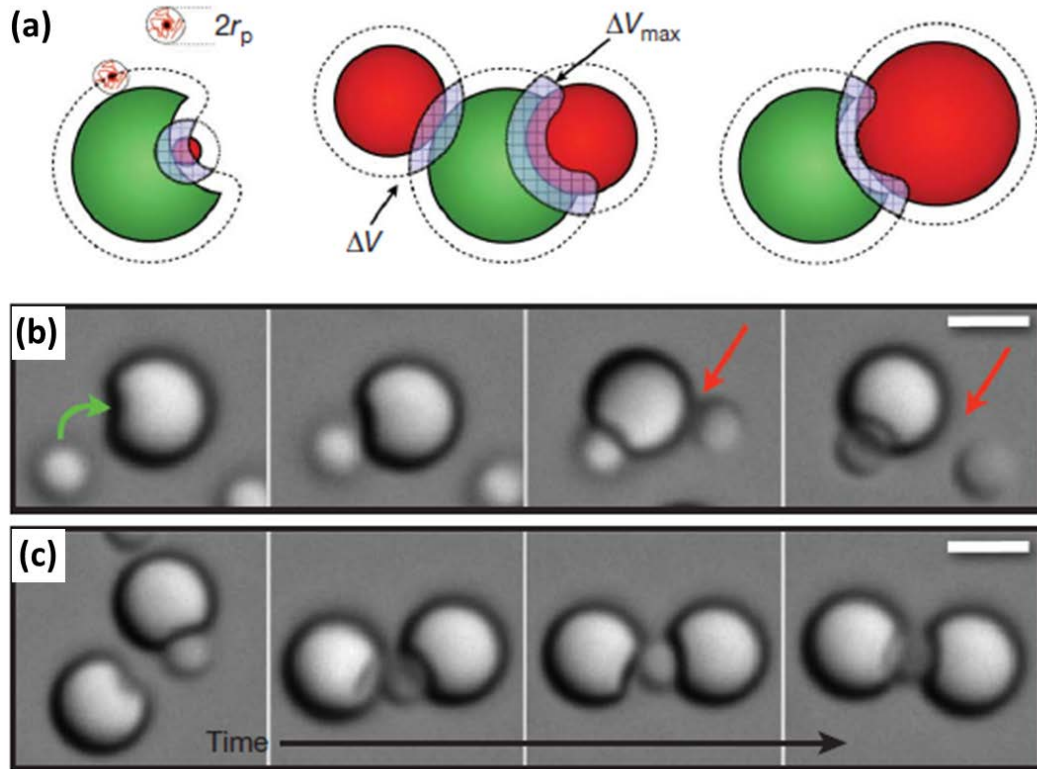
Figure 2.7. (a) Lock-key interaction of colloid particles is determined by overlapping volume between the lock and key particles. (b) Optical microscopy images for illustrating successful and unsuccessful lock-key bindings. (c) Development of a multiple lock-key system with time.[24] Reproduced with permission from Ref 24.

Another typical example for directing assembly of colloid particles is the building of colloidal kagome lattice reported by Chen et al.[25] The spherical colloid particles they designed are electrically charged in the equator section and decorated with hydrophobic patterns on the two opposite poles of surfaces. These particles also are referred to as

triblock Janus particles, which can be induced to self-organize into two dimensional kogome lattice, driving by the hydrophobic attraction at the two poles and electrostatic repulsion in the equators (see Figure 2.8).
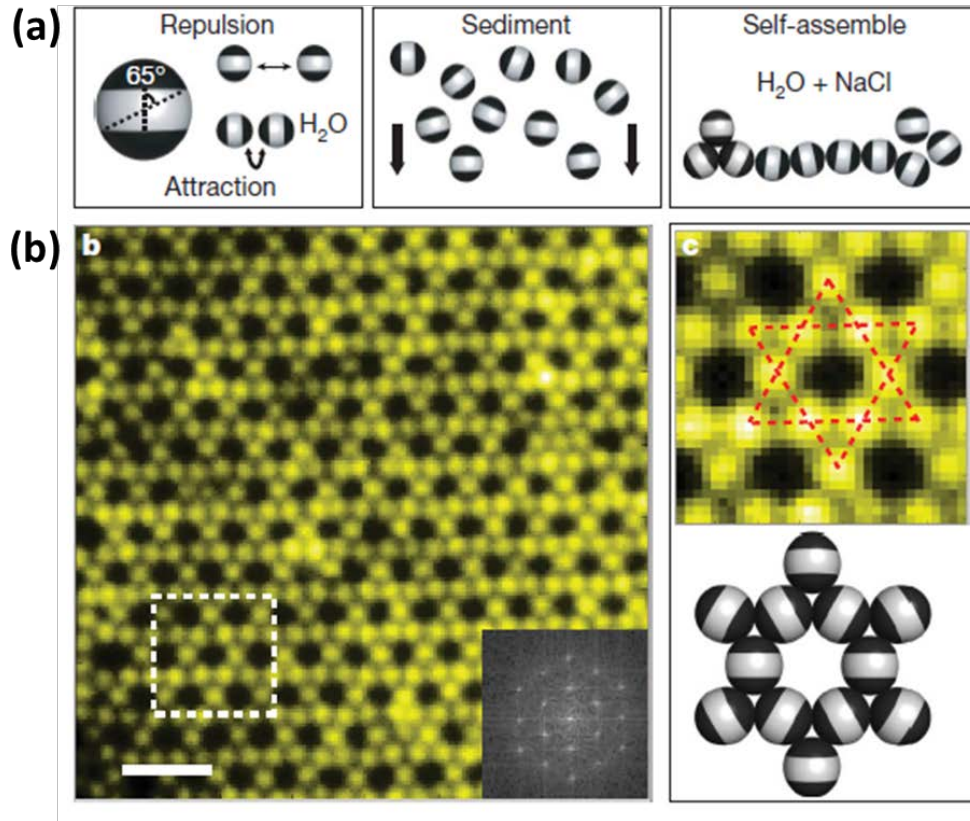
Figure 2.8. (a) The triblock Janus colloidal particles with hydrophobic coating on the poles and charged surfaces in the middle; (b) the formation of kagome lattice.[25] Reproduced with permission from Ref 25.

2.2 Self-assembly Beyond Fundamental Building Blocks

Over the past several decades, tremendous efforts have been made on utilizing above-mentioned four fundamental building blocks as the basis to self-assemble into a variety of nanostructures with different shapes and compositions, and further to fabricate

nanomaterials with particular properties and functions. With the fleeting revolution of the science and technologies in recent years, higher demands have been brought up for next generation materials, which are expected to equip more precise structures, more advanced properties and more diversified availabilities for specific applications. To approach this goal, many novel fundamental building blocks with distinct shape and anisotropic interactions are proposed and utilized as the "atom" and "molecules" to build up today's and even tomorrow's advanced materials by assembling them into useful hierarchical structures.[26] A new excitement to this field has been brought as we recognize the potential importance of these anisotropic building blocks for engineering the targeted materials with complex structures and desirable properties. Thanks to the unprecedented revolution in computer science and technologies, a myriad of new building blocks have been designed by computer simulation and their intriguing self-assembly behaviors have been theoretically predicted. [3, 27, 28]

(a) Patchy particles

(b) Assembled Structures
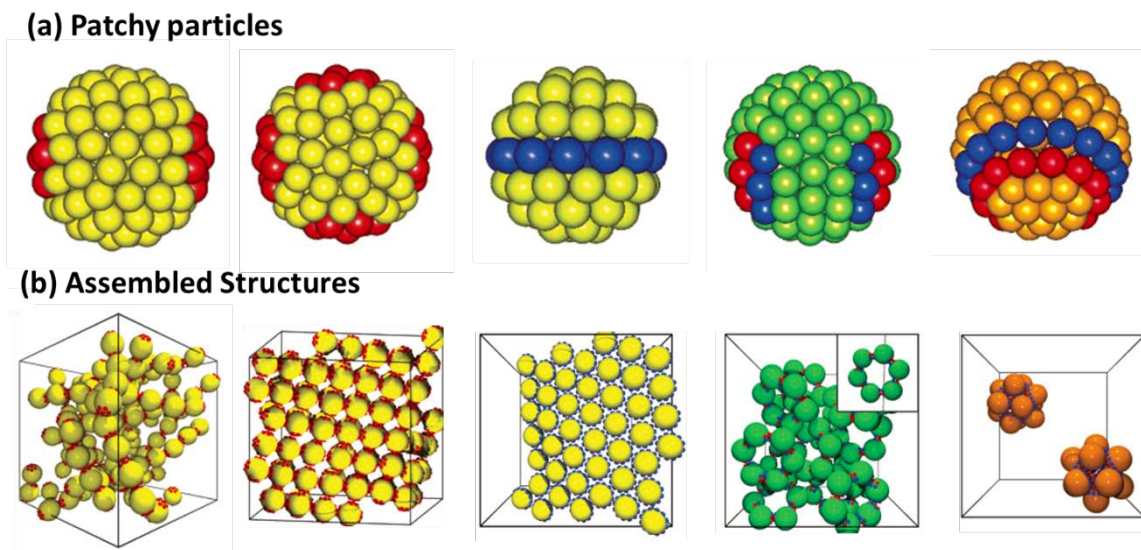
Figure 2.9. (a) Patchy particles and (b) their corresponding assembled structures predicted by computer simulation, which are chains, sheets with a square or hexagonal packing, rings and icosahedra.[28] Reproduced with permission from Ref 28.

One of typical examples of novel building blocks is patch particles, whose surface are elaborately introduced discrete and attractive interaction sites.[28] The asymmetric, selective and directional interactions between patchy particles can results in unconventional assembled structures. For example, a series of patchy particles with different number, shape and position of patches were designed by Zhang et al.[28, 29] The results of computer simulation demonstrate that these patchy particles can self-arrange into various assembled structures such as chains, sheets with a square or hexagonal packing, rings and icosahedra and so on (Figure 2.9 b). For the shape of patchy particles, it is not necessary to be spherical. Many non-spherical patchy particles and their corresponding assembled structures have also been systematically studied in their work.[28, 30]

In addition to patchy particles, computer simulation also successfully predicts rich assembly behaviors of "shape amphiphiles", which is a type of novel building blocks created by attaching tethers to nanoparticles at precise location.[31] For instance, it was demonstrated that a shape amphiphiles consisting of a spherical rigid nanoparticle as a head tethered by one soft matter flexible chain as a tail form micelles when the nanoparticles are solvophilic and flexible chains are solvophobic. However, the formation of bilayer sheets was observed if the solvent conditions are reversed such that flexible chains are solvophilic and the nanoparticles are solvophibic (Figure 2.10 a). For the shape amphiphiles composed of two different flexible chains, monolayer sheets and hexagonally arranged cylindrical shells can be formed depending on nanoparticles concentration and system temperatures (Figure 2.10 b).

While the great successes have been achieved by computer simulations, it remains to be a challenging goal in material science to experimentally construct the novel building block and study their assembling behaviors. It is mainly due to difficulties in developing appropriate model systems, which are expected to process definite shape, anisotropic symmetry, precisely defined molecular structures, architectures as well as topologies. Our group recently aims at developing these novel building blocks and directing their assembly into various hierarchical structures in solution, bulk and thin film states. The emergence of "giant molecules" provides an excellent opportunity to achieve this goal, and open a new door for engineering nanostructures with domain size below 10 nm.

(a)

Micelles   Bilayers

(b)

Monolayers   Cylinders
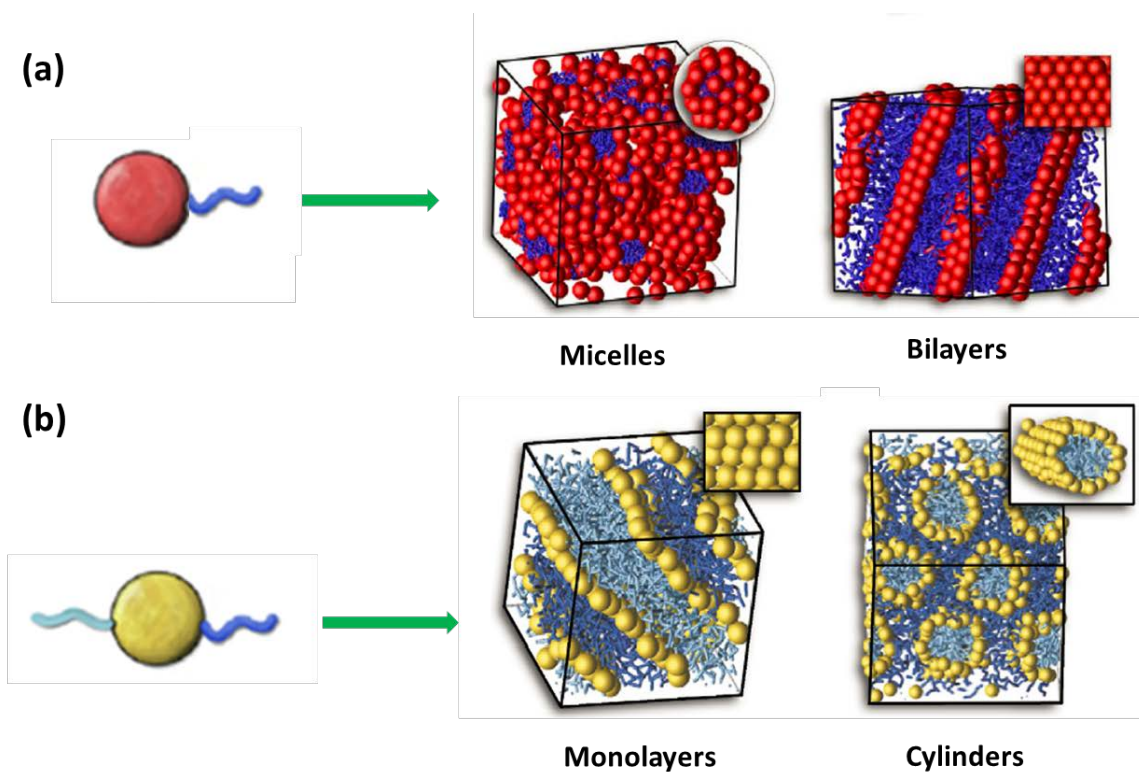
Figure 2.10. Shape amphiphiles and their corresponding predicted assembled structures formed in different conditions.[31] Reproduced with permission from Ref 31.

2.3 Molecular Design and Assembly of Giant Molecules.

In general, the word of "giant molecules" has been used to describe molecules with large molecular weight or regarded to those chemical structures containing a huge number of atoms.[32-35] It has to point out that the concept of "giant molecules" we proposed is different from their traditional meaning. The word of "giant molecules" used here is referred to precisely defined macromolecules made from molecular nanoparticles (MNPs) subunits or its conjugates with other molecular nanobuilding blocks.[36] They were originally derived from the amplified size of small molecular analogues, but built from MNPs as "nanoatoms".

2.3.1 Molecular Nanoparticles as "Nanoatoms"

Bottom-up based self-assembly approach has achieved great successes in creating hierarchical supramolecular structures across various length scales. For building up materials, this approach generally starts from regular atoms, which are chemically connected by chemical bonds to form molecules. Supramolecular structures arising from assembly of molecules provide a versatile platform to bridge molecules and materials. In other words, the hierarchical supramolecular structures play a critical role in transferring microscopic functionalities of molecules to macroscopic properties of bulk materials (Figure 2.11 up). One of the best examples for demonstrating the paramount importance of hierarchical supramolecular structures is proteins where only precise arrangement of atoms in a linear polypeptide chain with a proper folding can express a specific function. With regard to synthetic macromolecules, it is still an extremely challenging task in polymer communities to precisely control their molecular weight without any dispersity like small molecules or the definite sequence of individual monomer units with a large size like proteins. As a result, the assembly of synthetic macromolecules is not able to produce the hierarchical supramolecular structures as precise, versatile and controllable as those from small molecules or biomacromolecules.
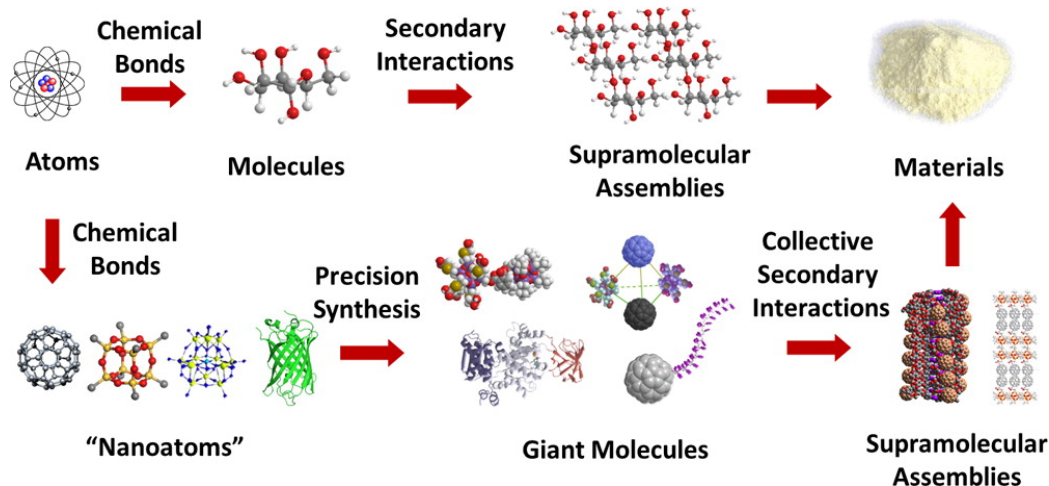
Figure 2.11. Construction of materials by two bottom-up assembly approaches from traditional molecules (up) and giant molecules (down).[36] Reproduced with permission from Ref 36.

To this end, our group has made great efforts along this direction by using the nanoatom-based giant molecules. The design of giant molecules mimics the molecular topologies of small molecules but with amplified sizes, since the size of nanoatoms is much larger than that of traditional atoms. Starting from nanoatoms, giant molecules will be obtained by precise synthesis such as "click" chemistry (this will be further discussed later). The as-prepared giant molecules will serve as building blocks to establish the hierarchical assembled structures by collective secondary interactions, which are expected to be much stronger than that exists between small molecules due to the multiple functional groups carrying on each nanoatom. Finally, materials with tunable properties will be afforded on the basis of the hierarchical assembled structures (Figure 2.11 bottom)

45

To construct the giant molecules, the first step is to seek for appropriate basic building blocks as nanoatoms. The nanoatoms we used are MNPs with persistent volume and shape, well-defined molecular structures, specific symmetry as well as modifiable functionality. Typically, they include, but are not limited to, polyhedral oligomeric silsesquioxane (POSS), [60]fullerene (C_{60}), polyoxometalate (POM) and folded globular proteins. A variety of functional groups can be introduced onto these MNPs via many synthetic methods such as site-selective mono-functionalization, regio-selective multi-functionalization as well as simultaneous multisite functionalization.

Since the focus of this dissertation is C_{60}-based giant molecules, only C_{60} will be discussed in following part. The other three MNPs including POSS, POM and folded globular proteins will be briefly introduced here. POSS is a silica nanocage with a diameter of ~ 1 nm. There are many members in the family of POSS with diversified size, symmetry and architectures, among which T_8 POSS (Figure 2.12) is the most widely used one.[37] On the surface of T_8 POSS, there are eight reaction sites that can be selectively functionalized with tunable functional groups. POMs are a class of anionic nanoclusters with rigid 3D molecular framework formed by early-transition metals.[38] Similar to POSS, the members of POMs family vary in size, shape, composition and symmetry. Lindquist, Keggin and Anderson are three most typical types of POMs. For folded proteins, while hundreds of them might be considered as the candidates of MNPs, those with enough thermal stability (such as surviving in boiling water) can be experimentally employed as ideal nanoatoms for constructing giant molecules.[39, 40]
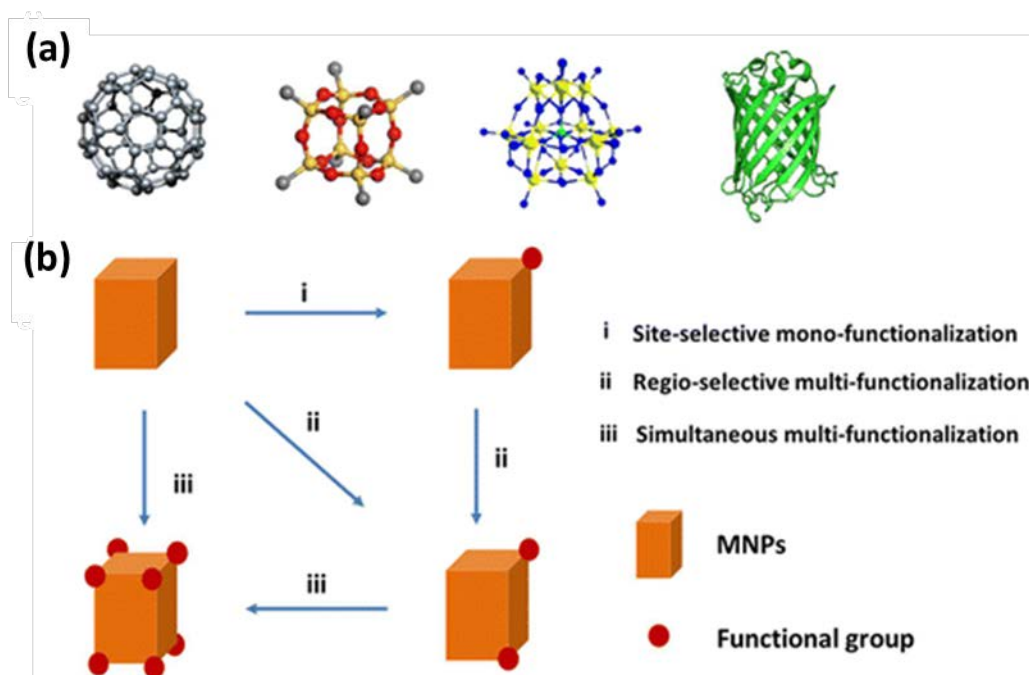
Figure 2.12. (a) Schematic illustration of four typical MNPs, including C_{60}, T_8 POSS, POM and a folded globular protein from left to right; (b) functionalization strategies for MNPs.[36] Reproduced with permission from Ref 36.

2.3.2 [60]Fullerenes (C_{60})

Fullerenes are a unique class of spherical molecules consisting solely of carbon atoms connecting by five- and six-member rings in a conjugated π system. As a class of carbon allotropes, fullerenes contain many members differentiating in the number of carbon atoms ranging from 60, 70, 76, 78, 80, 82, 84, even up to 100. Fullerene containing 60 carbon atoms is known as C_{60} or buckyball with a diameter about 1.1 nm, which is the smallest stable, the most abundant, and the highest symmetric fullerene.[41] A huge number of studies have been focused on fullerenes since the buckminsterfullerene was discovered in 1985,[42] among which major attentions have been paid on C_{60}.[43-46] This

is because of not only their amazing molecular structures with high symmetry, persistent volume and shape, but also excellent properties in electrical,[47-50] optical,[51, 52] magnetic,[53, 54] and biological applications.[55-57]

The molecular structure of C_{60} is a truncated icosahedron containing twenty pentagonal and twelve hexagonal rings. Each carbon atom has identical chemical environment, located at the intersection of one pentagon and two hexagons. There are two types of carbon bonds on C_{60}. One is double bonds between two six-member rings ([6,6]-bonds); the other one is the single bond joining between a five-member ring and a six-member ring([6,5-bonds]). The deviation from planar double bonds and the driving force to relieve the large ring strain endow the rich reactivity of C_{60}.[58] Therefore, a variety of synthetic approaches have been developed to functionalize C_{60}, such as [1+2] cycloaddition, [2+2] cycloaddition, [3+2] cycloaddition, [4+2] Diels-Alder cycloaddition, Bingel-Hirsch reaction, R_h-catalyzed arylation and so on (Figure 2.13), among which Bingel-Hirsch reaction is one of the most important methods for cycloaddition to [6,6] double bonds. Various stereo-chemically well-defined adducts ranging from monoadducts to hexakiadducts can be synthesized by Bingel-Hirsch reaction. Importantly, monoadducts and hexakiadducts can be obtained with precisely defined structures without containing others isomers, while for the other adducts the mixtures of isomers are always produced by Bingel-Hirsch reaction. It is worth noting that hexakiadducts of C_{60} possess T_h-symmetrical structures, resembling array of an octahedral in the core of C_{60} where six [6,6] double bonds are arranged at the six vertices (Figure 2.14). Considering their unique molecular structures, outstanding physical and chemical properties, C_{60} has been regarded as an ideal nano-motif for constructing giant molecules. The nanoatoms

48

designed in this dissertation are all C_{60} hexakiadducts that are derived from further functionalization of monoadducts.[59]

CARBENE ADDITION
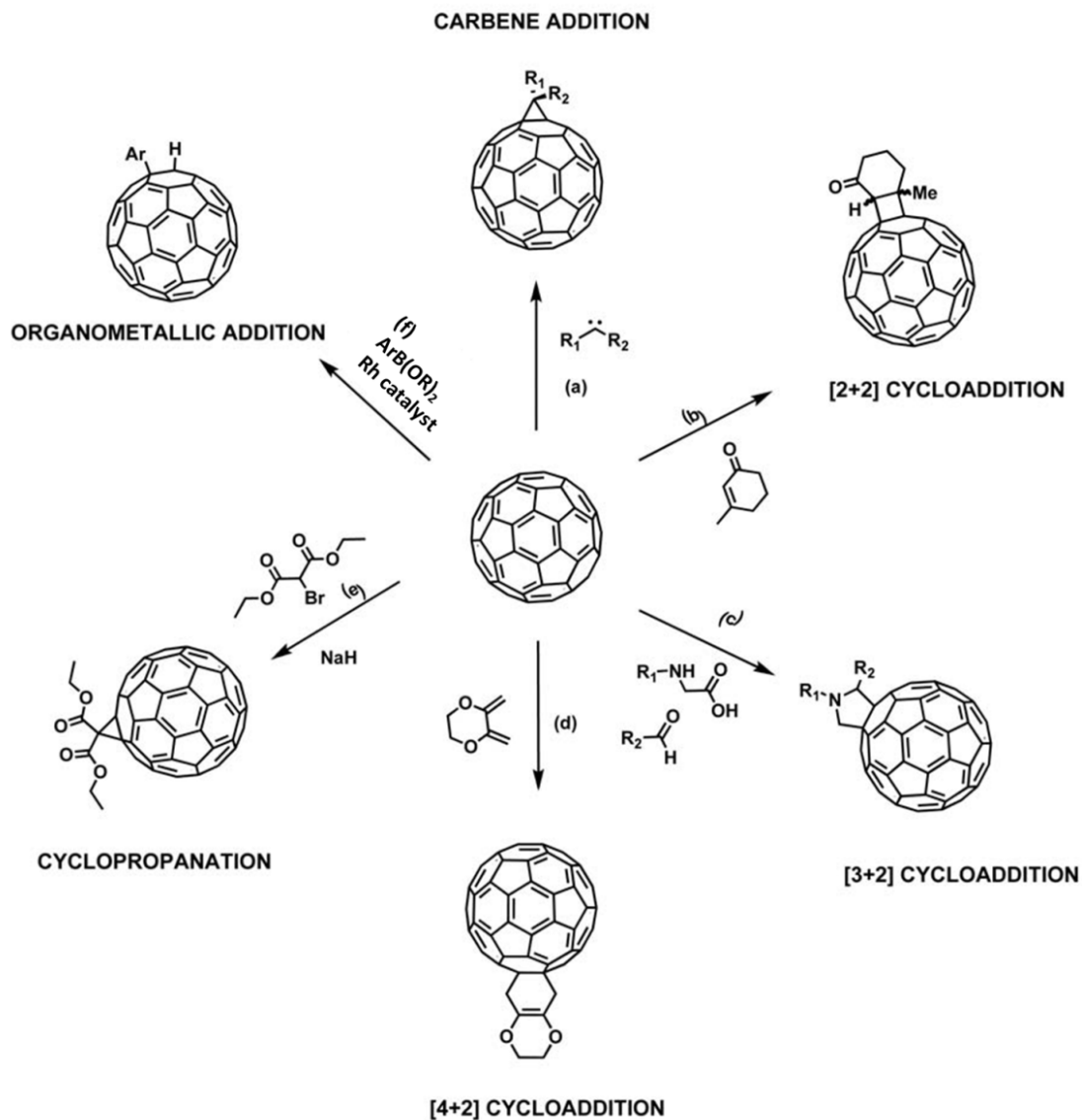
Figure 2.13. Exemplary synthetic approaches for functionalization of C_{60}.[58] Reproduced with permission from Ref 58.
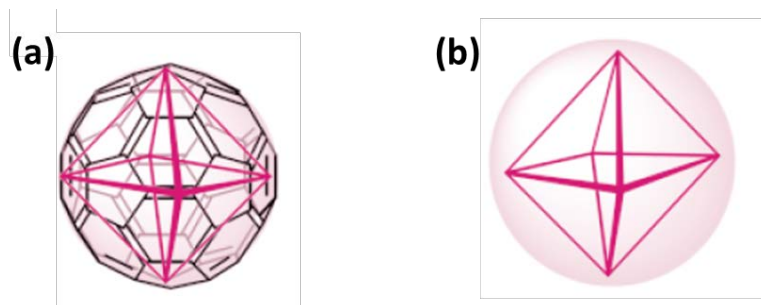
Figure 2.14. (a) VB-Structure of C_{60} where six [6,6] double bonds are arrayed at six vertices of a pseudooctahedra and (b) schematic illustration of the T_h-symmetrical structure.[59] Reproduced with permission from Ref 59.
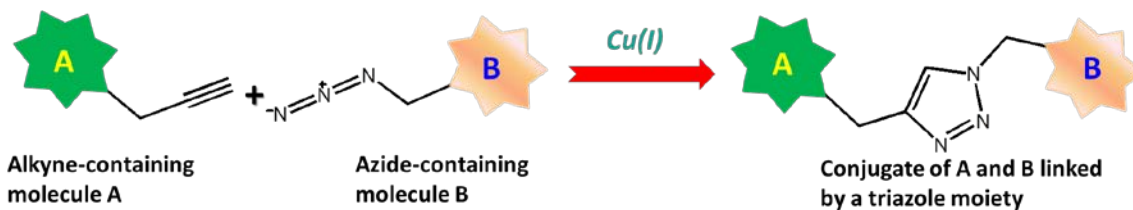
Figure 2.15. Schematic illustration of copper(I)-catalyzed [3+2] azide-alkyne cycloaddition (CuAAC) "Click" reaction.

2.3.3 From Nanoatoms to Giant Molecules

With nanoatoms available, the next step is to construct giant molecules. Considering the large size of nanoatoms and the involvement of multiple functionalities, traditional synthetic approaches can't allow us to accurately control the molecular structures, composition and architectures of giant molecules. Fortunately, the emergence of "click" chemistry provides us a feasible and versatile tool to conquer this difficulty. Click chemistry is referred to those idea reactions characterized by high efficiency, mild reaction condition, high yields, and requiring simple or no workup procedures for

purification.[60] Typical click reactions include copper(I)-catalyzed [3+2] azide-alkyne cycloaddition (CuAAC),[61] strain-promoted azide−alkyne cycloaddition (SPAAC),[62] thiol-ene reaction,[63, 64] oxime ligation,[65] Diels-Alder reaction.[66] Among these click reactions, CuAAC is perhaps the most popular and the most widely used one, which will be applied to synthesize most of giant molecules designed in this dissertation. Figure 2.15 gives a very simple but straightforward demonstration of CuAAC.

Typically, giant molecules can be categorized into three major classes, including "giant surfactants", "giant shape amphiphiles" and "giant polyhedral" (see Figure 2.16). While the classification may not be very strict and perhaps certain overlap exists among these three categories, this categorization is based on the essential features of molecular structures, aiming to provide a guideline for further molecular design.

Analogous to small molecular surfactants containing polar head group and nonpolar flexible alkyl chain tail(s), giant surfactants are the first category of giant molecules composed of MNPs tethered by polymeric tails. Giant surfactants capture the essential features of small molecular surfactant but with amplified sizes that are comparable to amphiphilic macromolecules. Similar to prototype of small molecular surfactants having various molecular architectures such as bola-form-like, gemini-like, zwitterionic, multi-headed and multi-tailed surfactants, their analogues of giant surfactants can be readily designed by independently tuning the number, functionalities, compositions, as well as architectures of MNP head and polymer tails. A variety of giant surfactants have been developed in our group, some of which is shown in Figure 2.16 (a). It has to be pointed out that monodispersed polymers should be used to prepare giant surfactants on the basis of strict definition of giant molecules. Nevertheless, it is

51

extremely difficult to synthesize single-molecular-polymer, let alone controlling their compositions, molecular length and architectures. Narrowly dispersed polymers that can be readily synthesized by living/controlled radical polymerization are practically used as alternatives.

The first example of the synthesis and self-assembly of giant surfactant was reported by Yu et al.[67] They used a carboxylic acid-functionalized POSS (APOSS) as head, to which a polystyrene (PS) tail synthesized via living anionic polymerization was grafted. The as-synthesized APOSS-PS forms various micellar morphologies in solution including vesicles, worm-like cylinders and spheres (Figure 2.17). The morphological transition from vesicle to sphere can be tuned by increasing the degree of ionization of carboxylic group on APOSS. More importantly, it was found that the PS chains are highly stretched in these micelle cores. This feature is different from the assembly of amphiphilic macromolecules but similar to that of small molecular surfactants, where the flexible chains are stretched in their micelle cores.

(a) Giant Surfactants
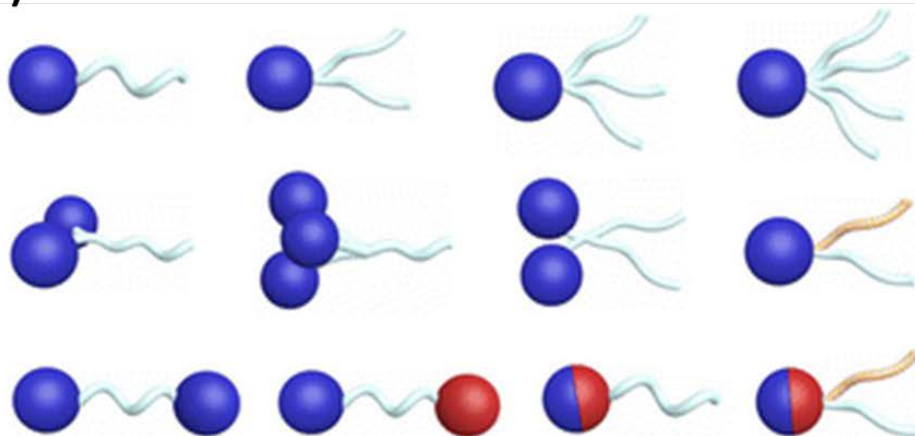
(b) Giant Shape Amphiphiles
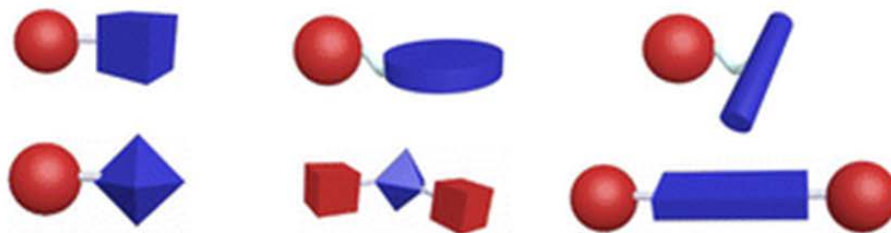
(c) Giant Polyhedra
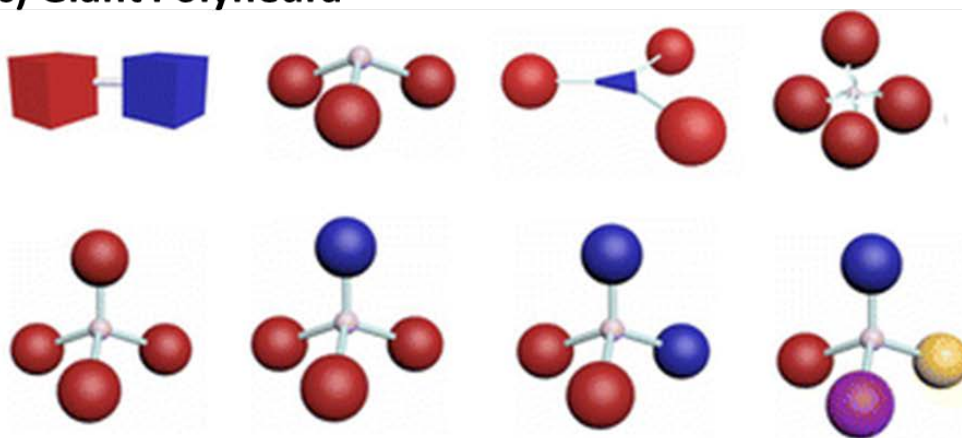
Figure 2.16. Three typical categories of giant molecules include (a) giant surfactants, (b) giant shape amphiphiles and (c) giant polyhedras.[36] Reproduced with permission from Ref 36.
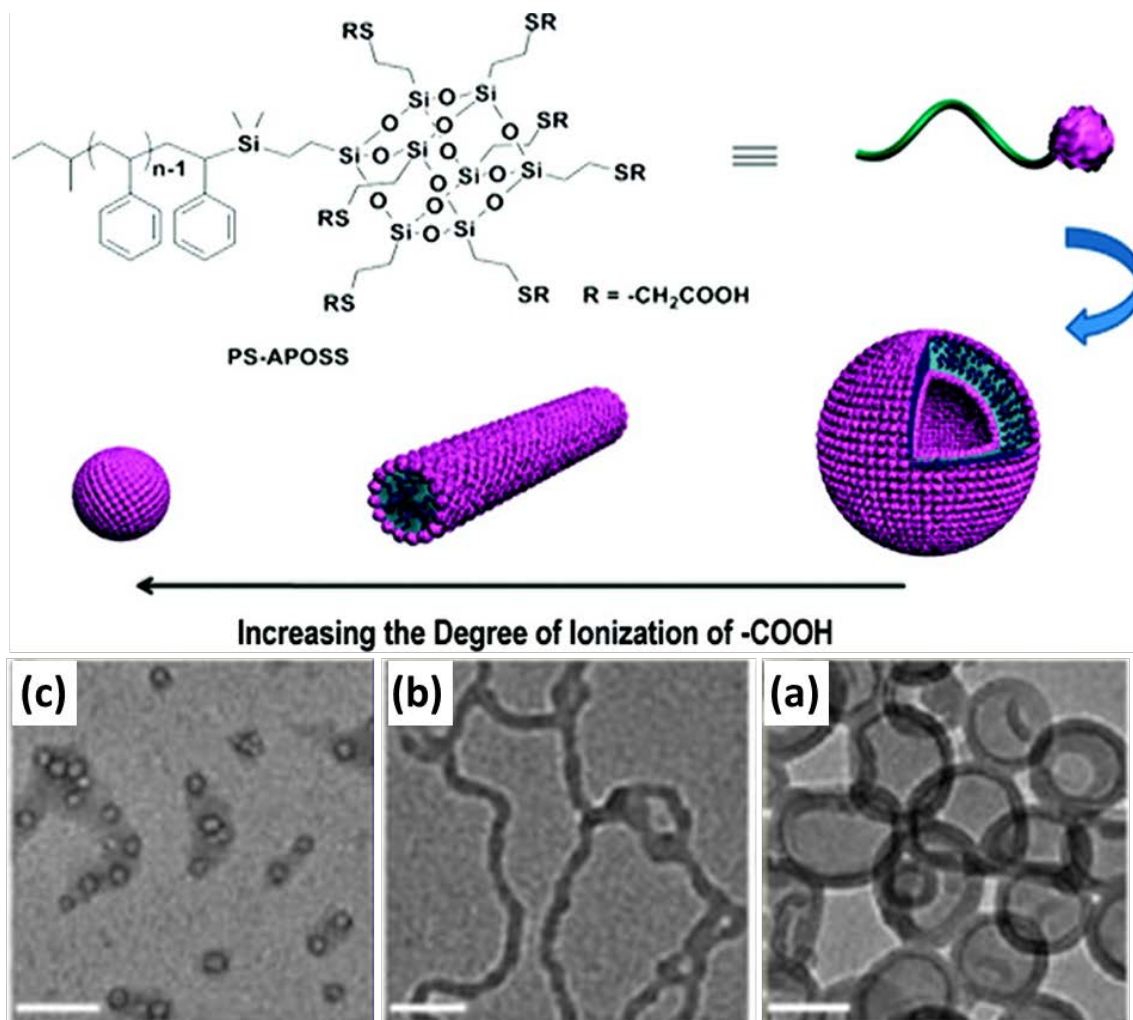
Figure 2.17. Chemical structure of APOSS-PS$_n$ and their micellar morphologies including sphere, cylinders and vesicles formed in different solvents (a) 1,4-dioxane, (b) DMF, (c) DMF/NaOH, with increasing the degree of ionization of carboxylic acid groups on APOSS.[67] Reproduced with permission from Ref 67.

Following the above work, they developed another set of giant surfactants based on C$_{60}$, namely, carboxylic acid-functionalized C$_{60}$ (AC$_{60}$) tethered by one (AC$_{60}$-PS$_n$) or two PS chain(s) (AC$_{60}$-2PS$_n$) at one junction point.[68] The hydrophilic AC$_{60}$ heads carrying ten carboxylic acid groups and one or two alkyne group(s) are [5:1]-

hexakiadducts of C_{60}, afforded by sequential Bingel-Hirsch cyclopropanation reaction. The hydrophilic PS tails with different molecular length were connected onto the AC_{60} head by CuAAC "click" chemistry. The detailed synthetic route is shown in Figure 2.18.
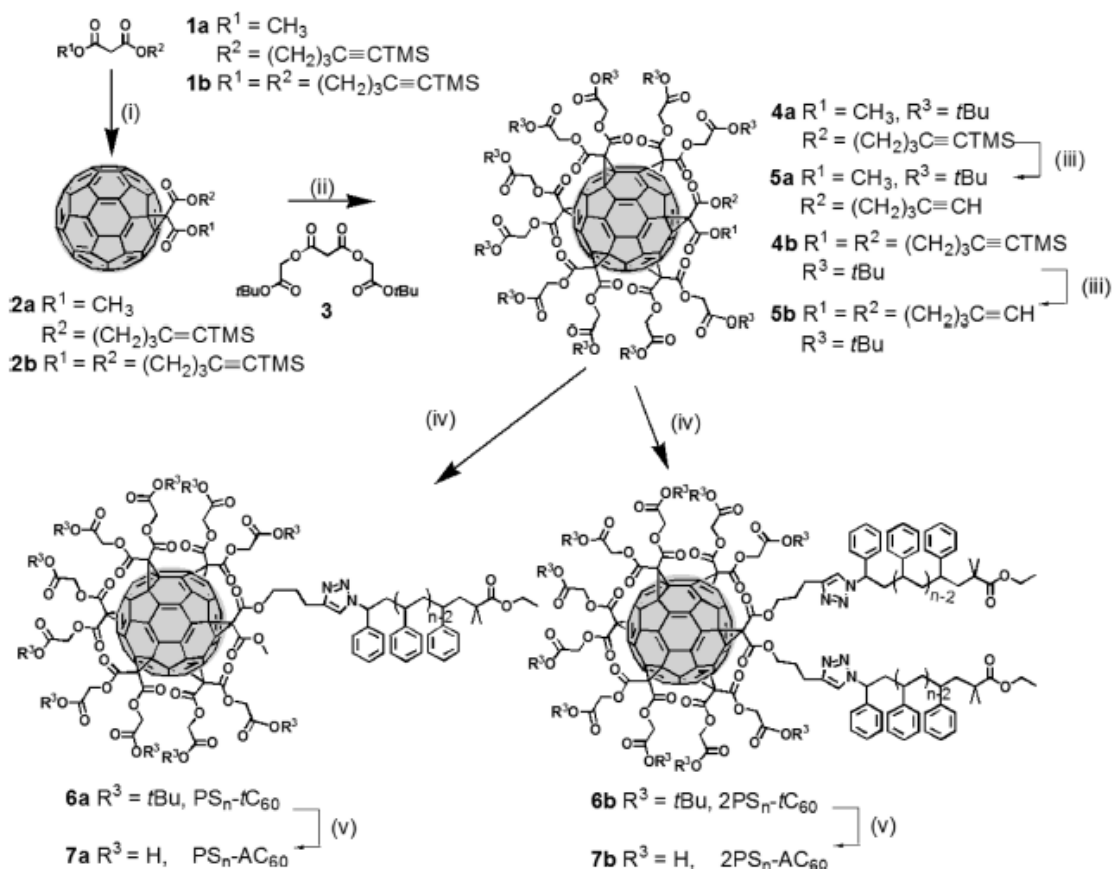
Figure 2.18. Synthetic route of AC_{60}-PS_n and AC_{60}-$2PS_n$.[68] Reproduced with permission from Ref 68.

The as-synthesized giant surfactants AC_{60}-PS_n and AC_{60}-$2PS_n$ exhibits intriguing self-assembly behaviors in solution. Various parameters affecting the assembly of giant surfactants were systematically explored, including initial molecular concentration, PS tail length, common solvents and molecular topologies. With either increasing the PS tail

length or the initial molecular concentration, a series of phase transitions from spheres, to cylinders, further to mixed morphologies of cylinders and vesicles, and finally to vesicles were observed from the self-assembly of AC_{60}-PS_n in DMF/1,4-dioxane/water system (Figure 2.19 a). The driving force of this morphological transition can be attributed to increasing the concentration of free counterions as well as the dimension of assembled aggregates. A phase diagram was established on the basis of their experimental observation (Figure 2.19 b).
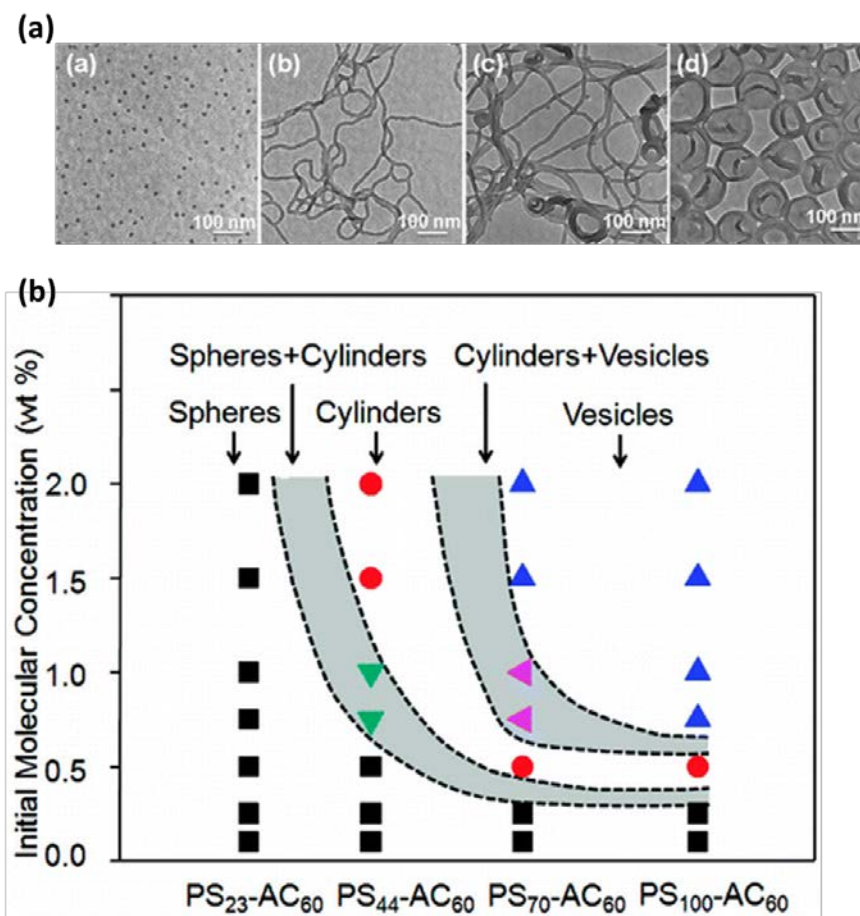
Figure 2.19. (a) Micellar morphological transition of AC_{60}-PS_n from sphere (0.1 (wt) %), to cylinder (0.5 (wt) %), to mixed morphology of cylinder and vesicle (1 (wt) %) and

finally to vesicle (2 (wt) %), with increasing initial molecular concentration; (b) phase diagram of AC_{60}-PS_n in DMF/1,4-dioxane/water relying on the PS length and the initial molecular concentration.[68] Reproduced with permission from Ref 68.
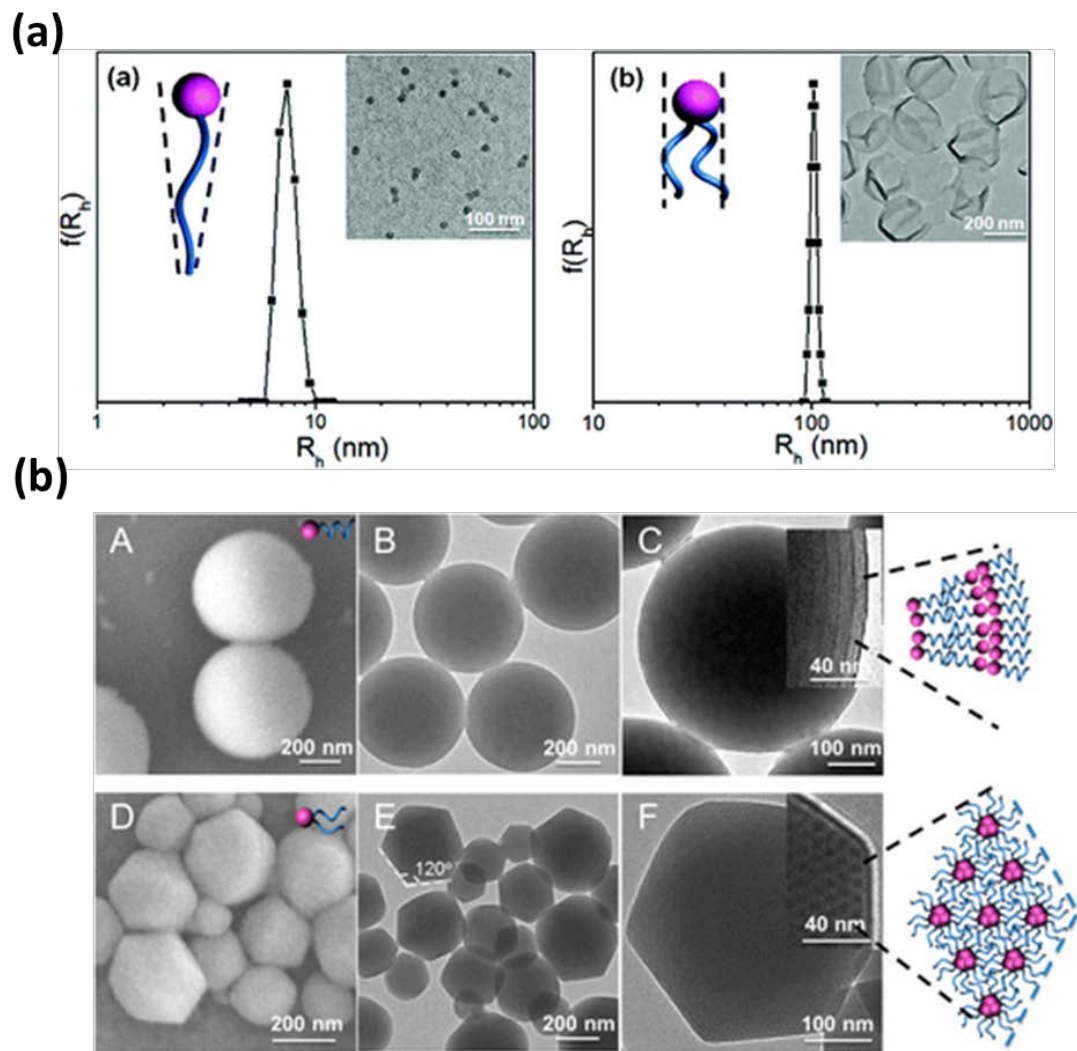
Figure 2.20. Micellar morphologies and colloid particles were formed by a pair of topological isomer AC_{60}-PS_{44} and AC_{60}-$2PS_{23}$ in (a) DMF/1,4-dioxane/water and (b) 1,4-dioxane/water.[68, 69] Reproduced with permission from Ref 68 and 69.

To study the influence of molecular topologies on assembly, they specifically designed and synthesized a pair of topological isomers containing overall identical molecular weight of PS tails but with different numbers of tails, namely, AC_{60}-PS_{44} and AC_{60}-$2PS_{23}$. It was found the assembly behavior of this set of giant surfactant is sensitive to their molecular topologies. In DMF/1,4-dioxane/water, spheres were formed by AC_{60}-PS_{44} and while vesicles were generated by AC_{60}-$2PS_{23}$ (Figure 2.20 a). The difference is associated with the molecular shape aspect ratio (P) of two giant surfactants, which is determined by the cross-section areas ratio of the head and tail (S_{head} / S_{tail}).[70] It is speculated that AC_{60}-PS_{44} possess a wedge-like molecular shape with P>1, while AC_{60}-$2PS_{23}$ have a cylindrical molecular shape with P~1. In 1,4-dioxane/water, the spherical colloid particles with onion-like inner structures were obtained by assembly of AC_{60}-PS_{44}, while the generation of double-truncated conical particles with hexagonally packing cylinders inner structures were observed from AC_{60}-$2PS_{23}$ (Figure 2.20 b). The formation of these colloidal particles can be attributed to the delicate balance between strong segregation strengths of head and tail, and the conformational rigidity of heads, which was rarely observed in traditional amphiphilic small molecules and macromolecules.[69]

In order to systematically tune the surface functionalities of nanoatoms and further design diverse giant surfactants, Kan et al developed a highly efficient and modular sequential click approach combining grafting-to and post-functionalization strategies to synthesize POSS-based giant surfactants with a variety of functional groups (Figure 2.21).[71] Polymeric tails were tethered onto a VPOSS head carrying seven vinyl groups by first "click" reaction. Various functional groups such as carboxylic groups or hydroxyl

groups can be installed on the VPOSS periphery via second click-type thiol-ene reaction, achieving systematic variation of functionalities on the head of giant surfactants.
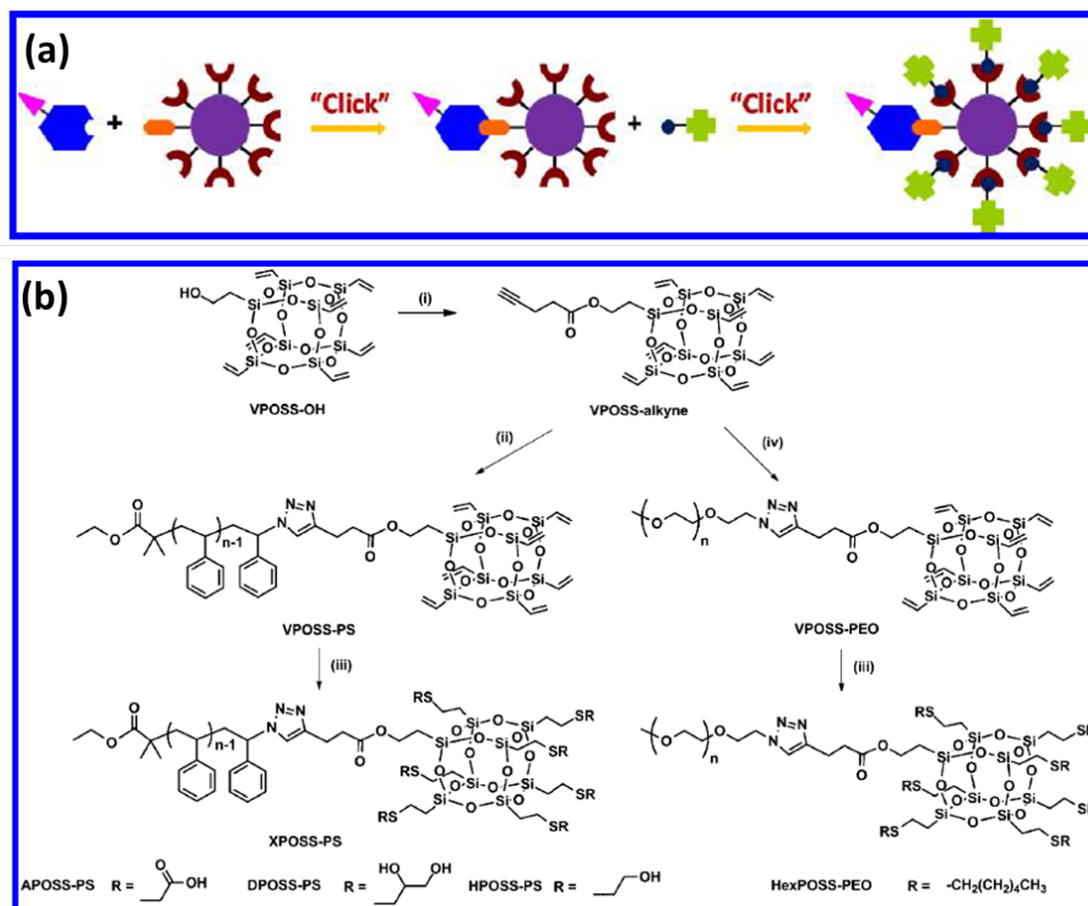
Figure 2.21. (a) Schematic illustration of sequential "click" approach; (b) synthetic route for XPOSS-PS.[71] Reproduced with permission from Ref 71.

The as-prepared giant surfactants composed of a DPOSS functionalized by fourteen hydroxyl groups tethered by one PS tail undergoes nanophase separation and assemble into a variety of ordered structures in bulk, including lamellae (Lam), double gyroids (DG), hexagonally packed cylinders (Hex) and body-centered cubic spheres (BCC). This phase transition occurs with increasing volume fraction of PS (Figure

59

2.22).[69] Notably, the feature size of these ordered structures are all around or smaller than 10 nm, which is difficult to be achieved from assemble of traditional block copolymers.
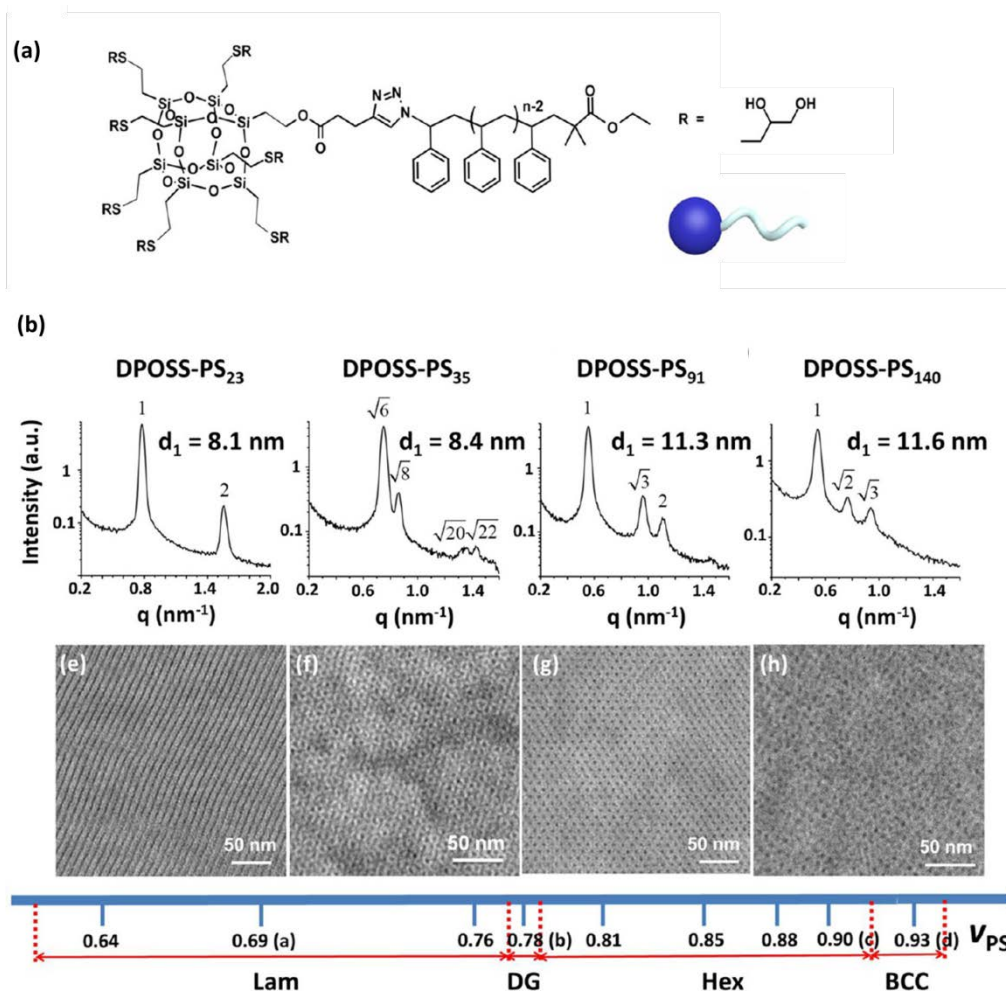
Figure 2.22. (a) Chemical structure of $DC_{60}-PS_n$ (b) ordered structures formed by self-assembly of $DC_{60}-PS_n$ with changing volume fraction of PS (from left to right: Lam, DG, Hex and BCC with increasing molecular length of PS).[69] Reproduced with permission from Ref 69.

Besides the volume fraction of PS, the resulting assembled structures of giant surfactants exhibit an exceptional sensitivity to their molecular topologies. For example,

DPOSS-PS$_{35}$ and DPOSS-2PS$_{17}$ was designed as a pair of topological isomers. It was found that the former giant surfactants form DG structures, while the latter samples create Hex structures in the same condition. Similar phenomenon was observed from the assembly of another pair of AC$_{60}$-based topological isomers in bulk, namely, AC$_{60}$-PS$_{44}$ (Lam) and AC$_{60}$-PS$_{23}$ (Hex). Such structural sensitivity is a characteristic of small molecules but less significant in macromolecules. The emergence of giant surfactants offers us a versatile platform for engineering nanomaterials and nanostructures with desirable features.

Giant shape amphiphiles are molecules composed of immiscible segments with distinct shape and competing interactions. The concept of shape amphiphiles was first termed by Date et al to describe a rod-disk conjugate.[72] This conjugate can homogenize the immiscible rod-like and disk-like liquid crystals. Later, it was used to describe a class of emerging materials consisting of building blocks possessing specific volume and shape with certain geometry, symmetry and anisotropic interaction.[31] Here, those shape amphiphiles derived from MNP-based nanoatoms will be referred to as giant shape amphiphiles. Figure 2.16 (b) exemplifies some typical molecular models of giant shape amphiphiles such as sphere-rod, sphere-disk, sphere-cube, sphere-octahedron, cube-octahedron and so on. The design of giant shape amphiphiles is not limited to these demonstrated examples only. Chemical components with other persistent shapes and precisely well-defined structures such as nanorods and gold nanoparticles can be considered as building blocks to construct giant shape amphiphiles.

Computer simulation has predicted rich assembly behaviors and diversified resulting hierarchical structures of shape amphiphiles.[31, 73-76] In recent years, many giant

61

shape amphiphiles have been experimentally explored and many unusual assembled supramolecular structures were achieved.[77-86] Here, three of them will be taken as typical examples to demonstrate the versatile self-assembly of giant shape amphiphiles.

The molecular design of first giant shape amphphile is a sphere-cubic dyad composed of a C_{60} covalently linked with a POSS functionalized by isobutyl groups.[79] Since C_{60}/POSS are organic/ inorganic nanoparticles, they are generally immiscible. The conjugation of these two types of nanoparticles via Steglich esterification results in interesting crystallization characteristics of C_{60}-POSS conjugates. They can form two different crystal structures with either orthorhombic or hexagonal packing lattices in solid state. Within both crystals, alternating bilayered structure of C_{60} and POSS are proposed (Figure 2.23). The formation of these two different types of crystals was attributed to the distinct packing orientation of POSS in the layers.
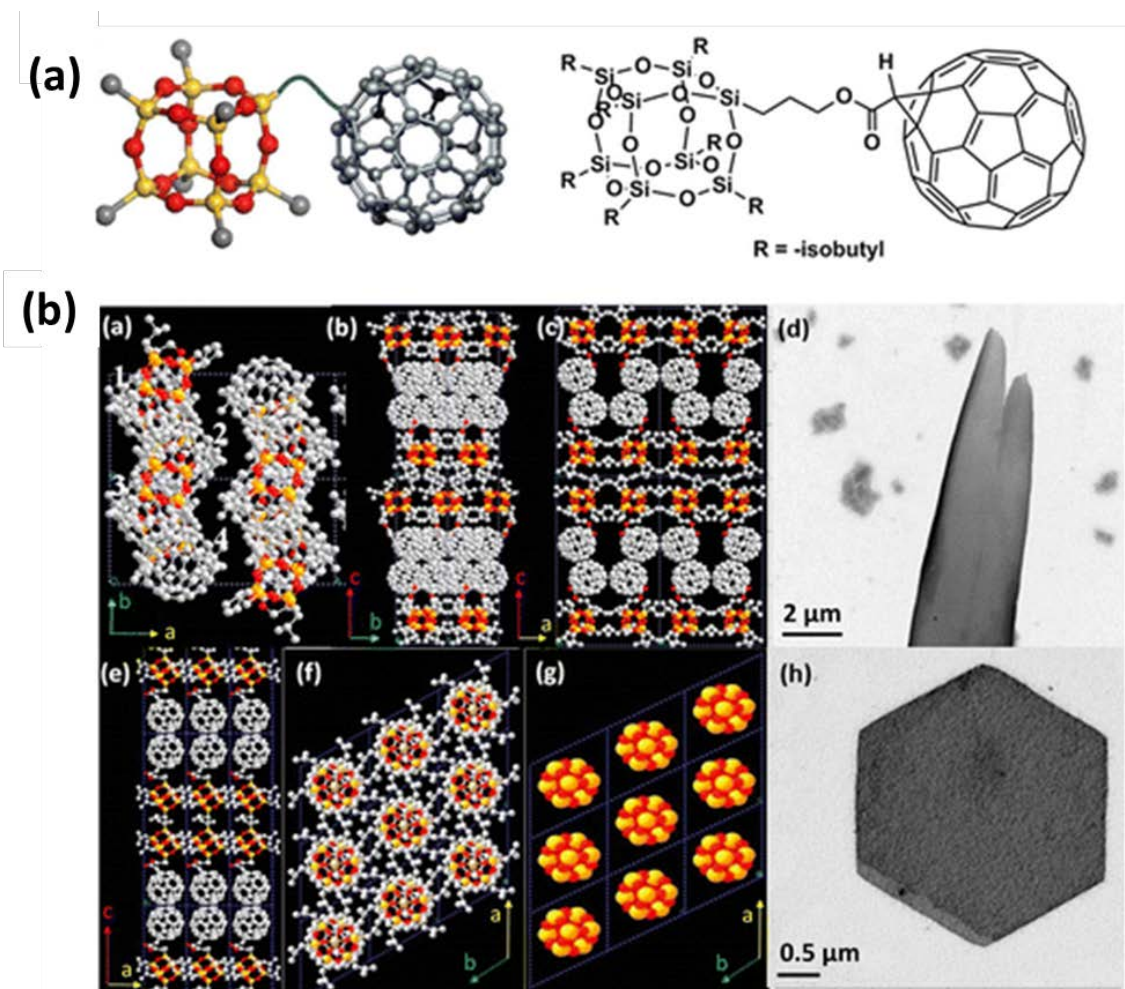
Figure 2.23 (a) Molecular structure of C_{60}-POSS giant shape amphiphiles (b) two types of crystal structures formed by C_{60}-POSS giant shape amphiphiles.[79] Reproduced with permission from Ref 79.

Secondly, Liu et al developed a set of giant shape amphiphiles using the derivatives of POSS, C_{60} and Lindqvist-type POM as nanoatoms.[80] Since the POSS derivatives (BPOSS, yellow balls in Figure 2.24) are hydrophobic and C_{60}-based and POM-based nanoatoms (blue balls in Figure 2.24) are hydrophilic and even ionized in polar solvents, these giant shapes amphiphiles are also regarded as amphiphilic Janus

particles. Driven by the crystallization of BPOSS, 2D nanocrystals with double layers of molecular packing are generated in polar solvents with an exact thickness. Stabilization of the assembled 2D nanocrystals can be attributed to strong repulsive interaction between solvents and ionized nanoatoms locating on the surface of 2D nanocrystals, preventing aggregation alone direction perpendicular to layer. Polarity of selected solvents, the number and size of counterions, and the size of nanoatoms are all critical factors determining the formation of 2D nanocrystals.
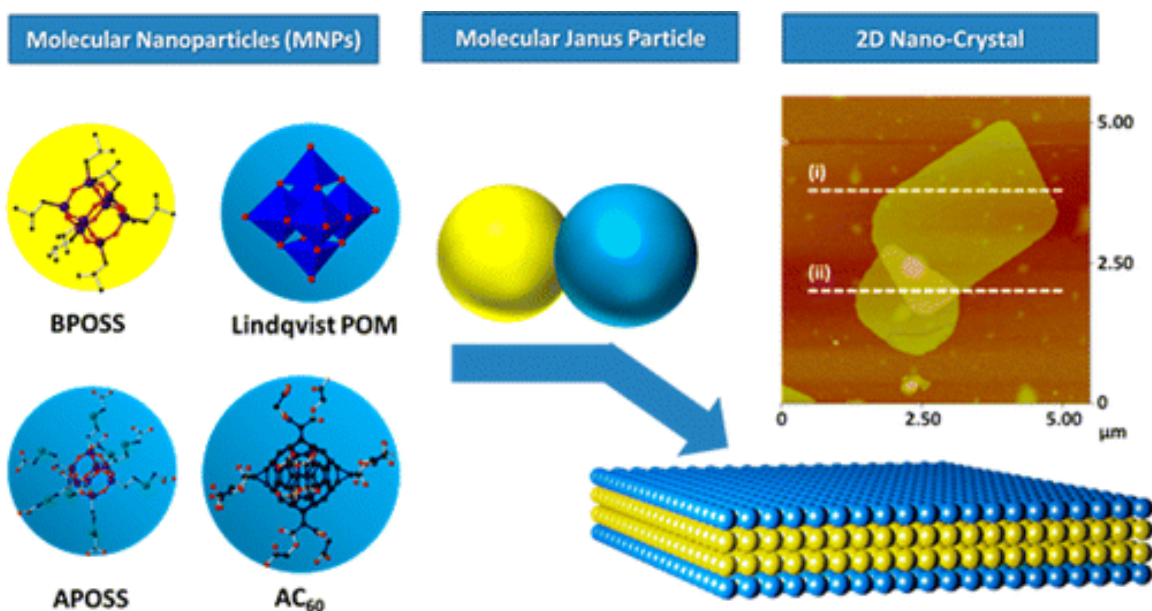
Figure 2.24. Schematic illustration of the formation of 2D nanocrystal generated by assembly of the amphiphilic Janus particles.[80] Reproduced with permission from Ref 80.
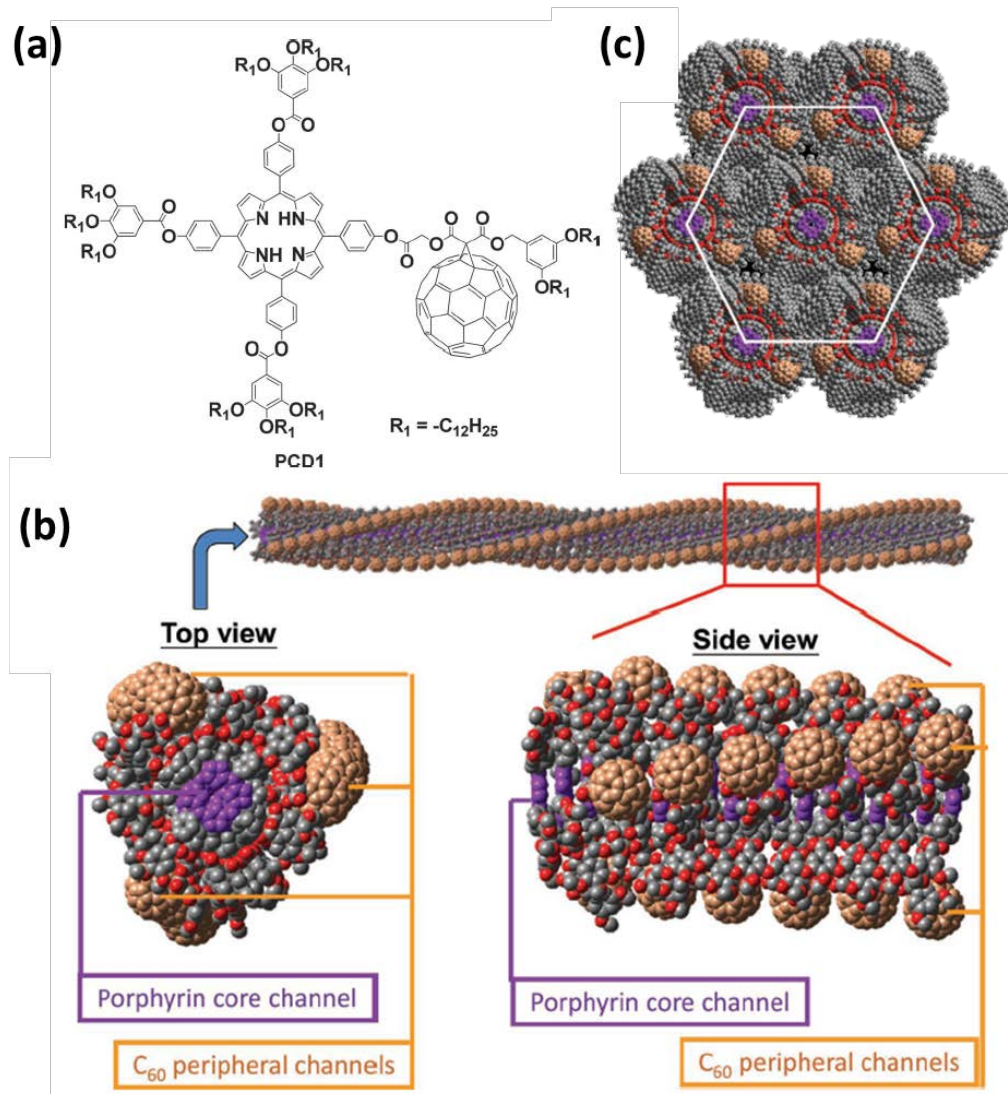
Figure 2.25. (a) Chemical structure of C_{60}-porphyrin dyad; (b) supramolecular "double-cable" helical structures; (c) hexagonally packing of double-cable columns.[86] Reproduced with permission from Ref 86.

The third example of giant shape amphiphiles is a C_{60}-porphyrin dyad.[86] It was observed this sphere-disk-like molecules self-assembled into well-defined supramolecular "double-cable" structures with porphyrin core columnar channel

surrounding by three helical C_{60} peripheral channels, induced by the cooperative intermolecular C_{60}-C_{60} and porphyrin-porphyrin interaction. The double-cable columns further pack into hierarchical structures with hexagonally packing lattices. The C_{60}-porphyrin and resulting hierarchical structures possess long lifetime as photogenerated carriers due to separated connecting channels as well as large C_{60}/ porphyrin interface.

Different from giant surfactants and giant shape amphiphiles usually using flexible spacers to link nanoatoms, giant polyhedra are built up from nanoatoms covalently connected by rigid linker to endow a specific molecular shape. For example, a giant tetrahedron can be obtained when we place four nanoatoms at four apexes of a tetrahedron. Interestingly, chirality can be involved in a giant tetrahedron if four nanoatoms possessing different functionalities. Additional unique hierarchical structures with propagation of chirality may be created by the self-assembly of these chiral giant polyhedra. It has to be point out that given their particular molecular shape, diverse assembly behavior may be feasible even when the difference in functionalities of nanoatoms is absent for one giant polyhedra.[87] Nevertheless, due to the grand challenge in synthesis of giant polydedra, experimental investigations on this class of material are scarce in literatures so far. To the best of my knowledge, the only one example is demonstrated by Huang et al in their recent publication.[88] The details about this work will be discussed in the following section.

They designed a family of novel giant tetrahedra by placing different POSS (hydrophilic or hydrophobic) at the four vertices of a rigid tetrahedral core. Hydrophobic POSS (BPOSS) are functionalized by isobutyl groups, while hydrophilic POSS are functionalized by either hydroxyl (DPOSS) or carboxylic acid (APOSS) groups. Based

on the number of hydrophilic and hydrophobic POSS containing in one molecule, these giant tetrahedra can be classified into four categories, namely, four hydrophobic POSS (A_4), three hydrophobic POSS with one hydrophilic POSS (A_3B_1), two hydrophobic POSS with two hydrophilic POSS (A_2B_2), one hydrophobic POSS with three hydrophilic POSS (A_1B_3), as shown in Figure 2.26. They were synthesized by sequential "click" reactions. All of them possess precisely defined chemical structures without any dispersity.
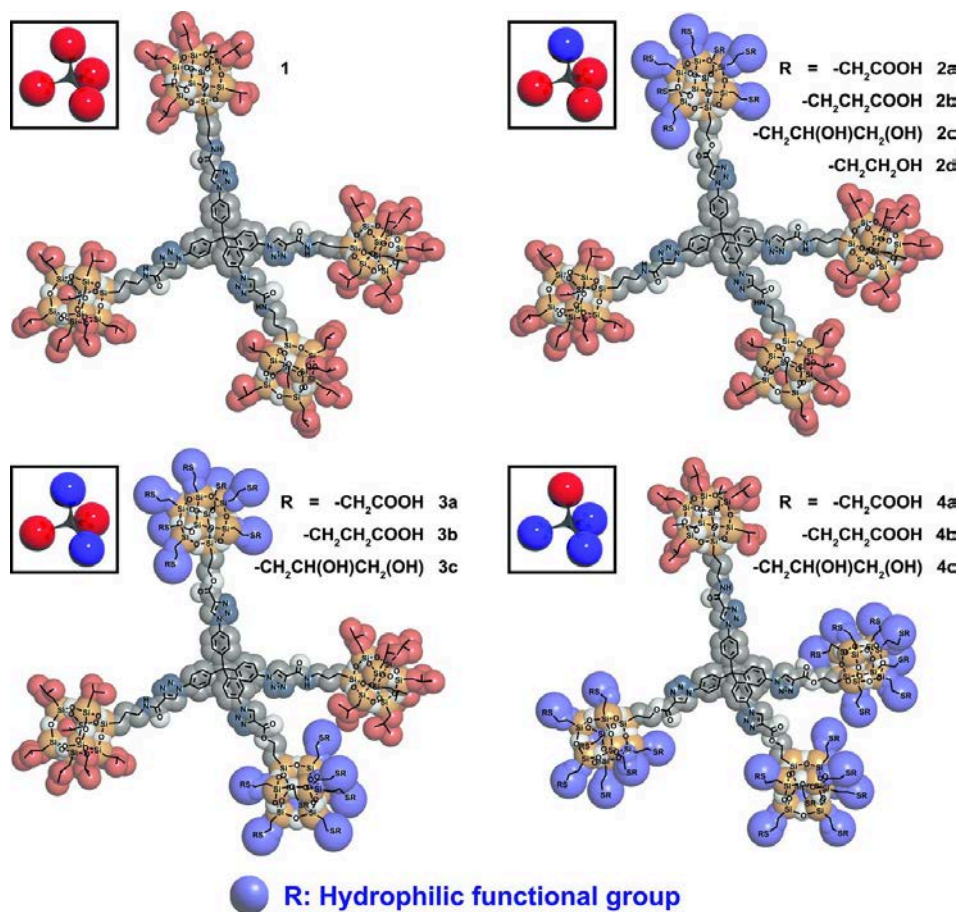
Figure 2.26. Chemical structures and molecular models of various giant tetrahedrals. where the blue and red spheres in the inserted boxes represent the hydrophilic and hydrophobic POSS.[88] Reproduced with permission from Ref 88.

Figure 2.27 summarizes the self-assembled hierarchical structures generated by various giant tetrahedras and the corresponding assembly mechanism. For A_4 molecules containing four hydrophobic POSS, a crystalline structure with a triclinic unite cell was obtained. As BPOSS has strong tendency to crystallize, this crystalline structure is driven by the crystallization of BPOSS. After replacing one BPOSS with one hydrophilic POSS, A_3B_1 molecules self-organize into Lam structures at room temperature by solution evaporation. Since the volume fraction and interaction of hydrophilic and hydrophobic POSS is unmatched, the Lam has been regarded as density-frustrated Lam, the formation of which is dominated by crystallization of BPOSS either. As the temperature was risen up to the melting temperature of BPOSS crystals, a very intriguing phase transition was observed from frustrated Lam to spherical aggregates, which further packed into Frank-Kasper A15 phase (Figure 2.27 a). Two different types of spherical aggregates accommodating with different number of giant tetrahedral molecules were identified within A15 phase. Both types of aggregates have hydrophilic POSS collecting in the core and hydrophobic POSS surrounding around the corona. Compared with A_3B_1, A_2B_2 molecules are more symmetric. Normal double-layered Lam structures were found at room temperature because of the crystallization of BPOSS. When BPOSS crystals were melted at an elevated temperature, the formation of either extended Lam or DG structure was observed, depending on the functionalities of hydrophilic POSS. For A_1B_3 molecules, only inversed Hex structures with BPOSS wrapping in the core and hydrophilic POSS filling in the matrix were formed regardless of temperature. This can be attributed to the fact that once the strong collective hydrogen bonding among the hydrophilic POSS matrix, it is very difficult to be reopened as changing temperature. One the other hand,

68

the overall free energy of system tends to minimize by maximizing the contact of hydrophilic POSS. Therefore, the inversed Hex would be the most favorable phase for this set of A_1B_3 giant tetrahedra.
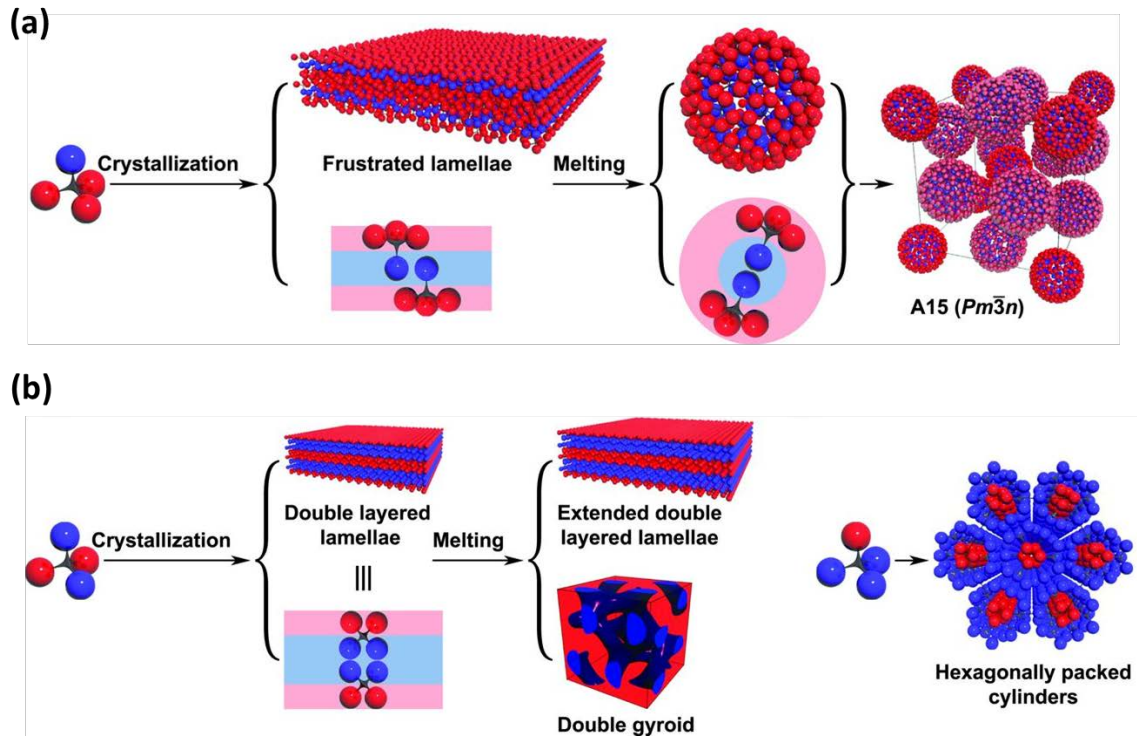
Figure 2.27. Schematic illustration of assembly of giant tetrahedral to form (a) A15 phase and (b) lamellae, double gyroid and hexagonally packed cylinders.[88] Reproduced with permission from Ref 88.

CHAPTER III

SELF-ASSEMBLY OF FULLERENE-BASED JANUS PARTICLES IN SOLUTION:

EFFECTS OF MOLECULAR ARCHITECTURE AND SOLVENT

3.1 Introduction

Since the concept of "Janus grains" was introduced by de Gennes in his Nobel prize lecture,[89] tremendous attention has been paid on their "symmetry-breaking" structures, self-assembly behaviors and unique properties.[90-92] Progresses have been made for design and synthesis of organic/inorganic micellar or colloidal Janus particles with the availability of sophisticated synthetic techniques.[93-96] In those studies, the size of these Janus particles usually ranges from hundreds of nanometers to micrometers. If a Janus grain is based on a well-defined molecular structure with nanometer size and persistent shape, it may be considered as a molecular Janus particle (MJP).[36, 92] Two symmetry breakings are involved in MJPs: geometric and chemical symmetry. Various efforts have so far been made to prepare MJPs with flexible conformations such as amphiphilic dendrimers,[97-99] block copolymers[100-102] and polymeric brushes,[103, 104] all of which canself-assemble into intriguing structures in the bulk[97] and solution.[98, 99] Yet it remains largely unexplored to construct MJPs with precisely-defined molecular nanoparticles with fixed shape, volumes and functionalities that can retain their asymmetrical geometry and chemistry during self-assembly.

Recently, molecular nanoparticles have been conceptually proposed as the elemental nano-building blocks, or "nano-atoms" for building precise macromolecules.[36] "Nano-atoms" refers to shape- and volume-persistent molecular nanoparticles such as [60]fullerene (C_{60}), polyhedral oligomeric silsesquioxanes (POSS), polyoxometalates (POM), and folded globular proteins.[36] They possess precisely-defined primary chemical structures and surface functionalities, and are ready for the precision synthesis of giant molecules utilizing efficient methods such as the sequential "click" approach.[71] MJPs based on POSS[79, 105] and POM[106] derivatives have been reported to self-organize into bilayered structures in the bulk. Yet the examples are rare. It is thus of interest to further expand the scope of MJPs and investigate how they can be directed to assemble into different hierarchical structures, and how to further promote transformations and amplifications of microscopic functionalities towards macroscopic properties.[26, 79, 107]

Among those molecular nanoparticles, C_{60} is a spherical nanoparticle with truncated icosahedral (I_h) symmetry. Surfaces of C_{60} can be precisely functionalized by regio-selective chemical reactions.[59, 108] Several C_{60}-based amphiphiles have exhibited interesting self-assembly behaviors in solution.[109-115] For instance, a series of penta-substituted fullerene potassium salt can self-assemble into bilayer vesicles in THF/water.[113-115] We have recently synthesized new C_{60} derivatives bearing ten carboxylic-acid functionalized groups (AC_{60}) and further tethered them with one or two polystyrene (PS) tails to construct a new class of "giant surfactants".[68] With increasing initial molecular concentration or the PS tail length, micellar morphologies can be tuned from spheres, to cylinders and finally, to vesicles. The PS tails have been recognized to be stretched in their micelles, similar to the feature of small molecular surfactants.[67, 68, 116]

In this chapter, we report our recent study on design, synthesis and self-assembly of two new MJPs based on C_{60}, namely, AC_{60}-C_{60} and AC_{60}-$2C_{60}$, by "clicking" a hydrophilic AC_{60} with one or two hydrophobic C_{60}. The resulting amphiphilic MJPs are expected to exhibit versatile self-assembly behaviors in different solvent systems.

3.2 Experimental Section

In this section, the synthesis, chemical structure characterization, and solution assembly procedures of two molecular Janus particles will be described.

3.2.1 Chemicals and Solvents

[60]Fullerene (C_{60}, MTR Ltd., 99.5%), methyl malonyl chloride (Aldrich, 97%), malonyl chloride (Aldrich, 97%), 5-trimethylsilyl-4-pentyn-1-ol (Aldrich, 96%), pyridine (Aldrich, 99.8%), *tert*-butyl bromoacetate (Aldrich, 98%), 3-bromo-1-propanol (Aldrich, 98%), iodine (Aldrich, 99.8%), CuBr (Aldrich 98%), 1,8-diazabicyclo[5.4.0]undec-7-ene (DBU, Aldrich, 99%), *N,N',N',N'',N''*-pentamethyldiethylenetriamine (PMDETA, Aldrich, 99%), malonic acid (Aldrich, 99%), chloroform-*d* (CDCl$_3$, Aldrich, 99.8 at %D) and dimethyl sulfoxide-d_6 (DMSO-d_6, Aldrich, 99.8 at %D) were used as received. Toluene (Aldrich, 99.5%) and 1,2-dichlorobenzene (ODCB, Aldrich, 99%) were stirred with CaH$_2$ and redistilled prior to use.

3.2.2 Characterizations

All ^{1}H NMR and ^{13}C NMR spectra were obtained using a Varian Mercury 300 or Varian NMRS 500-01 spectrometer. NMR samples were prepared with concentration of 10-15 mg/mL in CDCl$_3$ or DMSO-d_6 for ^{1}H NMR experiments or 40-60 mg/mL for ^{13}C NMR experiments. The ^{1}H NMR spectra were referenced to δ 7.27 ppm in CDCl$_3$ or δ

2.50 ppm in DMSO-d_6, and ^{13}C NMR spectra were referenced to δ 77.00 ppm in CDCl$_3$ or δ 39.43 ppm in DMSO-d_6.

Matrix-assisted laser desorption/ionization-time of flight (MALDI-TOF) mass spectra measurements were performed on a Bruker Ultraflex III TOF/TOF mass spectrometer (Bruker Daltonics, Inc., Billarica, MA), equipped with a Nd : YAG laser emitting at a wavelength of 355 nm. All spectra were collected in the positive reflection or linear mode. External polystyrene samples were used as standards to calibrate instrument prior to each measurement. *Trans*-2-(3-(4-*t*-butyl-phenyl)-2-methyl-2-propenylidene) malononitrile (DCTB) matrix (20 mg/mL in THF) was severed as matrix and sodium trifluoroacetate (NaTFA) (10 mg/mL in THF) was used as cationizing agent. They were mixed in the ratio of 10/1 (v/v). In the sample preparation, 0.5 μL of the matrix/NaTFA mixture was deposited on microtiter plate wells (MTP 384-well ground steel plate), followed by depositing 0.5 μL of each sample (10 mg/mL in THF) on top of dry matrix/NaTFA spot. Then, another 0.5 μL of matrix/NaTFA mixture was added on the top of the dry sample. After evaporation of solvent, the target plate was loaded for data collection. Data analysis was carried out using Bruker's flex Analysis software.

Infrared spectra of as-synthesized products were collected on an Excalibur Series FT-IR spectrometer (DIGILAB, Randolph, MA). Samples were prepared by depositing sample solution with concentration of about 10 mg/mL in THF onto a KBr plate, followed by drying with blowing air at room temperature to give drop-casting films. The data were analyzed using the Win-IR software.

Infrared experiments for the measurement of degree of ionization of carboxylic acids were performed on a Diffuse Reflectance Infrared Fourier Transform cell (DRIFT

cell, Harrick scientific HVC-DRP), which was attached to a Nicolet 6700 FT-IR. Samples were prepared by dropping micelle solution onto a flat aluminum foil, followed by recording the spectrometer of sample in solution state. The data were analyzed using the Win-IR software. The degree of ionization (α) can be estimated from the ratio of the intensity of the v (COO$^-$) peak to the sum of the intensities of the v (COO$^-$) and v (COOH) peaks according to the following equation:

$$\alpha = \frac{I_{v\,(COO^-)}}{I_{v\,(COO^-)} + I_{v\,(COOH)}} \times 100\%.$$

At the specified concentrations for preparing the micelles, the degree of ionization (α) of AC$_{60}$-C$_{60}$ in THF and DMF/water are calculated to be 22 % and 47 %, and the α of AC$_{60}$-2C$_{60}$ in THF and DMF/water are calculated to be 18 % and 51 %, respectively (see Figures 3.17 and 3.18).

Dynamic light scattering (DLS) experiments were carried out using a Brookhaven Instrument coupled with a Bi-200SM goniometer, BI-9000AT correlator, and an EMI-9863 photomultiplier tube for photo counting. A Meller Griot 35 mW He-Ne laser was used as light source (633 nm). A cylindrical glass scattering tube with diameter of 12 mm containing 2 mL of micelle solution was placed at the center of a thermostatic bath (± 0.1□C), into which decahydronaphthalene was added for refractive index matching. Correlation functions at 90° and other angles were recorded at 25 °C. The intensity-intensity time-correlation function G$^{(2)}$(t) of the distributed object in self-beating mode was measured.[1] It is related to the normalized first-order electric field time correlation function g$^{(1)}$(t). A Laplace inversion program, CONTIN, was applied to analyze g$^{(1)}$(t) to obtain the hydrodynamic radius, R_h, as well as its distribution. To obtain the R_h of

cylinder, the measurement was conducted at various scattering angles of 45°, 60°, 75° and 90°, and extrapolated to zero scattering angle. DLS experiments of micelles under ultrasonication were carried out at a scattering angel of 90° after treating the as-prepared micelles solution with Branson Ultrasonic 3510 for different times.

Static light scattering (SLS) experiment was carried out at scattering angles θ from 30° to 120°, at 2° intervals. To obtain the radius of gyration, R_g, a partial Zimm plot was employed to analyze the SLS data. The partial Zimm plot derives from the following approximate formula: $1/I = C(1 + R_g^2 q^2/3)$, and R_g is determined from the slop and intercept of a plot of $1/I$ vs. q^2.

Bright filed images of transmission electron microscope (TEM) were taken in a JEOL-1230 microscope with an accelerating voltage of 120 kV. Samples were prepared by depositing a small volume of as-prepared micelle solution onto carbon coated copper grids, followed by wicking away the excess solution with filter paper. After evaporation of solvent under ambient conditions, TEM images were collected on a digital CCD camera and processed with the accessory digital imaging system.

Atomic force microscopy (AFM) experiments were performed on a Dimension Icon AFM (Bruker AXS). Samples were prepared by drop-casting the micelle solution on the silica wafer. The images were taken in the tapping mode over 1×1 μm^2 at the scanning rate of 0.5 Hz.

3.2.3 General Synthetic Procedures

3-Azido-1-propanol. 3-Bromo-1-propanol (2.0 g, 14.5 mmol) was dissolved in 6 mL DMF, into which excessive sodium azide (2.83 g, 43.5 mmol) was added. After

stirring for two days at room temperature, the mixture solution was dissolved in 100 mL of CH_2Cl_2 and treated with brine for three times to remove inorganic salts. The organic layer was collected and dried over anhydrous sodium sulfate (Na_2SO_4) overnight. After removal of the organic solvent, transparent liquid product was obtained with a yield of 85%. ^{1}H NMR (CDCl$_3$, 300 MHz, ppm, δ): 3.73 (t, J = 6.0 Hz, 2H), 3.43 (t, J = 6.0 Hz, 2H), 1.82 (p, J = 6.0 Hz, 2H).
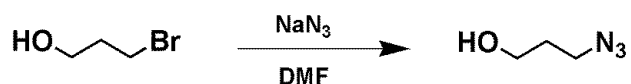
Scheme 3.1. Synthetic route of 3-azido-1-propanol.

Compound 1. 3-Azido-1-propanol (1.01 g, 10 mmol) and pyridine (0.79 g, 10 mmol) were dissolved in anhydrous CH_2Cl_2 (60 mL) at 0 °C, into which methyl malonyl chloride (1.36 g, 10 mmol) was added dropwise in 1 h. After 2 h, the mixture was allowed to warm up to room temperature, then stirred for additional 24 h. The mixture was filtered, treated with brine and dried over anhydrous Na_2SO_4 overnight. After evaporation of the solvent, the residue was purified by column chromatography on silica gel with hexanes/ethyl acetate (v/v = 4/1) as the eluent to give Compound 1 (1.53 g, 76%) as a colorless oil. ^{1}H NMR (CDCl$_3$, 300 MHz, ppm, δ): 4.25 (t, J = 6.0 Hz, 2H), 3.75 (s, 3H), 3.40 (t, J = 6.0 Hz, 4H), 1.93 (p, J = 6.0 Hz, 2H). ^{13}C NMR (CDCl$_3$, 75 MHz, ppm, δ): 166.5, 166.5, 62.5, 52.1, 47.7, 40.9, 27.7.
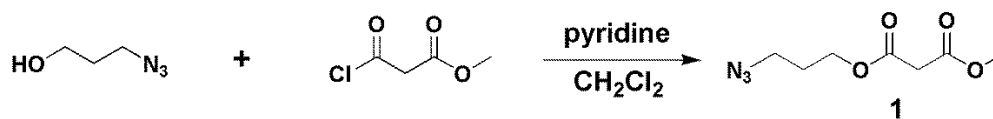
Scheme 3.2. Synthetic route of Compound 1.

Compound 2. C_{60} (200 mg, 0.278 mmol) and anhydrous toluene (200 mL) was added into a 500 mL round-bottom flask equipped with a magnetic stirrer. After dissolving completely, DBU (84.5 mg, 0.556 mmol), I_2 (70.5 mg, 0.278 mmol) and **1** (55.9 mg, 0.278 mmol) were added under nitrogen atmosphere. The mixture was stirred for 7 h at room temperature, and then concentrated and applied onto a column of silica gel that was eluted with the mixed solvent of toluene/hexanes (v/v = 2/1) to give **2** (130 mg, 51%). ^{1}H NMR (CDCl$_3$, 300 MHz, ppm, δ): 4.61 (t, J = 3.0 Hz, 2H), 4.13 (s, 3H), 3.54 (t, J = 3.0 Hz, 2H), 2.14 (p, J = 3.0 Hz, 2H). ^{13}C NMR (CDCl$_3$, 75 MHz, ppm, δ): 164.0, 163.4, 145.3, 145.2, 145.1, 145.0, 144.9, 144.7, 144.6, 143.9, 143.1, 143.0, 142.2, 142.0, 141.0, 139.2, 139.0, 128.9, 71.5, 64.1, 54.1, 48.1, 29.9, 28.2. MS (MALDI-TOF): Calcd for $C_{69}H_9O_4N_3$: 919.1; Found: 919.2 (M$^+$).

Compound 3. [5:1]-Hexakisadducts of C_{60} were synthesized by sequential cyclopropanation reactions to give the "clickable" C_{60} derivatives **3a−b**, carrying one or two terminal alkyne groups and ten protected carboxylic acid groups. The specific synthetic routes have been reported in our recent publication.[68]

C_{60}-tC_{60} (4a) and C_{60}-AC_{60} (5a). 3a (100 mg, 0.04 mmol), 2 (44 mg, 0.048 mmol), CuBr (1 mg, 0.007 mmol) and toluene (15 mL) were added into a Schlenk flask equipped with a magnetic stirrer. The mixture was degassed by three freeze-pump-thaw cycles. Then, PMDETA (10 µL) was introduced into the mixture under nitrogen protection. After one more freeze-pump-thaw cycle, the mixture was then stirred at room temperature for 24 h, and applied onto a column filled with silica gel. The column was eluted with toluene first to remove the excess Compound 2. It was then further eluted with toluene/ethyl acetate (v/v = 2/1) to give a colored fraction 4a (110 mg, 81%). Compound

4a was dissolved in mixture of CH_2Cl_2 and CF_3COOH (v/v = 4/1) and stirred for 8 h. Removal of the solvent gave 5a (85 mg, > 90%).

Compound 4a: ^{1}H NMR ($CDCl_3$, 500 MHz, ppm, δ): 4.81-4.50 (m, 22H), 4.34 (m, 2H), 4.14 (s, 6H), 3.93 (m, 2H), 2.81 (m, 2H), 2.48 (m, 2H), 2.14 (m, 2H), 1.44 (m, 90H). ^{13}C NMR ($CDCl_3$, 125 MHz, ppm, δ): 165.4, 164.0, 163.4, 162.7, 145.8, 145.3, 145.2, 145.1, 145.0, 144.9, 144.6, 143.9, 143.1, 142.2, 142.0, 141.0, 139.3, 138.7, 82.7, 71.4, 68.8, 65.9, 63.8, 63.0, 54.3, 46.7, 44.5, 29.6, 28.0, 23.8, 22.9, 22.6, 21.9, 14.0. MS (MALDI-TOF): Calcd for $C_{89}H_{49}O_4N_3$: 3471.7; Found: 3472.1 (M^+).

Compound 5a: ^{1}H NMR (DMSO-d_6, 500 MHz, ppm, δ): 5.00-4.60 (m, 20H), 4.50 (m, 2H), 4.37 (m, 2H), 4.07 (s, 6H), 3.88 (m, 2H), 2.73 (m, 2H), 2.34 (m, 2H), 2.01 (m, 2H). ^{13}C NMR ($CDCl_3$, 125 MHz, ppm, δ): 168.3, 163.6, 163.0, 162.7, 145.8, 145.3, 145.2, 145.1, 145.0, 144.9, 144.6, 143.9, 143.1, 142.2, 142.0, 141.0, 139.3, 138.7, 71.8, 68.8, 67.9, 66.9, 64.9, 63.4, 55.0, 46.6, 44.5, 29.6, 23.8, 22.9, 21.8, 14.3. MS (MALDI-TOF): Calcd for $C_{69}H_9O_4N_3$: 2911.1; Found: 2911.3 (M^+).

$2C_{60}$-tC_{60} (4b) and $2C_{60}$-AC_{60} (5b). 3b (104 mg, 0.04 mmol), **2** (88 mg, 0.096 mmol), CuBr (1 mg, 0.007 mmol) and anhydrous toluene (15 mL) were added into a Schlenk flask equipped with a magnetic stirrer. The mixture was degassed by three freeze-pump-thaw cycles. Then, PMDETA (10 μL) was introduced into the mixture under nitrogen protection. After one more freeze-pump-thaw cycle, the mixture was then stirred at room temperature for 24 h and applied onto a column filled with silica gel. The column was eluted with toluene first to remove the excess Compound 2. It was then further eluted with toluene/ethyl acetate (v/v = 2/1) to give a colored fraction 4b (142 mg,

80%). Compound 4b was dissolved in mixture of CH_2Cl_2 and CF_3COOH (v/v = 4/1) and stirred for 8 h. Removal of the solvent gave 5b (114 mg, > 90%).

Compound 4b: ^1H NMR ($CDCl_3$, 500 MHz, ppm, δ): 4.87-4.51 (m, 28H), 4.36 (m, 4H), 4.14 (s, 6H), 2.83 (m, 4H), 2.49 (m, 4H), 2.16 (m, 4H), 1.46 (m, 90H). ^{13}C NMR ($CDCl_3$, 125 MHz, ppm, δ): 166.1, 165.8, 165.7, 165.3, 145.9, 145.8, 145.3, 145.2, 145.1, 145.0, 144.9, 144.6, 143.8, 143.1, 143.0, 142.9, 141.1, 140.9, 139.2, 82.2, 71.4, 68.8, 63.9, 63.0, 54.4, 53.7, 50.5, 46.6, 29.8, 29.4, 28.1. MS (MALDI-TOF): Calcd for $C_{282}H_{142}O_{52}N_6$: 4442.8; Found: 4442.9 (M^+).

Compound 5b: ^1H NMR (DMSO-d_6, 500 MHz, ppm, δ): 5.00-4.54 (m, 28H), 4.45 (m, 4H), 4.03 (s, 6H), 2.68 (m, 4H), 2.31 (m, 4H), 2.00 (m, 4H). ^{13}C NMR ($CDCl_3$, 125 MHz, ppm, δ): 168.5, 168.3, 168.0, 166.2, 165.7, 145.9, 145.8, 145.3, 145.2, 145.1, 145.0, 144.9, 144.6, 143.8, 143.1, 143.0, 142.9, 141.1, 140.9, 139.2, 71.6, 68.7, 63.9, 63.0, 54.4, 53.7, 50.5, 46.6, 29.8, 29.4. MS (MALDI-TOF): Calcd for $C_{242}H_{62}O_{52}N_6$: 3882.2; Found: 3882.4 (M^+).

3.2.4 Preparation of micelles of AC_{60}-C_{60} and AC_{60}-$2C_{60}$.

Strategy 1: For the formation of vesicular micelles, 5 mg AC_{60}-C_{60} or AC_{60}-$2C_{60}$ were dissolved in 5 g THF at 50 °C, stirring to ensure complete dissolution, followed by cooling down to room temperature and filtering through a filter of 0.45 μm pore size. The filtered solution was stored for characterizations.

Strategy 2: For the preparation of spherical and cylindrical micelles, 10 mg of AC_{60}-C_{60} or AC_{60}-$2C_{60}$ were dissolved in 2 g DMF and stirred at room temperature overnight, followed by filtering through a filter of 0.22 μm pore size to remove any dust.

Filtered de-ionized water was added dropwise into the solution of AC_{60}-C_{60} or AC_{60}-$2C_{60}$ using a syringe pump till the content of water reaches 80 wt%. For TEM characterizations, the micelle solution was dialyzed against de-ionized water for three days.

3.3 Results and Discussion

In this section, the formation of various assembled structures from two molecular Janus particles in different solvents will be discussed.

3.3.1 Synthesis of Molecular Janus Particles

AC_{60}-C_{60} and AC_{60}-$2C_{60}$ are synthesized by combining the regio-selective Bingel-Hirsh reaction[117-119] and the highly efficient Huisgen 1,3-dipolar cycloaddition "click" reaction,[60] as outlined in Scheme 3.3. Mono-tethered C_{60} derivative 2 with an azide group was prepared via reaction of compound 1 with C_{60} under the Bingel reaction conditions.[117] Precisely defined [5:1]-hexakisadducts of C_{60} with one (3a) or two (3b) terminal alkyne group and ten protected carboxylic acid groups, were synthesized based on the procedures described in our previous publication.[68] Azide-alkyne "click" reaction was successfully utilized to link the mono-functionalized C_{60} (2) with the surface modified C_{60} derivatives (3a-b) in high yields ($\geq$ 80%), resulting in conjugates of a protected carboxylic acid group functionalized C_{60} tethering with one (4a, tC_{60}-C_{60}) or two C_{60}s (4b, tC_{60}-$2C_{60}$). The disappearance of azide resonance at $\sim$ 2100 cm^{-1} and alkyne resonance at $\sim$ 3300 cm^{-1} in IR spectra of 4a-b provides the evidence of successful reaction between 2 and 3a-b (see Figure 3.1). The amphiphilic feature of final products, namely, AC_{60}-C_{60} (5a) and AC_{60}-$2C_{60}$ (5b), was endowed after deprotection of the *tert-*

butyl esters groups on 4a-b. Chemical structures of AC_{60}-C_{60} and AC_{60}-$2C_{60}$ were unambiguously confirmed by ^1H NMR and ^{13}C NMR spectra (see Figures 3.2-3.5). Moreover, the most convincing evidence is given by matrix-assisted laser desorption/ionization time-of-flight (MALDI-TOF) mass spectra as shown in Figure 3.6. Monoisotopic mass peaks observed at $m/z = 2911.3$ for AC_{60}-C_{60} and 3882.4 for AC_{60}-$2C_{60}$ are in good agreement with the calculated values, which are 2911.1 and 3882.2, respectively.
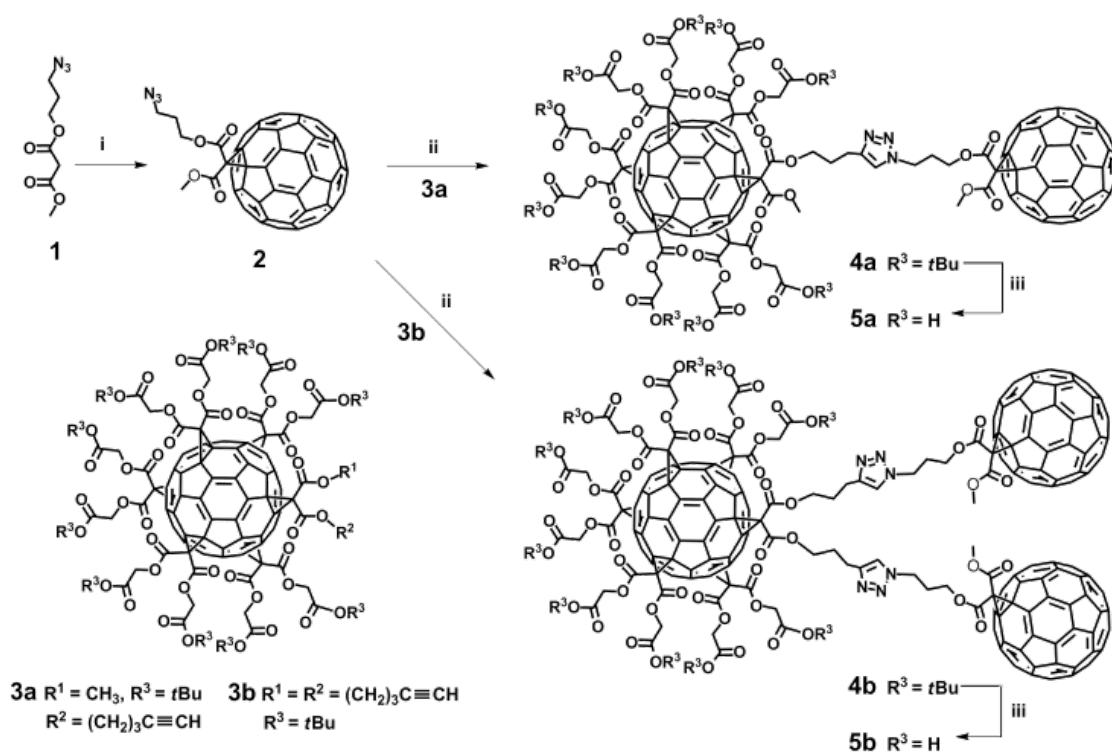
Scheme 3.3. Synthetic route of AC_{60}-C_{60} and AC_{60}-$2C_{60}$. (i) C_{60}, toluene, I_2, DBU, rt (compound **2**, 51%); (ii) toluene, CuBr, PEDETA, r. t. (compound 4a, 81%, compound 4b, 80%); (iii) CH_2Cl_2, r.t. (compound 5a, 90%, compound 5b, 90%).

81
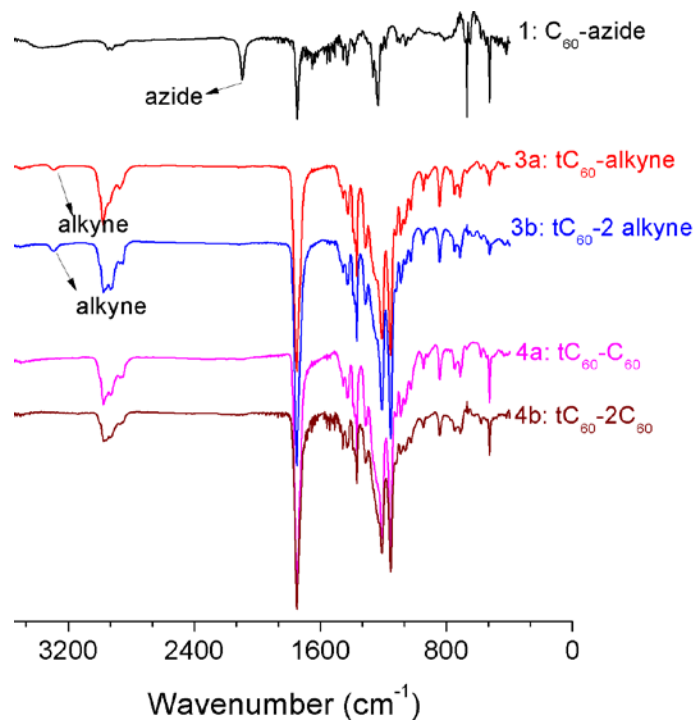
Figure 3.1. FT-IR spectra of 1, 3a, 3b, 4a, and 4b.
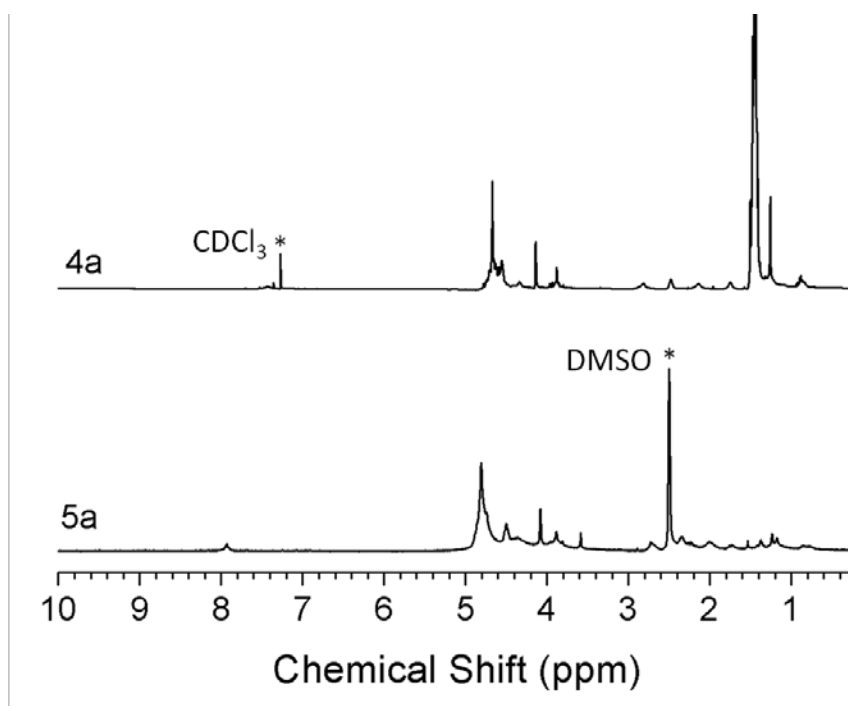
Figure 3.2. ^{1}H NMR spectra of 4a and 5a.
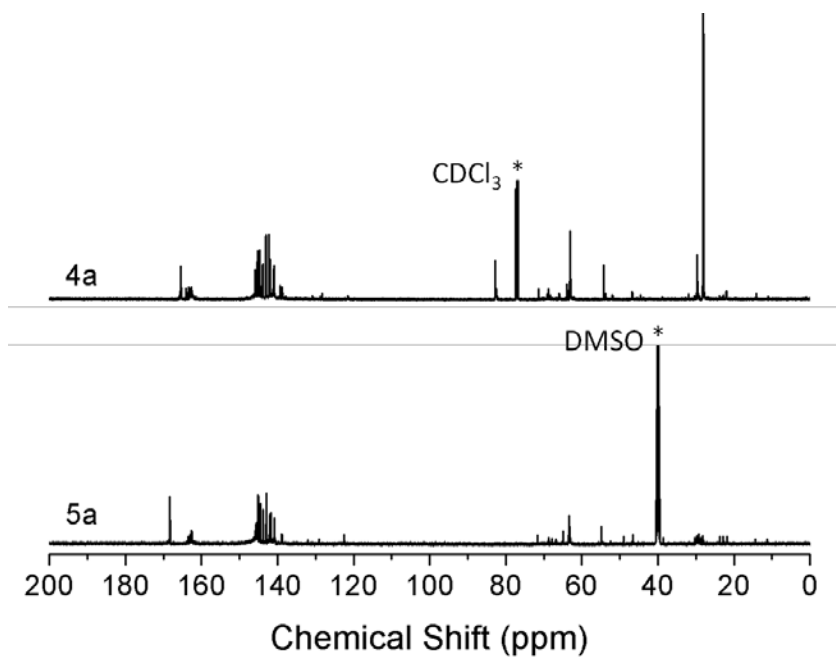
Figure 3.3. ^{13}C NMR spectra of 4a and 5a.
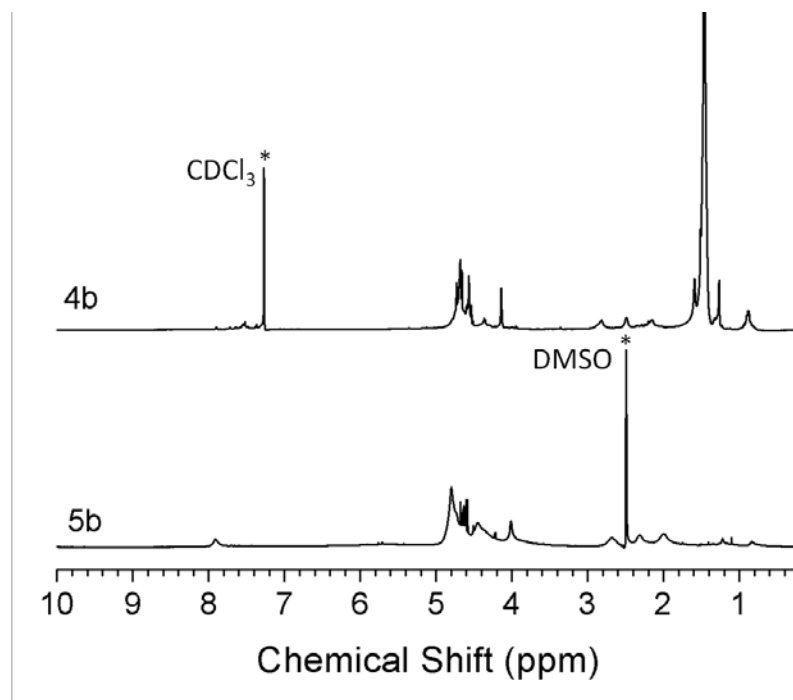
Figure 3.4. ^{1}H NMR spectra of 4b and 5b.
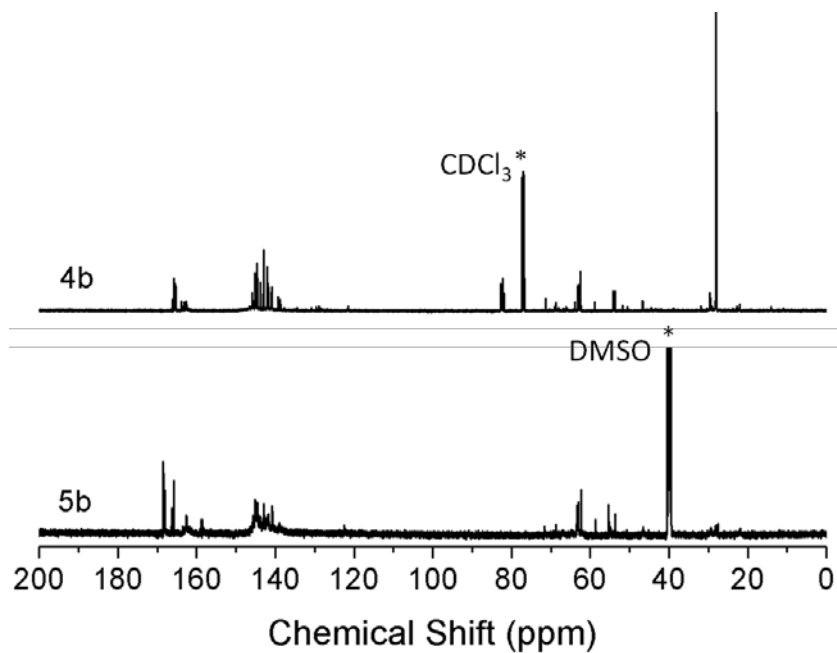
Figure 3.5. ^{13}C NMR spectra of 4b and 5b.
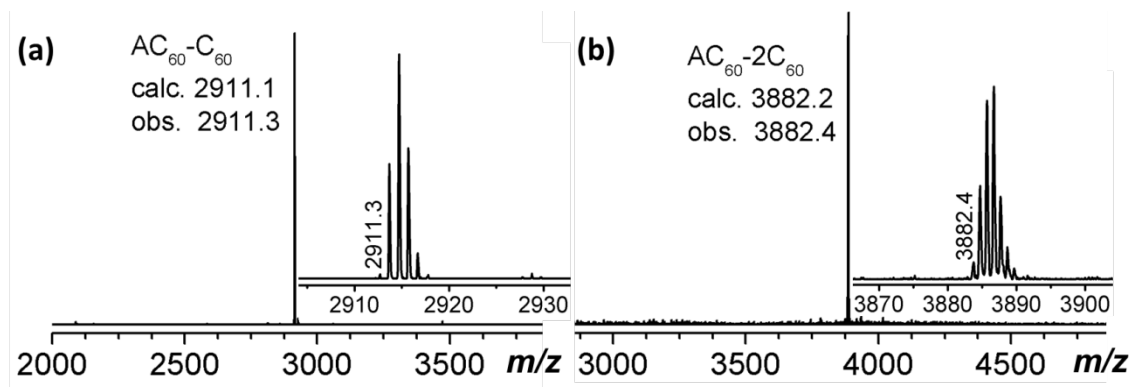
Figure 3.6. MALDI-TOF mass spectra of (a) AC_{60}-C_{60} and (b) AC_{60}-$2C_{60}$.

3.3.2 Solution Self-assembly of Molecular Janus Particles

The micellar behaviors of these MJPs are of great interest since they possess distinct molecular architectures and consist of shape and volume-persistent molecular nanoparticles. Self-assembly of these MJPs in solution was investigated via two different strategies (see the experimental section for details). For both AC_{60}-C_{60} and AC_{60}-$2C_{60}$, when following the first strategy, vesicles were observed in THF, as suggested by the bright-field TEM images shown in Figures 3.7a and b. The overall layer thicknesses of these vesicles are measured to be around 12 - 16 nm from TEM images. Since the layer thickness values are much larger than the long-axis dimensions of AC_{60}-C_{60} and AC_{60}-$2C_{60}$, which are ~ 4 nm in fully extended conformation (Figure 3.8), it is suggested that the vesicles are constructed by a double-layered molecular packing model.[114, 115, 120, 121] The vesicular morphologies were further confirmed by light scattering experiments. As shown in Figures 3.7c and d, the hydrodynamic radii (R_h) of the vesicles obtained from dynamic light scattering (DLS) measurements are ~ 60 nm and ~ 79 nm, respectively, for AC_{60}-C_{60} and AC_{60}-$2C_{60}$, which are consistent with the average radii measured from TEM images (~ 57 nm for AC_{60}-C_{60} and ~ 82 nm for AC_{60}-$2C_{60}$). Furthermore, the radii of gyration (R_g) of the vesicles measured by static light scattering (SLS) are ~ 56 and ~79 nm, respectively (Figure 3.9). The measured ratios of R_g/R_h are thus both close to unity (0.93 for AC_{60}-C_{60} and 1.0 for AC_{60}-$2C_{60}$), validating the formation of self-assembled vesicular structures.[113-115]
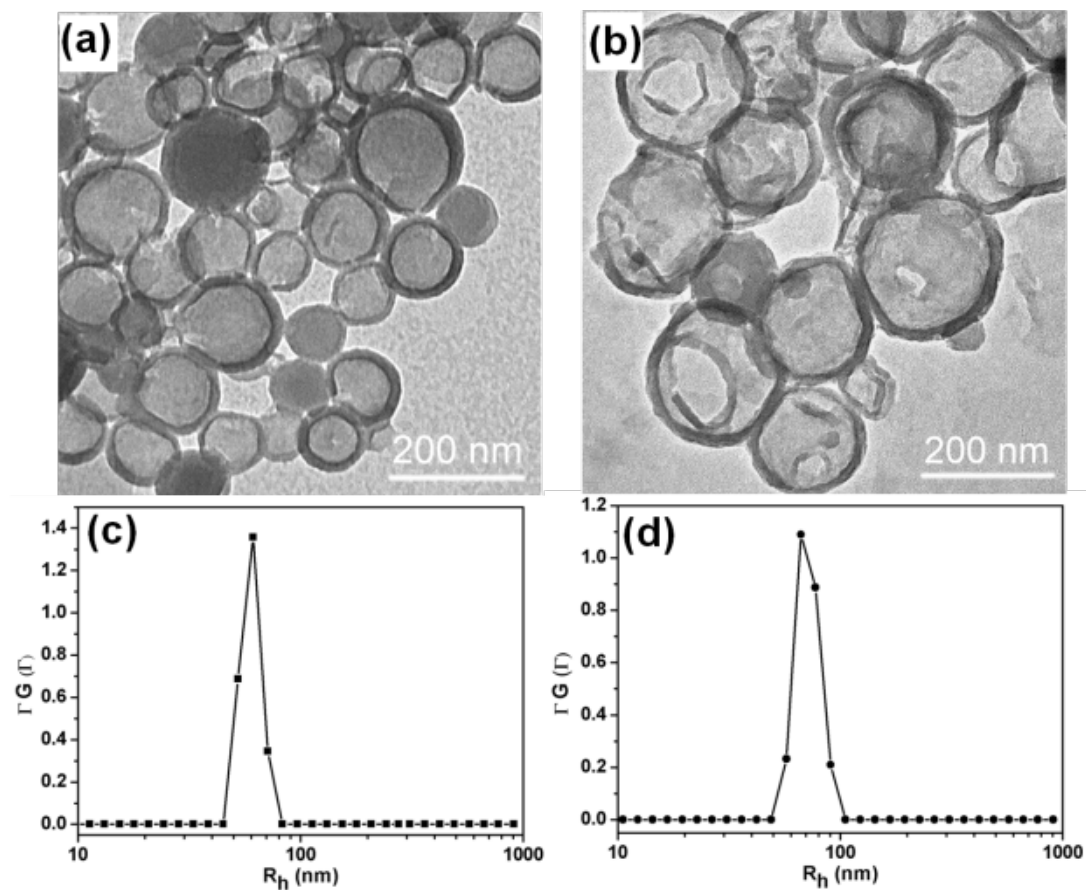
Figure 3.7. TEM images and DLS results of the self-assembled vesicle morphologies of (a) and (c) for AC_{60}-C_{60}, (b) and (d) for AC_{60}-$2C_{60}$ in THF.
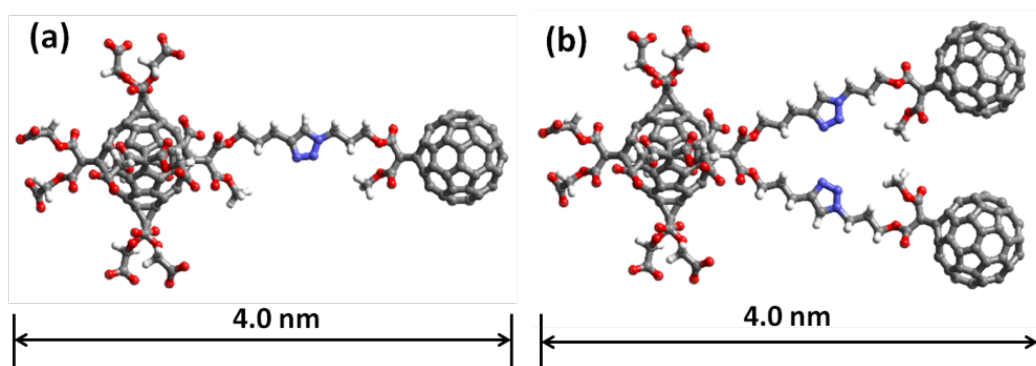
Figure 3.8. Three dimensional chemical structures of (a) AC_{60}-C_{60} and (b) AC_{60}-$2C_{60}$ and their estimated lengths.

The driving force for the micellar formation in THF must be attributed to the aggregation of hydrophobic C_{60} particles, since THF is a poor solvent for C_{60} at room temperature. Therefore, the outer and inner layers of the vesicles are formed by AC_{60}, while the hydrophobic C_{60}s are located in the middle region between these two AC_{60} layers to form a bilayered structure in the vesicles. This is also consistent with the previously reported self-assembled bilayered vesicles from amphiphilic fullerene derivatives in fullerene-phobic solvents.[113-115, 120] Interestingly, when the vesicles are subjected to ultrasonication in THF solution, the measured R_h remains constant for at least 5h (Figure 3.10), indicating that the vesicles prepared in THF are quite stable and robust. This can be attributed to the π-π interaction between the hydrophobic C_{60}s and the strong hydrogen bonding interaction between the hydrophilic AC_{60}s.
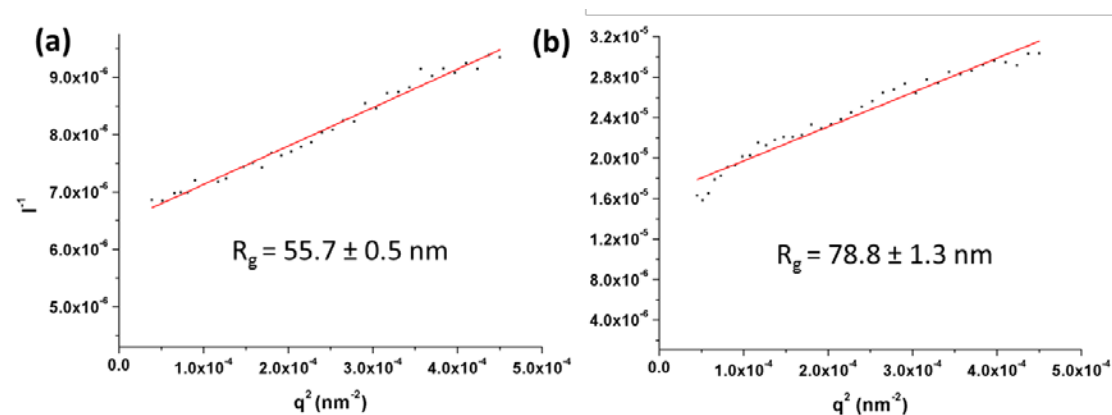
Figure 3.9. The Guinier plot for the vesicles formed by (a) AC_{60}-C_{60} and (b) AC_{60}-$2C_{60}$ in THF.
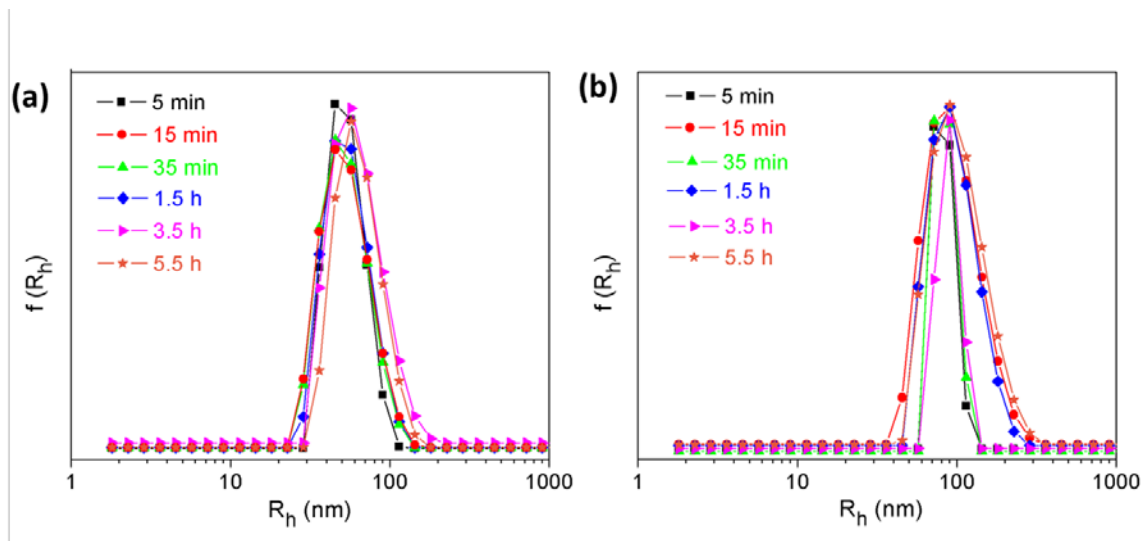
Figure 3.10. DLS results of the vesicles formed by (a) AC_{60}-C_{60} and (b) AC_{60}-$2C_{60}$ in THF subjected to ultrasonication for various times.

In order to reveal the effect of molecular architectures on the self-assembly behaviors of these two MJPs, we further studied their self-assemblies in DMF/water system following the second strategy. The critical water concentrations (C_{CWC}) for AC_{60}-C_{60} and AC_{60}-$2C_{60}$ to form micelles were determined to be 13.7 wt% and 2.2 wt%, respectively (Figure 3.11). The difference of these two C_{CWC} values can be attributed to the largely increased hydrophobicity of AC_{60}-$2C_{60}$ compared to that of AC_{60}-C_{60}. Despite the C_{CWC} difference, we choose to explore and compare self-assembled morphologies of these two MJPs at relatively high and identical water contents. Therefore, AC_{60}-C_{60} and AC_{60}-$2C_{60}$ were first dissolved in DMF at an initial concentration of 0.5 wt% and then, water was added dropwise to reach a final water content of 80 wt%. Surprisingly, spherical micelles with an average diameter of ~ 8 nm are observed for AC_{60}-C_{60}, as shown in Figure 3.13a; while worm-like cylinders with an average diameter of ~ 13 nm

88

and an aspect ratio larger than 10 are observed for AC_{60}-$2C_{60}$ under identical conditions (Figure 3.12b).
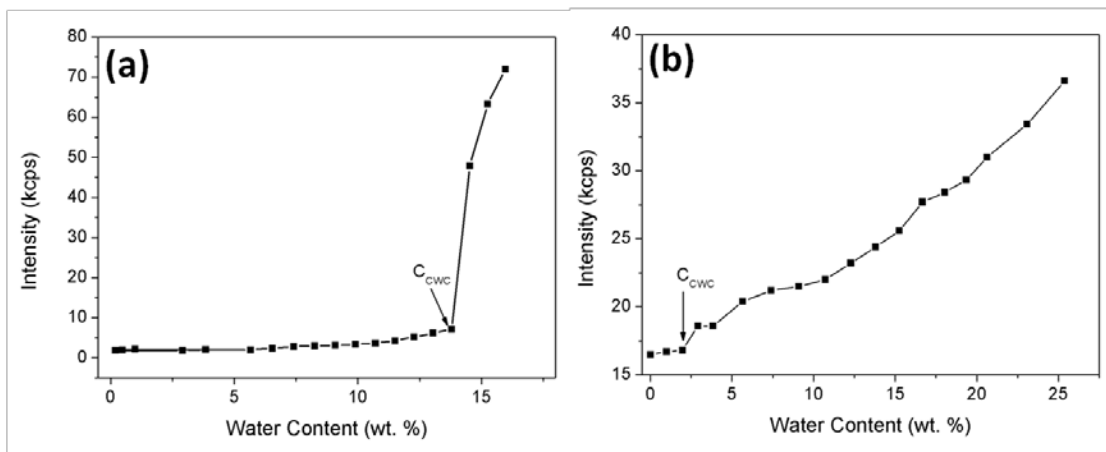
Figure 3.11. Light scattering intensity versus water content in the DMF/water system with an initial molecular concentration of 0.5 wt% for (a) AC_{60}-C_{60} and (b) AC_{60}-$2C_{60}$. The arrows show the critical water concentration (C_{CWC}) for the corresponding curves.
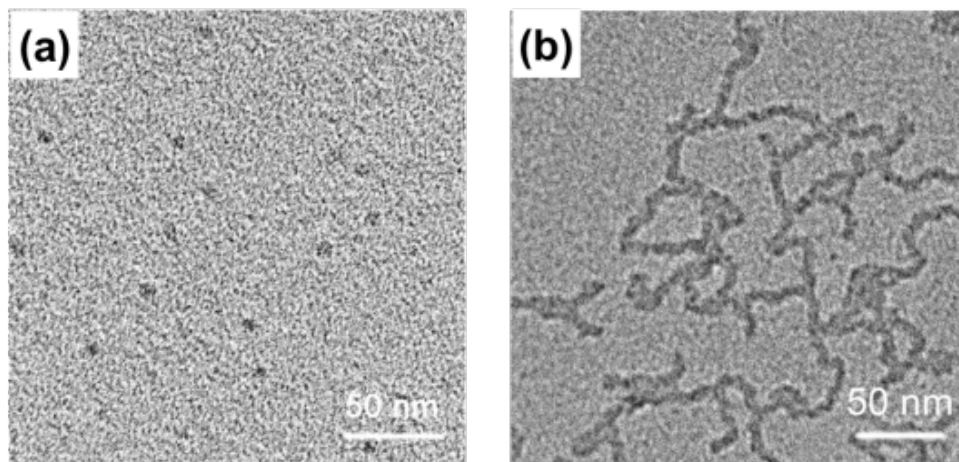
Figure 3.12. TEM images of the self-assembled morphologies of (a) AC_{60}-C_{60} and (b) AC_{60}-$2C_{60}$ in the solution of DMF with an initial concentration of 0.5 wt% as water was dropwise added to reach an 80 wt% content.

To obtain the macroscopic average information of these micellar morphologies, DLS experiments were performed. As shown in Figure 3.13, the R_h of the spherical micelles from AC_{60}-C_{60} has a relatively broad distribution centred at around 3 nm, which is qualitatively consistent with that measured from TEM images. The formation of cylinders from AC_{60}-$2C_{60}$ can also be verified by the fact that the R_h varies as changing the scattering angles in DLS experiments (Figure 3.14). The R_h value of the cylinders is estimated as 115 ± 10 nm, by extrapolating the scattering angles to zero, as shown in Figure 3.15. Furthermore, the R_g of the cylinders was measured as $\sim 308 \pm 5$ nm (Figure 3.16). The ratio of R_g/R_h is thus ~ 2.7, which further confirms the formation of cylinders from AC_{60}-$2C_{60}$.

The formation of various micellar morphologies from these two MJPs could be rationalized by the argument of self-assembly of hydrocarbon amphiphiles put forward by Israelachvili et al.[70, 122] The self-assembled structures of amphiphiles can be predicted by the packing parameter (P), which is defined as:

$$P = V/(A \cdot l_c)$$

where V is the volume occupied by the hydrophobic moiety, l_c is the critical length of the hydrophobic moiety, and A is the optimal area occupied by the hydrophilic moiety.
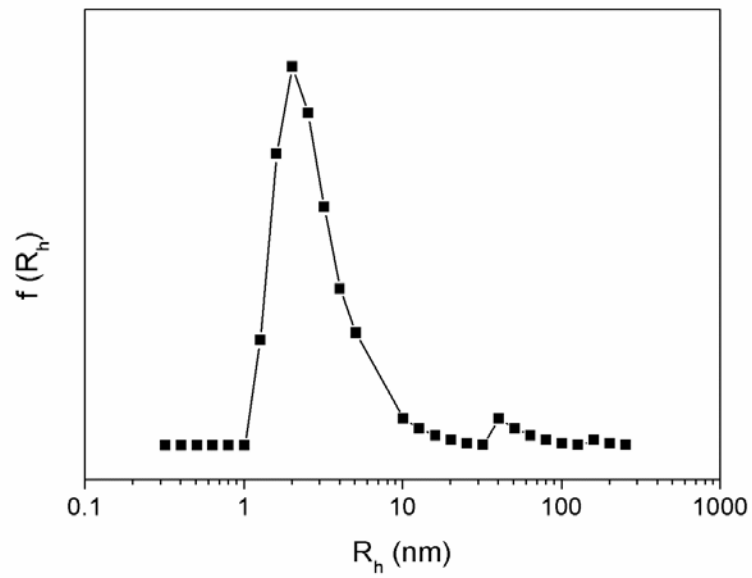
Figure 3.13. CONTIN analysis of the dynamic light scattering data of AC_{60}-C_{60} in DMF/Water mixture.
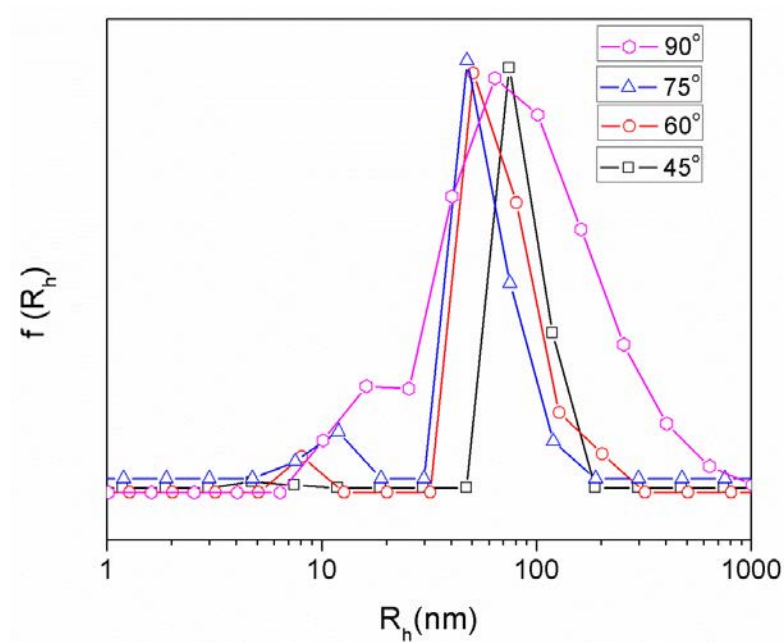
Figure 3.14. CONTIN analysis of the DLS data of AC_{60}-$2C_{60}$ at difference angles in DMF/Water mixture.
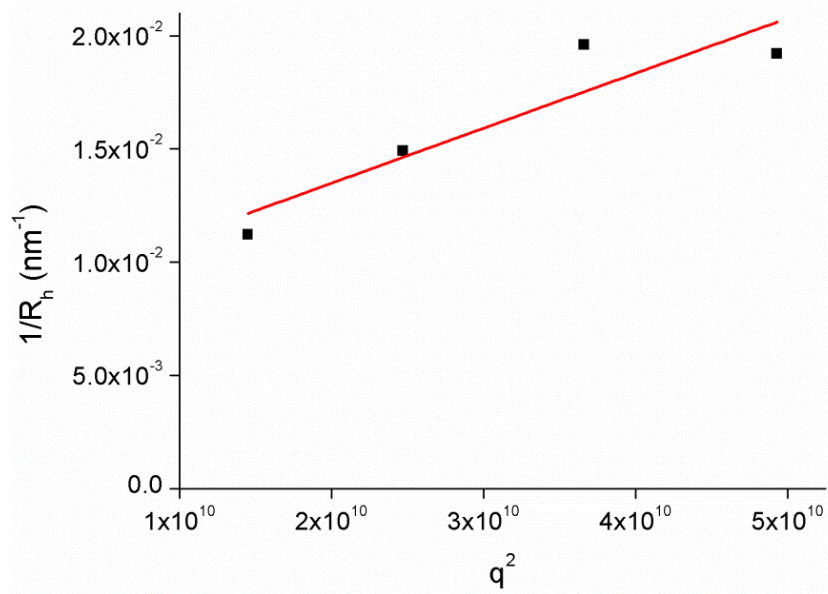
Figure 3.15. The plot for DLS data of AC_{60}-$2C_{60}$ at difference angles in DMF/Water mixture.
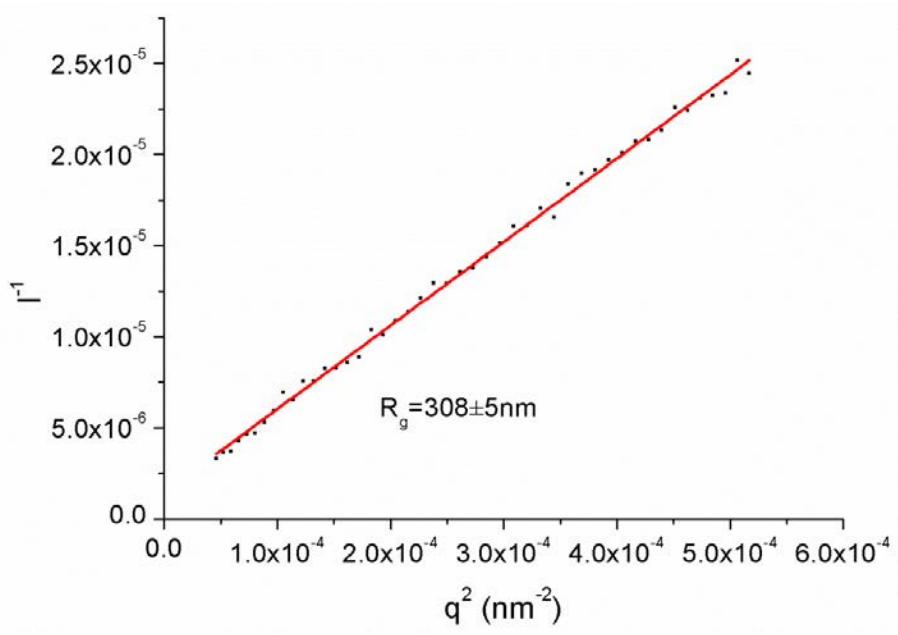
Figure 3.16. The Guinier plot for the cylinder formed by AC_{60}-$2C_{60}$ in DMF/water mixture.

Based on this argument, the preferred self-assembled structures of amphiphilic molecules vary with increasing P from spheres ($P < 1/3$), to cylinders ($1/3 < P < 1/2$), to vesicles ($1/2 < P < 1$). In our system, since hydrophobic C_{60} possesses well-defined structure with a fixed volume, the value of V_{C60} and l_{C60} can be obtained from the volume and diameter of C_{60}, respectively ($V_{C60} = 0.52$ nm^3 and $l_{C60} = 1$ nm).[42] For the hydrophilic AC_{60}, its smallest A_{AC60} can be estimated to be 1.5 nm^2 in the solution without considering solvation of the surface carboxylic acid groups.[123] This serves as the lowest limit value of A_{AC60}. When using these values to calculate the P value of AC_{60}-C_{60} and AC_{60}-$2C_{60}$, it turns out that $P_{AC60-C60} = 0.35$ ($\geq 1/3$) and $P_{AC60-2C60} = 0.69$ ($> 1/2$), indicating that the micelles of AC_{60}-C_{60} are near the boundaries between the cylinders and spheres (but in the cylinder side), while that the micelles of AC_{60}-$2C_{60}$ are located in the vesicular phase.

In reality, however, the hydrodynamic size of AC_{60} is expected to increase as the degree of ionization (α) of carboxylic acid groups increases. Therefore, it is necessary to consider the effect of α on the value of A_{AC60} in pure THF and the mixture of DMF/water. The α value can be estimated based on the results of FT-IR spectroscopy as a first approximation. Figures 3.17 and 3.18 show four FT-IR spectra of the micelle solutions prepared in both THF and DMF/water mixtures for two samples. The highlighted absorption bands at ~ 1740 cm^{-1} and ~ 1620 cm^{-1} are attributed to the C=O stretching band of the native –COOH and ionized group –COO$^-$, respectively.[67] As exhibited in Figures 3.17a and 3.18a, since the α of carboxylic acid groups for AC_{60} in THF is rather low ($\sim 20\%$), the A value of AC_{60} in THF can still be approximated by 1.5 nm^2. It gives

rise to a P value of 0.35 and 0.69 for AC_{60}-C_{60} and AC_{60}-$2C_{60}$ in THF, respectively. Based on this estimation, we should observe cylindrical ($1/3 < P < 1/2$) for AC_{60}-C_{60} and vesicular morphologies ($1/2 < P < 1$) for AC_{60}-$2C_{60}$. In Figure 3.7, the vesicles are indeed observed for AC_{60}-$2C_{60}$. However, experimentally, AC_{60}-C_{60} also forms vesicles in THF, which differs from the estimation based on the calculations.

In order to provide a reasonable explanation for this discrepancy, we put our argument forward in the following way: As described above, AC_{60} particles located at both outside and inside surfaces of the vesicles, while the C_{60} particles located in the middle of the vesicles due to the poor solubility of C_{60} in THF. We further propose that within the vesicles of AC_{60}-C_{60}, the C_{60} particles are arranged in an interdigitated packing manner (Figure 3.19a). In contrast, the C_{60} particles construct a bilayer within the vesicles of AC_{60}-$2C_{60}$, as schematically shown in Figure 3.19b. This is similar with the case of reported fullerene amphiphiles.[114] In this argument, the geometrical arrangement for both cases becomes identical with the same cross-section areas, but differs in molecular packing topologies.
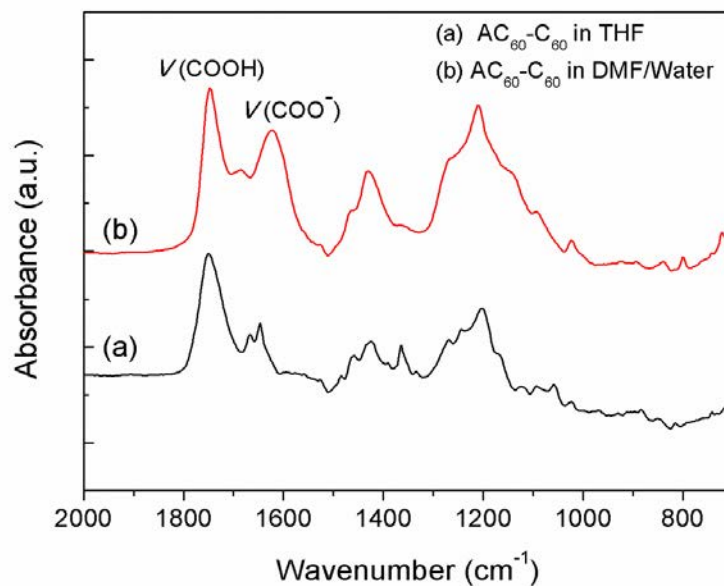
Figure 3.17. FT-IR spectra of AC_{60}-C_{60} micelle solutions in different solvent (a) THF and (b) DMF/water.
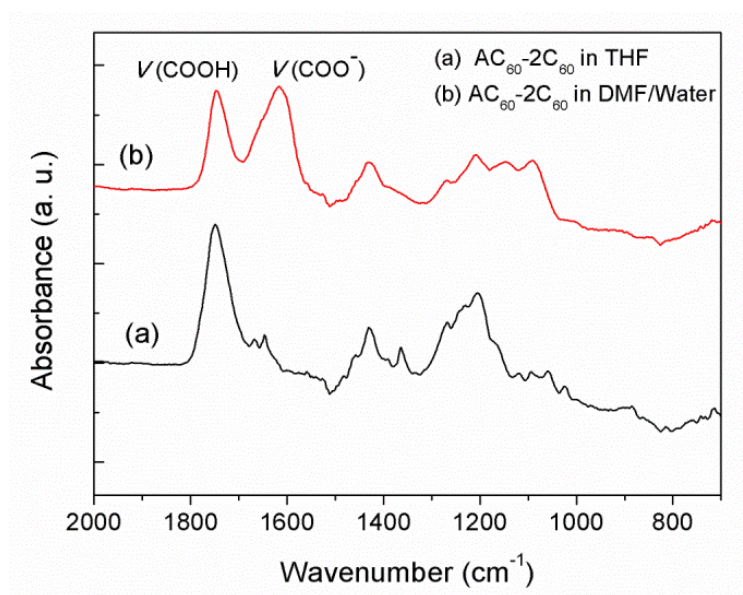
Figure 3.18. FT-IR spectra of AC_{60}-$2C_{60}$ micelle solutions in different solvent (a) THF and (b) DMF/water.

95
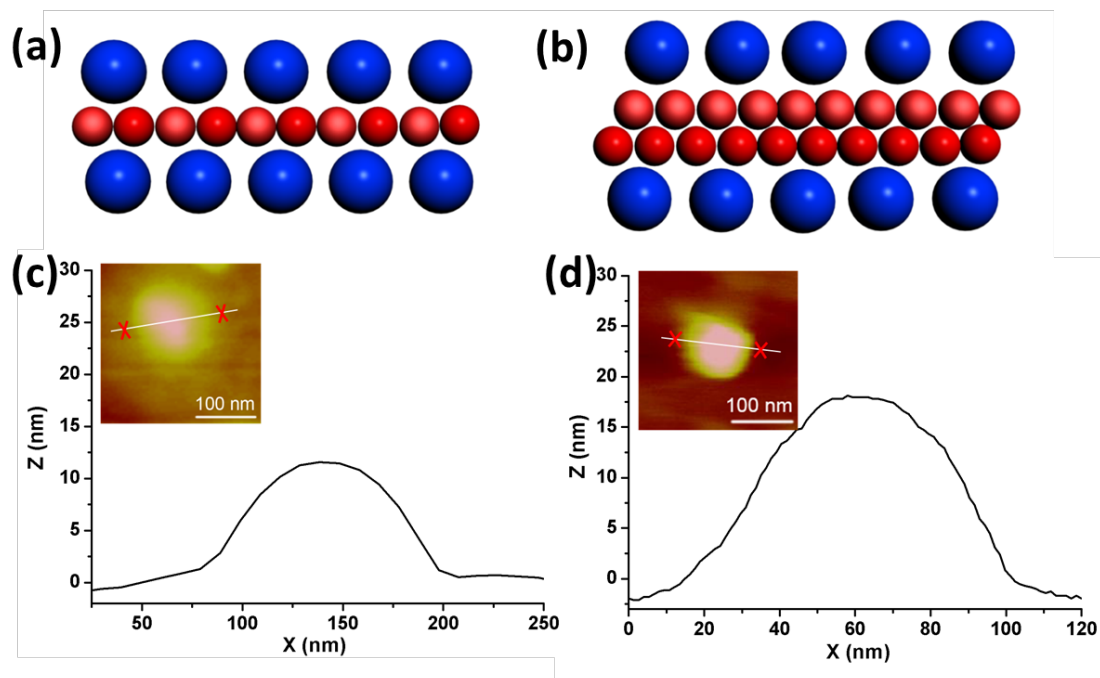
Figure 3.19. Schematic illustrations of two packing models of vesicles. (a) Interdigitated structure for AC_{60}-C_{60} and (b) bilayered structure for AC_{60}-$2C_{60}$. AFM height profiles of vesicles formed by (c) AC_{60}-C_{60} and (d) AC_{60}-$2C_{60}$ in THF. Insets are AFM images of two individual vesicles.

To verify the proposed packing models, atomic force microscopy (AFM) was utilized to measure the layer thickness of the collapsed vesicles after evaporating the solvent. Only those vesicles possessing smooth surface were selected to measure their heights, as illustrated by the two typical height profiles shown in Figures 3.19c and 3.19d. The average thickness of vesicles obtained from ten independent measurements are 12.5 $\pm$ 1.3 nm for AC_{60}-C_{60}, and 16.2 $\pm$ 1.5 nm for AC_{60}-$2C_{60}$, respectively, resulting in a ratio of 0.77 between the two thicknesses. The theoretical double thicknesses of interdigitated and bilayered layers are calculated as 7.6 nm and 9.6 nm, respectively, by

assuming that the diameter of C_{60} is 1.0 nm and that the diameter of AC_{60} is 1.4 nm (which is estimated from $A_{AC60} = 1.5$ nm^2 in THF). Since it is difficult for the layers of C_{60} and AC_{60} to pack closely after micelles collapse, the theoretical thicknesses of interdigitated and bialyered layers are smaller than the measured ones. However, the theoretically calculated ratio between the thicknesses of interdigitated layer and bilayer is 0.79, which is in good agreement with the measured ratio (0.77). Therefore, the bilayered and interdigitated packing models are at least partially confirmed.

In the DMF/water system, a much higher α value is observed (~ 50%), which results in a larger A value of AC_{60}. As a result, as long as $A > 1.5$ nm^2, $P_{AC60-C60}$ would decrease to below 1/3, suggesting a sphere morphology. In the case of AC_{60}-$2C_{60}$, it is even more difficult to quantitatively estimate the $P_{AC60-2C60}$ value. We speculate that it locates between 1/3 and 1/2, when the A_{AC60} value is in somewhere between 2.1 and 3.1 nm^2, suggesting the formation of cylindrical morphology in the mixture of DMF/water.

3.4 Conclusion

In summary, two precisely defined fullerene-based MJPs with distinct molecular architectures (AC_{60}-C_{60} and AC_{60}-$2C_{60}$) have been designed and synthesized via regio-selective sequential Bingel-Hirsh reactions and the "click" chemistry. Self-assembly of these two MJPs has been investigated in solution. In THF, vesicles with interdigitated and bilayered molecular packing arrangements have been observed for AC_{60}-C_{60} and AC_{60}-$2C_{60}$, respectively. In the DMF/water system, however, spherical and cylindrical morphologies are formed for AC_{60}-C_{60} and AC_{60}-$2C_{60}$, respectively. The degree of ionization of the carboxylic acid groups on AC_{60} plays an essential role in influencing

their packing parameters (P) and determining the micelle morphologies formed in different solvent systems. This work introduces a new approach to the design of molecular Janus grains, their precision synthesis, and diverse self-assembly behaviors in solution. It may expand the scope of traditional amphiphilic molecules and provide a platform to further study the self-assembly behaviors of shape-persistent MJPs.
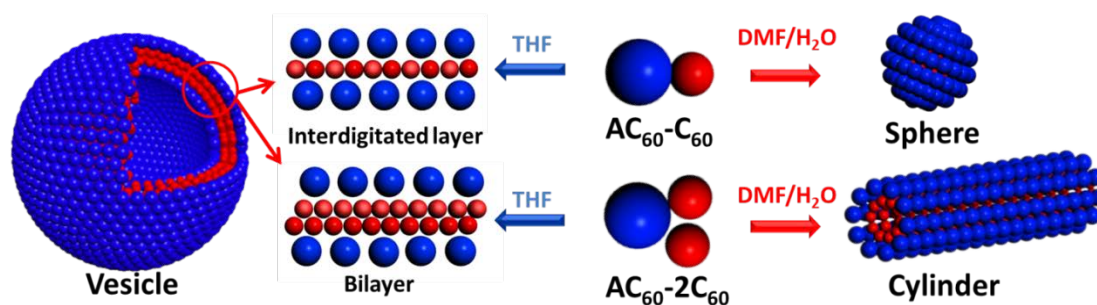
Figure 3.20. General story of chapter III[*]

CHAPTER IV

SEQUENTIAL "CLICK" SYNTHESIS OF "NANO-DIAMOND-RING-LIKE" GIANT

SURFACTANTS BASED ON FUNCTIONALIZED HYDROPHILIC POSS/C_{60}

TETHERED WITH CYCLIC POLYSTYRENES

4.1 Introduction

Over the past decade, we have witnessed explosive efforts in studying self-assembly[1, 2, 124] of fundamental building blocks (typically atoms, molecules, macromolecules and colloid particles) to construct various nano-structures, which serves as the basis for the alternative "bottom-up" approach towards manufacturing nano-materials with unique properties.[1, 2, 124-127] Creating hierarchical self-assembled nano-structures with molecular-level precision beyond those from traditional amphiphilic moieties[20, 128, 129] remains to be one major challenge in material sciences.[25, 26, 130] The emergence of "giant molecules" based on "nano-atoms" provides new opportunities to achieve this goal. Using molecular nanoparticles (MNPs) as the "nano-atoms" (or basicnano-sized building blocks), giant molecules with precisely defined structures can be obtained by conjugating MNPs with other nanobuilding blocks.[36] Specifically, giant surfactants,[67, 69] composed of MNPs tethered by polymer tails, are one of the representative prototype giant molecules. Giant surfactants capture the essential structural

features of small-molecule surfactants, but possess amplified sizes which are comparable to block copolymer amphiphiles.[69] Due to the use of sequential "click-type" reactions[60, 63, 131-135] in the synthetic approaches, chemical structures and properties of giant surfactants can be tuned by separately changing the chemical compositions[68, 71, 136, 137] and molecular architectures[68, 138] of the MNP heads and the polymer tails, in a modular and systematic manner.

Our group has been developing a library of MNPs with precisely defined chemical structures and surface functionalities for the construction of giant surfactants, among which polyhedral oligomeric silsesquioxane (POSS)[37, 139-141] and [60] fullerene (C_{60})[42, 142] derivatives are the most promising candidates. POSS and C_{60} are cage-like molecules with persistent three-dimensional conformations and monodisperse size around 1 nm. At the periphery of the silicon-oxygen cubic backbones of the POSS molecules[37, 140, 141] and the truncated icosahedral framework of C_{60} moieties,[59, 142] different functional groups can be introduced by well-established elegant chemistry, resulting in a set of homo- or hetero-functionalized POSS[71, 143, 144] and C_{60} derivatives[68] as versatile functionalized building blocks.

Giant surfactants deriving from POSS/C_{60} based "nano-atoms" have demonstrated rich and unique self-assembly behaviors in solution, thin film and the bulk states.[67-69] For example, giant surfactants constructed from a hydrophilic C_{60} (carboxylic acid-functionalized AC_{60}) head and polystyrene (PS) tails can form different micellar and colloidal particle morphologies in solution, depending on the selection of common solvent, initial molar concentration and the length of the PS tails.[67-69] More interestingly, comparison between two sets of topological isomers indicates that their self-assembly is

extremely sensitive to the molecular architecture. Giant surfactants constructed by a hydrophilic C_{60} (AC_{60}) tethered with one long or two short PS chains (AC_{60}-PS_{44} or AC_{60}-$2PS_{23}$), both of which possess comparable overall molecular weights, exhibit considerably different self-assembled morphologies in the bulk and solution.[68, 69] Similar architectural influence on self-assembled structures has also been displayed in dihydroxyl-functionalized POSS-PS systems.[69] These distinct differences in self-assembly behaviors between the topological isomers drive us to further investigate the molecular architecture effect.

Cyclic polymers are known to possess a variety of unique properties that are distinguishable from their linear analogues, including effects relating to no chain ends, reduced overall dimension, lower viscosity and increased glass transition temperature (T_g).[145] As a result, a substantial body of work[146-148] has been devoted to efficient preparation of cyclic homopolymers[149-159] or cyclic block copolymers,[160-164] as well as to their physical characterizations. Recently, the development of a few highly efficient cyclization methods utilizing, for example, the copper-catalyzed alkyne-azide Huisgen [3+2] cycloaddition reaction,[149] the Diels-Alder reaction,[159] or even the genetically encoded SpyTag−SpyCatcher chemistry,[165] has greatly facilitated the preparation of various cyclic polymers and the study on their physical properties. For example, gels formed from cyclic poly(5-hydroxy-1-cyclooctene) (PACOE) exhibit notably greater swelling ability and larger strain at break than those from linear PACOEs;[155] thermal stabilities of micelles are greatly enhanced through a linear-to-cyclic conversion of triblock amphiphilic copolymer;[160] smaller ordered domains in thin film are achieved from cyclic polystyrene-*b*-poly(ethylene oxide) (PS-*b*-PEO) block copolymers than those

from the linear counterparts;[162] tadpole-shaped linear-cyclic (c-PNIPAM)-*b*-PCL block copolymers exhibit improved drug loading and releasing capacity compared with linear amphiphilic diblock PNIPAM-*b*-PCL copolymers,[164] among many others. These inspiring results further drive us to use cyclic polymers as the building blocks to design and construct MNP-based giant surfactants, and to investigate their self-assembling behaviors. To the best of our knowledge, there is no report on the synthesis of giant surfactants on the basis of cyclic polymer-tethered MNPs.

In this chapter, we strive to introduce a new member to the family of giant surfactants based on "nano-atoms". The molecular design is to tether a cyclic hydrophobic PS chain onto a hydrophilic POSS/C_{60} head, which can be viewed as "nano-diamond-ring-like" giant surfactants. To achieve an efficient, facile and modular synthetic approach, we design a synthetic approach that combines several steps of highly efficient reactions, which fulfills the "click" criteria. First, we use the CuAAC reaction[60, 131, 149] in the cyclization step[149] to synthesize a cyclic PS with a vinyl group (Vinyl-CPS), which can be converted to an azide group via the thiol-ene reaction.[63, 132, 134] The azide mono-functionalized CPS building block (CPS-N_3) is then compatible with the reported sequential "click" strategy[71] towards POSS/C_{60} based giant surfactants. The developed synthetic route is highly efficient, and all of the important intermediates and final products have been well characterized. Moreover, the CPS-N_3 might serve as a versatile building block and can be easily applied to afford other giant surfactants. These "nano-diamond-ring-like" giant surfactants prepared and reported here possess distinctive and unique molecular structures and are excellent targets to investigate the structure-property relationships in our giant surfactant systems.

102

4.2 Experimental section

In this section, the detailed synthetic procedures and characterizations for "nano-diamond-ring-like" giant surfactants will be described.

4.2.1. Chemicals and solvents

Methanol (reagent grade, Fisher Scientific), chloroform (Certified ACS, Fisher Scientific), dichloromethane (DCM, Fisher Scientific), ethyl acetate (EA, Fisher Scientific), tetrahydrofuran (THF, Fisher Scientific), N,N-dimethylformamide (DMF, anhydrous 99.8%, Sigma-Aldrich), and hexanes (Certified ACS, Fisher Scientific) were used as received. Toluene (ACS grade, EMD) and styrene (99%, Sigma-Aldrich) were used after purification in a manner reported previously.[166] Anhydrous sodium sulfate (Na_2SO_4), N,N,N',N'',N''-pentamethyldiethylenetriamine (PMDETA, 99%, Sigma-Aldrich), copper(I) bromide (98%, Acros Organics), 2-hydroxy-4'-(2-hydroxyethoxy)-2-methylpropiophenone (Irgacure 2959, 98%, Sigma-Aldrich), 1-thioglycerol ($\geq$98%, Fluka), trifluoroacetic acid (99%, Sigma-Aldrich), sodium azide (NaN_3, 99.5%, Sigma-Aldrich), [60]fullerene (C_{60}, MTR ltd., 99.5%) and octavinyl-POSS (OVPOSS, > 97%, Hybrid Plastics) were used as received. The functionalized POSS derivative containing seven vinyl groups and one alkyne group (VPOSS-alkyne)[71] and C_{60} derivative installing ten protected carboxylic acid groups and one alkyne group (TC$_{60}$-alkyne)[68] were prepared according to our previous publications. Triethylamine (TEA, 99%, Alfa Aesar), N,N'-diisopropyl carbodiimide (DIPC, 99%, Acros Organics), 4-dimethylaminopyridine (DMAP, $\geq$ 99%, Sigma-Aldrich), 4-pentynoic acid (99%, Sigma-Aldrich), 3-(allyloxy)propane-1,2-diol (99%, Sigma-Aldrich), 2-bromoisobutyryl bromide (98%,

Sigma-Aldrich), bis-(2-hydroxyethyl) disulfide (90%, Alfa Aesar), dithiothreitol (DTT, 98%, Sigma-Aldrich). Bis(2-azidoethyl)disulfide (**3**) was synthesized according to procedures described in the literature.[167]

4.2.2. Characterization

All ^{1}H NMR and ^{13}C NMR spectra were collected using a Varian Mercury 300 or Varian NMRS 500-01 spectrometer. NMR samples were prepared with concentration of 10-20 mg/mL in CDCl$_3$ or DMSO-d_6 for ^{1}H NMR or 50-80 mg/mL for ^{13}C NMR. The ^{1}H NMR spectra were referenced to δ 7.27 ppm in CDCl$_3$ or δ 2.50 ppm in DMSO-d_6, and ^{13}C NMR spectra were referenced to δ 77.00 ppm in CDCl$_3$ or δ 39.43 ppm in DMSO-d_6. For VPOSS-CPS or TC$_{60}$-CPS, the integration ratio between the characteristic vinyl peaks on POSS at δ 6.20-5.84 ppm (21H per VPOSS) or characteristic peaks on C$_{60}$ at δ 4.89-4.47 ppm (20H per TC$_{60}$) and the peaks at δ 7.45-6.35 ppm (aromatic protons in PS) gives the number-average degree of polymerization (DP) of the PS. The calcuated molecular weight ($M_{n,NMR}$) can then be obtained by the summation of $M_{n,PS}$ (DP × 104.1 g/mol), $M_{Iniator}$ (323.1 g/mol), $M_{2-azidoethanethiol}$ (103.0 g/mol), and $M_{POSS/C60}$ (730.0 g/mol for VPOSS, 1486.1 g/mol for DPOSS, 2552.7 g/mol for TC$_{60}$, and 1991.9 g/mol for AC$_{60}$). In DOSY experiments, the samples were dissolved in CDCl$_3$ to make a solution of 15 mg/mL in NMR tube with a height of 5 cm. Measurements were performed at 25 °C on a Varian NMRS 500 spectrometer. An interval of 100 ms between the gradient pulse and 1 ms duration of gradient pulse were applied. The gradient strength was varied in 32 gradient steps within a range from 0.1 to 10 T/m.

Infrared spectra were collected on an Excalibur Series FT-IR spectrometer (DIGILAB, Randolph, MA). Samples were prepared by depositing polymer solution with concentration of about 10 mg/mL in THF onto a KBr plate, followed by drying with blowing air at room temperature to give drop-casting films. The data were analyzed using the Win-IR software.

Size-exclusion chromatography (SEC) analyses were carried out using a Waters 150-C Plus instrument equipped with three HR-Styragel columns [100 Å, mixed bed (50/500/10^3/10^4 Å), mixed bed (10^3/10^4/10^6 Å)] and a double detector system, which is consisted of a differential refractometer (Waters 410) and a laser light scattering detector (Wyatt Technology, DAWN EOS, λ = 670 nm). THF was used as the eluent with a flow rate of 1.0 mL/min at 30 °C and as the solvent to prepare sample solutions with the concentration of *ca.* 5-10 mg/mL. The sample solutions were filtered through a 0.45 μm Teflon filter prior to injection. Regular SEC calibrations were conducted based on PS standards (Polymer Laboratories).

Matrix-assisted laser desorption/ionization-time of flight (MALDI-TOF) mass spectra were obtained on a Bruker Ultraflex III TOF/TOF mass spectrometer (Bruker Daltonics, Inc., Billarica, MA), equipped with a Nd : YAG laser emitting at a wavelength of 355 nm. Positive reflection or linear mode was applied to measure all of spectra. Calibration with external PS standards was required before each measurement. Trans-2-(3-(4-t-butyl-phenyl)-2-methyl-2-propenylidene) malononitrile (DCTB) was served as matrix (20 mg/mL in CHCl$_3$) and sodium trifluoroacetate (NaTFA) was used as the cationizing agent (10 mg/mL in methanol). Both of them were mixed in the ratio of 10/1 (v/v). In sample preparation, 0.5 μL of the matrix/NaTFA mixture was deposited on

microtiter plate wells (MTP 384-well ground steel plate), followed by depositing 0.5 μL

of sample solution (*ca.* 10 mg/mL in THF) on the top of a dry matrix/NaTFA spot and

adding another 0.5 μL of the matrix/NaTFA mixture. After evaporation of solvent, the

target plate was loaded for data collection. Data analysis was performed with the

Bruker's flexAnalysis software.

Compound 1. 3-(Allyloxy)propane-1,2-diol (0.06 mol, 9.84 g, 1 equiv) and TEA

(0.12 mol, 20 mL, 2 equiv) were dissolved in 50 mL anhydrous THF under magnetic

stirring. The solution was cooled to 0 °C in an ice bath and 2-bromoisobutyryl bromide

(0.06 mol, 9.53 mL, 1 equiv) diluting in 10 mL THF was added dropwise in 2 h. The

mixtures were allowed to warm up to room temperature and stir for another 24 h. After

that, 200 mL CH_2Cl_2 was added and the resulting mixture was washed with water and

brine for three times, dried over anhydrous Na_2SO_4 overnight. After removal of solvent,

the residue was purified by flash column chromatography on silica gel with hexane/EA

(v/v = 4:1) as eluent to obtian Compound **1** (12.1 g) as a colorless oil. Yield: 58%. ^{1}H

NMR (CDCl$_3$, 500 MHz, ppm): δ 5.85 (m, 1H), 5.26-5.15 (m, 2H), 4.21 (m, 2H), 3.99 (m,

3H), 3.50 (m, 2H), 1.90 (s, 6H). ^{13}C NMR (CDCl$_3$, 125 MHz, ppm): δ 171.5, 134.2,

117.4, 72.3, 70.7, 68.4, 66.5, 55.8, 30.7.
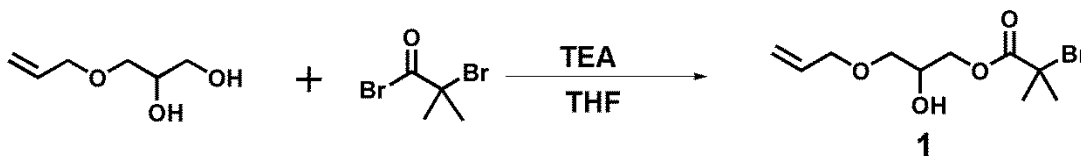
Scheme 4.1. Synthesis of Compound 1.

Compound 2. 4-Pentynoic acid (0.024 mol, 2.35 g, 1.2 equiv), DMAP (0.004 mol, 0.49 g, 0.2 equiv) and 1 (0.02 mol, 5.66 g, 1 equiv) were added into a round-bottomed flask equipped with a magnetic stirrer, followed by addition of anhydrous CH_2Cl_2 (20 mL). The resulting solution was cooled to 0 °C. DIPC (0.03 mol, 3.78 g, 1.5 equiv) was added dropwise to the above mixture, which were stirred at ambient temperature for 24 h. After the precipitate was removed via filtation, the filtrate was washed with brine and water, and drived over anhydrous Na_2SO_4. After removal of solvent, the residue was transferred onto a silica gel column. Eluting with a mixed solvent of hexane/EA (v/v = 5:1) afforded the pure compound 2 (4.73 g) as a colorless oil. Yiled: 65%. ^{1}H NMR (CDCl$_3$, 500 MHz, ppm): δ 5.83 (m, 1H), 5.25 (m, 2H), 5.18 (m, 1H), 4.41 (m, 1H), 4.28 (m, 1H), 3.98 (m, 2H), 3.59 (d, J = 5.0 Hz, 2H), 2.59 - 2.43 (m, 4H), 1.95 (t, 1H), 1.90 (s, 6H). ^{13}C NMR (CDCl$_3$, 125 MHz, ppm): δ 171.2, 170.9, 134.1, 117.4, 82.2, 72.3, 70.3, 69.1, 67.9, 64.0, 55.4, 33.3, 30.7, 14.3.
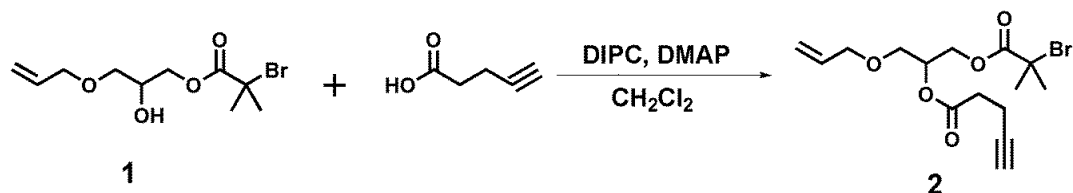
Scheme 4.2. Synthesis of Compound 2.

2-Azidoethanethiol (Compound 4). Compound 3 (0.004 mol, 0.82 g, 1 equiv), DTT (0.0048 mol, 0.74 g, 1.2 equiv) and TEA (0.008 mol, 0.81 g, 2 equiv) were added into a round-bottomed flask equipped with a magnetic stirrer, followed by addition of anhydrous THF (8 mL). The mixtures were stirred for 2 h at room temperature. After removal of solvent, the residue was dissolved in 50 mL CH_2Cl_2, washed with dilute HCl

(0.01 mol/L) solution and water for three times, and dried over anhydrous Na_2SO_4. After removal of solvent, the residue was purified by flash column chromatography on silica gel with CH_2Cl_2 as eluent to obtian Compound 4 (0.60 g) as a colorless oil. Yeild: 73%.

^{1}H NMR (CDCl$_3$, 300MHz, ppm): δ 3.49 (t, $J = 6.0$ Hz, 2H), 2.70 (q, $J = 6.0$ Hz, 2H).
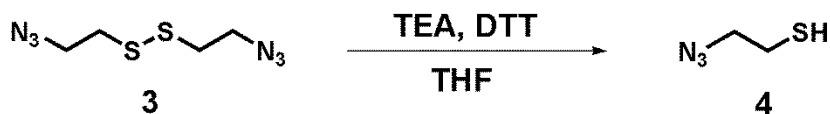
Scheme 4.3. Synthesis of Compound 4.

LPS-Br. Compound 2 (200 mg, 0.557 mmol, 1 equiv), CuBr (80.2 mg, 0.557 mmol, 1 equiv), styrene (11.6 g, 0.11 mol, 200 equiv) and freshly distilled toluene (8 mL) were added into a 100 mL Schlenk flask equipped with a magnetic stirrer. The mixture was degassed by three freeze-pump-thaw cycles, followed by adding PMDETA (96.4 mg, 0.557 mmol, 1 equiv) under nitrogen protection. After one further freeze-pump-thaw cycle, the flask was immersed into a 110 °C oil bath. The reaction was quenched in liquid nitrogen after a prescribed time. Then the crude mixture was directly transferred onto a short silica gel column to remove copper salts, and THF was used to elute the product. The concentrated mixture was precipitated into the methanol, collected by vacuum filtration, and dried *in vacuo* to afford the product as a white powder. ^{1}H NMR (CDCl$_3$, 500 MHz, ppm): δ 7.21-6.31 (br, 140H), 5.85 (s, 1H), 5,19 (m, 2H), 5.05 (m, 2H), 4.45 (m, 2H), 3.96 (m, 2H), 3.43 (m, 2H), 2.53-2.43 (m, 4H), 2.31-1.24 (br, 84H), 0.92 (m, 6H). ^{13}C NMR (CDCl$_3$, 125 MHz, ppm): δ 176.7, 170.7, 145.4, 134.6, 128.7-125.3, 117.3, 82.3, 72.2, 70.5, 69.1, 68.3, 62.2, 46.3-39.6, 33.3, 26.7, 14.4. FT-IR (KBr) v (cm^{-1}): 3303, 3082, 3060, 3026, 2924, 2851, 1942, 1735, 1601, 1493, 1452, 1367, 1154, 1128, 1068,

1028, 907, 758, 698, 539. $M_{n,NMR}$ = 3.3 kg/mol. SEC results: $M_{n,SEC}$ = 3.3 kg/mol, $M_{w,SEC}$ = 3.4 kg/mol, Đ = 1.04.

LPS-N$_3$. Sodium azide (0.26 g, 4 mmol, 10 equiv) was added into a solution of LPS-Br ($M_{n,NMR}$ = 3.3 kg/mol, Đ = 1.04, 1.5 g, 0.4 mmol, 1 equiv) in DMF. The mixture was stirred at room temperature for 48 h. The resultant mixture was diluted with 200 mL CH$_2$Cl$_2$ and washed with water for three times to remove unreacted salts. After concentrating the organic fraction, the mixture was precipitated into a cold methanol, followed by filtrating and drying *in vacuo* to afford the polymer product (1.3 g) as a white powder. Yield: 87%. ^{1}H NMR (CDCl$_3$, 500 MHz, ppm): δ 7.26-6.31 (br, 140H), 5.85 (m, 1H), 5,20 (m, 2H), 5.04 (m, 2H), 4.45 (m, 2H), 3.96 (m, 2H), 3.42 (m, 2H), 2.58-2.43 (m, 4H), 2.33-1.26 (br, 84H), 0.91 (m, 6H). ^{13}C NMR (CDCl$_3$, 125 MHz, ppm): δ 176.7, 170.7, 145.4, 134.6, 128.7-125.3, 117.3, 82.3, 72.2, 70.5, 69.1, 68.3, 62.2, 46.3-39.6, 33.3, 26.7, 14.4. FT-IR (KBr) v (cm^{-1}): 3297, 3082, 3055, 3018, 2924, 2832, 2095, 1946, 1732, 1601, 1489, 1443, 1367, 1154, 1128, 1070, 902, 752, 687, 539. $M_{n,NMR}$ = 3.3 kg/mol. SEC results: $M_{n,SEC}$ = 3.3 kg/mol, $M_{w,SEC}$ = 3.4 kg/mol, Đ = 1.05.

Vinyl-CPS. To a 2 L round-bottomed flask equipped with a magnetic stirrer, CuBr (500 mg) and freshly dried toluene (1 L) were added and bubbled with nitrogen for 24 h. Then, PMDETA (500 mg) was injected into the above mixture via gas-tight syringe. LPS-N$_3$ ($M_{n,NMR}$ = 3.3 kg/mol, Đ = 1.05, 300 mg, 0.09 mmol) was dissolved in 20 mL freshly dried toluene and degassed by three freeze-pump-thaw cycles, followed by slowly injecting into the round-bottomed flask in 48 h at 50 °C via syringe pump. After completing injection, the reaction was carried out for another 24 h. After removal of solvent, the crude mixture was transferred directly onto a short column of silica gel,

which was first eluted by mixing solvent of toluene/hexane (v/v = 3/1) to remove any unreacted LPS precursor. The fraction containing Vinyl-CPS was obtained by using a mixture solvent of toluene/EA (v/v = 2/1) as eluent. After removal of solvent, the residues were precipitated into cold methanol. Vinyl-CPS (240 mg) was afforded by filtration and drying *in vacuo* as a white powder. Yield: 80%. ^{1}H NMR (CDCl$_3$, 500MHz, ppm): δ 7.38-6.31 (m, 140H), 5.83 (m, 1H), 5,19 (m, 2H), 5.04 (m, 2H), 3.93 (m, 2H), 3.40 (m, 2H), 2.93 (m, 2H), 2.64 (m, 2H), 2.41-1.17 (br, 84H), 0.93 (m, 6H). ^{13}C NMR (CDCl$_3$, 125 MHz, ppm): δ 175.7, 170.6, 144.6, 133.4, 127.8-124.1, 116.2, 71.1, 70.5, 69.5, 67.2, 61.4, 45.2-40.4, 39.5, 28.7, 19.0, 8.2. FT-IR (KBr) v (cm^{-1}): 3082, 3064, 3018, 2915, 2841, 1946, 1741, 1601, 1489, 1442, 1023, 902, 172, 696, 538. $M_{n,\text{NMR}}$ = 3.3 kg/mol. SEC results: $M_{\text{n,SEC}}$ = 3.1 kg/mol, $M_{\text{w,SEC}}$ = 3.3 kg/mol, Đ = 1.07.

CPS-N$_3$. Vinyl-CPS ($M_{n,\text{NMR}}$ = 3.3 kg/mol, Đ = 1.07, 200 mg, 0.06 mmol, 1 equiv), 2-azidoethanethiol (20 mg, 0.18 mmol, 3 equiv) and photoinitiator Irgacure 2959 (2 mg, 0.009 mmol, 0.15 equiv) were dissolved in 2 mL of THF, followed by irradiation with UV (365 nm) for 30 min. The solution was then precipitated in the cold methanol twice and collected by filtration. The white dried product was given after drying in vacuum oven overnight. Yield: 76%. ^{1}H NMR (CDCl$_3$, 500MHz, ppm): δ 7.26-6.44 (m, br, 140H), 5.02 (m, 2H), 3.94 (m, 2H), 3.44 (m, 4H), 2.94 (m, 2H), 2.82-2.53 (m, 6H), 2.45-1.25 (m, br, 86H), 0.94 (m, 6H). ^{13}C NMR (CDCl$_3$, 125 MHz, ppm): δ 172.1, 170.6, 145.8, 129.2-125.1, 70.3, 69.7,69.3, 65.3, 62.2, 51.2, 46.8-39.6, 31.5, 29.6, 29.0 21.1. FT-IR (KBr) v (cm^{-1}): 3083, 3064, 3027, 2924, 2850, 2095, 1946, 1741, 1601, 1489, 1442, 1023, 892, 752, 696, 528. $M_{n,\text{NMR}}$ = 3.4 kg/mol. SEC results $M_{\text{n,SEC}}$ = 3.1 kg/mol, $M_{\text{w,SEC}}$ = 3.3 kg/mol, Đ = 1.06.

VPOSS-CPS. CPS-N$_3$ ($M_{n,\text{NMR}}$ = 3.4 kg/mol, Đ = 1.06, 150 mg, 0.045 mmol, 1 equiv), CuBr (1 mg, 0.007 mol, 0.15 equiv), VPOSS-alkyne (36 mg, 0.049 mmol, 1.1 equiv) and freshly distilled toluene (10 mL) were added into a 100 mL Schlenk flask equipped with a magnetic stirrer. The mixture was degassed by three freeze-pump-thaw cycles, followed by introducing PMDETA (8 mg, 0.045 mmol, 1 equiv) under nitrogen protection. After one further freeze-pump-thaw cycle, the reaction was carried out for 16 h at room temperature. Then the crude mixture was directly applied onto a short column filled with a silica gel. CH$_2$Cl$_2$ was first used as eluent to remove excessive VPOSS-alkyne and then the mixing solvent of CH$_2$Cl$_2$/EA (v/v = 4/1) was used to give resulting fraction. After removal of solvent, the mixture was precipitated in the methanol, collected by vacuum filtration, and dried *in vacuo* to afford the product as a white powder (149 mg). Yield: 82%. ^{1}H NMR (CDCl$_3$, 500 MHz, ppm): δ 7.34-6.42 (m, br, 140H), 6.16-5.89 (m, 21H), 5.00 (m, 2H), 4.44 (m, 2H), 4.25 (m, 2H), 3.39 (m, 4H), 3.02-2.94 (m, 4H), 2.92-2.54 (m, 8H), 2.45-1.52 (m, br, 86H), 1.21 (m, 2H), 0.92 (m, 6H). ^{13}C NMR (CDCl$_3$, 125 MHz, ppm): δ 173.3, 145.6, 137.6, 130.2-126.1, 122.2, 69.2, 68.0, 61.2, 50.2, 47.6-38.9, 33.7, 32.0, 30.3, 29.6, 28.7, 27.4, 22.6, 20.9, 13.1. FT-IR (KBr) v (cm^{-1}): 3083, 3064, 3027, 2924, 2850, 1732, 1601, 1498, 1442, 1120 (Si-O-Si, asymmetric stretching), 892, 762, 696, 575. $M_{n,\text{NMR}}$ = 4.1 kg/mol. SEC results: $M_{n,\text{SEC}}$ = 3.4 kg/mol, $M_{w,\text{SEC}}$ = 3.6 kg/mol, Đ = 1.05.

DPOSS-CPS. To an open 20 mL vial were added VPOSS-CPS ($M_{n,\text{NMR}}$ = 4.1 kg/mol, Đ = 1.05, 100 mg, 0.025 mmol, 1 equiv), 1-thioglycerol (27 mg, 0.25 mmol, 10 equiv), photoinitiator Irgacure 2959 (1 mg, 0.0045 mmol, 0.18 equiv) and 2 mL of THF. The mixture was then irradiated with UV (365 nm) for 20 min. The solution was then

directly precipitated into methanol/water mixture (v/v = 1/1) twice and the product was collected by filtration. After drying *in vacuo* the product was obtained as a white powder (83 mg). Yield: 70%. ^{1}H NMR (CDCl$_3$, 500 MHz, ppm): δ 7.34-6.42 (m, br, 140H), 5.32-4.40 (m, 16H), 4.21 (m, 2H), 3.92-3.47 (m, 21H), 3.46-2.92 (m, 8H), 2.91-2.42 (m, 36H), 2.41-1.32 (m, br, 86H), 1.27 (m, 2H), 1.22-0.77 (m, 20H). ^{13}C NMR (CDCl$_3$, 125 MHz, ppm): δ 173.3, 145.6, 130.2-126.1, 69.2, 68.0, 61.2, 50.2, 47.6-38.9, 33.7, 32.0, 30.3, 29.6, 28.7, 27.4, 22.6, 20.9. FT-IR (KBr) v (cm^{-1}): 3345 (br), 3083, 3056, 3021, 2924, 2845, 1733, 1654, 1601, 1498, 1444, 1120 (Si-O-Si asymmetric stretching), 1024, 893, 770, 691, 542. $M_{n,NMR}$ = 4.9 kg/mol. SEC results: $M_{n,SEC}$ = 4.0 kg/mol, $M_{w,SEC}$ = 4.2 kg/mol, Đ = 1.06.

TC$_{60}$-CPS. The CPS-N$_3$ ($M_{n,NMR}$ = 3.4 kg/mol, Đ = 1.06, 100 mg, 0.03 mmol, 1 equiv), CuBr (1 mg, 0.007 mmol, 0.23 equiv), TC$_{60}$-alkyne (70 mg, 0.027 mmol, 0.9 equiv) and freshly distilled toluene (10 mL) were added into a 100 mL Schlenk flask equipped with a magnetic stirrer. The mixture was degassed by three freeze-pump-thaw cycles, followed by introducing PMDETA (5 mg, 0.03 mmol, 1 equiv) under nitrogen protection. After one further freeze-pump-thaw cycle, the reaction was carried out for 16 h at room temperature. Then the crude mixture was directly applied onto a short column filled with a silica gel. Toluene/EA (v/v = 10/1) was first used as eluent to remove excessive CPS-N$_3$ and then the mixing solvent of CH$_2$Cl$_2$/EA (v/v = 2/1) was used to give resulting fraction. After removal of solvent, the mixture was precipitated in the methanol, collected by vacuum filtration, and dried *in vacuo* to afford the product as a red powder (131 mg). Yield: 80%. ^{1}H NMR (CDCl$_3$, 500 MHz, ppm): δ 7.26-6.44 (m, br, 140H), 5.02 (m, 2H), 4.87-4.53 (m, 20H), 4.48 (m, 2H), 3.99-3.83 (m, 5H), 3.39 (m, 4H), 2.96-

2.46 (m, 10H), 2.45-1.25 (m, br, 178H), 0.94 (m, 6H). ^{13}C NMR (CDCl$_3$, 125 MHz, ppm): δ 165.6, 162.6, 145.8, 140.6, 129.2-125.1, 83.5, 63.2, 50.7, 46.8-39.6, 31.5, 29.6, 29.0, 28.1. FT-IR (KBr) v (cm^{-1}): 3083, 3058, 3024, 2922, 2846, 1939, 1744, 1600, 1490, 1448, 1363, 1312, 1210, 1151, 1024, 837, 753, 702, 541. $M_{n,NMR}$ = 6.0 kg/mol. SEC results: $M_{n,SEC}$ = 4.5 kg/mol, $M_{w,SEC}$ = 4.7 kg/mol, $Đ$ = 1.05.

AC$_{60}$-CPS. TC$_{60}$-CPS ($M_{n,NMR}$ = 6.0 kg/mol, $Đ$ = 1.05, 100 mg, 0.017 mmol) was dissolved in mixture of 4 mL CH$_2$Cl$_2$ and 1 mL CF$_3$COOH. The resulting mixture was stirred at room temperature for 8 h. After removal of solvent, the residue was re-dissolved in 3 mL benzene. After freeze drying, the product was obtained as a red powder (80 mg). Yield: 89%. ^{1}H NMR (DMSO-d_6, 500 MHz, ppm): δ 7.26-6.44 (m, br, 140H), 5.02 (m, 2H), 4.98-4.60 (m, 20H), 4.46 (m, 2H), 3.99-3.83 (m, 5H), 3.39 (m, 4H), 2.96-2.46 (m, 10H), 2.45-1.25 (m, br, 88H), 0.94 (m, 6H). ^{13}C NMR (DMSO-d_6, 125 MHz, ppm): δ 165.6, 162.6, 145.8, 140.6, 129.2-125.1, 83.5, 62.7, 50.7, 46.8-39.6, 31.5, 29.6, 29.0. FT-IR (KBr) v (cm^{-1}): 3082, 3060, 3026, 2925, 1958, 1745, 1645, 1601, 1493, 1453, 1431, 1364, 1203, 1122, 1066, 1028, 906, 759, 719, 540. $M_{n,NMR}$ = 5.4 kg/mol. SEC results: $M_{n,SEC}$ = 3.9 kg/mol, $M_{w,SEC}$ = 4.2 kg/mol, $Đ$ = 1.09.

4.3 Results and Discussion

In this section, the successful synthesis of "nano-diamond-ring-like" giant surfactants will be fully characterized, as well as the facile, efficient, and modular nature of the synthetic approach will be discussed.

4.3.1 Synthesis of the linear PS precursor.

The synthetic route outlined in Scheme 4.4 is quite straightforward, aiming to fulfill the criteria of the "click" reaction, which requires only stoichiometric conditions, minimum setup and work-up procedures but achieves quantitative conversions.[60, 135] The CuAAC reaction has been regarded as one of most widely used "click" reactions.[61, 131] Since the first report to use the CuAAC reaction in the synthesis of a cyclic PS by Grayson et al,[149] the CuAAC chemistry becomes prevalent in preparation of cyclic homopolymer,[151-154, 168] cyclic block polymer,[161-163] and other cyclic polymer-based functionalized materials with complex architectures.[156, 169-175] The synthesis of "diamond-ring-like" giant surfactants by tethering cyclic polymer with MNPs requires a functional CPS building block. To this end, an initiator (compound 2) containing vinyl, alkyne and bromo groups was specifically designed and synthesized, as illustrated in Scheme 4.2. The chemical structure of 2 was unambiguously characterized by ^{1}H NMR and ^{13}C NMR (Figures 4.1). In the ^{1}H NMR spectrum, the resonance signals of vinyl and alkyne protons could be clearly observed at 5.89, 5.27 and 1.95 ppm, which could also be confirmed by the appearance of *sp^2* and *sp* carbon at 134.1 and 117.4 ppm as well as 82.2 and 69.1 ppm in the ^{13}C NMR spectrum (Figure 4.1b).
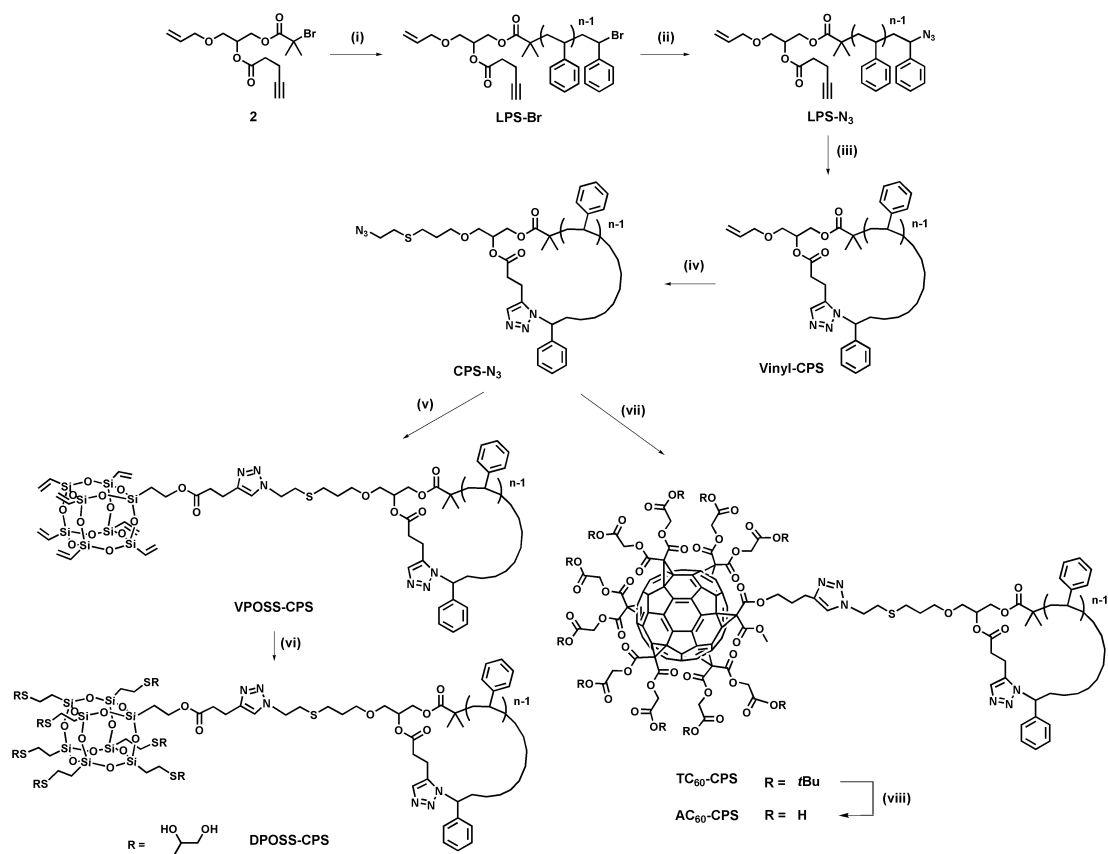
Scheme 4.4. Synthesis of DPOSS-CPS and AC_{60}-CPS. Reagents and conditions: (i) Styrene, CuBr, PMDETA, toluene, 110 °C, 20%; (ii) NaN_3, DMF, room temperature (r.t.), 87%; (iii) CuBr, PMDETA, toluene, r.t., 80%; (iv) $N_3CH_2CH_2SH$, Irgacure 2959, THF, *hv*, 30 min, r.t., 76%; (v) VPOSS-alkyne, CuBr, PMDETA, toluene, r.t., 82%; (vi) THF, 1-thioglycerol, Irgacure 2959, *hv*, 20 min, 70%; (vii) TC_{60}-alkyne, CuBr, PMDETA, toluene, r.t., 80%; (viii) CF_3COOH, CH_2Cl_2, r.t., 89%.
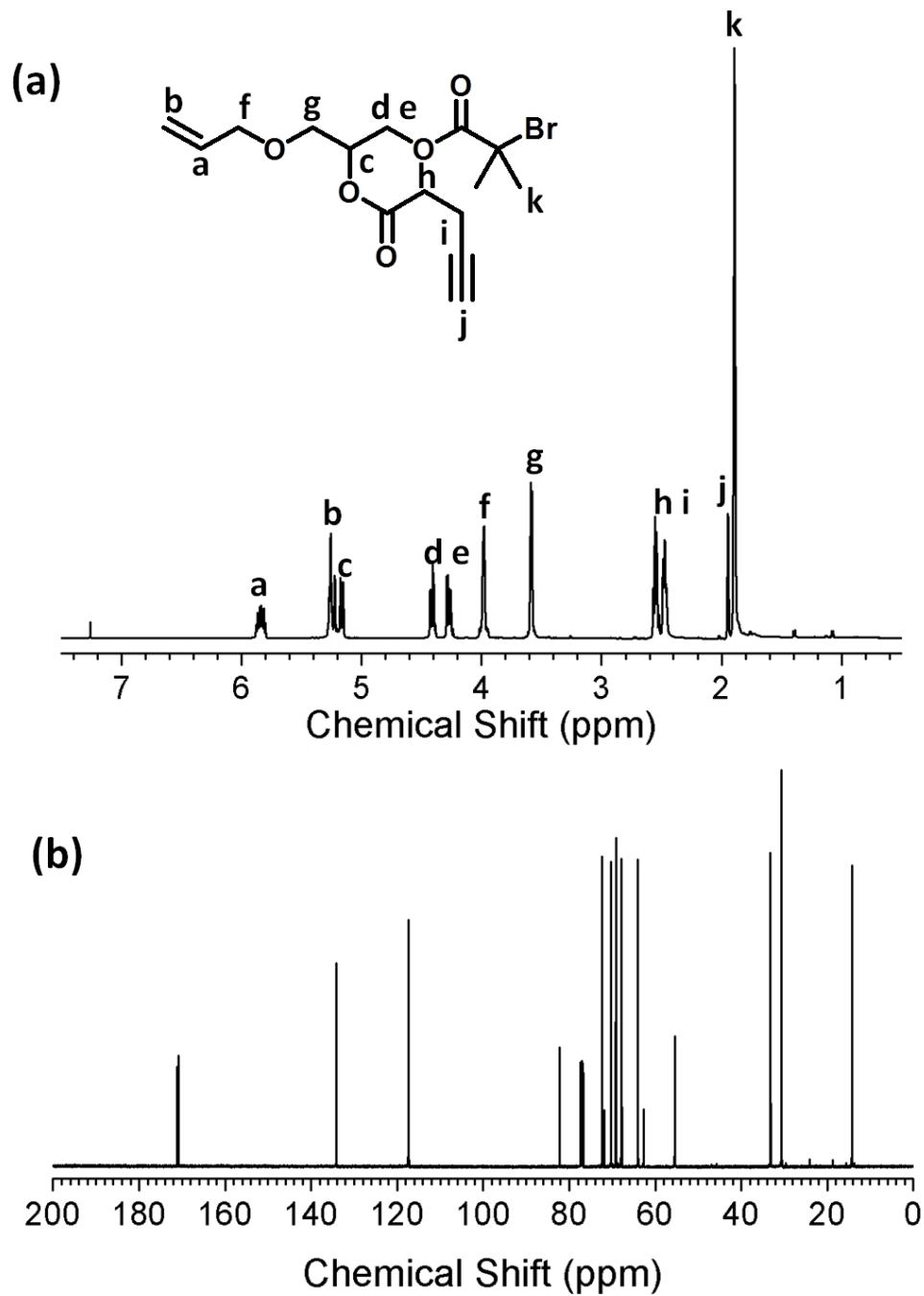
Figure 4.1. ¹H NMR (a) and ¹³C NMR (b) spectra of Compound 2.
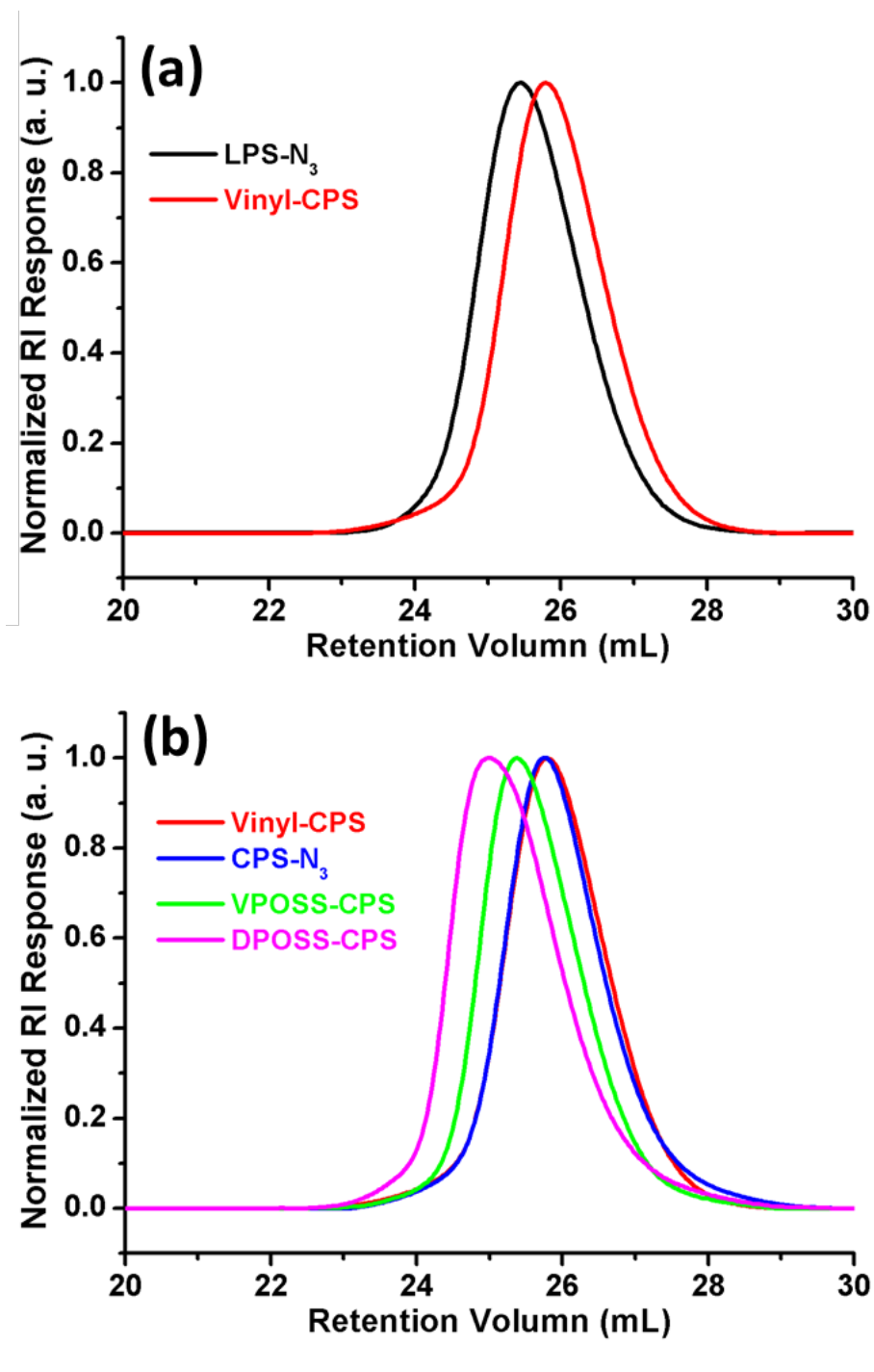
Figure 4.2. SEC overlay of (a) LPS-N_3 (black curve) and Vinyl-CPS (red curve), (b) Vinyl-CPS (red curve), CPS-N_3 (blue curve), VPOSS-CPS (green curve) and DPOSS-CPS (pink curve).

117
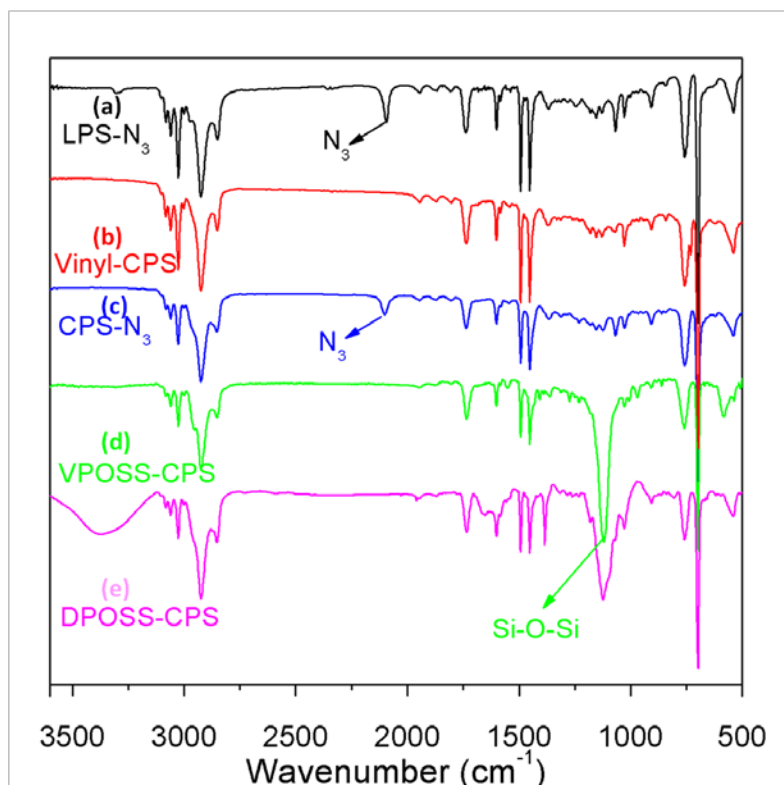
Figure 4.3. FT-IR spectra of (a) LPS-N$_3$ (black curve), (b) Vinyl-CPS (red curve), (c) CPS-N$_3$ (blue curve), (d) VPOSS-CPS (green curve) and (e) DPOSS-CPS (pink curve).

Using this initiator, LPS-Br was readily prepared under the typical conditions for ATRP. After treating LPS-Br with sodium azide, a "clickable" azide group was installed at the chain end to give LPS-N$_3$. As shown in Figure 4.2a, the SEC curve reveals a monomodal and symmetric elution profile with narrow dispersity of LPS-N$_3$ ($Đ$ = 1.05). In the FT-IR spectrum, the absorbance band around 3300 cm^{-1} and 2100 cm^{-1} verifies the successful introduction of alkyne and azide groups in the LPS-N$_3$ chain (Figure 4.3). Efforts to calculate the chain-end functionalities of LPS-N$_3$ or LPS-Br based on the ^{1}H NMR spectra were hampered by the fact that the resonance signals of the concerned protons cannot be fully deconvoluted from the other signals. Instead, the chain-end

functionalities of LPS-N_3 were estimated from its MALDI-TOF mass spectrum. As shown in Figure 4.4a, only the mass distributions related to the structure of LPS-N_3 can be observed. Since the detection limit of MALDI-TOF is around 5%,[176] chain end functionalities of LPS-N_3 is thus believed to be no less than 95%.
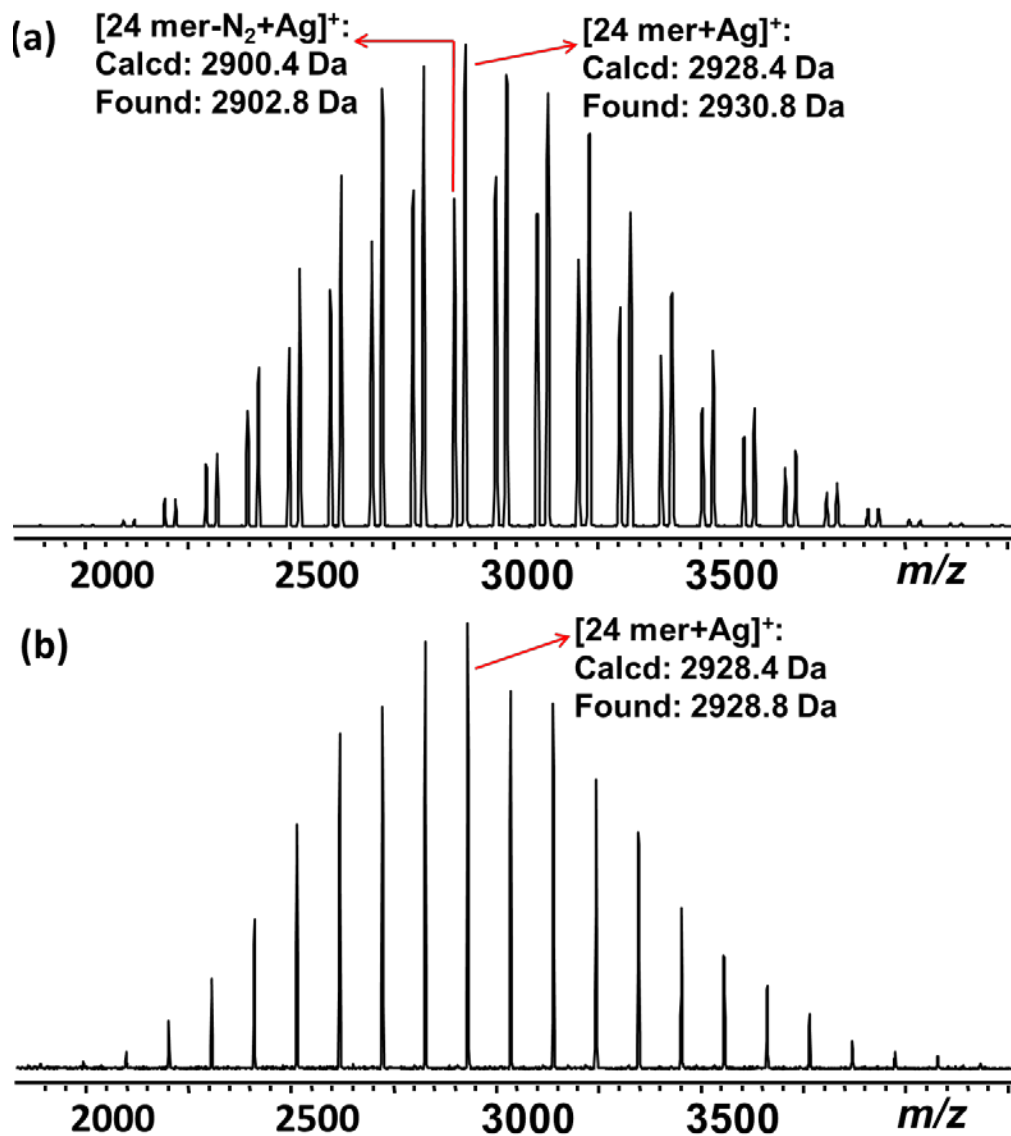
Figure 4.4. MALDI-TOF mass spectra of (a) LPS-N_3 and (b) Vinyl-CPS.

4.3.2 Synthesis of Vinyl-CPS via the CuAAC chemistry

In the cyclization step, concentration of the starting linear polymer solution is the primary factor in determining the preference between intermolecular or intramolecular reactions.[149] The "click" cyclization reaction was carried out at a very dilute solution (0.3 mg/mL) to ensure fully intramolecular cyclization. Moreover, a continuous dropwise addition was utilized to maintain the infinitesimal concentration of linear polymer precursors during intramolecular cyclization.[149, 177] Over a time period of 48 hours, 300 mg LPS-N$_3$ in a 20 mL toluene solution was slowly added into 1 L warm toluene containing CuBr and PMDETA via syringe. After stirring for additional 24 h, the reaction was completed and the CPS product (Vinyl-CPS) was conveniently obtained by purification with flash column chromatography on silica gel.

The formation of Vinyl-CPS is unambiguously characterized by ^{1}H NMR, FT-IR and SEC, as well as MALDI-TOF mass spectrometry. The complete disappearance of azide and alkyne resonances in FT-IR spectra (Figure 4.3) provides the evidence of a successful CuAAC reaction. An increased retention volume of Vinyl-CPS relative to LPS-N$_3$ can be clearly seen in the SEC overlay (Figure 4.2a), which is corresponding with a smaller hydrodynamic volume of cyclic polymer, in comparison to their linear analogues.[147, 149] The monomodal SEC profile with narrow distribution ($Đ$ = 1.07) is remained, suggesting high uniformity of Vinyl-CPS with no byproducts of intermolecular reactions. The cyclization of LPS-N$_3$ to afford Vinyl-CPS was further confirmed by the MALDI-TOF mass spectroscopy. As shown in Figure 4.4a, two distinct molecular weight distributions corresponding to $[M + Ag]^+$ and $[M - N_2 + Ag]^+$ were observed for LPS-N$_3$, where $[M - N_2 + Ag]^+$ is caused by post-source expulsion of N$_2$ gas from the ionized

LPS-N$_3$ sample.[178] After cyclization, the mass spectrum of Vinyl-CPS exhibits only one single symmetric distribution of [M + Ag]$^+$, where the molecule weights of Vinyl-CPS remains identical to its linear precursor polymer (see Figure 4.4b). A representative peak m/z value of 2928.8 Da corresponding to 24-mer of CPS with a silver ion is in good agreement with the calculated mass ([24mer·Ag]$^+$, calcd. mass 2928.4 Da). (Figure 4.5a) The difference between two neighboring peaks is equivalent to the mass of one styrene repeating unit (104.1 Da). These data clearly validate the precisely defined structure and molecular homogeneity of Vinyl-CPS. The yield of cyclization is as high as 80%, and the purification can be readily achieved by flash column chromatography with no fractionation required.

We have also applied dynamic light scattering (DLS) technique and diffusion-ordered spectroscopy (DOSY) to further confirm the success of cyclization. Although it is known that the R_h values of linear and cyclic polymers with the same molecular weights are different due to the lack of chain ends and thus a more compact chain conformation in cyclic polymers,[179] dynamic light scattering (DLS) results of the LPS-N$_3$ precursor and the Vinyl-CPS fail to give a clear difference in their R_h values (data not shown). This could be attributed to the low molecular weights of the polymers used in the demonstrative synthesis (~ 3000 Da), resulting in very small R_h difference in solution.[179] On the other hand, DOSY experiments of the LPS-N$_3$ and Vinyl CPS indeed show that under the same conditions, the diffusion constant (D) of the Vinyl-CPS is larger than that of the LPS-N$_3$ precursor (see Figure 4.6), which is qualitatively in good agreement with previously reported results.[180, 181]
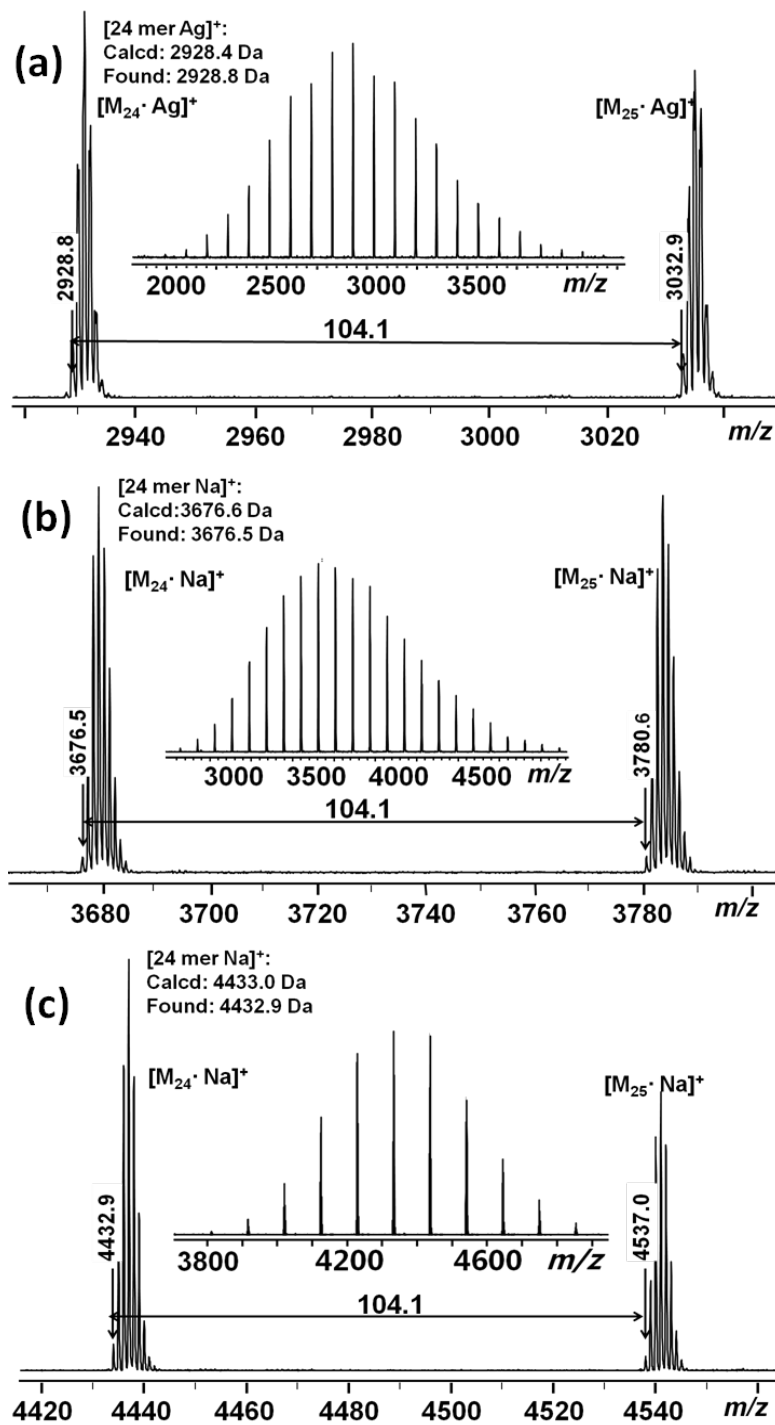
Figure 4.5. MALDI-TOF mass spectra of (a) Vinyl-CPS, (b) VPOSS-CPS and (c) DPOSS-CPS. All these data were acquired with monoisotopic resolution. The insets show the full spectra.

122
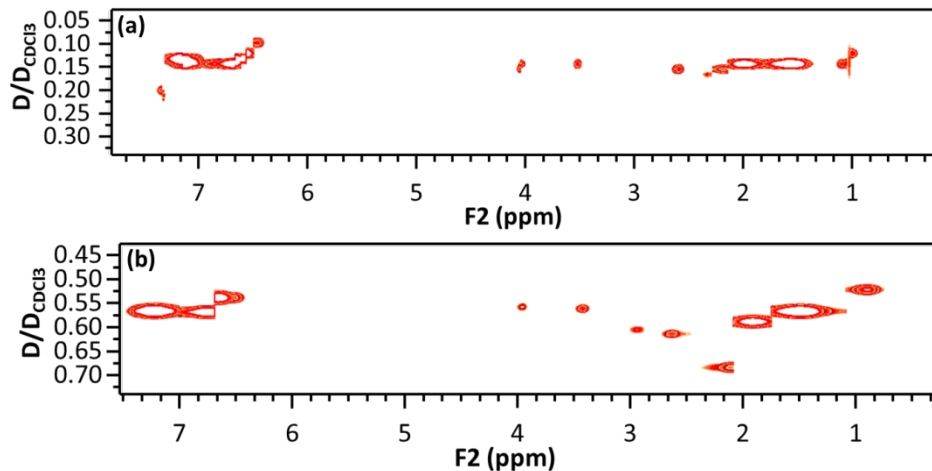
Figure 4.6. DOSY results of (a) LPS-N3 and (b) Vinyl-CPS in CDCl$_3$.

4.3.3 Synthesis of DPOSS-CPS via thiol-ene chemistry

Thiol-ene addition reaction is another widely applied chemistry possessing mostly "click" features for various purposes.[63, 132, 133] It is particularly powerful for situations involving multiple functionalization or sites of poor reactivity such as polymer or dendrimers. The vinyl group[182] installed on Vinyl-CPS is subjected to the thiol-ene reaction to introduce an azide group in one step with high efficiency, affording the azido-functionalized cyclic PS building block. Efficient addition reaction between Vinyl-CPS and 2-azidoethanethiol was supported by the complete disappearance of the vinyl proton resonance peaks at 5.83 and 5.19 ppm, and the appearance of resonances from the thiol-ether methylene protons at 3.44 and 2.70 ppm (Figure 4.7b). In addition, a strong absorption band appeared around 2100 cm^{-1} in the FT-IR spectra of the resulting product (Figure 4.3c), indicating the existence of the azide group. It should be noted that, via the thiol-ene reaction, the Vinyl-CPS precursor can be converted to other functional cyclic polymers with not only an azide group but also various other functional groups, such as

hydroxyls and carboxylic acids,[71, 136] enabling the as-prepared Vinyl-CPS as a common precursor. With azide-functionalized CPS (CPS-N_3) available, the general and efficient sequential "click" approach[71] would be applied to afford the desired "nano-diamond-ring-like" giant surfactants.

The CuAAC reaction between CPS-N_3 and VPOSS-alkyne proceeds at room temperature for overnight to achieve quantitative conjugation between the two building blocks. After purification by flash column chromatography on silica gel, the pure VPOSS-CPS was collected in a high yield (82%). In the ^{1}H NMR and ^{13}C NMR spectra of VPOSS-CPS, the signals of major characteristic protons and carbons attributing to vinyl groups of VPOSS can be clearly observed in the Figure 4.7c (see also in Figure 4.8). In the FT-IR spectra (Figure 4.3d), the disappearance of the azide absorption peak, as well as the appearance of a strong band at *ca.* 1123 cm^{-1} corresponding to the asymmetric stretching of Si-O-Si, is evident of successful reaction between CPS-N_3 and VPOSS-alkyne. The formation of VPOSS-CPS is also clearly exhibited in the SEC overlay (Figure 4.2b), where the curve of VPOSS-CPS shifts to lower retention volume comparing to CPS-N_3 due to increased molecular weight (Figure 4.2b). We also obtained the MALDI-TOF mass spectrum of VPOSS-CPS, as shown in Figure 4.5b, which displays only one symmetric molecular weight (MW) distribution. The isotopic MW observed from the mass spectrum agrees well with the calculated one. For example, the calculated isotopic MW for [24mer·Na]$^+$ is 3676.6 Da, while the measured value is 3676.5 Da. The molecular characterization data are summarized in Table 4.1.
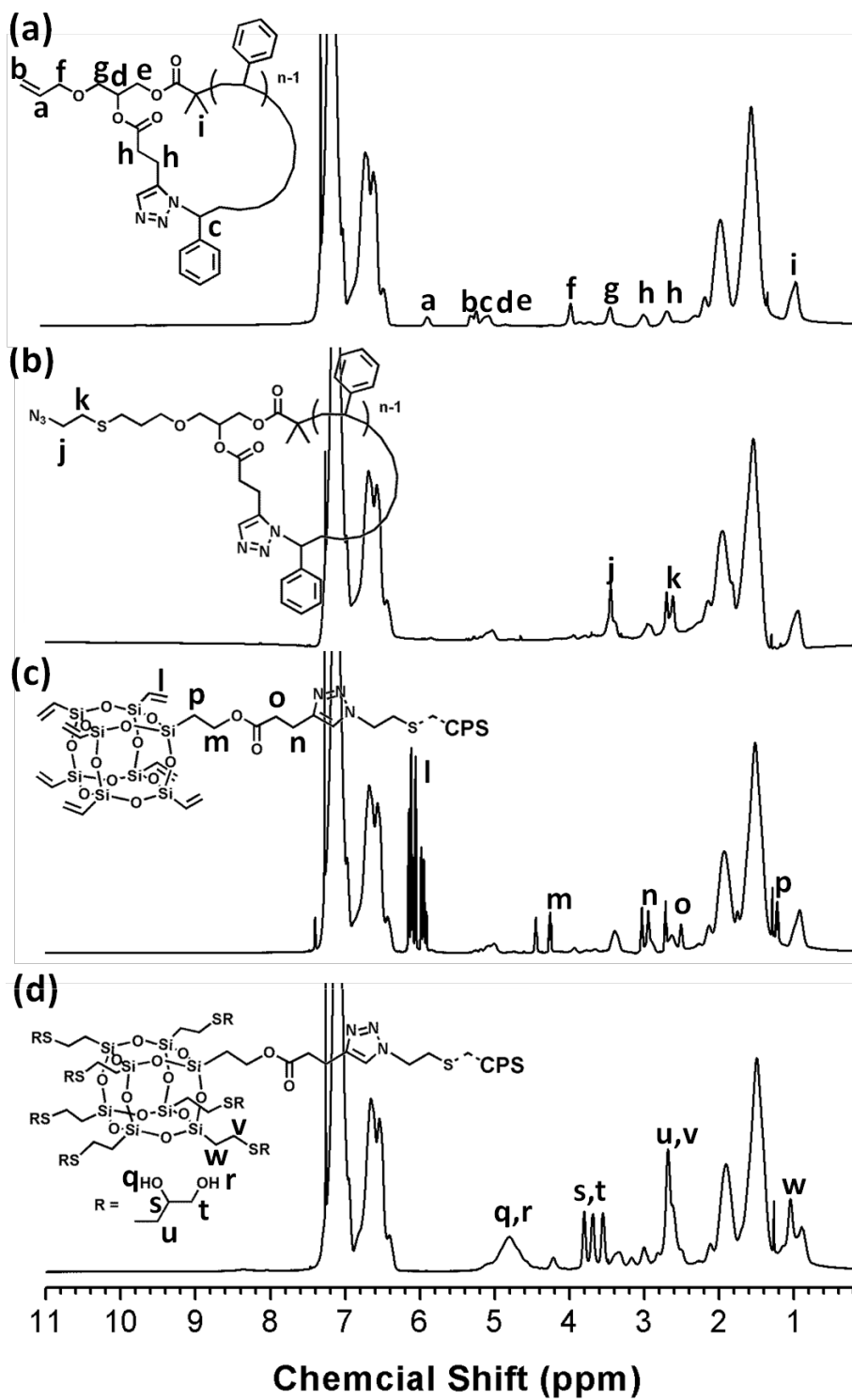
Figure 4.7. ^{1}H NMR spectra of (a) Vinyl-CPS, (b) CPS-N$_3$, (c) VPOSS-CPS, (d) DPOSS-CPS.

125
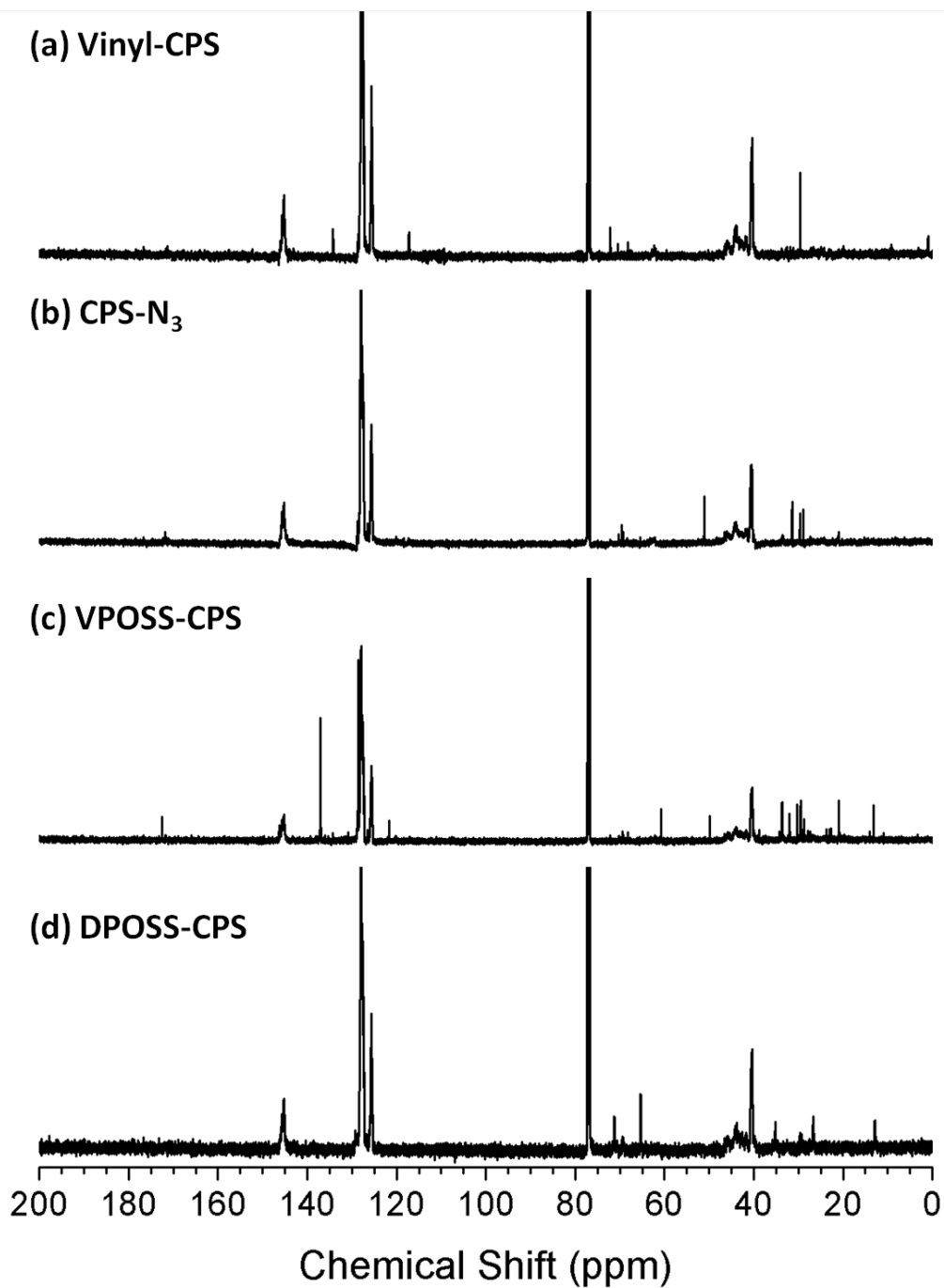
Figure 4.8. ^{13}C NMR spectra of (a) Vinyl-CPS, (b) CPS-N$_3$, (c) VPOSS-CPS and (d) DPOSS-CPS.

Table 4.1 Summary of molecular characterizations.

Sample	Molecular Formula	M_{Calcd} (Da)	M_{Found} (Da)	$M_{n,NMR}$[c] (kg/mol)	$M_{n,SEC}$[d] (kg/mol)	$M_{w,SEC}$[d] (kg/mol)	$Đ$[d]
LPS-Br	-	-	-	3.3	3.3	3.4	1.04
LPS-N$_3$	-	-	-	3.3	3.3	3.4	1.05
Vinyl-CPS	$C_{207}H_{213}N_3AgO_5$[a]	2928.4[a]	2928.8[a]	3.3	3.1	3.3	1.07
CPS-N$_3$	-	-	-	3.4	3.1	3.3	1.06
VPOSS-CPS	$C_{230}H_{248}N_6NaO_{19}SSi_8$[b]	3676.6[b]	3676.5[b]	4.1	3.4	3.6	1.05
DPOSS-CPS	$C_{251}H_{304}N_6NaO_{33}S_8Si_8$[b]	4433.0[b]	4432.9[b]	4.9	4.0	4.2	1.06
TC$_{60}$-CPS	-	-	-	6.0	4.5	4.7	1.05
AC$_{60}$-CPS	-	-	-	5.4	3.9	4.2	1.09

[a] These data are based on 24mer with a silver ion ([24mer·Ag]$^+$). [b] These data are based on 24mer with a sodium ion ([24mer·Na]$^+$). [c] These data are calculated based on ^{1}H NMR spectra. [d] These data are obtained from SEC measurements.

We have demonstrated that all the vinyl groups on the POSS cage could be efficiently and completely converted to various functional groups via the thiol-ene reaction.[71, 136] Here, thiol-ene reactions were performed to install fourteen hydroxyl groups onto the VPOSS cage to impart the hydrophilicity of giant surfactants, under the similar reaction conditions as reported in our previous publications.[71] The well-defined

structure of the final giant surfactant DPOSS-CPS was unambiguously determined by NMR, SEC and MALDI-TOF mass spectrum. In the ^{1}H NMR spectra, complete disappearance of vinyl resonance peaks at 6.16-5.89 ppm and the emergence of new characteristic thiol ether protons resonance at 4.79, 3.80, 3.68 and 2.68 ppm reveal the complete addition reactions (Figure 4.7). Due to the larger hydrodynamic volume of DPOSS, in comparison to VPOSS, the SEC curve of DPOSS-CPS shift to a lower retention volume than that of VPOSS-CPS, where the symmetric and monomodal peak with narrow dispersity was maintained. Strikingly, we even successfully obtained a clean MALDI-TOF mass spectrum of the final product DPOSS-CPS. One symmetric MW distribution was clearly exhibited in Figure 4.5c, where the observed MW is consistent with calculated one (*e.g.*, for [24mer·Na]$^+$, the found MW is 4432.9 Da, while the calculated MW is 4433.0 Da).

4.3.4 Extending to AC$_{60}$-CPS system.

A perfect "ring" is designed to enable one to decorate it with various "diamonds" on the basis of specific designs. Similarly, the as-prepared cyclic PS ring is expected to be able to install not only functionalized POSS moieties, but also other different "nano-atoms" ("diamonds") to construct a variety of giant surfactants. Benefiting from the modular synthetic design, CPS-N$_3$ is indeed a versatile building block that can be decorated with various alkyne functionalized building blocks. Here, a precisely functionalized C$_{60}$ derivative with one terminal alkyne and ten protected carboxylic acid groups (TC$_{60}$-alkyne)[68] was utilized as example to extend the versatility of CPS ring.

Due to the high polarity of TC_{60}-alkyne, a slightly excess amount of $CPS-N_3$ was used to ensure complete consumption of TC_{60}-alkyne. After the CuAAC ligation, the excess $CPS-N_3$ was readily removed by flash chromatography on silica gel using a mixture of toluene/EA (v/v = 10/1) as the eluent. The target product TC_{60}-CPS was eluted with CH_2Cl_2/EA (v/v = 2/1), and collected as a red powder after precipitation in methanol, filtering and drying *in vacuo*. The disappearance of the absorption bands from azide group at *ca.* 2100 cm^{-1} and alkyne group at *ca.* 3300 cm^{-1} in the FT-IR spectra indicates successful reaction between $CPS-N_3$ and TC_{60}-alkyne (Figure 4.9). The well-defined structure of TC_{60}-CPS was further evidenced by ^1H NMR, ^{13}C NMR and SEC. The amphiphilic features of final product, namely, AC_{60}-CPS, was endowed after deprotection of *tert*-butyl groups on TC_{60}, which was feasibly achieved by treating with CF_3COOH in CH_2Cl_2 without any further purification. The final products were fully characterized. The disappearance of *tert*-butyl protons at 1.47 ppm (Figure 4.10) in ^1H NMR spectrum and *tert*-butyl carbons at 28.2 ppm 82.9 ppm (Figure 4.11) confirms the complete deprotection. The well-defined structure of AC_{60}-CPS is also verified by the SEC overlay (Figure 4.12), where the curve of AC_{60}-CPS clearly shifts to higher retention volume after deprotection of *tert*-butyl groups, maintaining symmetric and monomodal peak with narrow dispersity. Notably, although the AC_{60}-CPS sample has ten carboxylic acid groups after deprotection, its SEC curve remains quite symmetric. This indicates that AC_{60}-CPS does not have significant interactions with the columns used in SEC experiments, and is in agreement with our previous SEC results of either the APOSS-PS conjugates, where each APOSS cage has seven carboxylic acid groups,[71] or

the AC_{60}-PS conjugates.[68] The data for molecular characterizations are summarized in Table 4.1.

It is anticipated that the functional $CPS-N_3$ building block should be applicable to "click" with various other "nano-atoms" bearing single or multiple alkyne groups, giving rise to giant surfactants with diverse and unique architectures. In fact, this $CPS-N_3$ has been employed in our group for preparation of nanoatom-based multi-headed/multi-tailed giant surfactants. The cyclic polymer based giant surfactants are expected to exhibit distinct self-assembling behaviors and create unique hierarchical structures in comparison to their linear analogues. For example, the giant surfactants composed of DPOSS tethered with a linear PS have been proved to be able to form ordered nanostructures with feature size around or smaller 10 nm in bulk and thin films.[69] It is anticipated that owing to more compact polymer structure of CPS, DPOSS-CPS with the same PS molecular weight should construct nanostructures with even smaller periodicities than those of the DPOSS-LPS conjugates. Those sub-10-nm structures are not only of scientific interests but also practical importance, since traditional top-down lithography techniques encounter serious challenges in achieving such small ordered domains.[183] The AC_{60}-based giant surfactants and their self-assembled micelles in solution might show potential applications in biology such as DNA cleavage[184] and enzyme inhibition[185] due to the interaction of water-soluble organofullerenes with DNA, proteins and living cells.[55] The systematic investigation on the self-assembly behaviors of the nano-diamond-ring-like giant surfactants will be discussed in future publications.

130
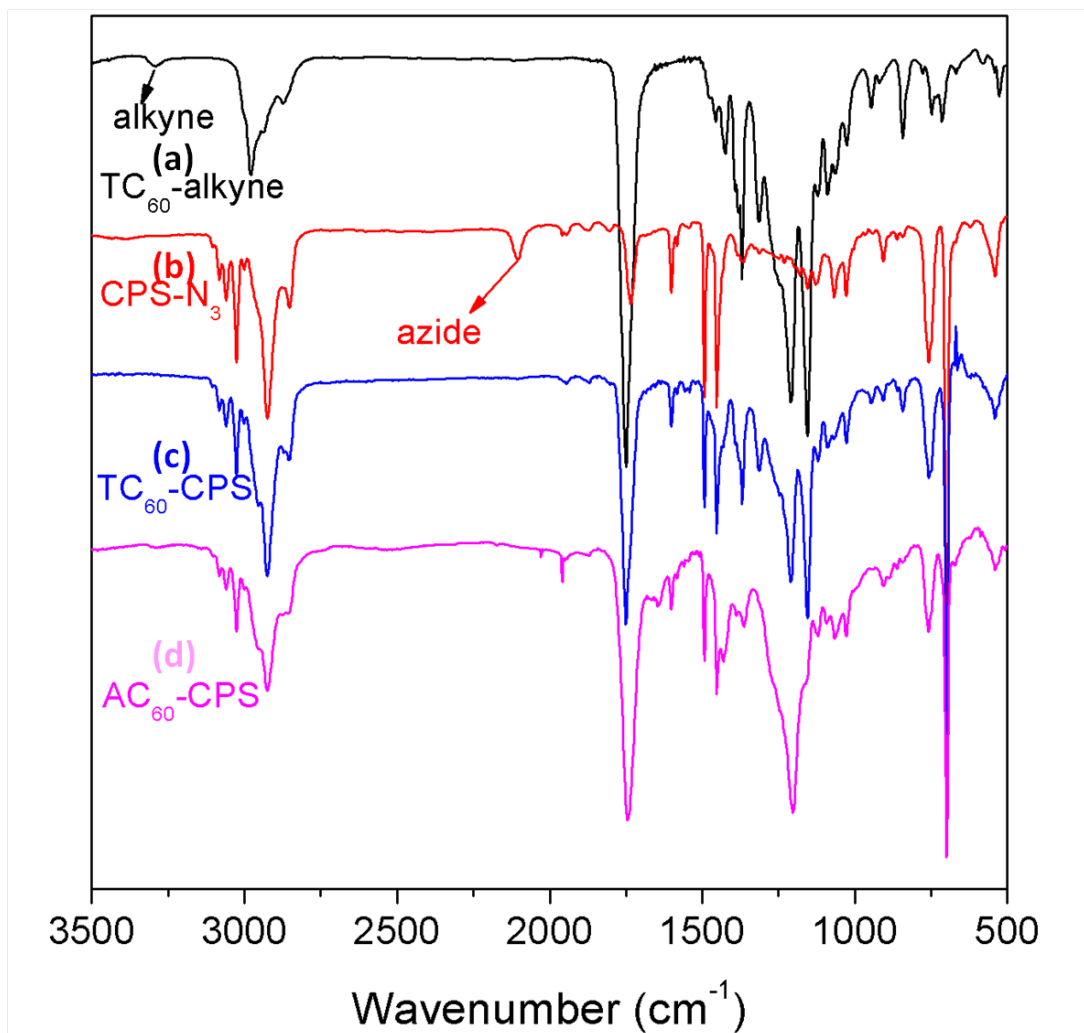
Figure 4.9. FT-IR spectra of (a) TC_{60}-alkyne (black curve), (b) CPS-N_3 (red curve), (c) TC_{60}-CPS (blue curve) and (d) AC_{60}-CPS (pink curve).
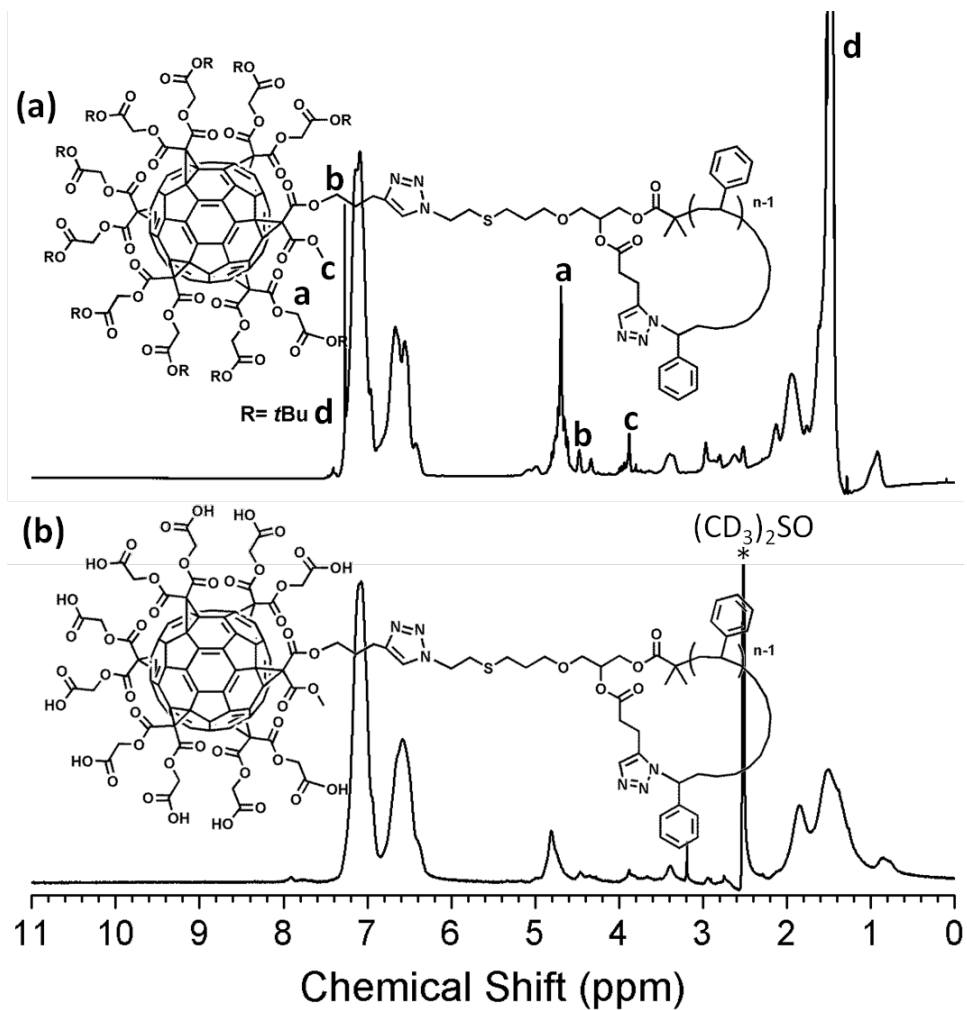
Figure 4.10. ^{1}H NMR spectra of (a) TC$_{60}$-CPS and (b) AC$_{60}$-CPS.
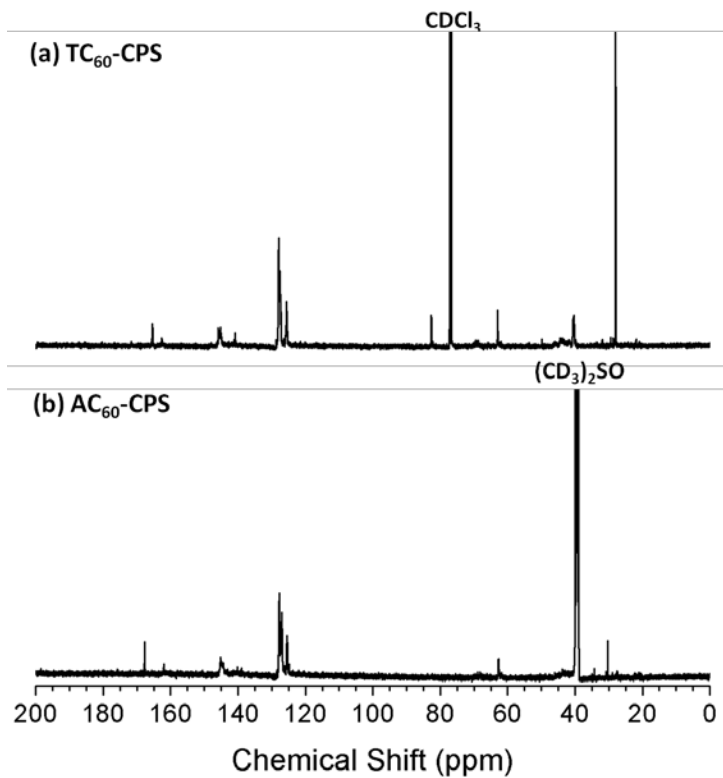
Figure 4.11. ^{13}C NMR spectra of (a) TC_{60}-CPS and (b) AC_{60}-CPS.
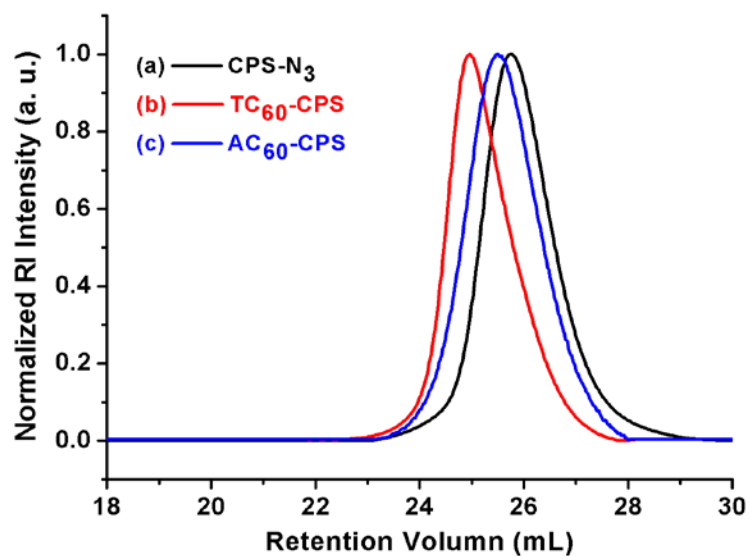
Figure 4.12. SEC overlay of (a) CPS-N_3 (black curve), (b) TC_{60}-CPS (red curve) and (c) AC_{60}-CPS (blue curve).

4.4 Conclusion

In summary, two series of novel "nano-diamond-ring-like" giant surfactants based on hydrophilic DPOSS and AC_{60} tethered with a CPS tail have been successfully synthesized using a combination of the CuAAC and the thiol-ene "click" reactions. Vinyl CPS was first prepared from a trifunctional linear PS precursor via the CuAAC "click" cyclization. Thiol-ene reaction was then applied to introduce an azide group onto the CPS, affording the cyclic CPS-N_3 building block to further react with alkyne-bearing building blocks, such as the VPOSS-alkyne and TC_{60}-alkyne. Due to the modular nature of the synthetic approach, it is expected that CPS-N_3 is compatible with any other alkyne-functionalized building blocks to construct a variety of nanomaterials. The resulting giant surfactants with cyclic polymer tails possess unique structural features other than their linear analogues. Study on their self-assembly behaviors is ongoing in our laboratory and will be discussed in future publications.
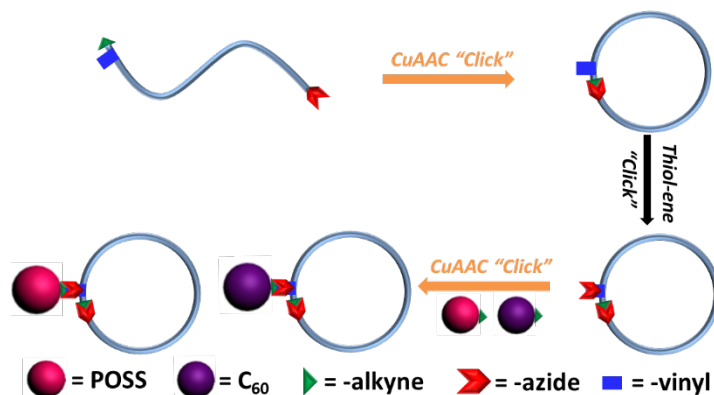
Figure 4.13. General story of chapter IV.*

CHAPTER V

HYDROGEN BONDING INDUCED NANOPHASE SEPARATION IN GIANT

SURFACTANTS CONSISTING OF HYDROPHILIC [60] FULLERENE TETHERED

TO BLOCK COPOLYMERS AT DIFFERENT LOCATIONS

5.1 Introduction

Precise assemblies of hybrid materials containing functionalized nanoparticles (NPs) over multiple length scales have been one of the most essential themes in the fields of nanotechnology over the past two decades.[2, 26, 80, 125, 186, 187] Diblock copolymers (BCPs) with immiscible blocks can form a variety of periodically ordered structures including lamellae (Lam), double gyroid (DG), hexagonally packed cylinder (Hex) and body-centered cubic sphere (BCC) phases through nanophase separation.[21, 188-190] When physically blending NPs with BCPs, these nanophase-separated structures may serve as facile templates for controlling the NPs locations and distributions within the structures.[191-199] Alternatively, chemically tethering polymers onto NPs provides another robust approach to create hierarchical nanostructures with controlled NP composition.[75, 200-204]

Recently, we have developed a library of new hybrid materials based on polymer-tethered molecular NPs (MNPs).[36, 67, 69, 71, 205] They have been regarded as giant surfactants since they capture the structural features of small-molecule surfactants, yet

135

possess much larger sizes comparable to BCPs.[36, 206] It has been demonstrated that giant surfactants exhibit intriguing self-assembling behaviors in the bulk and solution states.[68, 69, 206-208] One representative example is the giant surfactant composed of a hydroxyl-group functionalized polyhedral oligomeric silsesquioxane (POSS) tethered by a polystyrene (PS) tail. They are able to self-assemble into various nano-ordered structures in the bulk with a feature size around or below 10 nm.[69] The majority of studies so far are focusing on the giant surfactants composed of MNP(s) tethered by homopolymer(s). Incorporating BCP with heterogeneous compositions into giant surfactants are not only of scientific interest in creating new and diversified hybrid self-assembled nanostructures, but also practical importance to achieve specific and tunable properties for technological applications.[209-213]

Computer simulations have predicted rich and intriguing phase behaviors of giant surfactants composed of MNP tethered by BCP,[31, 214, 215] while experimental investigations of these giant surfactants are just beginning. In this chapter, we report our recent efforts on the design and synthesis of giant surfactants consisting of a carboxylic acid functionalized hydrophilic [60]fullerene (AC_{60}) tethered onto a polystyrene-*block*-poly(ethylene oxide) (PS-*b*-PEO) BCP. The physical location of AC_{60} is either at the PS block end (AC_{60}-PS-PEO) or at the junction point [PS-(AC_{60})-PEO] between the PS and PEO blocks to generate two different topologies. For PEO and PS blocks, their Flory interaction parameter is $\chi = 0.08$. This requires that a lower limit molecular mass of this BCP must exceed a threshold (in the vicinity of 16 kg/mol) in a lamellar form to reach a sufficient immiscibility (χN, N is the degree of polymerization), yet this molecular mass corresponds to a lower limiting domain size of 18-20 nm.[216-218] Since the PEO and PS

block molecular masses chosen in this study are sufficiently low, the PS-*b*-PEO precursors do not exhibit nanophase separation in the melt. Nevertheless, these two series of giant surfactants possess hydrogen bonds associated with the hydrophilic AC_{60} and PEO blocks, and they drive the nanophase separation, resulting in the formation of various ordered nanostructures, as illustrated in Scheme 5.1. Specifically, topological isomers with identical compositions and molecular masses but different AC_{60} locations in these giant surfactants provide an opportunity to illustrate the topological effect on the nanophase separated structures. This series of materials may thus provide a versatile and practical platform for manipulating the distribution of AC_{60} MNPs within the PEO block domains and tailoring the hybrid ordered structures with feature sizes down to sub-10 nm.
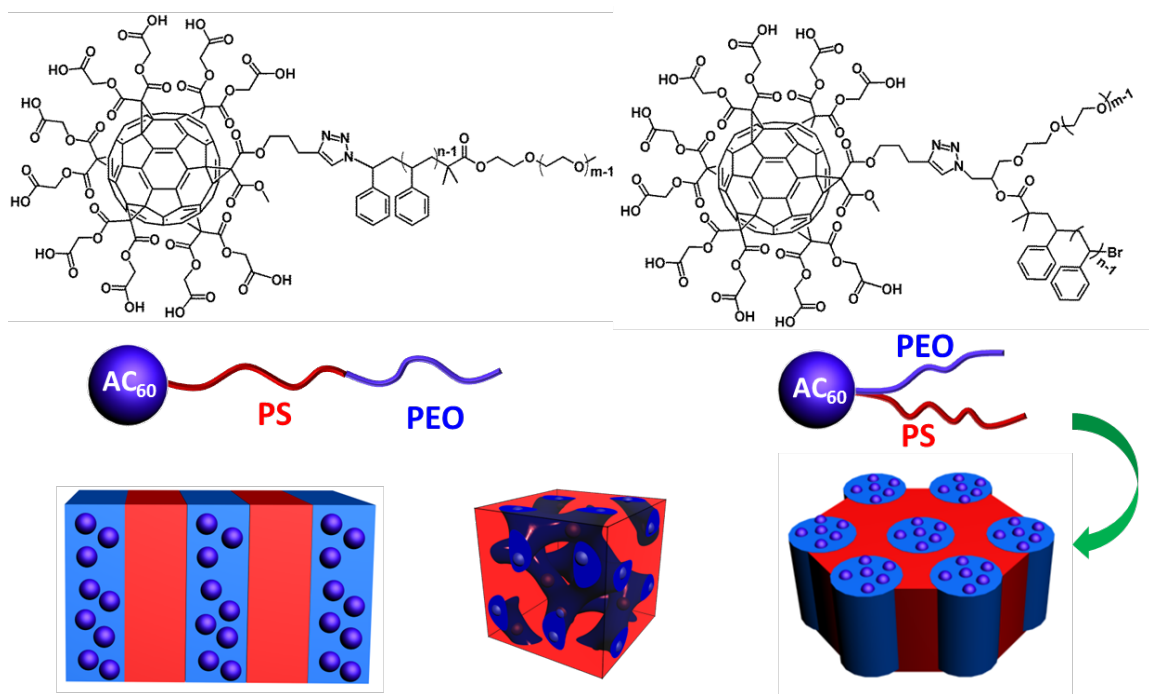
Scheme 5.1. Chemical structures and assemblies of AC_{60}-PS_n-PEO_m and PS_n-(AC_{60})-PEO_m giant surfactants.

5.2 Experimental Section

In this section, the detailed procedures for the synthesis, characterization and assembly of giant surfactants will be described.

5.2.1 Chemicals and Solvents.

[60]Fullerene (C_{60}, MTR Ltd., 99.5%), methyl malonyl chloride (Aldrich, 97%), 5-trimethylsilyl-4-pentyn-1-ol (Aldrich, 96%), pyridine (Aldrich, 99.8%), malonic acid (Aldrich, 99%), *tert*-butyl bromoacetate (Aldrich, 98%), 2-Bromoisobutyryl bromide (Aldrich, 98%), propargyl bromide (Aldrich, 98%), iodine (I_2, Aldrich, 99.8%), CuBr (Aldrich 98%), 1,8-diazabicyclo[5.4.0]undec-7-ene (DBU, Aldrich, 99%), *N,N',N',N'',N''*-pentamethyldiethylenetriamine (PMDETA, Aldrich, 99%), chloroform-*d* ($CDCl_3$, Aldrich, 99.8 at %D) and dimethyl sulfoxide-d_6 (DMSO-d_6, Aldrich, 99.8 at %D) were used as received. α-Hydroxy-ω-Azide Terminated Poly(ethylene glycol) (M_n = 2 kg/mol) was purchased from Polymer Source. Toluene (Aldrich, 99.5%) and 1,2-dichlorobenzene (ODCB, Aldrich, 99%) were stirred with CaH_2 and redistilled prior to use.

5.2.2. Characterization

All nuclear magnetic resonance (NMR) experiments were carried out on a Varian NMRS 500-01 spectrometer. The samples were prepared in $CDCl_3$ for TC_{60}-PS_n-PEO_m and PS_n-(TC_{60})-PEO_m or in DMSO-d_6 for AC_{60}-PS_n-PEO_m and PS_n-(AC_{60})-PEO_m. The concentration for ^{1}H NMR and ^{13}C NMR experiments is 15-20 mg/mL and 60-80 mg/mL, respectively. The ^{1}H NMR spectra and ^{13}C NMR spectra were referenced to the residual impurities in deuterated solvents, δ 7.27 ppm and δ 77.00 ppm in $CDCl_3$ or δ 2.50 ppm

and δ 39.43 ppm in DMSO-d_6, respectively. The number average degree of polymerization (DP) of PS was obtained by the integration ratio between the characteristic protons of PEO at δ 3.90-3.30 ppm (180 H for PEO_{45} or 1092 H for PEO_{273}) and that of PS at 7.45-6.35 (aromatic protons in PS).

Fourier-Transform Infrared (FTIR) spectra of polymer precursors and giant surfactants were obtained on an Excalibur Series FT-IR spectrometer (DIGILAB, Randolph, MA). To characterize the characteristic azide groups on the polymer, samples were prepared by casting polymer solution with concentration of 5-10 mg/mL in THF onto a KBr plate. The solvent was then removed by blowing air at room temperature to afford drop-casting films. To characterize hydrogen bonding between the AC_{60} and the PEO, the samples were prepared by pressing the powder samples into KBr pellets in solid states. The data were analyzed using the Win-IR software.

Size-exclusion chromatography (SEC) analyses were performed on a Waters 150-C Plus instrument equipped with three HR-Styragel columns [100 Å, mixed bed (50/500/10^3/10^4 Å), mixed bed (10^3/10^4/10^6 Å)] and a triple detector system. The three detectors consist of a differential refractometer (Waters 410), a laser light scattering detector (Wyatt Technology, DAWN EOS, λ = 670 nm) and a differential viscometer (Viscotek 100). THF was used as the eluent with a flow rate of 1.0 mL/min at room temperature. Samples were dissolved in THF with the concentration of *ca.* 5-10 mg/mL, which were filtered through a 0.45 μm Teflon filter prior to injection. Regular SEC calibrations were conducted based on PS standards (Polymer Laboratories).

Thermogravimetric analysis (TGA) were performed on a thermogravimetric analysis instrument (Model Q500, TA Instruments). Samples weighting *ca.* 5 mg were

placed in a sample holder of platinum crucible, elevating the temperature from 30 to 600 °C under a nitrogen atmosphere with a heating rate of 10 °C/min.

Differential Scanning Calorimetry (DSC) thermal diagrams of the samples were recorded on a PerkinElmer PYRIS Diamond DSC with an Intracooler 2P apparatus. The temperature and heat flow scales were calibrated at different heating and cooling rates (1-40 °C/min) utilizing a series of standard materials.

Wide Angle X-ray Diffraction (WAXD) experiments were carried out on a Rigaku 18 kW rotating anode generator equipped with an image plate as the detector. The instrument was calibrated using silicon powders with 2θ being 28.4° under Cu Kα radiation. The diffraction patterns were obtained with the subtraction of air scattering. The 1D WAXD curve was analyzed and integrated from the 2D image.

Sample Preparations for SAXS and TEM Experiments. The freeze-dried powder samples were first thermally annealed at 120 °C under nitrogen atmosphere for up to 12h. The samples were then cooled to room temperature and used for SAXS measurements. Thin slices of the bulk samples with the thickness of 60-80 nm were obtained at -120 °C utilizing a Reichert Ultracut S (Leica) microtome on annealed samples embedded in epoxy monolith. The slices were carefully collected onto copper grids coated with amorphous carbon for TEM experiments. When necessary, osmium tetroxide (OsO_4) staining of the samples was performed at room temperature overnight.

Small angle X-ray scattering (SAXS) patterns were collected on a Rigaku MicroMax 002+ instrument equipped with a two-dimensional (2D) multiwire area detector and a microfocus sealed copper tube. The wavelength of the X-ray is 0.154 nm, with working voltage and current of 45 kV and 0.88 mA, respectively. The scattering

vector (q) was calibrated using silver behenate with the primary reflection peak at $q = 1.067$ nm^{-1}. The SAXS diffraction patterns with the q value range between 0.15 and 3.0 nm^{-1} were collected. The recording time for each data was 15 min. The data were analyzed with the Rigaku SAXSgui software.

The bright field (BF) transmission electron microscopy (TEM) images of the microtomed samples were taken on a JEOL-1230 TEM equipped with a digital CCD camera and accessory digital imaging system, collecting with an accelerating voltage of 120 kV. The periodic domain sizes of ordered structures obtained from TEM images were based on an average of ten independent measurements. The calibration of the length scale on TEM images were carried out based on grating replica crossed lines.

5.2.3 General Synthetic Procedures.

N$_3$-PS-PEO ($M_{n,\text{NMR}} = 5.0$ kg/mol, Đ = 1.06, 150 mg, 0.031 mmol, 1 equiv), TC$_{60}$-alkyne (88 mg, 0.034 mmol, 1.1 equiv), CuBr (4 mg, 0.031 mmol, 1 equiv) and freshly distilled toluene (15 mL) were added to a 100 mL Schlenk flask equipped with a magnetic stirring bar. The resultant solution was degassed by three freeze-pump-thaw cycles before introducing PMDETA (5 mg, 0.03 mmol, 1 equiv) under nitrogen protection. Upon one further freeze-pump-thaw cycle, the mixture was stirred at room temperature for 16 h. After the reaction was completed, the mixture was directly applied onto a column filled with silica gel. A mixture of toluene/ethyl acetate (v/v = 8/1) was first used as the eluent to remove the excess TC$_{60}$-alkyne. The column was then further eluted with a mixture of CH$_2$Cl$_2$/methanol (v/v = 8/1) to give a colored fraction of TC$_{60}$-PS-PEO. The concentrated product was precipitated into methanol, collected by vacuum filtration and dried *in vacuo* to give the product as a red powder (186 mg, 81%). To

deprotect the *tert*-butyl groups on TC_{60}, TC_{60}-PS-PEO was dissolved in a mixture of CH_2Cl_2 and CF_3COOH (v/v = 4/1) and stirred at room temperature for 8 h. Upon removal of the solvent, the residue was re-dissolved in 3 mL of benzene. The targeted product, AC_{60}-PS-PEO, was obtained as a red powder (157 mg, 91%) after freeze drying.

Following similar synthetic procedures, where the samples of PS-(N_3)-PEO instead of N_3-PS-PEO were added into Schlenk flask, PS-(AC_{60})-PEO can also be prepared.

In order to synthesize AC_{60}-PEO-PS, a hydroxyl-terminated PS (PS-OH) was first prepared via ionic polymerization described in a previous publication.[219] To a mixture of PS-OH (Mn= 2.8 kg/mol, 1g, 0.36 mmol, 1 equiv) in anhydrous THF, NaH (86 mg, 3.6 mmol, 10 equiv) was added. The mixtures were allowed to stir at 40 °C for 1 h, followed by slowly adding propargyl bromide (0.42g, 3.6 mmol, 10 equiv) at 0 °C. The mixtures were then allowed to stir at room temperature for 48 h. After removal of THF, the product were treated with dilute HCl solution and deionized water, extracted by CH_2Cl_2, dried over Na_2SO_4 before precipitating into methanol to give PS-alkyne (0.8g, 80%) as a white powder. Following the similar procedures of "click" reaction between PS-alkyne and α-hydroxy-ω-azide terminated poly (ethylene glycol), PS-PEO-OH can be afforded. The bromination and azidation at the chain end of PS-PEO-OH to give PS-PEO-Br and then PS-PEO-N_3 can be readily achieved based on the procedures reported in our previous publication.[220] Finally, following similar synthetic procedures as the synthesis of AC_{60}-PS-PEO, where the samples of N_3-PEO-PS instead of N_3-PS-PEO were added into Schlenk flask, AC_{60}-PEO-PS can be afforded.

TC$_{60}$-PS$_{28}$-PEO$_{45}$: ^{1}H NMR (CDCl$_3$, 500 MHz, ppm): δ 7.31-6.31 (br, 140H), 4.79-4.51 (m, 22H), 4.22 (s, 3H), 3.92-3.47 (br, 180H), 3.39 (s, 3H), 2.30-1.06 (br, 178H), 1.03-0.79 (m, 8H). ^{13}C NMR (CDCl$_3$, 125 MHz, ppm): δ 165.5, 162.8, 146.6-144.6, 140.8, 137.9, 129.2-124.8, 82.7, 78.4, 71.9, 70.5, 68.0, 63.1, 59.1, 46.7-39.8, 29.7, 28.1, 25.7.

AC$_{60}$-PS$_{28}$-PEO$_{45}$: ^{1}H NMR (DMSO-d_6, 500 MHz, ppm): δ 7.36-6.24 (br, 140H), 4.94-4.61 (m, 22H), 4.29 (s, 3H), 3.90-3.30 (br, 180H), 3.23 (s, 3H), 2.31-1.02 (br, 88H), 0.98-0.70 (m, 8H). ^{13}C NMR (DMSO-d_6, 125 MHz, ppm): δ 168.4, 162.6, 147.0-144.3, 140.6, 139.2, 129.7-124.9, 78.4, 71.7, 70.3, 68.6, 60.7, 58.3, 57.9, 44.9-38.7, 29.1, 25.9.

PS$_{50}$-(TC$_{60}$)-PEO$_{45}$: ^{1}H NMR (CDCl$_3$, 500 MHz, ppm): δ 7.36-6.32 (br, 250H), 4.86-4.44 (m, 23H), 4.32 (s, 3H), 3.99-3.46 (br, 184H), 3.40 (s, 3H), 2.76 (m, 2H), 2.52-1.06 (br, 242H), 1.02-0.72 (m, 6H). ^{13}C NMR (CDCl$_3$, 125 MHz, ppm): δ 165.7, 162.7, 146.6-144.6, 140.9, 139.4, 129.1-125.2, 82.6, 78.4, 72.0, 70.5, 69.0, 63.2, 59.2, 46.9-39.8, 27.9.

PS$_{50}$-(AC$_{60}$)-PEO$_{45}$: ^{1}H NMR (DMSO-d_6, 500 MHz, ppm): δ 7.45-6.11 (br, 250H), 5.01-4.54 (m, 23H), 4.37 (s, 3H), 3.99-2.96 (br, 187H), 2.66 (m, 2H), 2.37-0.94 (br, 152H), 0.96-0.53 (m, 6H). ^{13}C NMR (CDCl$_3$, 125 MHz, ppm): δ 168.6, 147.9-144.3, 140.7, 130.9-125.0, 79.3, 72.9, 71.4, 68.4, 63.1, 58.1, 46.9-36.8.

5.2.4 Calculations of Volume Fractions of PS, PEO and AC$_{60}$.

Determination of the volume fractions relies on several assumptions. First, the density of the PS and PEO chains is assumed as the density of amorphous PS (1.05 g/cm^3) and PEO (1.09 g/cm^3). Second, it is assumed that the density of the AC$_{60}$ domains

143

remains the same as that of the corresponding model compounds, which has a measured density of 1.60 g/cm^3.[69] The volume fraction of the PS, PEO and AC$_{60}$ domain is given by

$$V_{PS} = \frac{M_{PS}/\rho_{PS}}{M_{PS}/\rho_{PS} + M_{PEO}/\rho_{PEO} + M_{AC60}/\rho_{AC60}}$$

$$V_{PEO} = \frac{M_{PEO}/\rho_{PEO}}{M_{PS}/\rho_{PS} + M_{PEO}/\rho_{PEO} + M_{AC60}/\rho_{AC60}}$$

$$V_{AC60} = \frac{M_{AC60}/\rho_{AC60}}{M_{PS}/\rho_{PS} + M_{PEO}/\rho_{PEO} + M_{AC60}/\rho_{AC60}}$$

Fourier filtering of the TEM image was carried out with the FFTW implementation. A circular mask of a radius of 0.0225 nm^{-1} was applied to the central peak in the frequency domain. All unmasked Fourier spectrum terms were set to zero, while the masked terms remained intact.

5.3 Results and Discussion

In this section, the successful synthesis of giant surfactants will be fully characterized, as well as their versatile assembly behaviors in bulk will be discussed.

5.3.1 Synthesis of AC$_{60}$-PS$_n$-PEO$_m$ and PS$_n$-(AC$_{60}$)-PEO$_m$ Giant Surfactants.

The syntheses of the AC$_{60}$-PS$_n$-PEO$_m$ giant surfactants are outlined in Scheme 5.2. Precisely defined [5:1]-hexakisadducts of C$_{60}$ bearing one terminal alkyne and ten protected carboxylic acid groups (TC$_{60}$-alkyne), the azide-functionalized PS-*b*-PEO at the

PS block end (N_3-PS_n-PEO_m) or at the junction point [PS_n-(N_3)-PEO_m] were synthesized according to the procedures reported in our previous publications.[68, 221] The conjugation of TC_{60}-alkyne and N_3-PS_n-PEO_m was achieved by azide-alkyne "click" chemistry to afford TC_{60}-PS_n-PEO_m. In Fourier transform infrared spectroscopy (FTIR) experiments, the complete disappearance of absorbance band from azide group at *ca.* 2100 cm^{-1} gives the evidence of successful reaction between TC_{60}-alkyne and N_3-PS_n-PEO_m (Figure 5.1).[71, 166, 205] The well-defined structures of TC_{60}-PS_n-PEO_m were unambiguously characterized by nuclear magnetic resonance (NMR) spectra including ^{1}H NMR, ^{13}C NMR experiments and size-exclusion chromatography (SEC) experiments (see Figures 5.2-5.4). In the ^{1}H NMR and ^{13}C NMR spectra, the signals of major characteristic protons and carbons attributed to the TC_{60}, PS and PEO can be clearly observed. In the SEC profiles, the curve of TC_{60}-PS_n-PEO_m shifts to lower retention volume relative to the N_3-PS_n-PEO_m owing to the increase of molecular weight. The monomodal profile remains with narrow polydispersity ($Đ$ = 1.06), revealing the high uniformity of TC_{60}-PS_n-PEO_m. The deprotection of *tert*-butyl groups on TC_{60} was readily achieved by treating with CF_3COOH in CH_2Cl_2. The final products (AC_{60}-PS_n-PEO_m) were obtained without any further purification. The complete deprotection was evidenced by the disappearance of *tert*-butyl protons at 1.47 ppm in ^{1}H NMR spectrum (Figure 5.2) and *tert*-butyl carbons at 28.1 ppm in ^{13}C NMR spectrum (Figure 5.3). Following similar synthetic procedures, AC_{60} was also successfully tethered at the junction point of PS-*b*-PEO, affording the PS_n-(AC_{60})-PEO_m series (Scheme 5.3). Following the designed synthetic procedures in Scheme 5.4, AC_{60} can be tethered at the PEO block end to afford AC_{60}-PEO_m-PS_n series. The well-defined structures of as-synthesized PS_n-(AC_{60})-PEO_m and AC_{60}-PEO_m-PS_n

were confirmed by the NMR, FTIR and SEC (see Figures 5.5-5.9). The molecular weight information of synthesized block copolymers and giant surfactant precursors is summarized in Table 5.1.
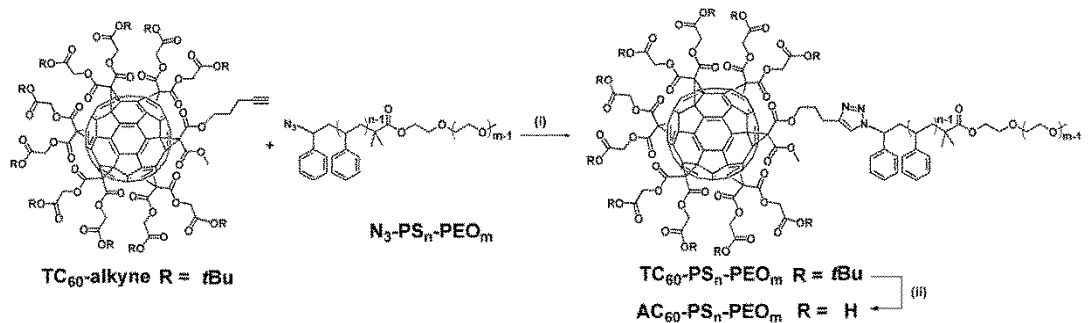
Scheme 5.2. Synthetic route of AC_{60}-PS_n-PEO_m. (i) Toluene, CuBr, PMDETA, RT; (ii) CH_2Cl_2, CF_3COOH, RT.
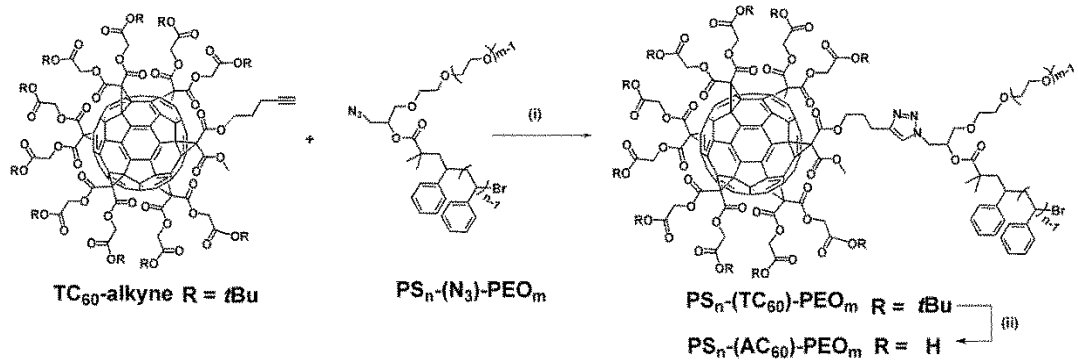
Scheme 5.3. Synthetic route of PS_n-(AC_{60})-PEO_m. (i) Toluene, CuBr, PMDETA, RT; (ii) CH_2Cl_2, CF_3COOH, RT.
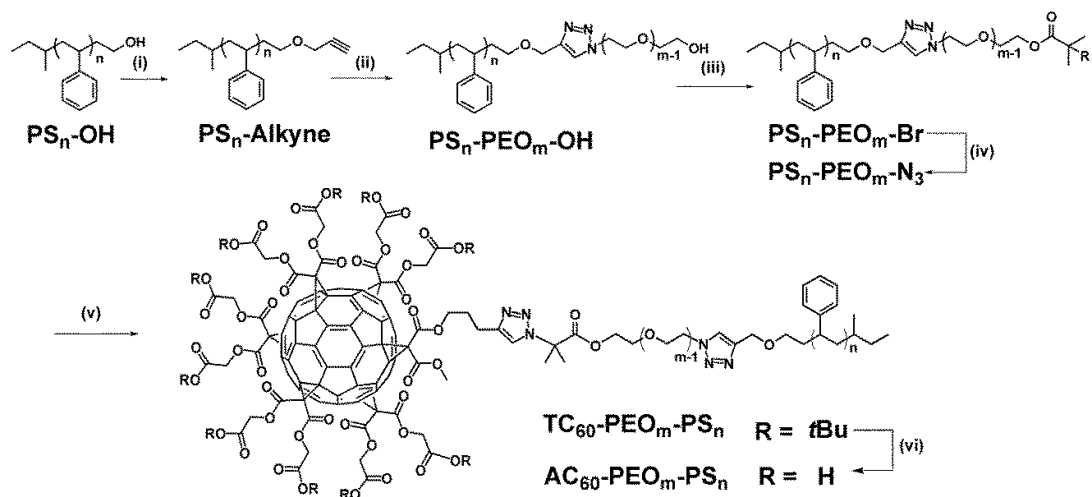
Scheme 5.4. Synthetic route of AC_{60}-PEO_m-PS_n. (i) THF, NaH, propargyl bromide; (ii) Toluene, CuBr, PMDETA, α-Hydroxy-ω-Azide Terminated Poly(ethylene glycol), RT; (iii) CH_2Cl_2, 2-Bromoisobutyryl bromide, TEA; (iv) DMF, NaN_3; (v) Toluene, TC_{60}-alkyne, CuBr, PMDETA, RT; (vi) CH_2Cl_2, CF_3COOH, RT.
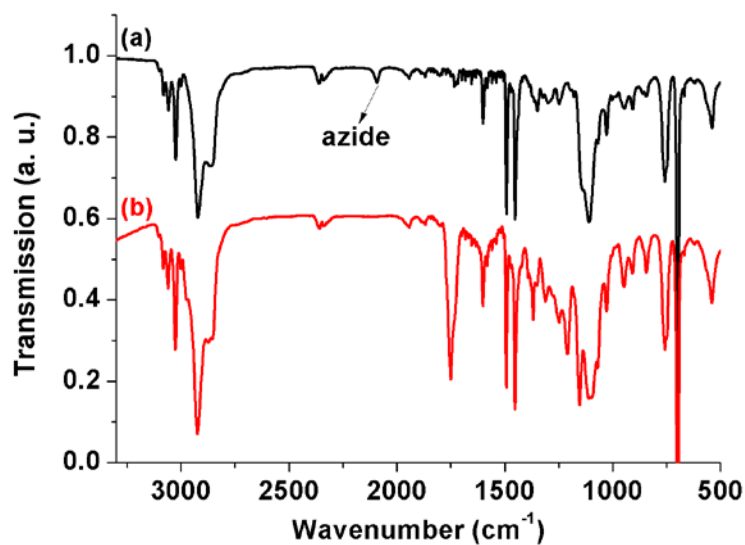
Figure 5.1. FTIR spectra of (a) N_3-PS_{28}-PEO_{45} (black curve) and (b) TC_{60}-PS_{28}-PEO_{45} (red curve).
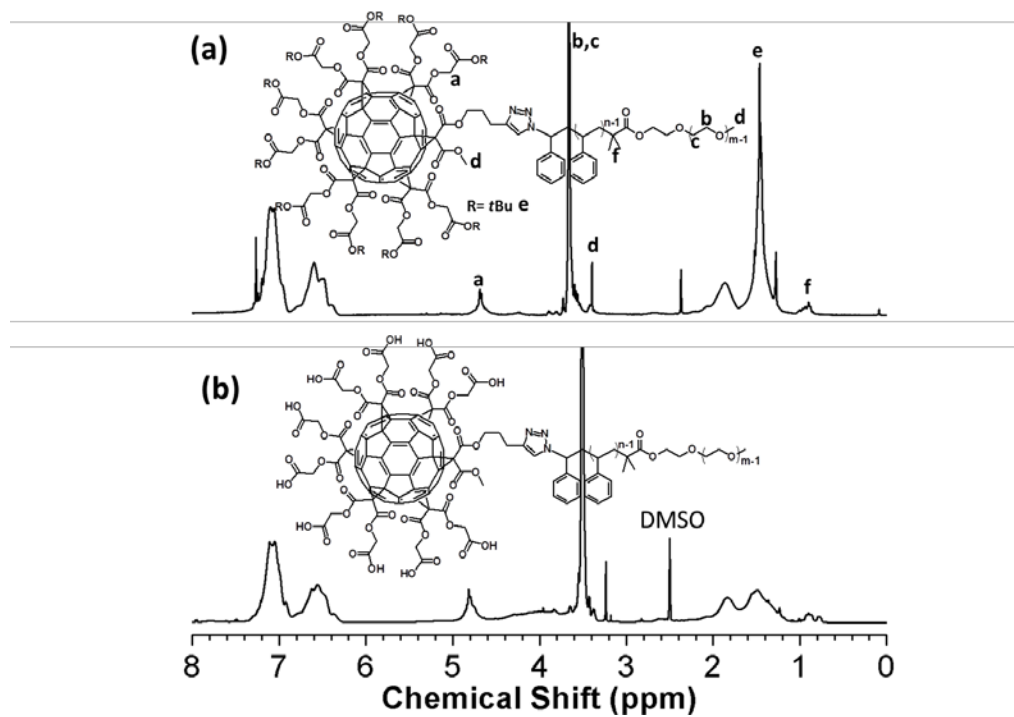
Figure 5.2. ^{1}H NMR spectra of (a) TC_{60}-PS_{28}-PEO_{45} and (b) AC_{60}-PS_{28}-PEO_{45}.
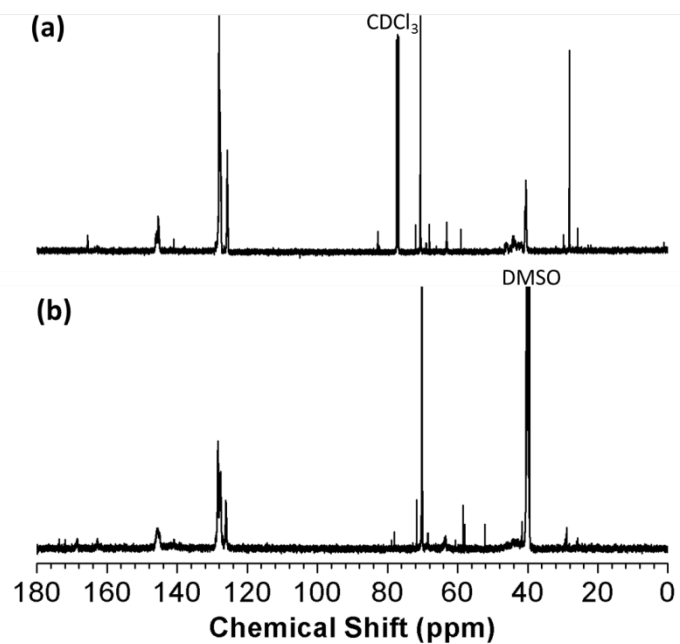
Figure 5.3. ^{13}C NMR spectra of (a) TC_{60}-PS_{28}-PEO_{45} and (b) AC_{60}-PS_{28}-PEO_{45}.
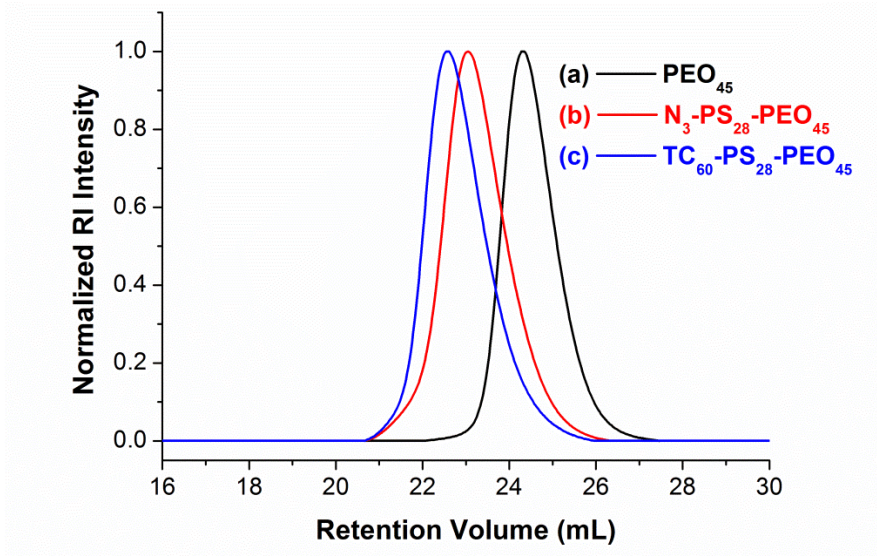
Figure 5.4. SEC overlay of (a) PEO$_{45}$ (black curve), (b) N$_3$-PS$_{28}$-PEO$_{45}$ (red curve), and

TC$_{60}$-PS$_{28}$-PEO$_{45}$ (blue curve).
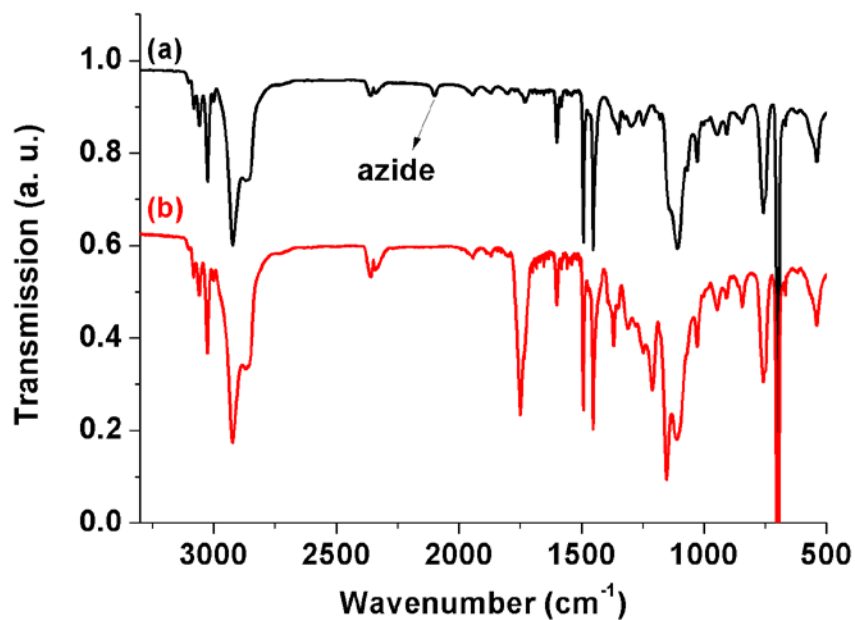
Figure 5.5. FTIR spectra of (a) PS$_{50}$-(N$_3$)-PEO$_{45}$ (black curve) and (b) PS$_{50}$-(TC$_{60}$)-PEO$_{45}$
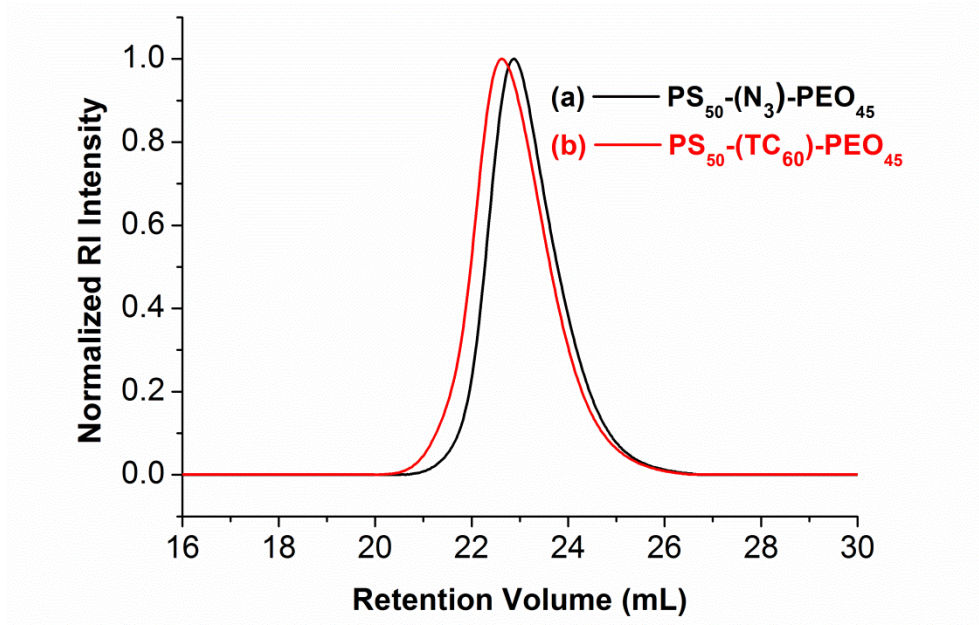
(red curve).

Figure 5.6. SEC overlay of (a) PS_{50}-(N_3)-PEO_{45} (black curve), and (b) PS_{50}-(TC_{60})-PEO_{45} (red curve).
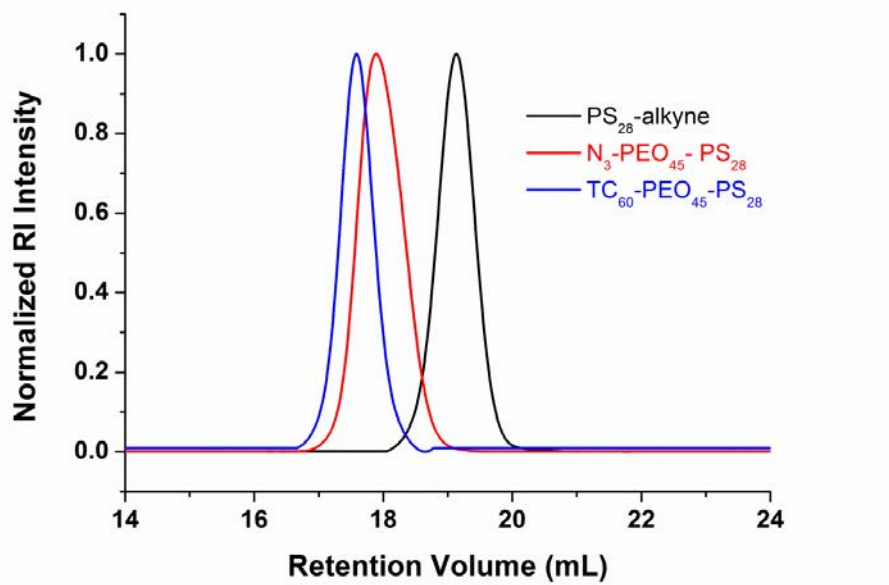
Figure 5.7. SEC overlay of (a) PS_{28}-alkyne (black curve), (b) N_3-PEO_{45}-PS_{28} (red curve), and (c) TC_{60}-PEO_{45}-PS_{28} (blue curve).
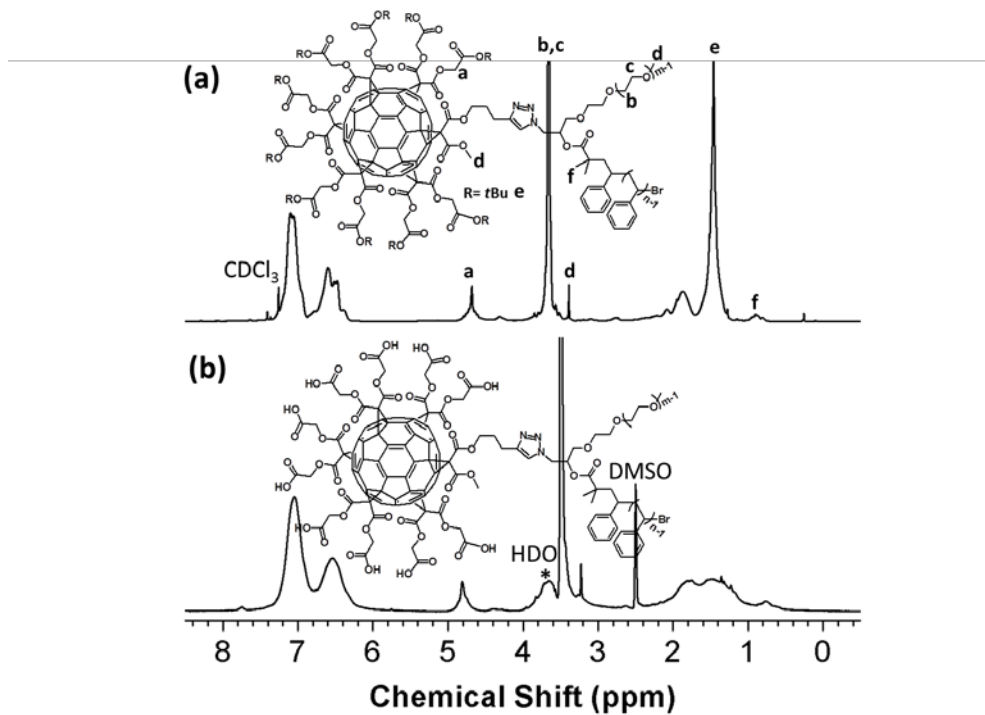
Figure 5.8. ^{1}H NMR spectra of (a) PS$_{50}$-(TC$_{60}$)-PEO$_{45}$ and (b) PS$_{50}$-(AC$_{60}$)-PEO$_{45}$.
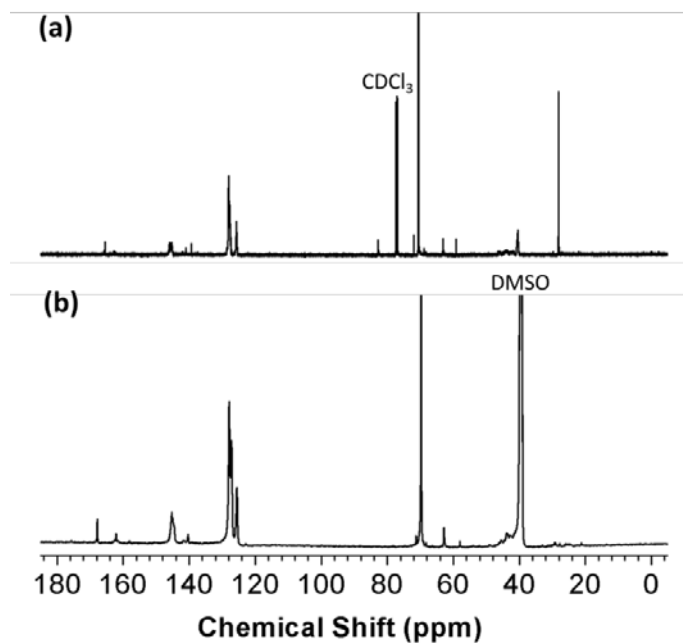
Figure 5.9. ^{13}C NMR spectra of (a) PS$_{50}$-(TC$_{60}$)-PEO$_{45}$ and (b) PS$_{50}$-(AC$_{60}$)-PEO$_{45}$

151

Table 5.1. Summarized molecular weight information of synthesized polymers and giant surfactants.

Sample	$M_{n, NMR}$ (kg/mol)	$M_{n, SEC}$ (kg/mol)	$Đ$
PS_{28}-b-PEO_{45}	5.0	5.2	1.07
TC_{60}-PS_{28}-PEO_{45}	7.5	7.9	1.06
PS_{50}-b-PEO_{45}	7.3	7.6	1.08
TC_{60}-PS_{50}-PEO_{45}	9.8	10.5	1.09
PS_{52}-b-PEO_{45}	7.5	7.8	1.09
TC_{60}-PS_{52}-PEO_{45}	10.0	10.8	1.07
PS_{64}-b-PEO_{45}	8.8	9.1	1.05
TC_{60}-PS_{64}-PEO_{45}	11.3	12.2	1.08
PS_{78}-b-PEO_{45}	10.2	10.6	1.06
TC_{60}-PS_{78}-PEO_{45}	12.7	13.6	1.07
PS_{160}-b-PEO_{273}	28.7	29.6	1.08
TC_{60}-PS_{160}-PEO_{273}	31.2	32.3	1.09
PS_{50}-(N_3)-PEO_{45}	7.4	7.9	1.07
PS_{50}-(TC_{60})-PEO_{45}	9.9	10.6	1.08
PS_{78}-(N_3)-PEO_{45}	10.3	10.9	1.06
PS_{78}-(TC_{60})-PEO_{45}	12.8	13.9	1.08

5.3.2 Assemblies of AC_{60}-PS_n-PEO_m Giant Surfactants in Lam Structures.

Table 5.2 summarizes molecular characterizations of the giant surfactants studied in this work. All the synthesized giant surfactants possess narrow polydispersities ($Đ$ <1.10) with well-defined chemical structures. Prior to thermal treatment of as-prepared samples, it is essential to examine their thermal stability. As illustrated by TGA analysis (see Figure 5.10), no apparent weight loss was observed at temperature lower than 200 °C at a hearing rate of 10 °C/min under N_2 atmosphere, indicating good thermal stability of the samples below 150 °C (our thermal annealing temperature was at 120 °C).

Table 5.2. Summary of characterization data for synthesized giant surfactants.

Sample	$M_{n,PS}$ (kg/mol) [a]	$M_{n,PEO}$ (kg/mol)	V_{PS} [b]	V_{PEO} [c]	V_{AC60} [d]	$Đ$ [e]	Phase structure [f]	d_1 (nm) [g]
AC_{60}-PS_{28}-PEO_{45}	2.9	2.0	0.47	0.31	0.22	1.06	Lam	8.0
AC_{60}-PS_{50}-PEO_{45}	5.2	2.0	0.62	0.23	0.15	1.09	Lam	8.8
AC_{60}-PS_{52}-PEO_{45}	5.4	2.0	0.63	0.22	0.15	1.07	DG	9.2
AC_{60}-PS_{64}-PEO_{45}	6.6	2.0	0.67	0.20	0.13	1.08	Hex	9.3
AC_{60}-PS_{78}-PEO_{45}	8.1	2.0	0.71	0.17	0.12	1.07	Hex	10.0
AC_{60}-PS_{160}-PEO_{273}	16.6	12.0	0.56	0.39	0.05	1.09	Lam	17.0
PS_{50}-AC_{60}-PEO_{45}	5.2	2.0	0.62	0.23	0.15	1.08	Lam	11.4
PS_{78}-AC_{60}-PEO_{45}	8.1	2.0	0.71	0.17	0.12	1.08	Hex	12.9
AC_{60}-PEO_{45}-PS_{28}	2.9	2.0	0.47	0.31	0.22	1.09	Lam	12.6

[a] Molecular weights of the PS blocks were calculated based on NMR results. [b, c, d] Volume fractions of the PEO, PS and AC_{60} were calculated from molecular weight and density values, see SI for detailed calculation. [e] Polydispersity of giant surfactants were obtained from SEC measurements using a PS standard calibration curve. [f] The phase structures were determined by SAXS and TEM. [g] The domain sizes were obtained based on SAXS results.
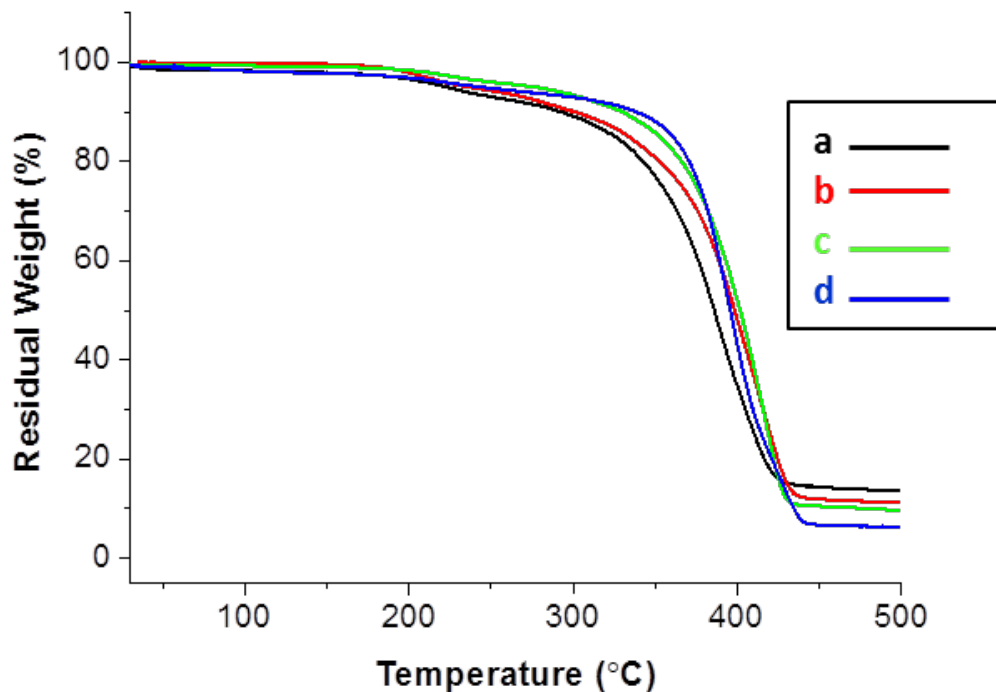
Figure 5.10. TGA results of (a) AC_{60}-PS_{28}-PEO_{45}, (b) AC_{60}-PS_{52}-PEO_{45}, (c) AC_{60}-PS_{64}-PEO_{45} and (d) AC_{60}-PS_{160}-PEO_{273}, with a scan rate of 10 °C /min.

Figure 5.11a shows a 1D SAXS pattern of AC_{60}-PS_{28}-PEO_{45}. There are two scattering peaks having a q-ratio of 1:2, representing a Lam structure with a periodic domain spacing of 8.0 nm (calculated via $d = 2\pi/q$, where the first order diffraction peak is centered at $q = 0.78$ nm^{-1}). It should be noted that since the molecular mass of PS_{28}-b-PEO_{45} is lower than the limiting value of the nanophase separation for PS-b-PEO copolymers (~16 kg/mol),[216-218] the BCP precursor does not form a nanophase separated, ordered structure in the melt (see SAXS pattern shown in Figure 5.12). The formation of Lam structure is also validated in real space via BF TEM images of the microtomed AC_{60}-PS_{28}-PEO_{45} bulk sample after OsO_4 staining as shown in Figure 5.11b. The

154

alternative dark (attributed to the AC_{60} and PEO blocks) and grey (the PS blocks) domains in parallel arrangement possess an overall thickness of 8.0 ± 0.3 nm, in good agreement with the calculated value based on the SAXS result.
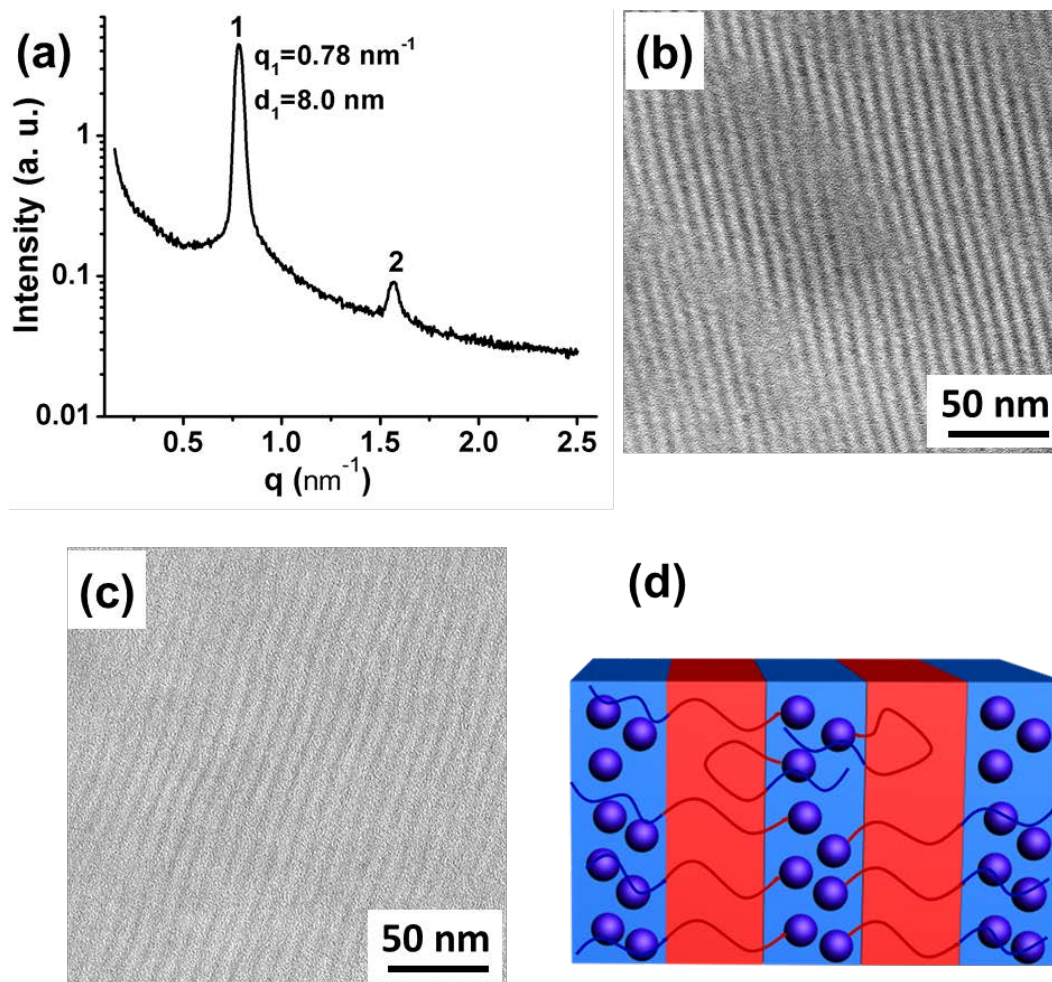
Figure 5.11. (a) 1D SAXS pattern and (b) BF TEM image of AC_{60}-PS_{28}-PEO_{45}. The BF TEM image is obtained after OsO_4-staining, where both AC_{60} and PEO are OsO_4-stained. (dark: the AC_{60} and PEO blocks, gray: the PS blocks). (c) BF TEM image of AC_{60}-PS_{28}-PEO_{45} without staining. (dark: AC_{60}; gray: PS blocks and PEO blocks) (d) Proposed lamellar model formed by AC_{60}-PS_{28}-PEO_{45} (red: the PS domains; blue: the PEO and AC_{60} mixed domains).

155
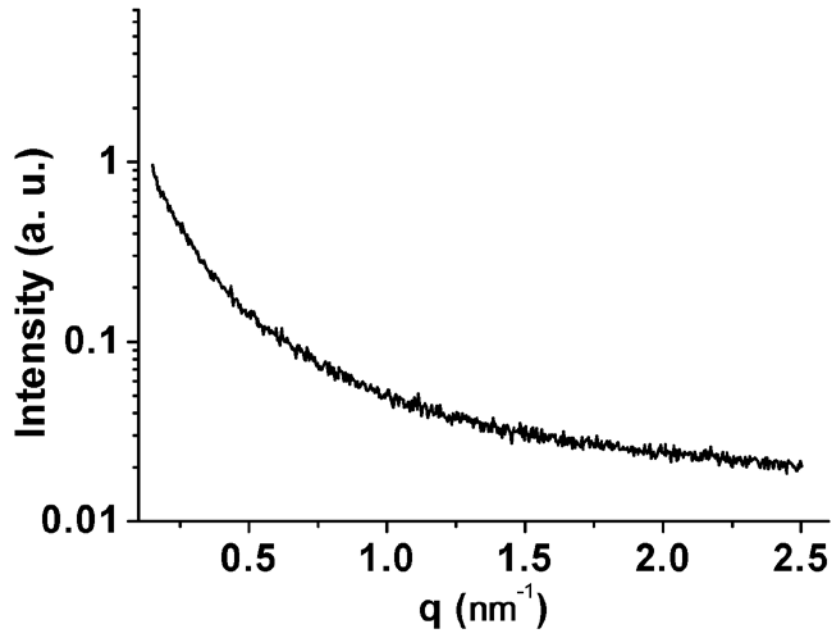
Figure 5.12. 1D SAXS pattern of PS_{28}-b-PEO_{45} after thermal annealing.

Figure 5.11c shows a BF TEM image for another AC_{60}-PS_{28}-PEO_{45} microtomed thin sample without OsO_4-staining. The dark domains with an average width of 3.5 ± 0.4 nm in this figure only represent the region where the AC_{60} MNPs are located due to its higher electron density. Compared with the stained samples with the width measured to be 4.0 ± 0.3 nm in Figure 5.11b, where both the AC_{60} MNPs and the PEO blocks are stained by OsO_4, this small difference indicates that the AC_{60} MNPs are distributed across the layer spacing of the AC_{60}/PEO block domain. Only the locations near the interfaces between the PEO and PS blocks may contain less AC_{60} MNPs.

Both the SAXS and TEM experimental results suggest that the conjugation of the AC_{60} MNP at the PS block end of PS_{28}-b-PEO_{45} enhances the immiscibility and promotes nanophase separation. In order to illustrate that the AC_{60} MNPs are interacting with the PEO blocks via hydrogen-bonding, we compared the crystallization behavior of the

156

precursor PS_{28}-*b*-PEO_{45} BCP observed in differential scanning calorimetry (DSC) with that of AC_{60}-PS_{28}-PEO_{45}. Both of the samples were first cooled down from 120 °C to -80 °C at a cooling rate of 10 °C/min and then, the samples were heated from that temperature to 120 °C. Figure 5.13 shows that in the DSC heating thermal diagram of PS_{28}-*b*-PEO_{45}, an endothermic peak of the PEO crystal melting can be observed at a temperature of ~ 42 °C. This indicates that PEO crystals were formed during the prior cooling process. However, the giant surfactant AC_{60}-PS_{28}-PEO_{45} does not show any thermal events in the same temperature range, revealing that the PEO blocks in AC_{60}-PS_{28}-PEO_{45} do not crystallize during the cooling process. This is indirect evidence to illustrate that the AC_{60} MNPs and PEO blocks are interacting with each other via hydrogen-bonding and thus, preventing crystallization of the PEO blocks in AC_{60}-PS_{28}-PEO_{45}. Direct evidence can be obtained via FTIR experiment. Figure 5.14 shows FTIR spectra of AC_{60}-PS_{28}-PEO_{45} before (neat dry samples once precipitating out in solution) and after thermal annealing (the nanophase separation has taken place). A new absorbance band centered at *ca.*1732 cm^{-1}, corresponding to the hydrogen-bonding between the carboxylic acid and PEO,[222] appears after the thermal annealing. This indicates that the hydrogen-bonding has evolved between the PEO blocks and AC_{60} MNPs to result in enhancement of the segregation strength with the PS blocks. It is worth noting that no ordered structures are formed in the TC_{60}-PS_{28}-PEO_{45} precursor (the samples before deprotection of carboxylic acid groups on C_{60} and thus, without hydrogen-bonding) after thermal annealing, revealed by a broad scattering halo in the

SAXS pattern (Figure 5.15). Thus, the AC_{60}/PEO block interaction facilitates the nanophase separation of AC_{60}-PS_{28}-PEO_{45}.
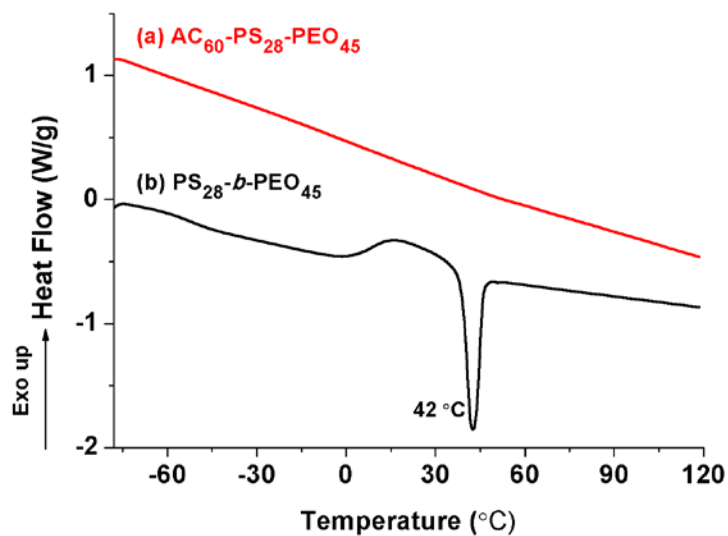
Figure 5.13. Heating DSC thermograms of (a) AC_{60}-PS_{28}-PEO_{45} and (b) PS_{28}-b-PEO_{45}.
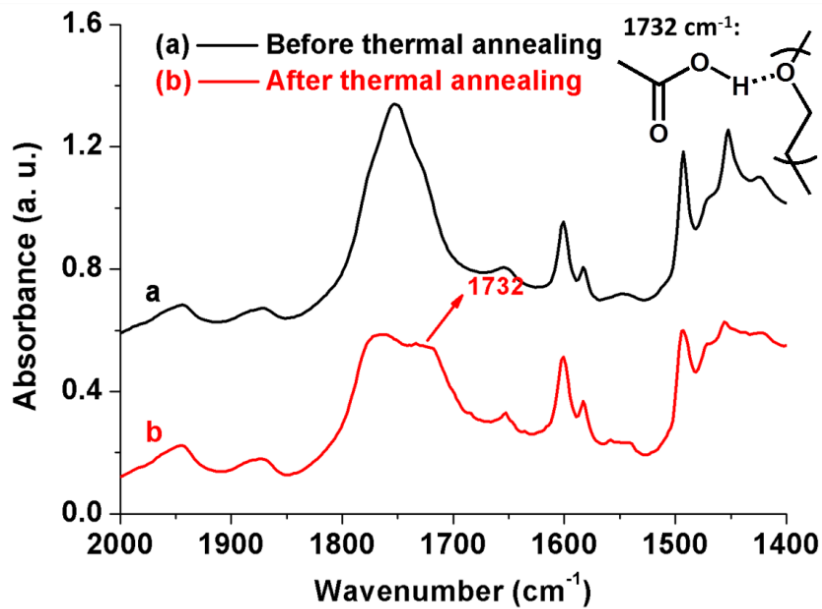
Figure 5.14. FTIR spectra of AC_{60}-PS_{28}-PEO_{45} (a) before and (b) after thermal annealing.
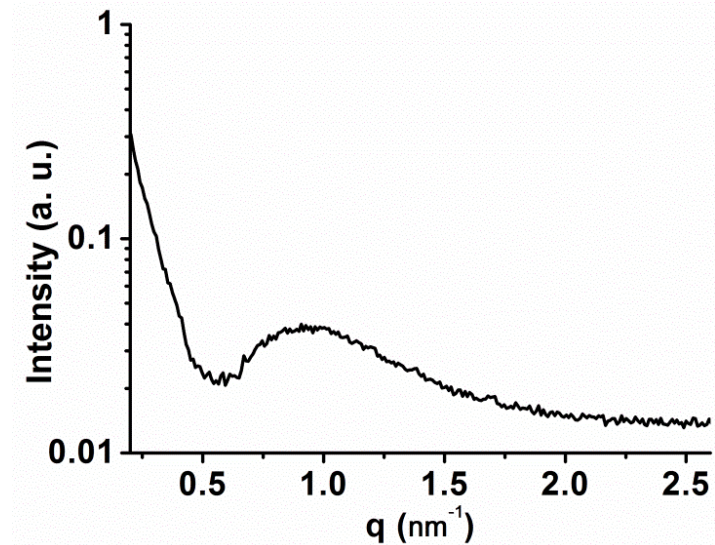
Figure 5.15. 1D SAXS pattern of TC_{60}-PS_{28}-PEO_{45}.
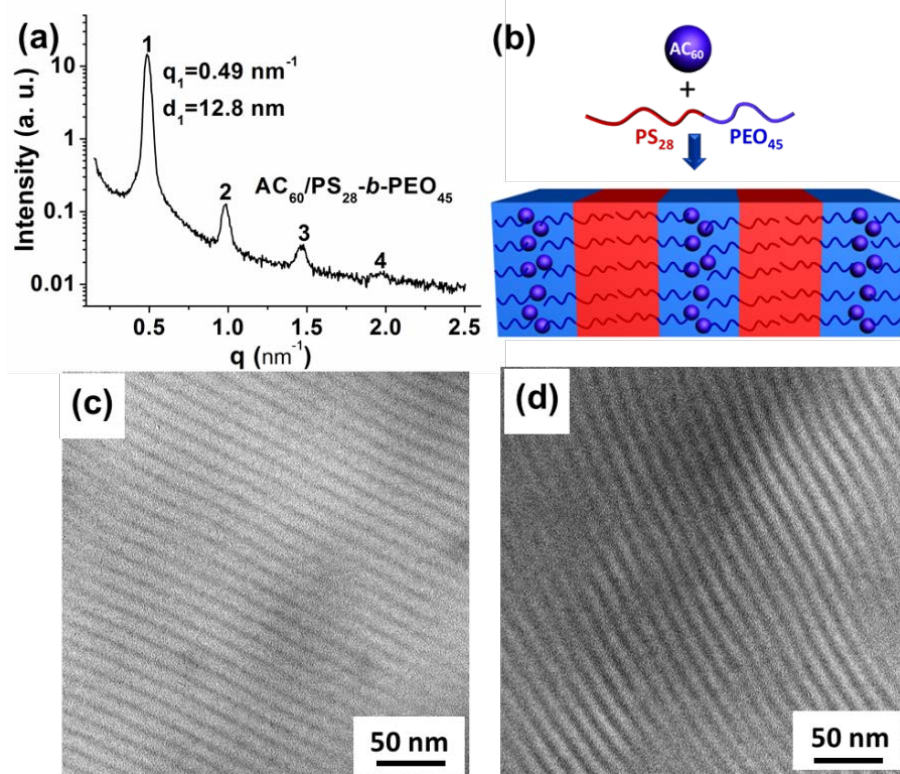
Figure 5.16. (a) 1D SAXS pattern of AC_{60}/PS_{28}-b-PEO_{45} blend with a molar ratio of 1/1 after thermal annealing. (b) Proposed lamellar model formed by AC_{60}/PS_{28}-b-PEO_{45}

blend. Bright-field TEM images of AC_{60}/PS_{28}-PEO_{45} blend with a molar ratio of 1/1 (c) without staining (dark: AC_{60}; gray: PS and PEO) and (d) with OsO_4- staining (dark: PEO and AC_{60}; gray: PS).
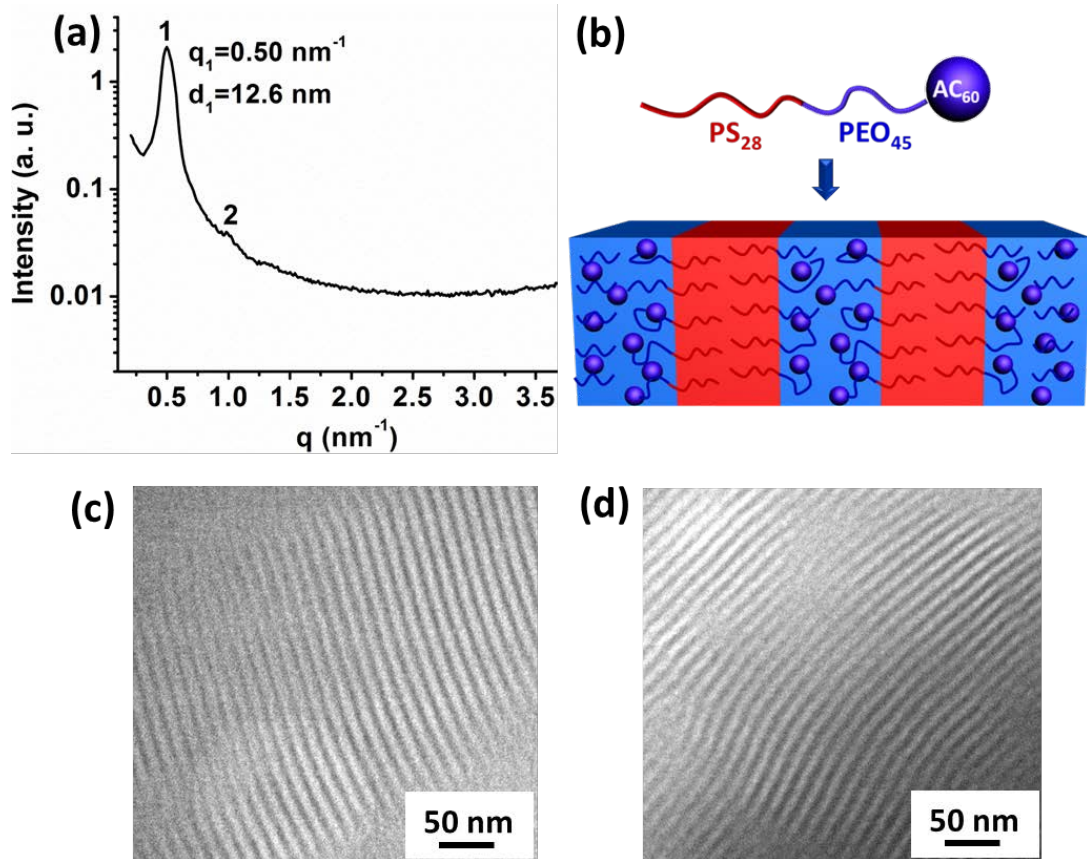
Figure 5.17. (a) 1D SAXS pattern of AC_{60}-PEO_{45}-PS_{28} after thermal annealing. (b) Proposed lamellar model formed by AC_{60}-PEO_{45}-PS_{28}. Bright-field TEM images of AC_{60}-PEO_{45}-PS_{28} (c) without staining (dark: AC_{60}; gray: PS and PEO) and (d) with OsO_4-staining (dark: PEO and AC_{60}; gray: PS).
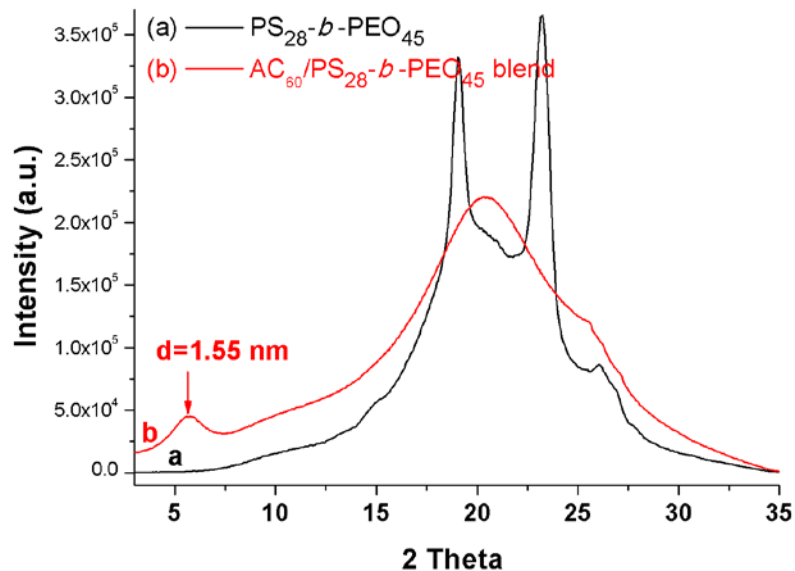
Figure 5.18. 1D WAXD pattern of (a) PS_{28}-*b*-PEO_{45} and (b) AC_{60}/PS_{28}-*b*-PEO_{45} blend with a molar ratio of 1/1 after thermal annealing.

To further illustrate that the interaction between the AC_{60} and PEO block increases the segregation strength and compare their self-assembly behaviors, a blend of AC_{60}/PS_{28}-PEO_{45} with the molar ratio of 1:1 as well as a new giant surfactant sample, AC_{60}-PEO_{45}-PS_{28} (the AC_{60} was tethered at the PEO block end), were prepared and subjected to the identical thermal annealing procedure of AC_{60}-PS_{28}-PEO_{45}. Ordered Lam structures with *d*-spacings of 12.8 nm and 12.6 nm were observed in the blend and AC_{60}-PEO_{45}-PS_{28}, respectively, based on the SAXS results (Figures 5.16a and 5.17a). Although AC_{60}/PS_{28}-*b*-PEO_{45} blend, AC_{60}-PEO_{45}-PS_{28} and AC_{60}-PS_{28}-PEO_{45} possess the exactly identical chemical composition and all of them form Lam structures, the periodic spacings of those lamellae for AC_{60}/PS_{28}-*b*-PEO_{45} blend (12.8 nm) and AC_{60}-PEO_{45}-PS_{28} (12.6 nm) are more than 55% larger than that of AC_{60}-PS_{28}-PEO_{45} (8.0 nm). To account

161

for this difference, we argue that the hydrophilic AC_{60} MNPs are concentrated at the center of the PEO domain surrounded by the PEO blocks in the blend, as schematically shown in Figure 5.16b, and the PS domain is constructed by a double layer structure.

The PEO blocks in the blend are also found to not crystallize (Figure 5.18), and this lamellar model for the blend can be proven by BF TEM images in Figures 5.16c and 5.16d. The wide angle X-ray diffraction (WAXD) pattern of PS_{28}-b-PEO_{45} samples (Figure 5.18a) exhibits two characteristic diffraction peaks belonging to the crystallization of PEO.[218] They disappear and a new diffraction peak corresponding to a d-spacing of 1.55 nm appears after blending with AC_{60} MNPs (Figure 5.18b). These results imply that the AC_{60} MNPs selectively aggregate in the PEO domain and prevent the crystallization of PEO. More convincing evidences come from the TEM observations. As elucidated in Figure 5.16 c, a dark domain with a width of 3.0 ± 0.5 nm is observed for the free-staining samples. Owing to the much higher electron density of AC_{60} relative to PEO and PS, the dark domain must be identified as AC_{60} rich region, indicating the aggregation of AC_{60} MNPs in polymer domain. After staining by OsO_4, the width of dark domain increases to 6.0 ± 0.5 nm because both PEO and AC_{60} were stained, which reasonably validate that the aggregation of AC_{60} rich region localize near center of PEO domain (Figure 5.16d).This is also consistent with the previously reported simulations[223, 224] and experimental observations[191, 192] that NPs are favorably located at the center of compatible polymer domain to balance the loss of translational entropy of NPs and potential polymer block stretching penalties created by distributing NPs throughout the domain.[191, 223]

For AC_{60}-PEO_{45}-PS_{28}, a double layer PS domain can also be expected, yet a random distribution of AC_{60} MNPs in the PEO domain can be deduced since no increase of the dark domain size after both AC_{60} MNPs and PEO were stained by OsO_4 in the BF TEM images (Figures 5.17c and 5.17d). For AC_{60}-PS_{28}-PEO_{45}, the AC_{60} MNPs are arranged throughout the PEO domain as shown in Figure 5.11d. Owing to the chemical linkage of AC_{60} MNPs with PS block ends, the hydrophobic PS domain within AC_{60}-PS_{28}-PEO_{45} lamellae has to be constructed by a single layer of PS blocks, as schematically shown in the Figure 5.11d. The single layer arrangement of PS blocks reduces the overall d-spacing of the AC_{60}-PS_{28}-PEO_{45} lamellae. Therefore, the more than 55% difference in the periodic spacings between AC_{60}/PS_{28}-b-PEO_{45} blend, AC_{60}-PEO_{45}-PS_{28} and AC_{60}-PS_{28}-PEO_{45} is caused by the double layer versus the single layer PS domains in these samples.
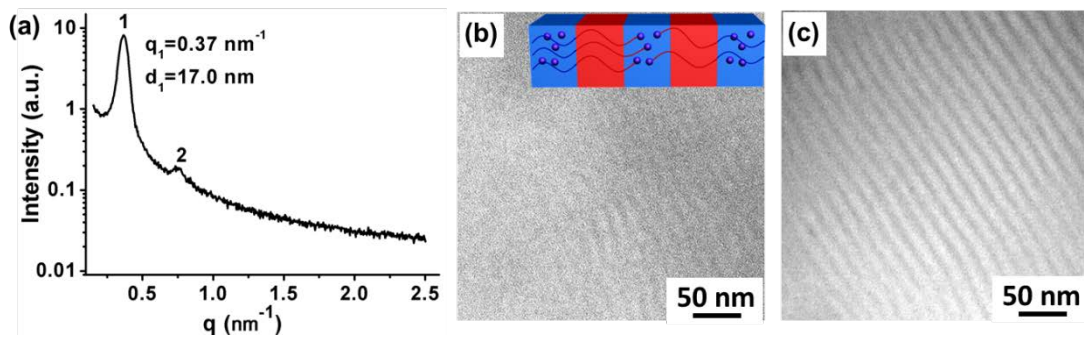
Figure 5.19. (a) 1D SAXS pattern of AC_{60}-PS_{160}-PEO_{273}. BF TEM images of AC_{60}-PS_{160}-PEO_{273} (b) without and (c) with OsO_4-staining. Inset is the proposed lamellar model for AC_{60}-PS_{160}-PEO_{273}.
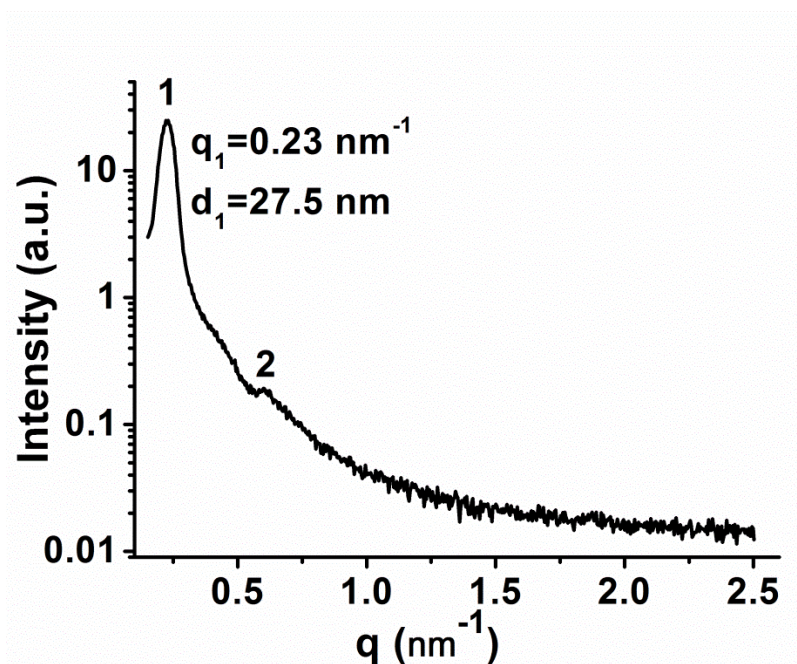
Figure 5.20. 1D SAXS pattern of PS_{160}-b-PEO_{273} after thermal annealing.

To confirm the proposed model in Figure 5.11d, PS_{160}-b-PEO_{273} and AC_{60}-PS_{160}-PEO_{273} with high molecular masses of both blocks were also prepared, since the PS and PEO blocks in this case possess sufficient segregation strength to generate the nanophase separation without incorporating with the AC_{60} MNPs. The SAXS and TEM results for AC_{60}-PS_{160}-PEO_{273} after the thermal annealing are shown in Figure 5.19 and the results of PS_{160}-b-PEO_{273} are shown in Figure 5.20. Lam structures are observed in both cases, as indicated by the two scattering peaks with a q-ratio of 1:2. The periodic spacing of PS_{160}-b-PEO_{273} is calculated to be 27.5 nm, while that of AC_{60}-PS_{160}-PEO_{273} is 17.0 nm. Again, this periodicity difference must be resulted from a single layer of the PS blocks in AC_{60}-PS_{160}-PEO_{273} versus a double layer of PS blocks in PS_{160}-b-PEO_{273}. Figures 5.19b and 5.19c show the BF TEM images of AC_{60}-PS_{160}-PEO_{273} without and with OsO_4-

staining. Owing to the relatively low volume fraction (*ca.* 5%) and random distribution of AC_{60} MNPs, it is difficult to observe the continuous dark AC_{60}-concentrated domain for the non-stained sample (Figure 5.19b). Upon staining, the dark domain consisting of the AC_{60} MNPs and PEO can be clearly identified (Figure 5.19c), where the periodic spacing of lamellae is measured as 17.0 ± 1.0 nm. It is in good agreement with that obtained in Figure 5.19a. These results further validate that the AC_{60} MNPs distribute throughout, instead of aggregate within the PEO domain.

5.3.3 Versatile Assemblies of AC_{60}-PS_n-PEO_m Giant Surfactants.

In addition to Lam structure, DG and Hex structures are readily formed in AC_{60}-PS_m-PEO_n giant surfactants by varying the PS block length. As the PS molecular mass increases to $N = 52$ (AC_{60}-PS_{52}-PEO_{45}), multiple scattering peaks with a *q*-ratio of $\sqrt{6}$:$\sqrt{8}$:$\sqrt{20}$:$\sqrt{22}$ are observed in the SAXS pattern (Figure 5.21a). The domain spacing of (211) is calculated to be 9.2 nm on the basis of the first scattering peak in this figure. The BF TEM image exhibits a wheel-like pattern with the distance of 9.0 ± 0.5 nm between two neighboring wheel centers (Figure 5.21b and the inset). Both results clearly verify the formation of a DG structure. A Hex structure is observed as further increasing the PS block length. It is evidenced by the SAXS pattern of AC_{60}-PS_{64}-PEO_{45} in Figure 5.21c where a *q*-ratio of 1:$\sqrt{3}$:$\sqrt{7}$ for three scattering peaks can be identified. The Hex structure is also confirmed by BF TEM image of a microtomed AC_{60}-PS_{64}-PEO_{45} thin film sample as shown in Figure 5.21d. The (100) *d*-spacing of this Hex structure is measured to be 9.5 ± 0.5 nm via the TEM observation, agreeing well with the calculated value of 9.3 nm based on the SAXS data. It can be expected that the AC_{60} MNPs are also associated with

the PEO blocks and separated from the PS blocks in the DG and Hex structures because of hydrogen bonding involved between the PEO blocks and AC_{60} and low molecular masses of PS_{52}-b-PEO_{45} and PS_{64}-b-PEO_{45}. Note that without AC_{60} MNPs, these two PS-b-PEO BCPs and two additional PS_{74}-b-PEO_{114} and PS_{115}-b-PEO_{45} BCPs with larger molecular masses are in the disordered melt due to the fact that their molecular masses are still smaller than the lower limiting value (16 kg/mol) required for nanophase separation (see absences of scattering peaks in the SAXS patterns as shown in Figures 5.22 and 5.23).

With increasing the PS block length (also the volume fraction of PS, V_{PS}, see Table 5.2), the assembled structures of giant surfactants (AC_{60}-PS_n-PEO_m) undergo their phase transitions from Lam ($V_{PS} = 0.47$), to DG ($V_{PS} = 0.63$) and further to Hex ($V_{PS} = 0.67$). This phase transition is in good agreement with that predicted by the self-consistent mean-field (SCMF) theory for flexible BCP[225] and previous experimental observations for PS-b-polyisoprene (PI),[21] where the following sequence of phases is observed as varying V_{PS} (Lam: $0.34 < V_{PS} < 0.62$; DG: $0.62 < V_{PS} < 0.66$; Hex: $0.66 < V_{PS} < 0.77$). These V_{PS} values at different phase structures also correspond well with the experimental observations of those values in PS-b-PEO diblock copolymers. [218, 226-228]
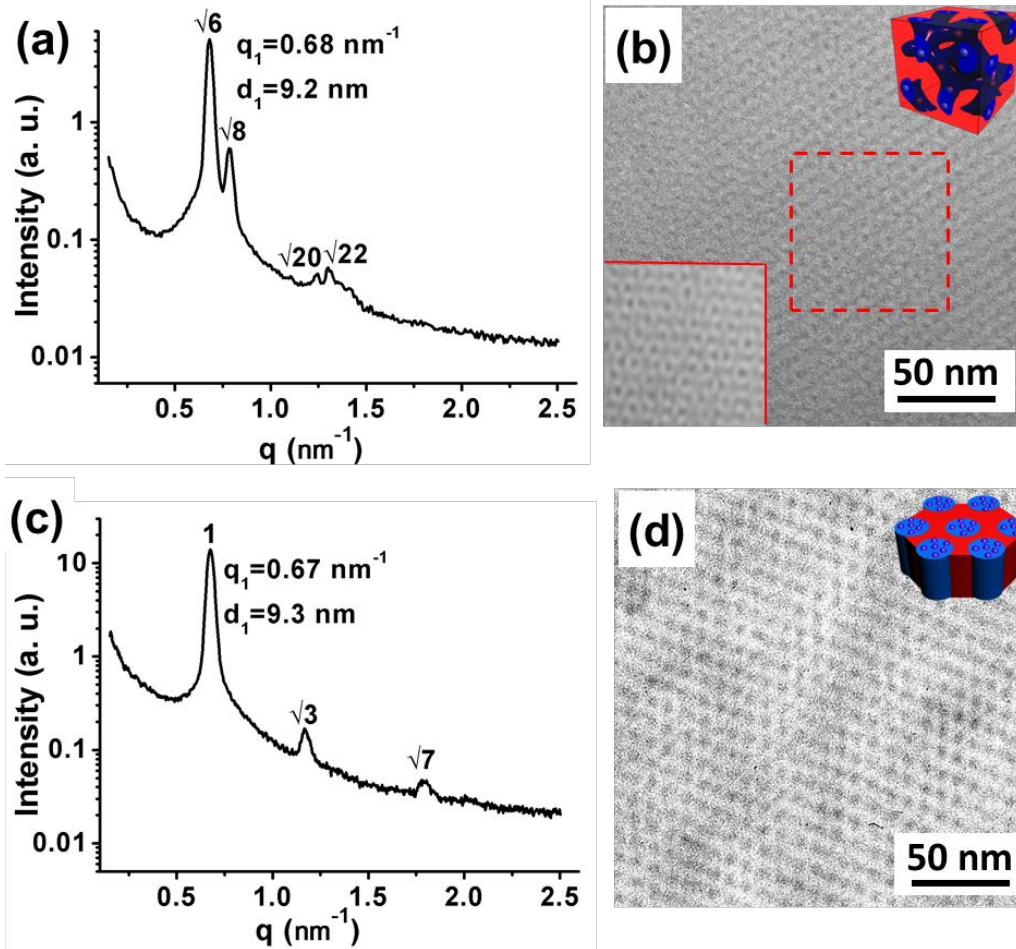
Figure 5.21. 1D SAXS patterns and BF TEM images of order structures of (a) and (b) for AC_{60}-PS_{52}-PEO_{45}, (c) and (d) for AC_{60}-PS_{64}-PEO_{45}. BF TEM images are obtained after both the AC_{60} and PEO are OsO_4-stained. Insets are TEM image (b, lower left) in selected area after Fourier filtering, models proposed for DG (b, upper right) and Hex (d, upper right), respectively.
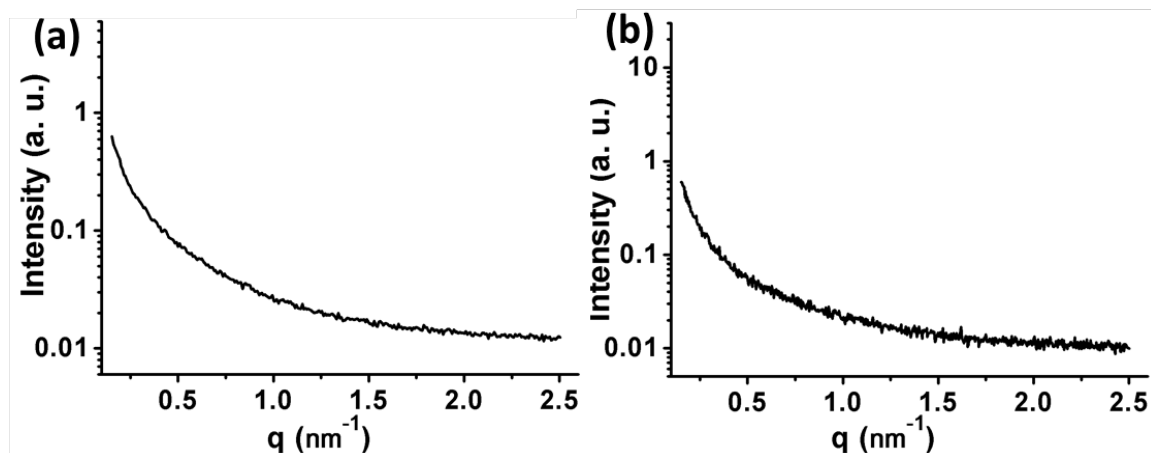
Figure 5.22. 1D SAXS patterns of (a) PS_{52}-b-PEO_{45} and (b) PS_{64}-b-PEO_{45} after thermal annealing.
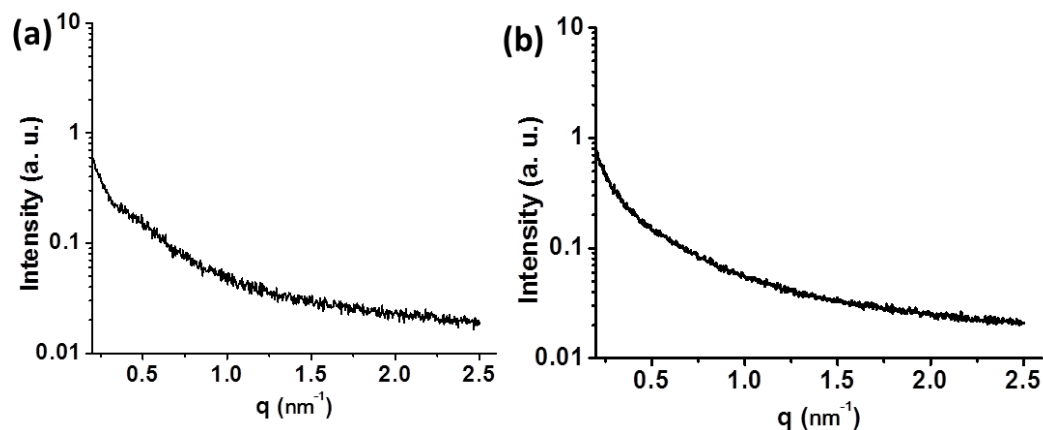
Figure 5.23. 1D SAXS patterns of (a) PS_{74}-b-PEO_{114} and (b) PS_{115}-b-PEO_{45} after thermal annealing.

Because of the weak segregation strength of BCP with low molecular masses, the preparation of ordered nanostructures with precise feature domain sizes smaller than 10 nm is generally challenging in neat BCP,[229-236] yet few reports are in BCP/NPs blend systems.[237] For the giant surfactants reported here, the dense carboxylic acid groups on

168

the periphery of AC_{60} MNPs enable the formation of hydrogen bonds between the PEO blocks and AC_{60} MNPs and thus, enhance the segregation strength to facilitate the nanophase separation of the PS-*b*-PEO at an overall molecular mass as low as 4.9 kg/mol. In addition, the mono-layer arrangement in the PS block domain for AC_{60}-PS_n-PEO_m further decreases the domain size of self-assembled hybrid ordered structures to smaller than 10 nm (with size of 8.0 nm for Lam, 9.2 nm for DG, and 9.3 nm for Hex).

5.3.4 Effect of Giant Surfactant Topology on Self-assembly.

In order to exploit the effect of topology on the assemblies, two pairs of topological isomers, namely, AC_{60}-PS_{50}-PEO_{45} and PS_{50}-(AC_{60})-PEO_{45} as well as AC_{60}-PS_{78}-PEO_{45} and PS_{78}-(AC_{60})-PEO_{45}, were specifically prepared. Each pair of topological isomers possesses identical molecular masses of the PEO and PS blocks, but the AC_{60} MNP is attached at different physical locations (at the PS block end or at the junction point between the PEO and PS blocks). As shown in Figures 5.24a and 5.24b, both AC_{60}-PS_{50}-PEO_{45} and PS_{50}-(AC_{60})-PEO_{45} possess Lam structures, but with different periodic domain spacings (8.8 nm versus 11.4 nm). This difference can only be attributed to the tethering locations of AC_{60} MNPs (and thus, the giant surfactant topology). The packing model of AC_{60}-PS_{50}-PEO_{45} is shown in Figure 1d (also inserted in Figure 5.24c). For PS_{50}-(AC_{60})-PEO_{45}, it is suggested that its packing model possesses a double layer of the PS blocks as shown in the inset of Figure 5.24d. The BF TEM images of microtomed samples of AC_{60}-PS_{50}-PEO_{45} and PS_{50}-(AC_{60})-PEO_{45} after OsO_4-staining are shown in Figures 5.24c and 5.24d. The widths of gray PS domains in AC_{60}-PS_{50}-PEO_{45} and PS_{50}-(AC_{60})-PEO_{45} are measured to be 5.0 ± 0.5 nm and 7.0 ± 0.6 nm, respectively. The size

difference of ~2 nm between these two PS domains is consistent with the results obtained

in SAXS experiments (2.6 nm).
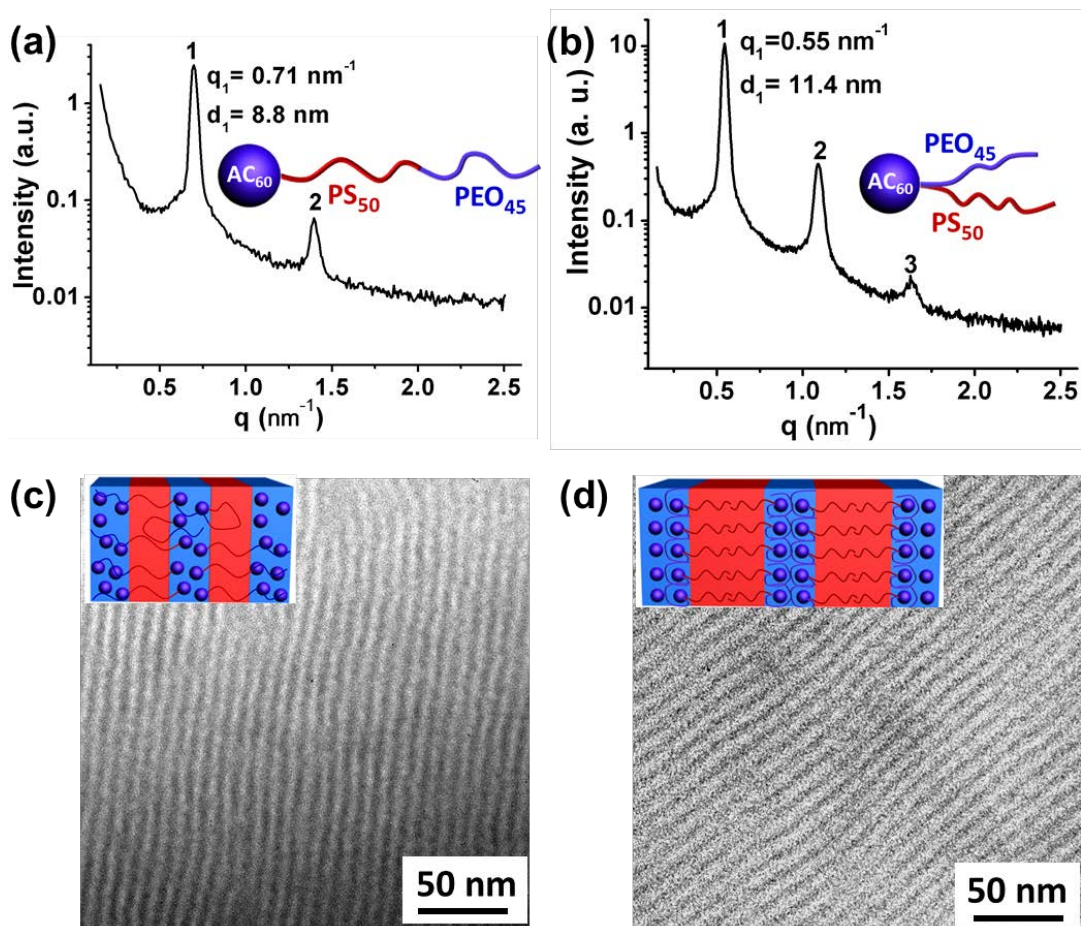
Figure 5.24. 1D SAXS patterns and BF TEM images of Lam structures of (a) and (c) for

AC_{60}-PS_{50}-PEO_{45}, (b) and (d) for PS_{50}-(AC_{60})-PEO_{45}. Insets are the models proposed for

AC_{60}-PS_{50}-PEO_{45} and PS_{50}-(AC_{60})-PEO_{45}. TEM images are obtained after staining by

OsO_4, where both AC_{60} and PEO are stained.
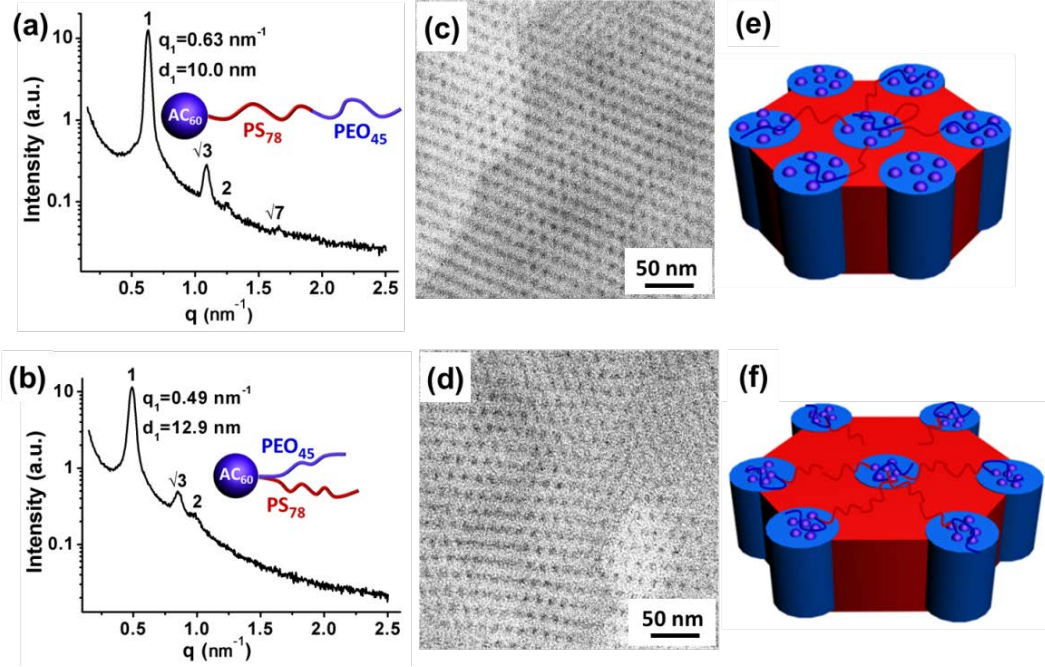
Figure 5.25. 1D SAXS patterns, BF TEM images and proposed models of Hex structures. (a), (c) and (e) for AC_{60}-PS_{78}-PEO_{45}, (b), (d) and (f) for PS_{78}-(AC_{60})-PEO_{45}.

Given the identical PS block lengths in these two topological isomers, one may ask why the PS domain spacing of PS_{50}-(AC_{60})-PEO_{45} (double layer, 7 nm) is only about 40 % larger but less than twice of the size compared with that of AC_{60}-PS_{50}-PEO_{45} (single layer, 5 nm). To address this issue, we calculate the stretching ratio (S) of the PS chains in the Lam, which can be characterized by

$$S = L / 2R_g \tag{1}$$

where L is obtained from the PS domain spacing in the single layer model (AC_{60}-PS_{50}-PEO_{45}), or one half of the PS domain spacing in the double layer model [PS_{50}-(AC_{60})-PEO_{45}]. R_g is the radius of gyration of PS chain that can be calculated by

$$R_g = (N_{PS}/6)^{1/2} b \tag{2}$$

171

where N_{PS} is the degree of polymerization of PS and b is the average statistical segment length of PS ($b = 0.68$ nm).[238] The value of S for both the PS blocks in AC_{60}-PS_{50}-PEO_{45} and PS_{50}-(AC_{60})-PEO_{45} are calculated to be 1.28 and 0.90, respectively. This reveals that the PS blocks in AC_{60}-PS_{50}-PEO_{45} are relatively stretched, while those in PS_{50}-(AC_{60})-PEO_{45} are more relaxed. This may be associated with the fact that the PS blocks have no free chain ends in AC_{60}-PS_{50}-PEO_{45}, in contrast to one free chain end of the PS blocks in PS_{50}-(AC_{60})-PEO_{45}.

Another set of topological isomers, AC_{60}-PS_{78}-PEO_{45} and PS_{78}-(AC_{60})-PEO_{45}, exhibit Hex structures with different periodic spacing (d_{100}) based on the SAXS patterns in Figures 5.25a and 5.25b. They are 10.0 nm and 12.9 nm, respectively. The center distance between two neighboring columns (d) in these two Hex structures are thus calculated to be 11.5 nm and 14.9 nm ($d = 2\,d_{100}/\sqrt{3}$), respectively. This difference can be confirmed by the results of BF TEM images in Figures 5.25c and 5.25d, where the d values of two Hex structures are measured as 12.0 ± 0.8 nm and 15.0 ± 0.9 nm, respectively. The difference in the d values for these two Hex structures can also be ascribed to the distinct PS conformations. As illustrated in the Figure 5.25e, in the Hex of AC_{60}-PS_{78}-PEO_{45}, the PEO and AC_{60} of each giant surfactant are located either in two neighboring columns or in the same column with a PS block that is folded back. In the Hex structure of PS_{78}-(AC_{60})-PEO_{45} (Figure 5.25f), the PEO and AC_{60} of each molecule are expected to be located in the same column, where the PS blocks arrange in the domain with a free chain end. The latter PS conformations are more likely to increase the distance between two neighboring columns. This may associate with the fact that the PS blocks with a free chain end in PS_{78}-(AC_{60})-PEO_{45} construct the PS domains via both the

172

tethered PS chains from neighboring columns, while in AC_{60}-PS_{78}-PEO_{45} the PS domain is formed by one PS block connected to two neighboring columns.

5.4 Conclusion

In summary, two series of giant surfactants with a AC_{60} MNP tethered onto a PS-*b*-PEO block copolymer either at the PS block end (AC_{60}-PS_m-PEO_n) or at the junction point [PS_m-(AC_{60})-PEO_n] of the block copolymers were designed and synthesized via "click" chemistry. Investigation of the assembly of these two series of giant surfactants reveals that the hydrogen bonding between the AC_{60} MNPs and the PEO blocks plays an essential role in facilitating the nanophase separation of originally disordered PS-*b*-PEO block copolymers and thus, affording the formation of various ordered nanostructures in the bulk, such as Lam, DG and Hex phases. In these ordered structures, the AC_{60} MNPs and PEO blocks are associated with each other in one domain and the PS blocks segregate into another. With a systematic study of their phase behaviors, we can conclude that: (1) comparison between the giant surfactant having MNP tethered block copolymer system with a system of mixing MNPs into block copolymers shows more controlled nanophase separations could be achieved with a smaller domain size; (2) comparison of two pairs of topological isomers, AC_{60}-PS_{50}-PEO_{45} and PS_{50}-(AC_{60})-PEO_{45}, as well as AC_{60}-PS_{78}-PEO_{45} and PS_{78}-(AC_{60})-PEO_{45} reveals that their Lam and Hex structures with different domain sizes result from the distinct PS block arrangements and their conformations in the domains; (3) this work introduces a practical approach to the design and fabrication of hierarchical nanostructures with sub-10-nm length scales.

173

Sub-10 nm Hybrid Ordered Structures
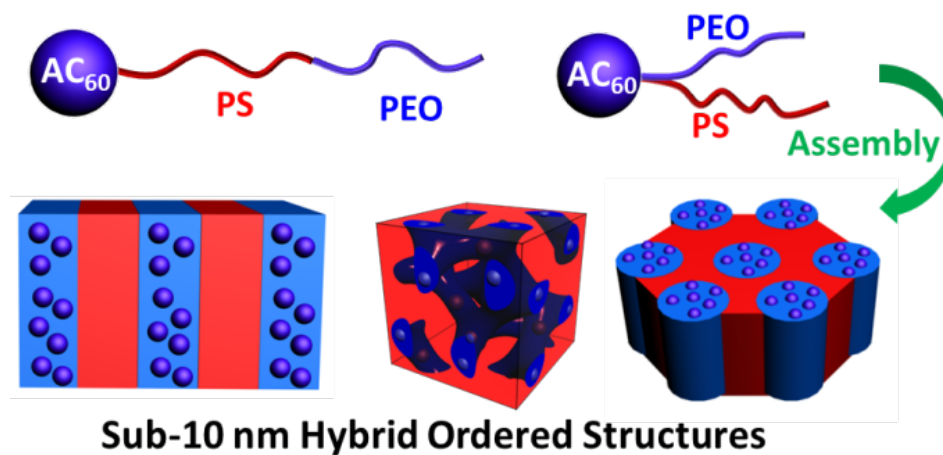
Figure 5.26. Genenal story of Chpater V.*

CHAPTER VI

GIANT SURFACTANTS BASED ON HYDROXYL FUNCTIONALIZED

FULLERENES: PRECISE SYNTHESIS AND SELF-ASSEMBLY IN BULK

6.1 Introduction

Capturing the structural characteristics of small-molecule surfactants consisting of polar head and nonpolar tails, polymer-tethered molecular nanoparticles (MNP) possessing amplified sizes are regarded as giant surfactants.[67] In recent years, giant surfactants have been emerging as one of important hybrid materials, not only because of their unique molecular features but also their intriguing assembly behaviors, bridging the gap between small molecules and macromolecules. Using polyhedral oligomeric silsesquioxane (POSS) as MNP, our group has developed a myriad of giant surfactants with different chemical composition, molecular architectures and topologies.[36] These POSS-based giant surfactants exhibit rich and diverse assembly behaviors in solution, bulk and thin films. For example, giant surfactants containing one hydroxyl-functionalized POSS (DPOSS) and one polystyrene (PS) chain can form a variety of nano-ordered structures in bulk, including lamellae (Lam), double gyroid (DG), hexagonally packed cylinders (Hex) and body centered cubic (BCC).[69] Despite the great success, the study is mainly focusing on POSS-based giant surfactants. POSS cage is built upon from silica containing materials, which are generally immiscible with PS. One

presentative example is polydimethylsiloxane (PDMS), which has very strong phase separation tendency with PS.[239-242] As a result, it remains to be a question that it is the nature of POSS or amphiphilicity of giant surfactants that drive the phase separation and dominate intriguing self-assembly behaviors.

In this chapter, we report our recent efforts on the synthesis and assembly of a new family of giant surfactants composed of hydroxyl groups functionalized C_{60} as a hydrophilic head tethered by hydrophobic PS as tail(s). The number of hydroxyl groups installing on the periphery of C_{60} can be ten (HC_{60}) or twenty (DC_{60}), giving rise to two different types of building blocks. The number of PS tails attached on DC_{60} was varied from one, to two, to four, affording three categories of giant surfactants, namely, DC_{60}-PS_n, and DC_{60}-$2PS_n$, and DC_{60}-$4PS_n$. Due to affinity between the aromatic ring on C_{60} and PS, the intact C_{60} are completely compatible with PS. Introducing the hydroxyl groups on the periphery of C_{60} induce phase separation between C_{60} domain and PS domain, resulting in various nano-ordered structures. The influence of functionalities, volume fraction of PS, molecular architectures as well as topologies on assembly of as-synthesized giant surfactant, will be systematically discussed.

6.2 Experimental Section

In this section, the detailed procedures for the synthesis, characterization and assembly of giant surfactants will be described.

6.2.1 Chemicals and Solvents.

[60]Fullerene (C_{60}, MTR Ltd., 99.5%), methyl malonyl chloride (Aldrich, 97%), malonyl chloride (Aldrich, 97%), DL-1,2-Isopropylideneglycerol (Aldrich, 98%),

triethylamine (TEA, 99%, Alfa Aesar), iodine (I_2, Aldrich, 99.8%), CuBr (Aldrich 98%), 1,8-diazabicyclo[5.4.0]undec-7-ene (DBU, Aldrich, 99%), *N,N',N',N'',N''-*pentamethyldiethylenetriamine (PMDETA, Aldrich, 99%), trifluoroacetic acid (CF_3COOH, Aldrich, 98%), chloroform-*d* ($CDCl_3$, Aldrich, 99.8 at %D) were used as received. Toluene (Aldrich, 99.5%) and 1,2-dichlorobenzene (ODCB, Aldrich, 99%) were stirred with CaH_2 and redistilled prior to use.

6.2.2 Characterization

. All nuclear magnetic resonance (NMR) experiments were carried out on a Varian NMRS 500-01 spectrometer. The samples were prepared in $CDCl_3$. The concentration for ^1H NMR and ^{13}C NMR experiments is 20 mg/mL and 80 mg/mL, respectively. The ^1H NMR spectra and ^{13}C NMR spectra were referenced to the residual impurities in deuterated solvents, δ 7.27 ppm and δ 77.00 ppm in $CDCl_3$.

Size-exclusion chromatography (SEC) analyses were performed on a Waters 150-C Plus instrument equipped with three HR-Styragel columns [100 Å, mixed bed ($50/500/10^3/10^4$ Å), mixed bed ($10^3/10^4/10^6$ Å)] and a triple detector system. The three detectors consist of a differential refractometer (Waters 410), a laser light scattering detector (Wyatt Technology, DAWN EOS, λ = 670 nm) and a differential viscometer (Viscotek 100). THF was used as the eluent with a flow rate of 1.0 mL/min at room temperature. Samples were dissolved in THF with the concentration of *ca.* 5-10 mg/mL, which were filtered through a 0.45 μm Teflon filter prior to injection. Regular SEC calibrations were conducted based on PS standards (Polymer Laboratories).

Matrix-assisted laser desorption/ionization-time of flight (MALDI-TOF) mass spectra were obtained on a Bruker Ultraflex III TOF/TOF mass spectrometer (Bruker Daltonics, Inc., Billarica, MA), equipped with a Nd : YAG laser emitting at a wavelength of 355 nm. Positive reflection or linear mode was applied to measure all of spectra. Calibration with external PS standards was required before each measurement. Trans-2-(3-(4-t-butyl-phenyl)-2-methyl-2-propenylidene) malononitrile (DCTB) was served as matrix (20 mg/mL in CHCl$_3$) and sodium trifluoroacetate (NaTFA) was used as the cationizing agent (10 mg/mL in methanol). Both of them were mixed in the ratio of 10/1 (v/v). In sample preparation, 0.5 μL of the matrix/NaTFA mixture was deposited on microtiter plate wells (MTP 384-well ground steel plate), followed by depositing 0.5 μL of sample solution (*ca.* 10 mg/mL in THF) on the top of a dry matrix/NaTFA spot and adding another 0.5 μL of the matrix/NaTFA mixture. After evaporation of solvent, the target plate was loaded for data collection. Data analysis was performed with the Bruker's flexAnalysis software.

Sample preparation for SAXS and TEM experiments is based on following procedures. The freeze-dried powder samples were first thermally annealed at 140 °C under nitrogen atmosphere for up to 12h. The samples were then cooled to room temperature and used for SAXS measurements. Thin slices of the bulk samples with the thickness of 60-80 nm were obtained at room temperature utilizing a Reichert Ultracut S (Leica) microtome on annealed samples embedded in epoxy monolith. The slices were carefully collected onto copper grids coated with amorphous carbon for TEM experiments. When necessary, osmium tetroxide (OsO$_4$) staining of the samples was performed at room temperature overnight.

178

Small Angle X-ray Scattering (SAXS) patterns were collected on a Rigaku MicroMax 002+ instrument equipped with a two-dimensional (2D) multiwire area detector and a microfocus sealed copper tube. The wavelength of the X-ray is 0.154 nm, with working voltage and current of 5 kV and 0.6 mA, respectively. The scattering vector (q) was calibrated using silver behenate with the primary reflection peak at $q = 1.067$ nm^{-1}. The SAXS diffraction patterns with the q value range between 0.15 and 3.0 nm^{-1} were collected. The recording time for each data was 15 min. The data were analyzed with the Rigaku SAXSgui software.

The bright field (BF) transmission electron microscopy (TEM) images of the microtomed samples were taken on a JEOL-1230 TEM equipped with a digital CCD camera and accessory digital imaging system, collecting with an accelerating voltage of 120 kV. The periodic domain sizes of ordered structures obtained from TEM images were based on an average of ten independent measurements. The calibration of the length scale on TEM images were carried out based on grating replica crossed lines.

Calculations of volume fractions of PS and DC_{60} are based on the following formulas. Determination of the volume fractions relies on several assumptions. First, the density of the PS chains is assumed as the density of amorphous PS (1.05 g/cm^3). Second, it is assumed that the density of the DC_{60} domains remains the same as that of the corresponding model compounds, which has a measured density of 1.60 g/cm^3. The volume fraction of the PS and DC_{60} domain is given by

$$V_{PS} = \frac{M_{PS}/\rho_{PS}}{M_{PS}/\rho_{PS} + M_{DC60}/\rho_{DC60}}$$

$$V_{DC60} = \frac{M_{DC60}/\rho_{DC60}}{M_{PS}/\rho_{PS} + M_{DC60}/\rho_{DC60}}$$

6.2.3 General Synthetic Procedures

Compound 2a. Methyl malonyl chloride (0.037 mol, 5 g, 1 equiv), DL-1,2-isopropylideneglycerol (0.038 mol, 5g, 1.02 equiv) and TEA (0.038 mol, 3.8g, 1.02 equiv) were dissolved in 100 mL anhydrous CH_2Cl_2 at 0 °C in an ice bath. The mixtures were allowed to warm up to room temperature in 2h and stir overnight. 100 mL CH_2Cl_2 was then added and the resulting mixture was washed with brine for three times, dried over anhydrous Na_2SO_4 overnight. After removal of solvent, the residue was purified by flash column chromatography on silica gel with hexane/EA (v/v = 4:1) as eluent to obtian 2a (7.5 g) as a colorless oil. Yield: 88%. ^{1}H NMR ($CDCl_3$, 500 MHz, ppm): δ 4.33-4.03 (m, 5H), 3.75 (s, 3H), 3.43 (s, 2H), 1.43 (d, 6H). ^{13}C NMR ($CDCl_3$, 125 MHz, ppm): δ 166.6, 166.1, 109.8, 73.2, 66.1, 65.5, 52.4, 41.0., 26.6, 25.2
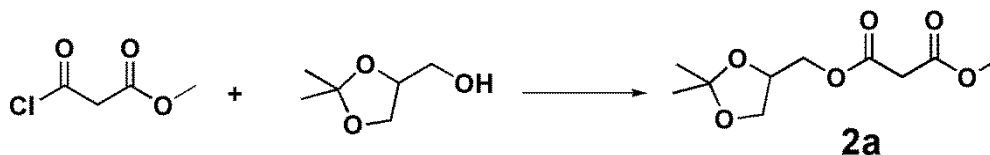
Scheme 6.1. Synthetic route of compound 2a.

Compound 2b. To the solution of DL-1,2-Isopropylideneglycerol and (0.076 mol, 10 g, 2.1 equiv) and TEA (0.076 mol, 7.7g, 2.1 equiv) in 100 mL CH_2Cl_2, malonyl chloride (0.036 mol, 5g, 1 equiv) were added dropwise in 0.5 h at 0 °C. The mixtures were allowed to warm up to room temperature in 2 h and stir overnight. 100 mL CH_2Cl_2 was then added and the resulting mixture was washed with brine for three times, dried over anhydrous Na_2SO_4 overnight. After removal of solvent, the residue was purified by

flash column chromatography on silica gel with hexane/EA (v/v = 2:1) as eluent to obtian 2b (10.6 g) as a colorless oil. Yield: 90%. ^{1}H NMR (CDCl$_3$, 500 MHz, ppm): δ 4.38-4.05 (m, 6H), 3.76 (m, 4H), 3.47 (s, 2H), 1.44 (d, 12H). ^{13}C NMR (CDCl$_3$, 125 MHz, ppm): δ 165.8, 109.4, 73.1 , 66.9, 65.3, 41.0, 26.4, 25.1.
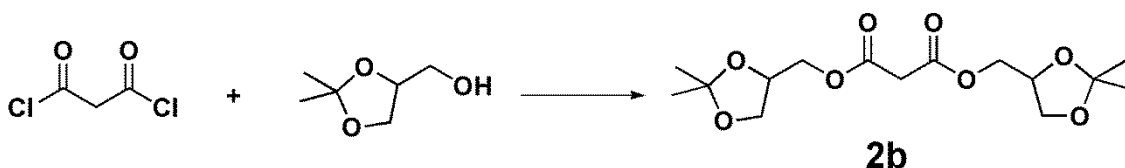
Scheme 6.2. Synthetic route of compound 2b.

[5:1]-Hexakisadducts 3a-3b. 1 was first synthesized based on our previous reported procedures.[68] To a solution of 2a (0.9g, 3.9 mmol, 10 equiv) or 2b (1.3g, 4.7 mmol, 10 equiv) dissolving in 50 mL ODCB, I$_2$ (0.98g, 3.9 mmol, 10equiv), and 1 (350 mg, 0.39 mmol, 1equiv) were added under nitrogen. The solution was stirring for 3h, followed by adding DBU (1.2g, 7.8 mmol, 20 equiv). The resulting mixture was stirring for 72h at room temperature, and then filtered through a short silica column to remove salts using CH$_2$Cl$_2$/EA(v/v=1:1) as the eluent. After removal of solvent, the residue was purified by flash column chromatography on silica gel with CH$_2$Cl$_2$/EA (v/v = 4 /1) or CH$_2$Cl$_2$/EA (v/v = 3/1) as eluent to give 3a (350mg, 44%) or 3b (445mg, 45%) as red powders.

3a ^{1}H NMR (CDCl$_3$, 500 MHz, ppm): δ 4.34 (m, 12H), 4.06 (m, 5H), 3.86 (s, 18H), 3.79 (m, 10H), 2.28 (m, 2H), 1.92 (m, 3H), 1.42 (d, 30H). ^{13}C NMR (CDCl$_3$, 125 MHz, ppm): δ 163.6, 145.7, 141.0, 109.8, 82.5, 72.9, 69.5, 66.5, 65.3, 53.6, 45.2, 29.7, 26.5, 25.2, 14.9. MS (MALDI-TOF): Calcd for C$_{119}$H$_{80}$O$_{34}$, 2052.5, Found: 2052.6.

181

3b ^{1}H NMR (CDCl$_3$, 500 MHz, ppm): δ 4.33-4.07 (m, 32H), 3.88 (s, 3H), 3.76 (m, 20H), 2.30 (m, 2H), 1.92 (m, 3H), 1.42 (d, 60H). ^{13}C NMR (CDCl$_3$, 125 MHz, ppm): δ 170.0, 166.5, 163.2, 145.9, 140.8, 110.0, 72.9, 72.7, 67.0, 66.5, 58.9, 54.0, 29.7, 26.7, 25.3, 14.9. MS (MALDI-TOF): Calcd for C$_{144}$H$_{120}$O$_{44}$, 2552.7, Found: 2552.8.

mC$_{60}$-2alkyne. 4 was first synthesized based on our previous reported procedures.[68] To a solution of 2b (1.3g, 4.7 mmol, 10 equiv) dissolving in 50 mL ODCB, I$_2$ (0.98g, 3.9 mmol, 10equiv), and 4 (370 mg, 0.39 mmol, 1equiv) were added under nitrogen. The solution was stirring for 3h, followed by adding DBU (1.2g, 7.8 mmol, 20 equiv). The resulting mixture was stirring for 72h at room temperature, and then filtered through a short silica column to remove salts using CH$_2$Cl$_2$/EA(v/v=1:1) as the eluent. After removal of solvent, the residue was purified by flash column chromatography on silica gel with CH$_2$Cl$_2$/EA (v/v = 3/1) as eluent to give mC$_{60}$-2alkyne (454mg, 45%) as red powders. ^{1}H NMR (CDCl$_3$, 500 MHz, ppm): δ 4.46-4.15 (m, 24H), 4.05 (m, 10H), 3.74 (m, 20H), 2.27 (m, 4H), 1.90 (m, 6H), 1.42 (d, 60H). ^{13}C NMR (CDCl$_3$, 125 MHz, ppm): δ 163.6, 145.7, 141.0, 109.8, 82.5, 72.9, 69.5, 66.5, 65.3, 53.6, 45.2, 29.7, 26.5, 25.2, 14.9. MS (MALDI-TOF): Calcd for C$_{148}$H$_{124}$O$_{44}$ 2604.7, Found: 2604.7

HC$_{60}$-PS$_n$ or DC$_{60}$-PS$_n$. PS$_n$-N$_3$ was first synthesized based on our previous reported procedures.[71] PS$_n$-N$_3$ ($M_{n,\text{NMR}}$ = 3.3 kg/mol, Đ = 1.06, 150 mg, 0.045mmol, 1.2 equiv), nC$_{60}$-alkyne (78 mg, 0.038 mmol, 1 equiv) or mC$_{60}$-alkyne (97 mg, 0.038 mmol, 1.1 equiv), CuBr (5 mg, 0.038 mmol, 1 equiv) and freshly distilled toluene (15 mL) were added to a 100 mL Schlenk flask equipped with a magnetic stirring bar. The resultant solution was degassed by three freeze-pump-thaw cycles before introducing PMDETA (6 mg, 0.038 mmol, 1 equiv) under nitrogen protection. Upon one further freeze-pump-thaw

cycle, the mixture was stirred at room temperature for 16 h. After the reaction was completed, the mixture was directly applied onto a column filled with silica gel. CH_2Cl_2 was first used as the eluent to remove the excess PS_n-N_3. The column was then further eluted with a mixture of CH_2Cl_2/methanol (v/v = 8/1) to give a colored fraction of nC_{60}-PS_n or mC_{60}-PS_n. The concentrated product was precipitated into methanol, collected by vacuum filtration and dried *in vacuo* to give the product as a red powder nC_{60}-PS_n (163 mg, 80%) or mC_{60}-PS_n (180 mg, 81%). To deprotect the terminated acetonide groups on nC_{60} or mC_{60}, nC_{60}-PS_n or mC_{60}-PS_n was dissolved in a mixture of CH_2Cl_2 and CF_3COOH (v/v = 4/1) and stirred at room temperature for 8 h. Upon removal of the solvent, the residue was re-dissolved in 3 mL of benzene. The targeted product, HC_{60}-PS_n (143 mg, 91%) or DC_{60}-PS_n (151 mg, 90%), was obtained as a red powder after freeze drying.

DC_{60}-$2PS_n$ or DC_{60}-$4PS_n$ $2PS_n$-N_3 was first synthesized based on our previous reported procedures.[243] mC_{60}-alkyne (52 mg, 0.02 mmol, 1 equiv), PS_n-N_3 (M_n,NMR = 4 kg/mol, Đ = 1.08, 192 mg, 0.048 mmol, 2.4 equiv) or $2PS_n$-N_3 (M_n,NMR = 4 kg/mol, Đ = 1.04, 192 mg, 0.048 mmol, 2.4 equiv), CuBr (6 mg, 0.04 mmol, 2 equiv) and freshly distilled toluene (25 mL) were added to a 100 mL Schlenk flask equipped with a magnetic stirring bar. The resultant solution was degassed by three freeze-pump-thaw cycles before introducing PMDETA (7 mg, 0.04 mmol, 2 equiv) under nitrogen protection. Upon one further freeze-pump-thaw cycle, the mixture was stirred at room temperature for 16 h. After the reaction was completed, the mixture was directly applied onto a column filled with silica gel. CH_2Cl_2 was first used as the eluent to remove the excess PS_n-N_3 or $2PS_n$-N_3. The column was then further eluted with a mixture of

CH$_2$Cl$_2$/methanol (v/v = 8/1) to give a colored fraction of mC$_{60}$-2PS$_n$ or mC$_{60}$-4PS$_n$. The

concentrated product was precipitated into methanol, collected by vacuum filtration and

dried *in vacuo* to give the product as a red powder mC$_{60}$-2PS$_n$ (173 mg, 82%) or mC$_{60}$-

4PS$_n$ (167 mg, 79%). To deprotect the terminated acetonide groups on mC$_{60}$, mC$_{60}$-2PS$_n$

or mC$_{60}$-4PS$_n$ were dissolved in a mixture of CH$_2$Cl$_2$ and CF$_3$COOH (v/v = 4/1) and

stirred at room temperature for 8 h. Upon removal of the solvent, the residue was re-

dissolved in 3 mL of benzene. The targeted products, DC$_{60}$-2PS$_n$ (148 mg, 90%) or DC$_{60}$-

4PS$_n$ (143 mg, 90%), were obtained as a red powder after freeze drying.
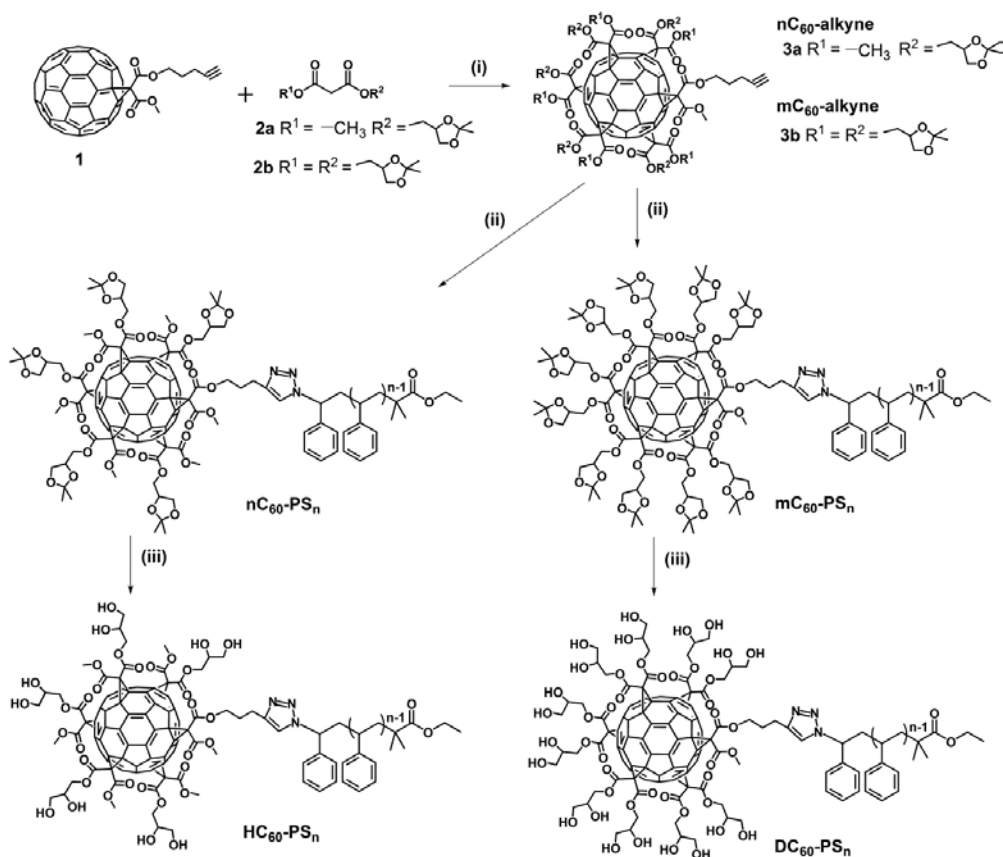
Scheme 6.3. Synthetic route of HC$_{60}$-PS$_n$ and DC$_{60}$-PS$_n$. (i) ODCB, I$_2$, DBU, rt (3a, 44%,

3b, 45%); (ii) PS$_n$-N$_3$, toluene, CuBr, PMDETA, rt (80%), (iii) CH$_2$Cl$_2$, CF$_3$COOH, rt

(90%).
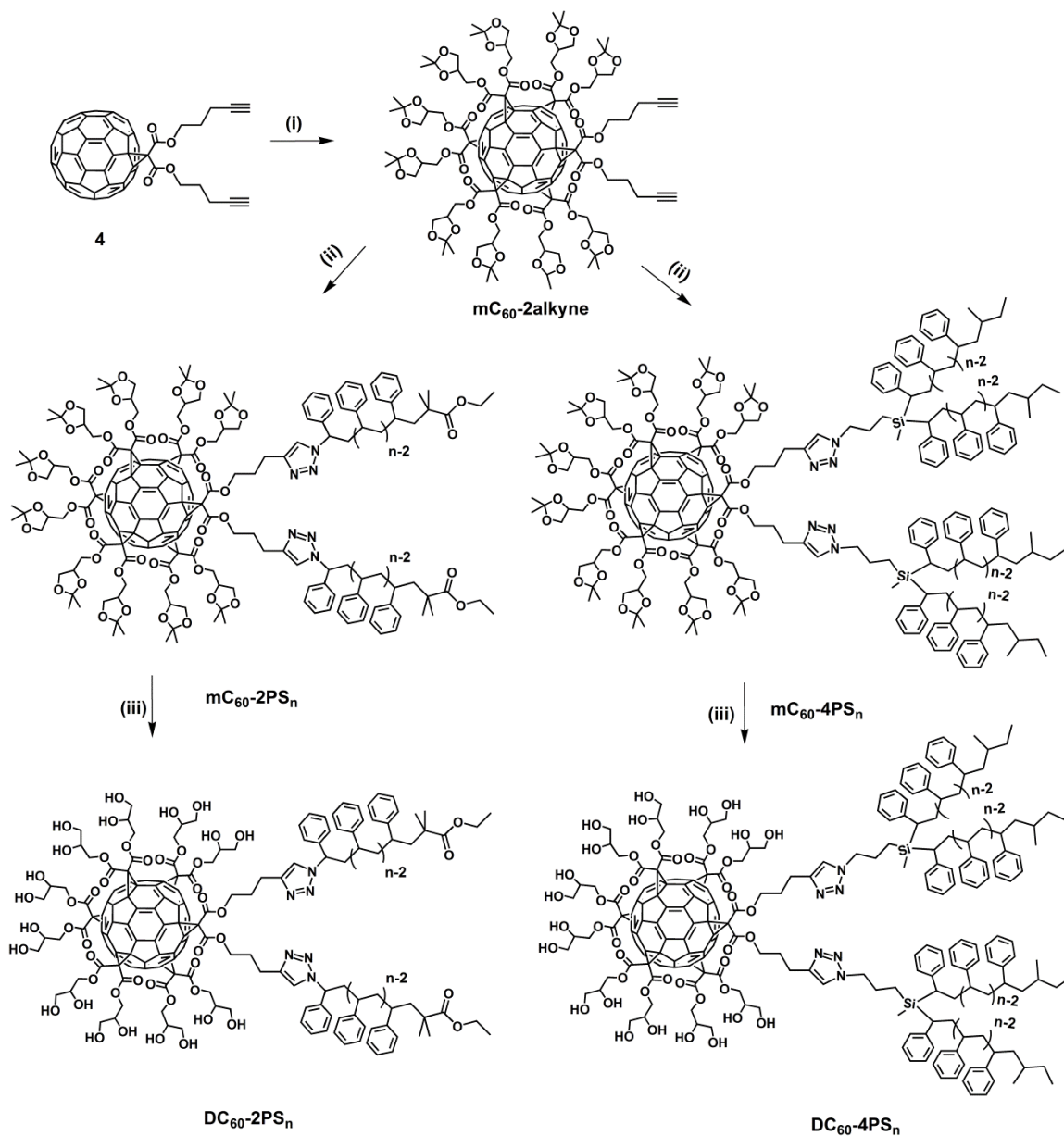
Scheme 6.4. Synthetic route of DC_{60}-$2PS_n$ and DC_{60}-$4PS_n$. (i) ODCB, I_2, DBU, rt (45%); (ii) PS_n-N_3 or $2PS_n$-N_3, toluene, CuBr, PMDETA, rt (80%), (iii) CH_2Cl_2, CF_3COOH, rt (90%).

6.3 Results and Discussion

In this section, the successful synthesis of giant surfactants will be fully characterized, as well as their versatile assembly behaviors in bulk will be discussed.

6.3.1 Synthesis of Giant Surfactants

The molecular design of HC_{60}-PS_n and DC_{60}-PS_n giant surfactants is quite straightforward by tethering a PS chain to a precisely defined C_{60} derivative functionalized by ten or twenty hydroxyl groups. The synthetic route of a HC_{60}-PS_n and DC_{60}-PS_n is illustrated in Scheme 6.3. Bingel-Hirsch cyclopropanation reaction is one of the most widely used reactions to prepare the hexakisadducts of C_{60}. It was utilized to synthesize the mono-functionalized C_{60} with one or two alkyne group (compound 1 and 4), based on the procedures reported in our previous publications.[68] The synthesis of the HC_{60} and DC_{60} building block requires the malonate containing protected hydroxyl groups. To this end, the compound 2a-b was designed and synthesized, as illustrated in Scheme 6.1 and 6.2. The chemical structure of 2a-b was unambiguously characterized by ^1H NMR and ^{13}C NMR (Figure 6.1). [5:1] Hexakisadducts of C_{60} bearing ten or twenty protected hydroxyl groups and one terminal alkyne group is achieved by sequential cyclopropanation. The well-defined structures of 3a-b were evidenced by the ^1H NMR and ^{13}C NMR. In the ^1H NMR spectrum (Figure 6.2 a and b), the resonance signals of all protons for 3a-b could be clearly observed. In the ^{13}C NMR spectra (Figure 6.2 d and e), the sp^3 carbon atoms at 69.0 ppm and the two different types of sp^2 carbon at 145.9 and 140.8 confirm the T_h-symmetry of the carbon cage of 3a-b. The precisely defined structures of 3a and 3b were further characterized by MADAL-TOF mass spectra. In

186

Figure 6.3, only single strong peak is exhibited for either 3a or 3b, where the observed monoisotopic masses are in good agreement with the calculated ones (2052.5 Da vs. 2052.6 Da and 2552.8 Da vs. 2552.7 Da). Following similar synthetic procedures but using compound 4 instead of 1 as the starting materials, another well-defined [5:1] Hexakisadducts of C_{60} bearing twenty protected hydroxyl groups and two terminal alkyne groups, namely, mC_{60}-2alkyne can also be synthesized. It can be used for preparing DC_{60}-based the giant surfactants with two or four PS tails, which will be further discussed later.
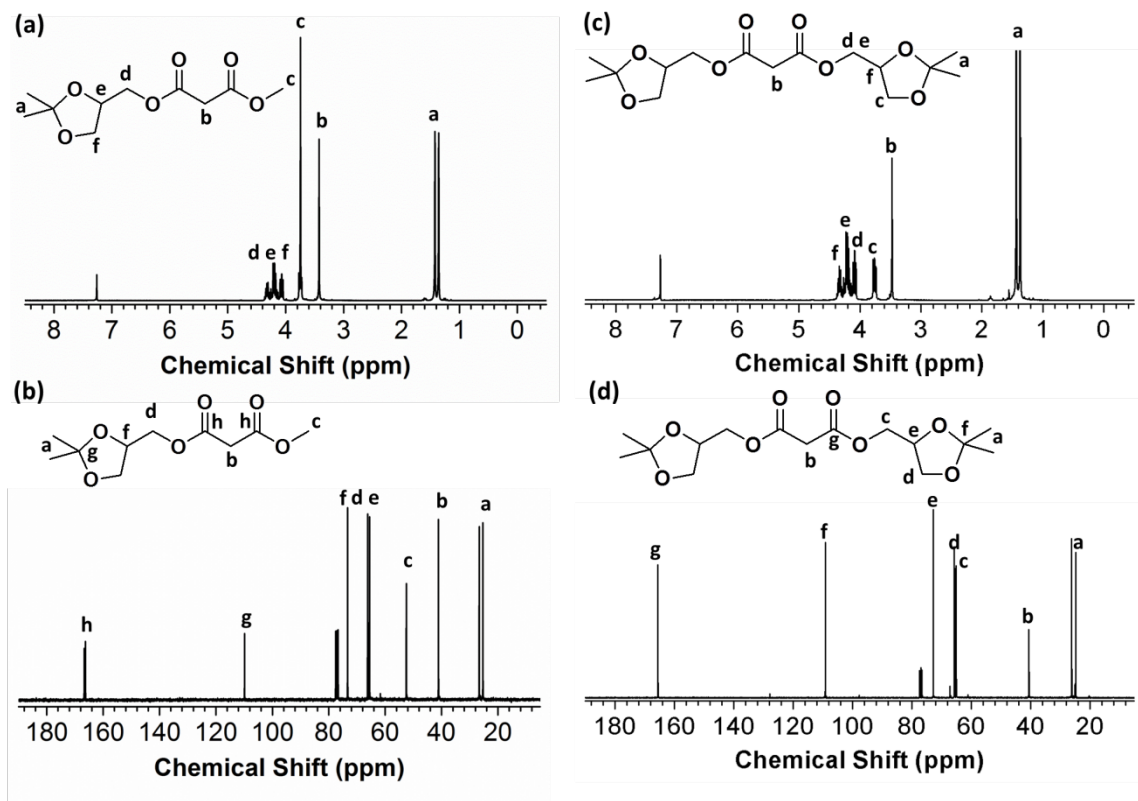
Figure 6.1 (a) ^{1}H NMR and (b) ^{13}C NMR spectra of 2a, (c)^{1}H NMR and (d) ^{13}C NMR spectra of 2b.
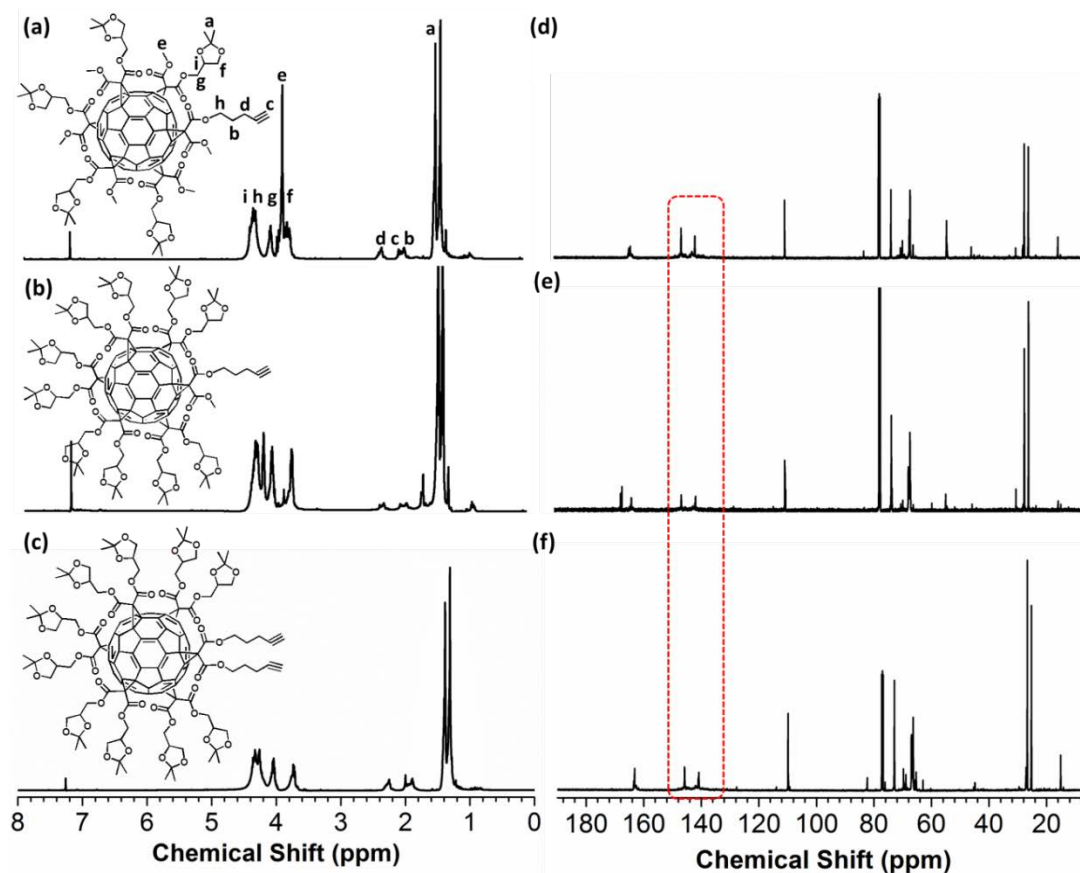
Figure 6.2. ^1H NMR and ^{13}C NMR spectra of nC_{60}-alkyne, mC_{60}-alkyne and mC_{60}-2alkyne. (a) and (d) for nC_{60}-alkyne, (b) and (e) mC_{60}-alkyne, (c) and (f) for mC_{60}-2alkyne.
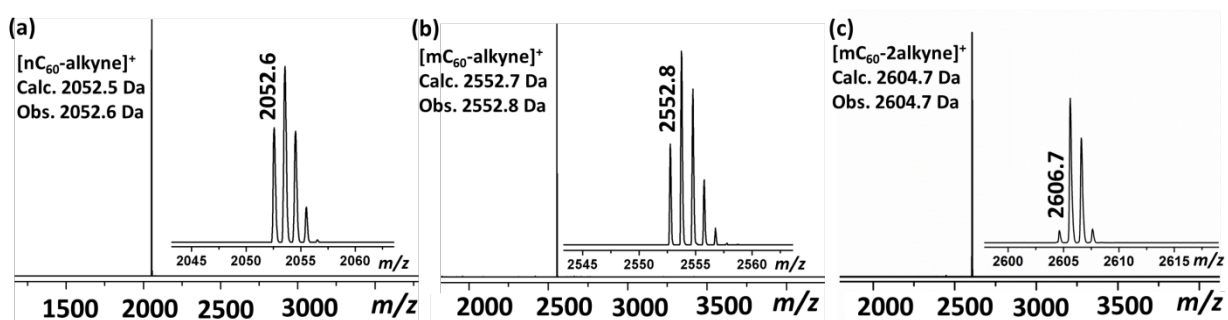
Figure 6.3. MALDI-TOF mass spectra of (a) nC_{60}-alkyne, (b) mC_{60}-alkyne and (c) mC_{60}-2alkyne.

The conjugation of nC_{60}-alkyne/mC_{60}-alkyne and PS_n-N_3 to afford nC_{60}-PS_n/mC_{60}-PS_n was achieved by the CuAAC click reactions. The inspection of ^1H NMR, ^{13}C NMR and SEC results clearly indicate the well-defined structure of nC_{60}-PS_n and mC_{60}-PS_n. In the SEC profiles, a monomodal and symmetric SEC curve with narrow distribution ($Đ = 1.07$) is exhibited for nC_{60}-PS_n and mC_{60}-PS_n, where it shifts to lower retention volume relative to PS_n-N_3, corresponding to the increased molecule weight after click reactions (Figure 6.4). The most striking evidence for the successful synthesis of nC_{60}-PS_n and mC_{60}-PS comes from the MALDL-TOF mass spectra. As shown in Figure 6.6, only one symmetric molecular weight distribution is displayed and the difference between two neighboring peaks is equivalent to the mass of one styrene repeating unit (104.1 Da). Specifically, a representative peak m/z value of 4085.2Da corresponding to 13-mer of mC_{60}-PS_{13} with a sodium ion agrees well with the calculated mass, which is 4085.6 Da for [13-mer·Na]$^+$. The deprotection of terminated acetonide groups on nC_{60} and mC_{60} was readily achieved in the mixed solvent of CH_2Cl_2 and CF_3COOH (v/v = 4/1), giving rise to the amphiphilic final products HC_{60}-PS_n and DC_{60}-PS_n. The chemical structures of final products are also well characterized by NMR, SEC and MALDL-TOF mass spectra.

Following the similar synthetic procedures of DC_{60}-PS_n, DC_{60}-$2PS_n$ and DC_{60}-$4PS_n$ can be achieved by conjugating the mC_{60}-2alkyne with either PS_n-N_3 or $2PS_n$-N_3, where the samples of $2PS_n$-N_3 with varying molecular length were prepared according to our previous publication.[243] The successful synthesis of DC_{60}-$2PS_n$ and DC_{60}-$4PS_n$ were confirmed from the evidences of SEC and MALDL-TOF mass spectra (Figure 6.7).
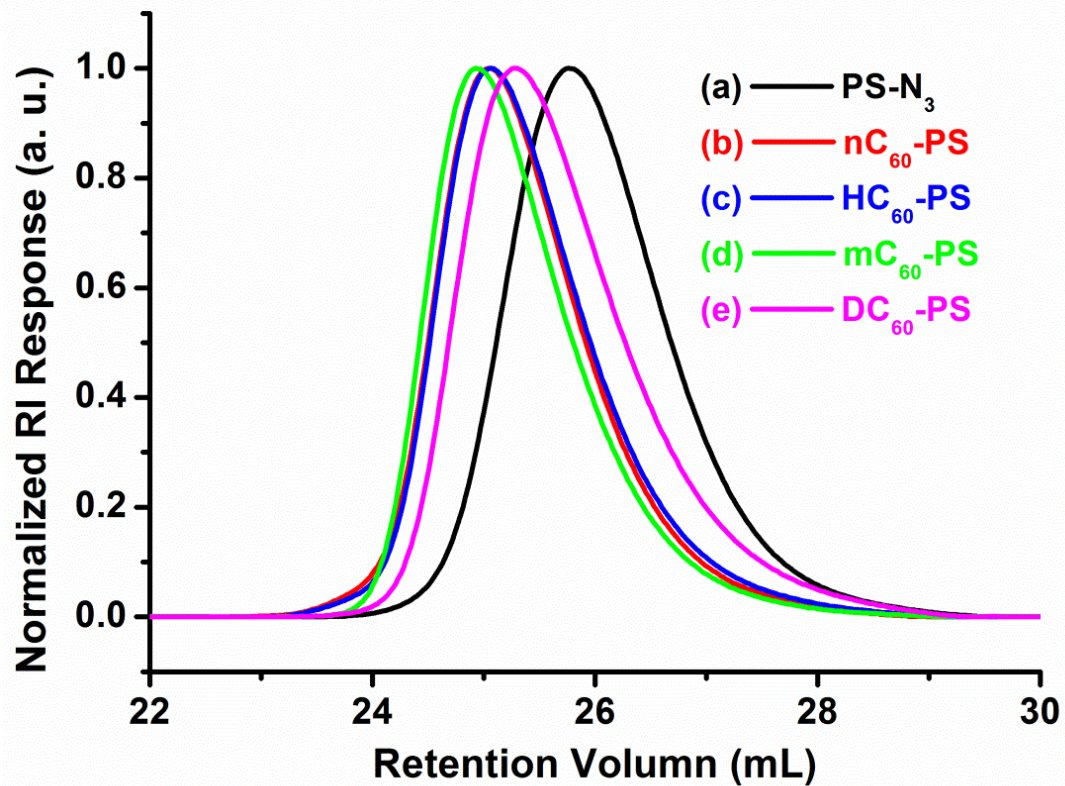
Figure 6.4. SEC overlay of (a) PS_n-N_3 (black curve), (b) nC_{60}-PS_n (red curve), (c) HC_{60}-PS_n (blue curve), (d) mC_{60}-PS_n (green curve) and (e) DC_{60}-PS_n (pink curve).
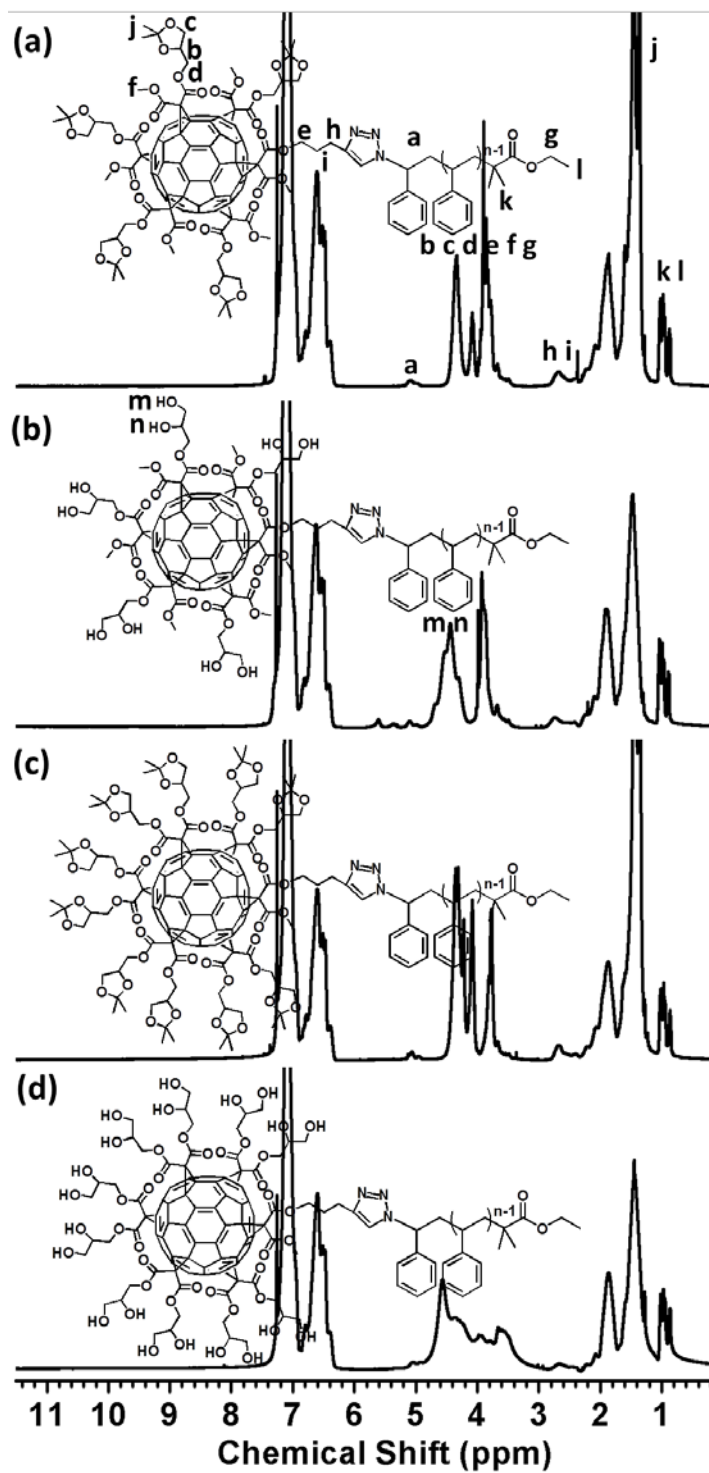
Figure 6.5. ^{1}H NMR spectra of (a) nC$_{60}$-PS$_n$, (b) HC$_{60}$-PS$_n$, (c) mC$_{60}$-PS$_n$ and (d) DC$_{60}$-PS$_n$.
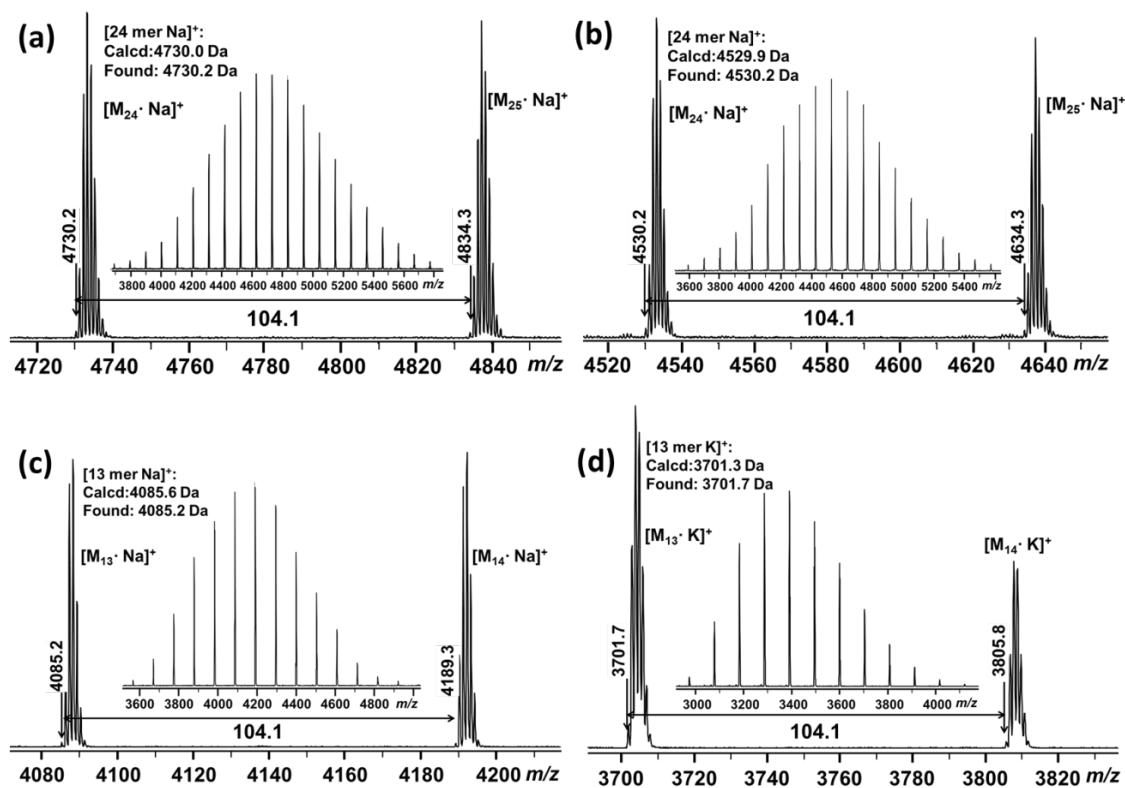
Figure 6.6. MALDI-TOF mass spectra of (a) nC_{60}-PS_n, (b) HC_{60}-PS_n, (c) mC_{60}-PS_n and (d) DC_{60}-PS_n. All these data were acquired with monoisotopic resolution. The insets show the full spectra.
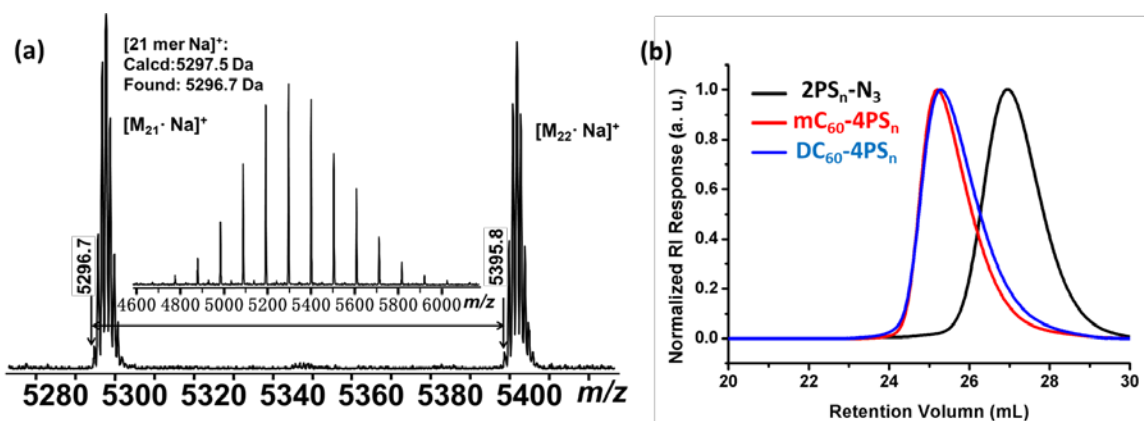
Figure 6.7. (a) MALDI-TOF mass spectra of mC_{60}-$4PS_n$, (b) SEC overlay of $2PS_n$-N_3 (black), mC_{60}-$4PS_n$ (red) and DC_{60}-$4PS_n$ (blue).
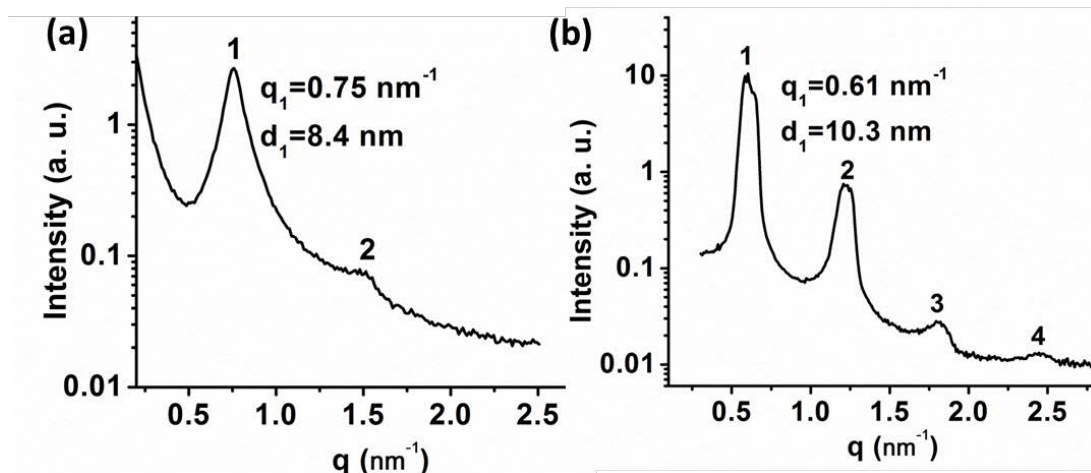
Figure 6.8. SAXS patterns of (a) HC_{60}-PS_{44} and (b) DC_{60}-PS_{44}.

6.3.2 Assembly of Giant surfactants in Bulk State

Figure 6.8 shows the SAXS patterns of HC_{60}-PS_{44} and DC_{60}-PS_{44}. Both samples possess identical molecular length of PS (N = 44), the different is the number of hydroxyl groups on the hydrophilic head. For the HC_{60}, there are ten hydroxyl groups on its periphery, while DC_{60} contains twenty hydroxyl groups. Broad first order with very weak second order scattering peaks are observed from HC_{60}-PS_{40}, indicating the segregation strength between HC_{60} and PS is relatively weak (Figure 6.8 a). When using DC_{60} as hydrophilic head, very sharp scattering peaks appear, where even the fourth ordered peak can be clearly identified (Figure 6.8 b). We have reported that giant surfactants composed of one DPOSS carrying fourteen hydroxyl groups tethered by a PS tail can self-organize into a variety of nano-ordered structures with very sharp interface boundary.[69] These results suggest the number of hydroxyl groups on the hydrophilic head plays a critical role on the phase separation between hydrophilic head and hydrophobic tails, since it is related to immiscibility (χN) of two components. For block copolymers, it has been

193

predicted by the mean field theory that the minimum value of χN to induce the phase

separation in a symmetric Lam is 10.5. It is difficult to quantitatively calculate the χN of

our giant surfactants with varying functionalities. However, based on our experimental

observations, we deduce that to induce a strong phase separation of our PS-based giant

surfactants, the critical number of hydroxyl groups on the hydrophilic heads should be

larger than 10 (e.g. 14 four DPOSS and 20 for DC_{60}). Therefore, DC_{60} will be used as the

major building block in the following section to investigate the influence of molecular

length, architectures and topologies on the assembly behaviors.

To create various nanophase separated structures, a series of DC_{60}-PS_n with

different molecular length were synthesized. The SAXS pattern of DC_{60}-PS_{40} is shown in

Figure 6.9a. Two scattering peaks possess a q-ratio of 1:2, indicating the formation of

Lam where DC_{60} and PS are alternatively arranged in a layer structure with a periodic

domain size of 10.0 nm (calculated via $d = 2\pi/q$, where the first order diffraction peak is

centered at $q = 0.63$ nm^{-1}). TEM results in Figure 6.9b further confirm alternatively

packed lamellar structures, where the dark and grey lines represent the DC_{60} and PS

concentrated domains, respectively. It was found that similar Lam structures were

observed when N equals to 18, 33, 40 and 52 (data not shown here). Hex structure was

observed as increasing N to N = 83, evidenced by the SAXS pattern of DC_{60}-PS_{83} (Figure

6.9c), where four scattering peaks with q-ratios of $1:\sqrt{3}:2:\sqrt{7}$ are clearly identified.

Considering the relatively small volume fraction of DC_{60} (0.14), it is expected that DC_{60}

are wrapped in the columns surrounding with continuous PS matrix in Hex structures.

This is verified by our TEM observation in Figure 6.9d, where the hexagonally packed

dark spots are attributed to the DC_{60}-concentrated columns and the gray domains are

194

associated with PS matrixes. Further increasing N to N = 180 results in the formation of BCC structures, as revealed by the q-ratio of $1:\sqrt{2}:\sqrt{3}$ in the SAXS pattern of DC_{60}-PS_{180} and TEM image with a characteristic square packing of DC_{60} dark spots embracing by PS matrixes (Figure 6.9e and f).
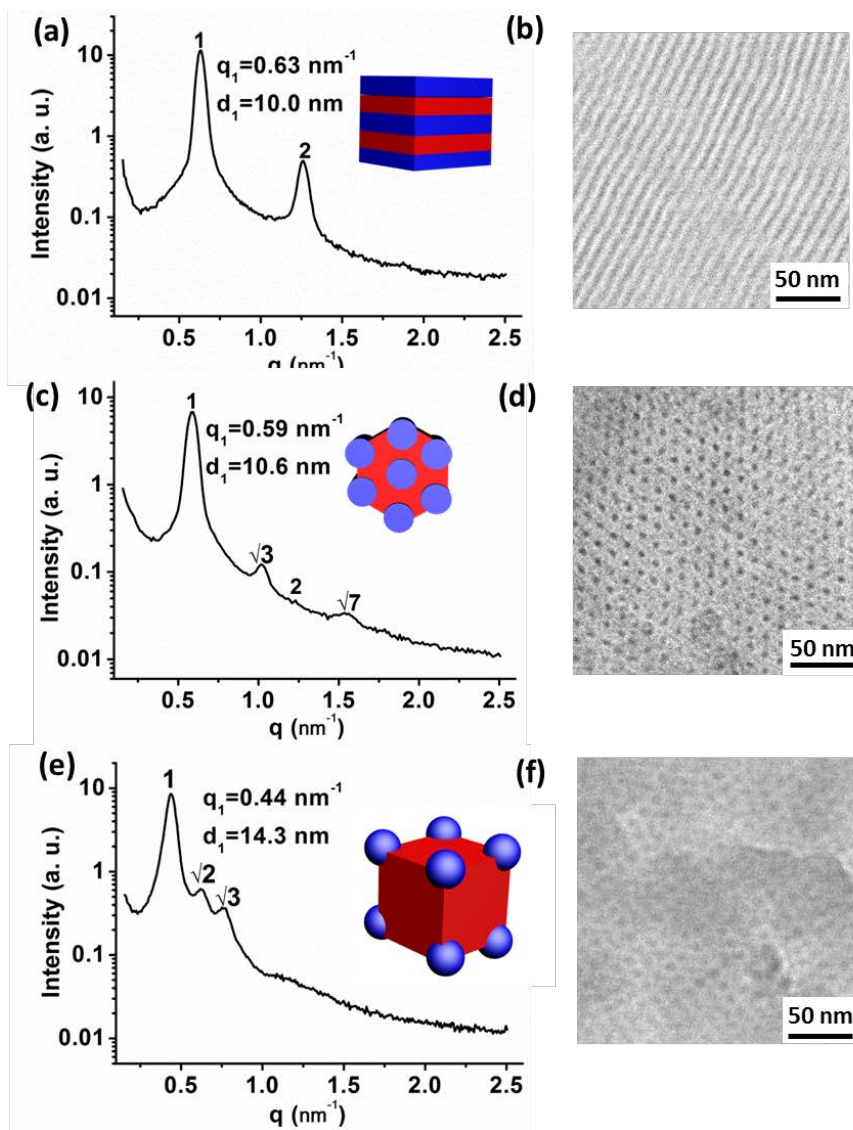
Figure 6.9. SAXS and TEM patterns of (a) and (b) DC_{60}-PS_{40}, (c) and (d) DC_{60}-PS_{80}, and (e) and (f) DC_{60}-PS_{180}. Insets are the cartoon model of corresponding assembled structures.

Tethering four PS tails with identical molecular weight onto one DC_{60} head gives rise to a set of new multi-tailed giant surfactants (DC_{60}-$4PS_n$). With increasing molecular length of PS from N= 6 to N = 43, a series of phase transition from Lam, to Hex and finally to BCC are revealed, as shown in Figure 6.10. Surprisingly, the formation of A15 was clarified between the Hex and BCC, evidencing by three characteristic scattering peaks with q-ratios of $\sqrt{4}$:$\sqrt{5}$:$\sqrt{6}$ (Figure 6.10c). While A15 is commonly observed in metal alloy and were formed by some dendrimers with delicate design of molecular structures,[244-246] few samples have been reported in polymer community. Considering the collective hydrogen bonds among DC_{60} heads, it is suggested that the DC_{60}-PS_{22} molecules are first self-assemble into spherical structures with DC_{60} in the core and PS in the corona. The as-assembled spherical structures further pack into A15 structures, which is similar to our previous reported A15 phase formed by giant tetrahedra.[88] It is worth to note that the domain size of these ordered are all below 8 nm, which is much smaller than those constructed from DC_{60}-PS_n, even though they contain similar overall molecular weight of PS. For example, DC_{60}-$4PS_{45}$ and DC_{60}-PS_{180} possess almost overall identical molecular weight PS and both samples form BCC. However, the domain size of DC_{60}-$4PS_{45}$ is 7.5 nm, in contrast to 14.3 nm of DC_{60}-PS_{180}.
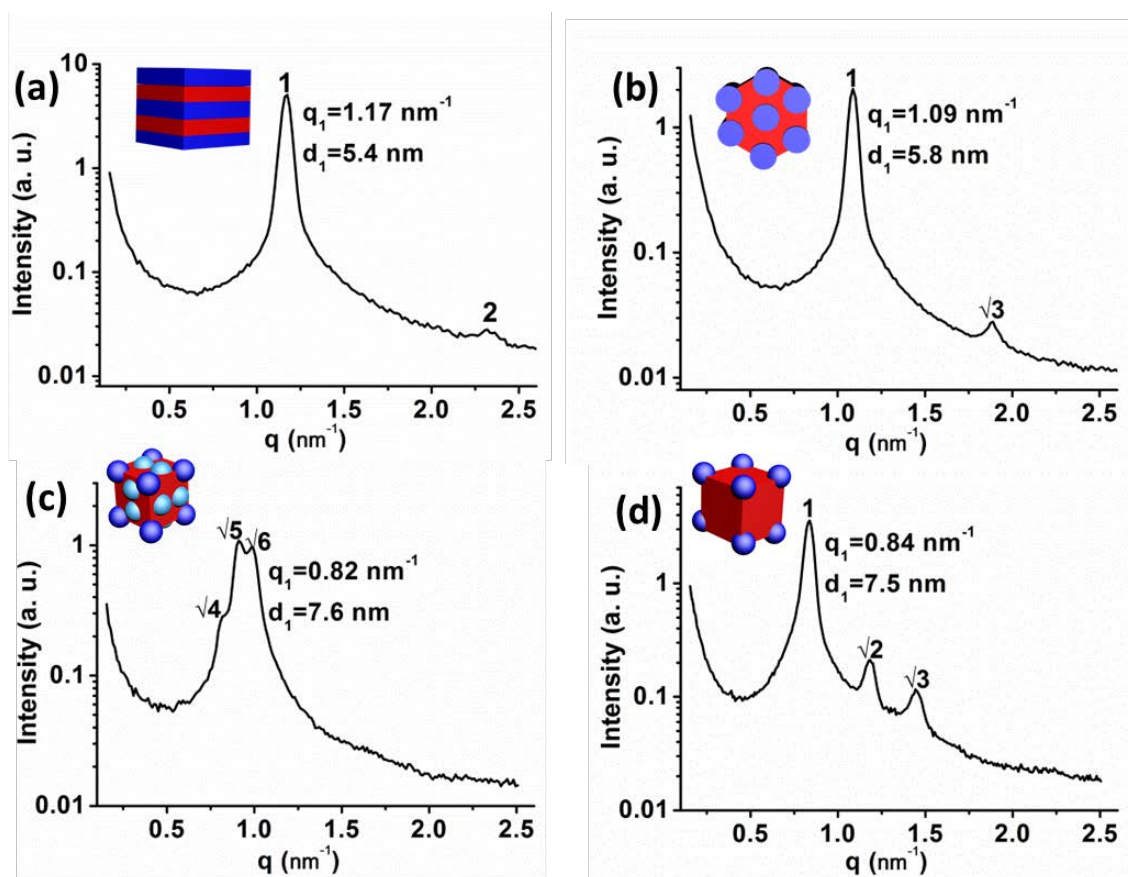
Figure 6.10. SAXS patterns of (a) $DC_{60}\text{-}4PS_6$, (b) $DC_{60}\text{-}4PS_{10}$, (c) $DC_{60}\text{-}4PS_{20}$ and $DC_{60}\text{-}PS_{45}$. Insets are the cartoon models of corresponding assembled structures.

In order to investigate the influence of molecular topologies, a set of topological isomers, composed of identical molecular weight of PS but with different number of tails, were specifically synthesized, namely, $DC_{60}\text{-}PS_{80}$, $DC_{60}\text{-}2PS_{40}$ and $DC_{60}\text{-}4PS_{20}$. Both $DC_{60}\text{-}PS_{80}$ and $DC_{60}\text{-}2PS_{40}$ form Hex structures, evidenced by SAXS in Figure 6.11 a and b. However, the Hex domain size of $DC_{60}\text{-}2PS_{40}$ is about 7.6 nm, which is 3 nm smaller than that of $DC_{60}\text{-}PS_{80}$ (10.6 nm). More interestingly, the A15 phase is generated by $DC_{60}\text{-}4PS_{20}$ (Figure 6.11c), which is replotted from Figure 6.10c in order to make a clear comparison. These results suggest that the phase behaviors of these giant surfactants are

197

sensitive to their topologies, which is rarely observed in traditional block copolymers. This sensitivity can be attributed to the predicted asymmetry at the interface between MNP and polymer tails.[247]
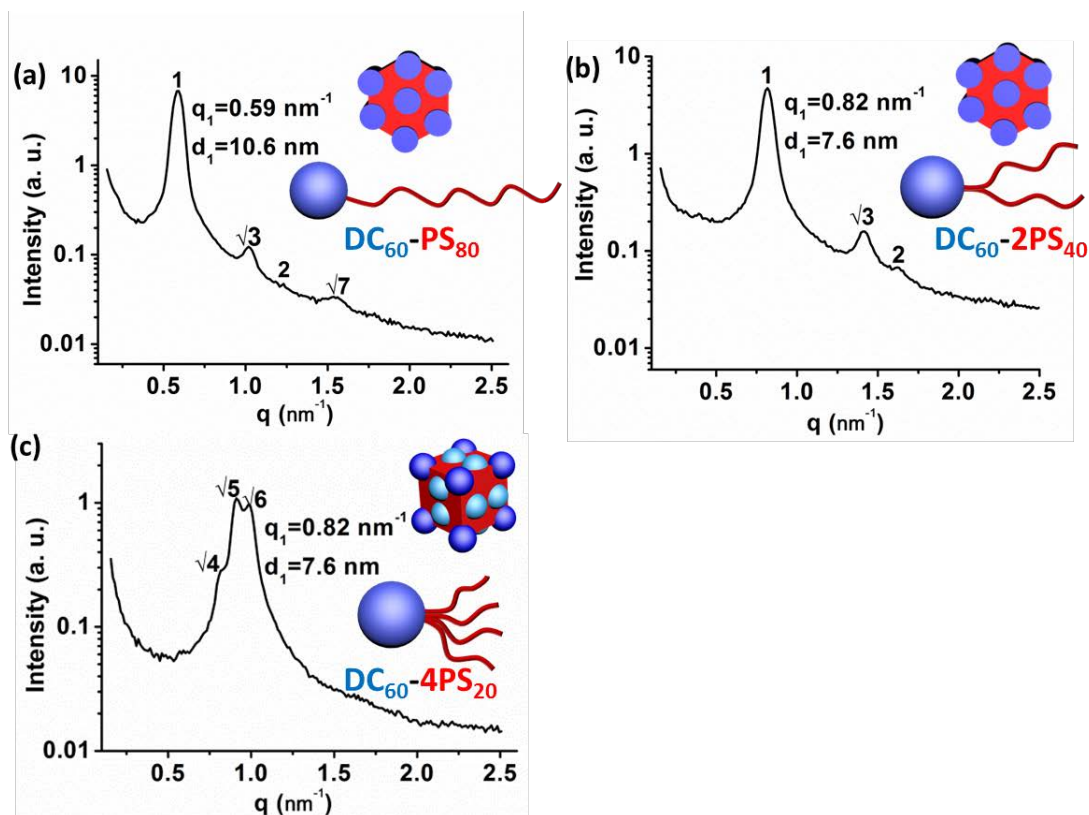
Figure 6.11. SAXS patterns of (a) DC_{60}-PS_{80}, (b) DC_{60}-$2PS_{40}$, (c) DC_{60}-$4PS_{20}$. Insets are the cartoon model of corresponding assembled structures.

6.4 Conclusion

In summary, giant surfactants with ten (HC_{60}) or twenty (DC_{60}) hydroxyl groups functionalized C_{60} head tethered onto PS tails with different architectures are synthesized. Functionalities of C_{60} play a critical role in driving nanophase separation. Compared with HC_{60}, phase separation strength between DC_{60} and PS is much stronger, leading to a

series of nano-ordered structures. Three types of DC_{60}-based giant surfactants with one (DC_{60}-PS_n), two (DC_{60}-$2PS_n$) and four PS (DC_{60}-$4PS_n$) tails were designed to investigate their phase behaviors. With increasing the molecular length of PS, phase transitions from Lam, to Hex and finally to BCC was observed from DC_{60}-PS_n and DC_{60}-$4PS_n$. Impressively, the A15 phase is formed by DC_{60}-$4PS_{20}$ between Hex and BCC, which is scarcely reported in block copolymer systems. The assembled structures of these giant surfactants exhibit significant sensitivity to their molecular topologies. These results prove that it is the immiscibility between functionalized MNP and polymeric tails drive the phase separation, regardless of the nature of MNP. This work not only provides new materials for engineering sub-10 nm nanostructures, but opens a way for seeking for relevant applications.
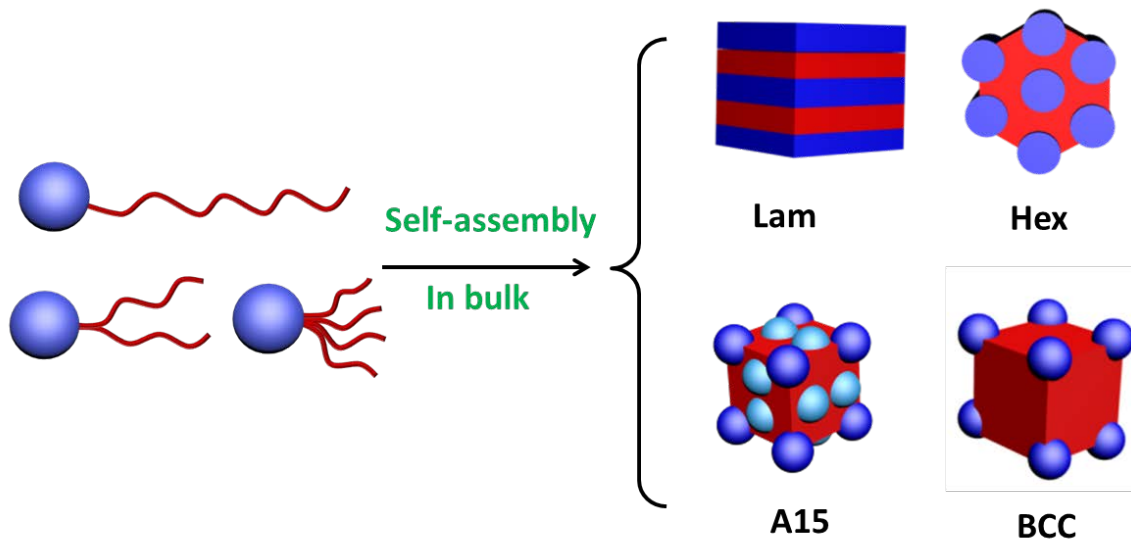
Figure 6.12. General story of Chapter VI.

CHAPTER VII

SUMMARY

In this dissertation, the molecule design, precise synthesis and self-assembly of various giant molecules are exploited. As a part of background introduction related to this research topic, the self-assembly of fundamental building blocks are briefly reviewed. Since these fundamental building blocks are more or less composed of flexible components (such as small molecules or polymers), the importance of shape and anisotropic interactions on self-assembly are generally not taken into account. The studies on recently developed novel building blocks with persistent volume and shape as well as isotropic interactions reveal that they are also key parameters in determining the self-assembly behaviors and the formation of nanostructures. The emergence of giant molecules provides excellent prototypes for studying such building blocks. Molecular design of giant molecules as well as several reported giant molecules and their self-assembly behaviors are also discussed in Chapter II. Analogous to small molecules but with amplified size, giant molecules discussed in this dissertation are referred to thosemolecules built upon from molecular nanoparticles (MNP)-based nanoatoms, which typically include POSS, C_{60}, POM and globular proteins. There are three typical categories of giant molecules, giant surfactants, giant shape amphiphiles and giant polyhedras. Computational studies have given us sufficient insights in understanding the

self-assembly of various giant molecules. However, experimental investigations are considerably preliminary. Aiming at experimentally studying giant molecules, various giant molecules based on C_{60} are synthesized and their diverse self-assembly behaviors are systematically explored.

In the Chapter III, two C_{60}-based molecular Janus particles with precisely-defined structures were synthesized. They are conjugates of one carboxyl-acid functionalized C_{60} (AC_{60}) with one (AC_{60}-C_{60}) or two (AC_{60}-$2C_{60}$) hydrophobic C_{60}. Their self-assembly in different solvents were investigated. Interdigitated and bilayered vesicles are formed by AC_{60}-C_{60} and AC_{60}-$2C_{60}$ in THF, respectively, while in DMF/water, the formation of spheres and cylinders was observed. The morphological transitions induced by molecular architectures and solvent polarity can be attributed to the variation of packing parameters (P). The calculated P of Janus particles to form vesicles, cylinders and spheres are $P>1/2$, $1/2>P>1/3$ and $P<1/3$, respectively, agreeing well with the theoretical prediction. This work provide a new strategy for designing molecular Janus grains, and open a gate for studying the nanobuilding blocks with persistent shape and anisotropic interactions.

Our subsequent study focused on the synthesis and assembly investigation on C_{60}-based giant surfactants. The first example we demonstrate is about "nano-diamond-ring-like" giant surfactants consisting of an AC_{60} and a cyclic polystyrene (CPS) tail. Starting from a linear PS, a CPS installing an azide group (CPS-N_3) was first synthesized by combining the CuAAC and thiol-ene "click" reaction. This CPS-N_3 was then applied as a versatile building block to further attach onto not only C_{60}-based but other MNP such as POSS by sequential click chemistry. This synthetic route is designed based on several types of click reactions, illustrating the highly efficient and modular features. These CPS-

based giant surfactants possess unique structural features other than our previously reported linear analogs.

Moreover, a series of giant surfactants deriving from AC_{60} tethered by a PS-*b*-PEO block copolymer were developed. To demonstrate the importance of molecular architectures, the AC_{60} specifically are located at three different positions, at terminal of either PS or PEO, or even at the junction point between PS and PEO. Physical characterization of these giant surfactants in condensed state reveal that the incorporation of AC_{60} MNP induces the nano-phase separation of intrinsically disordered PS-*b*-PEO with molecular masses as low as 4.8 kg/mol. A variety of ordered nanostructures were created including Lam, DG, and Hex with domain sizer below 10 nm. The different architectures of these giant surfactants provided evidences of how the MNPs are located and distributed within the nano-phase separated structures, and in turn, demonstrated significant effects of these MNPs on the stabilization of these originally unstable structures.

Finally, we extend our topic to study the influence of head functionalities and molecular topologies on assembled structures of giant surfactants. C_{60} bearing ten (HC_{60}) or twenty (DC_{60}) hydroxyl groups are used as heads, onto which one, two or four PS tails are tethered, giving rise to three major types of giant surfactants. It was found that compared with HC_{60}, DC_{60} possesses much stronger segregation strength with PS, inducing a strong phase separation between hydrophilic C_{60} domain and hydrophobic PS domain. As a result, well-ordered nanostructures (such as Lam, Hex, A15 and BCC) were observed from assembly of DC_{60}-based giant surfactants. Study on three topological isomers containing overall identical molecular weight but different topologies (e.g.DC_{60}-

PS$_{80}$, DC$_{60}$-2PS$_{40}$, and DC$_{60}$-4PS$_{20}$) reveals that the assembled structures of giant surfactants are not only dependent on their composition and volume fraction, but sensitive to their molecular topologies.

Research work enclosing in this dissertation is going near its end. Yet, the story is far away from the end. A few thoughts and possible further exploration related to the current research are thus put forward here:

(i) For molecular Janus particles, our previous or current researches are all based on amphiphilic prototypes. The essential rule for building up Janus particles is breaking symmetry. To break the symmetry, it is not necessary to base on amphiphilic interactions. For example, a zwitterionic Janus particle can be realized by conjugating one positively charged MNP with one negatively charged MNP. This zwitterionic Janus particle is expected to exhibit significantly different self-assembly behaviors from those of amphiphilic one. Moreover, if zwitterionic Janus particles are further used as heads of giant surfactants, the study on assembly of resultant zwitterionic giant surfactants will be also very interesting, since they are expected to demonstrate pH-responsive properties.

(ii) In the current molecular design of giant surfactants, we are focusing on the systems with flexible tails (such as PS and PS-*b*-PEO). It would be a desirable direction by replacing the flexible polymers with rigid polymers (such as conjugated polymers). For one thing, rigid polymers possess completely distinct molecular conformations from flexible polymers. The influence of molecular conformation on self-assembly is largely unexplored. The self-

203

assembly of current giant surfactants with flexible tails are mainly dominated by enthalpy. The involvement of rigid polymers in giant surfactants will heighten the importance of entropic contribution. This may lead to the distinct self-assembly behaviors compared with flexible polymer based giant molecules. On the other hand, if the conjugated polymers, which are usually used as p-type materials, are introduced into giant molecules and induced to self-organize into well-ordered structures with domain size below 10 nm. The resulting assembled structures will be promising heterojunction structures and may have potential applications in devices and solar cells.

(iii) Our previous studies on giant shape amphiphiles are concentrating on their anisotropic shape and more or less ignoring their anisotropic interaction (such as C_{60}-POSS, C_{60}-porphyrin). It would further break symmetry if hydrophilic nanobuilding blocks (such as AC_{60} or DC_{60}, DPOSS or APOSS) can be involved in shape amphiphiles. Nanobuilding blocks with more diversified shapes (such as triangles and rods) are also deserved to be tried. The combination of anisotropic shape and anisotropic interaction would result in the discovery of unconventional assembled structures beyond those from existing systems. More importantly, the study on these giant shape amphiphiles may open a new door for numerous related topics.

REFERENCES

1.   Whitesides, G. M.; Boncheva, M. *Proc. Natl. Acad. Sci. U.S.A.* **2002**, *99*, 4769-4774.

2.   Whitesides, G. M.; Grzybowski, B. *Science* **2002**, *295*, 2418-2421.

3.   Glotzer, S. C. *Science* **2004**, *306*, 419-420.

4.   Elghanian, R.; Storhoff, J. J.; Mucic, R. C.; Letsinger, R. L.; Mirkin, C. A. *Science* **1997**, *277*, 1078-1081.

5.   Antonietti, M.; Göltner, C. *Angew. Chem. Int. Ed.* **1997**, *36*, 910-928.

6.   Colvin, V. L.; Schlamp, M. C.; Alivisatos, A. P. *Nature* **1994**, *370*, 354-357.

7.   Reetz, M. T.; Winter, M.; Dumpich, G.; Lohau, J.; Friedrichowski, S. *J. Am. Chem. Soc.* **1997**, *119*, 4539-4540.

8.   Son, S. U.; Jang, Y.; Park, J.; Na, H. B.; Park, H. M.; Yun, H. J.; Lee, J.; Hyeon, T. *J. Am. Chem. Soc.* **2004**, *126*, 5026-5027.

9.   Nagy, A.; Mestl, G. *Appl. Catal. A* **1999**, *188*, 337-353.

10.   Hashmi, A. S. K. *Chem. Rev.* **2007**, *107*, 3180-3211.

11.   Aiken, J. D.; Finke, R. G. *J Mol. Catal. A* **1999**, *145*, 1-44.

12.   Xia, Y. N.; Xiong, Y. J.; Lim, B.; Skrabalak, S. E. *Angew. Chem. Int. Ed.* **2009**, *48*, 60-103.

13.   Frank, F. C.; Kasper, J. S. *Acta Cryst.* **1958**, *11*, 184-190.

14.   Frank, F. C.; Kasper, J. S. *Acta Cryst.* **1959**, *12*, 483-499

.15.   Xie, N.; Li, W. H.; Qiu, F.; Shi, A.-C. *ACS Macro Lett.* **2014**, *3*, 906-910.

16.   Holmberg, K.; Jönsson, B.; Kronberg, B.; Lindman, B. *Surfactants and Polymers in Aqueous Solution*; 2nd ed.; John Wiley & Sons Ltd.: Chichester, 2003.

17.   Israelachvili, J. N. *Intermolecular and Surface Forces*; 3rd ed.; Academic Press: Burlington, 2011.

18.   Lodge, T. P. *Macromol. Chem. Phys.* **2003**, *204*, 265-273.

19.   Zhang, L. F.; Eisenberg, A. *Polym. Adv. Technol.* **1998**, *9*, 677-699.

20.   Zhang, L. F.; Eisenberg, A. *Science* **1995**, *268*, 1728-1731.

21.   Bates, F. S.; Fredrickson, G. H. *Annu. Rev. Phys. Chem.* **1990**, *41*, 525-557.

22.   Khandpur, A. K.; Förster, S.; Bates, F. S.; Hamley, I. W.; Ryan, A. J.; Bras, W.; Almdal, K.; Mortensen, K. *Macromolecules* **1995**, *28*, 8796-8806.

23.   Bates, F. S.; Fredrickson, G. H. *Phys. Today* **1999**, *52*, 32-38.

24.   Sacanna, S.; Irvine, W. T. M.; Chaikin, P. M.; Pine, D. J. *Nature* **2010**, *464*, 575-578.

25.   Chen, Q.; Bae, S. C.; Granick, S. *Nature* **2011**, *469*, 381-384.

26.   Glotzer, S. C.; Solomon, M. J. *Nat. Mater.* **2007**, *6*, 557-562.

27.   Zhang, Z. L.; Horsch, M. A.; Lamm, M. H.; Glotzer, S. C. *Nano Lett.* **2003**, *3*, 1341-1346.

28.   Zhang, Z. L.; Glotzer, S. C. *Nano Lett.* **2004**, *4*, 1407-1413.

29.   Zhang, Z. L.; Keys, A. S.; Chen, T.; Glotzer, S. C. *Langmuir* **2005**, *21*, 11547-11551.

30.   Jankowski, E.; Glotzer, S. C. *J. Phys. Chem. B* **2011**, *115*, 14321-14326.

31.   Glotzer, S. C.; Horsch, M. A.; Iacovella, C. R.; Zhang, Z. L.; Chan, E. R.; Zhang, X. *Curr. Opin. Colloid Interface Sci.* **2005**, *10*, 287-295.

32.   Gratzer, W. B. *Giant Molecules: From Nylon to Nanotubes*; Oxford University Press: New York, 2009.

33.   Grosberg, A. I. U.; Khokhlov, A. R.; de Gennes, P.-G. *Giant Molecules: Here, There, and Everywhere*; 2nd ed.; World Scientific: Hackensack, NJ, 2011.

34.   Liu, T. *J. Am. Chem. Soc.* **2002**, *124*, 10942-10943.

35.   Robinson, I. *Nat. Mater.* **2008**, *7*, 275-276.

36.   Zhang, W.-B.; Yu, X.; Wang, C.-L.; Sun, H.-J.; Hsieh, I. F.; Li, Y.; Dong, X.-H.; Yue, K.; Van Horn, R.; Cheng, S. Z. D. *Macromolecules* **2014**, *47*, 1221-1239.

37.   Cordes, D. B.; Lickiss, P. D.; Rataboul, F. *Chem. Rev.* **2010**, *110*, 2081-2173.

38.   Song, Y. F.; Tsunashima, R. *Chem. Soc. Rev.* **2012**, *41*, 7384-7402.

39.   Pedelacq, J. D.; Cabantous, S.; Tran, T.; Terwilliger, T. C.; Waldo, G. S. *Nat. Biotechnol.* **2006**, *24*, 1170-1170.

40.   Link, A. J.; Mock, M. L.; Tirrell, D. A. *Curr. Opin. Biotech.* **2003**, *14*, 603-609.

41.   Bühl, M.; Hirsch, A. *Chem. Rev.* **2001**, *101*, 1153-1183.

42.   Kroto, H. W.; Heath, J. R.; Obrien, S. C.; Curl, R. F.; Smalley, R. E. *Nature* **1985**, *318*, 162-163.

43.   Kratschmer, W.; Lamb, L. D.; Fostiropoulos, K.; Huffman, D. R. *Nature* **1990**, *347*, 354-358.

44.   Guldi, D. M.; Illescas, B. M.; Atienza, C. M.; Wielopolskia, M.; Martín, N. *Chem. Soc. Rev.* **2009**, *38*, 1587-1597.

45.   Dresselhaus, M. S.; Dresselhaus, M.; Eklund, P. C. *Science of Fullerenes and Carbon Nanotubs*; Academic Press: San Diego, CA, 1996.

46.   Prato, M. *J. Mater. Chem.* **1997**, *7*, 1097-1109.

47.   He, P. M.; Xu, Y. B.; Zhang, X. J.; Zhen, X. B.; Li, W. Z. *J. Phys.Condens. Matter* **1993**, *5*, 7013-7016.

48.	Wen, C.; Li, J.; Kitazawa, K.; Aida, T.; Honma, I.; Komiyama, H.; Yamada, K. *Appl. Phys. Lett.* **1992**, *61*, 2162-2163.

49.	Martín, N.; Sánchez, L.; Illescas, B.; Pérez, I. *Chem. Rev.* **1998**, *98*, 2527-2547.

50.	Roncali, J. *Chem. Soc. Rev.* **2005**, *34*, 483-495.

51.	Dresselhaus, M. S.; Dresselhaus, G.; Rao, A. M.; Eklund, P. C. *Synthetic Met.* **1996**, *78*, 313-325.

52.	Ching, W. Y.; Huang, M. Z.; Xu, Y. N.; Harter, W. G.; Chan, F. T. *Phys. Rev. Lett.* **1991**, *67*, 2045-2048.

53.	Fowler, P. W.; Lazzeretti, P.; Malagoli, M.; Zanasi, R. *Chem. Phys. Lett.* **1991**, *179*, 174-180.

54.	Haddon, R. C.; Schneemeyer, L. F.; Waszczak, J. V.; Glarum, S. H.; Tycko, R.; Dabbagh, G.; Kortan, A. R.; Muller, A. J.; Mujsce, A. M.; Rosseinsky, M. J.; Zahurak, S. M.; Makhija, A. V.; Thiel, F. A.; Raghavachari, K.; Cockayne, E.; Elser, V. *Nature* **1991**, *350*, 46-47.

55.	Nakamura, E.; Isobe, H. *Acc. Chem. Res.* **2003**, *36*, 807-815.

56.	Jensen, A. W.; Wilson, S. R.; Schuster, D. I. *Bioorgan. Med. Chem.* **1996**, *4*, 767-779.

57.	Bosi, S.; Da Ros, T.; Spalluto, G.; Prato, M. *Eur. J. Med. Chem.* **2003**, *38*, 913-923.

58.	López, A. M.; Mateo-Alonso, A.; Prato, M. *J. Mater. Chem.* **2011**, *21*, 1305-1318.

59.	Hirsch, A.; Vostrowsky, O. *Eur. J. Org. Chem.* **2001**, 829-848.

60.	Kolb, H. C.; Finn, M. G.; Sharpless, K. B. *Angew. Chem. Int. Ed.* **2001**, *40*, 2004-2021.

61.	Rostovtsev, V. V.; Green, L. G.; Fokin, V. V.; Sharpless, K. B. *Angew. Chem. Int. Ed.* **2002**, *41*, 2596-2099.

62.   Agard, N. J.; Prescher, J. A.; Bertozzi, C. R. *J. Am. Chem. Soc.* **2005**, *127*, 11196-11196.

63.   Hoyle, C. E.; Bowman, C. N. *Angew. Chem. Int. Ed.* **2010**, *49*, 1540-1573.

64.   Kade, M. J.; Burke, D. J.; Hawker, C. J. *J. Polym. Sci. Polym. Chem.* **2010**, *48*, 743-750.

65.   Ulrich, S.; Boturyn, D.; Marra, A.; Renaudet, O.; Dumy, P. *Chem. Eur. J.* **2014**, *20*, 34-41.

66.   Tasdelen, M. A. *Polym. Chem.* **2011**, *2*, 2133-2145.

67.   Yu, X.; Zhong, S.; Li, X.; Tu, Y.; Yang, S.; Van Horn, R. M.; Ni, C.; Pochan, D. J.; Quirk, R. P.; Wesdemiotis, C.; Zhang, W.-B.; Cheng, S. Z. D. *J. Am. Chem. Soc.* **2010**, *132*, 16741-16744.

68.   Yu, X.; Zhang, W.-B.; Yue, K.; Li, X.; Liu, H.; Xin, Y.; Wang, C.-L.; Wesdemiotis, C.; Cheng, S. Z. D. *J. Am. Chem. Soc.* **2012**, *134*, 7780-7787.

69.   Yu, X.; Yue, K.; Hsieh, I.-F.; Li, Y.; Dong, X.-H.; Liu, C.; Xin, Y.; Wang, H.-F.; Shi, A.-C.; Newkome, G. R.; Ho, R.-M.; Chen, E.-Q.; Zhang, W.-B.; Cheng, S. Z. D. *Proc. Natl. Acad. Sci. U.S.A.* **2013**, *110*, 10078-10083.

70.   Israelachvili, J. N.; Mitchell, D. J.; Ninham, B. W. *J. Chem. Soc., Faraday Trans.* **1976**, *72*, 1525-1568.

71.   Yue, K.; Liu, C.; Guo, K.; Yu, X.; Huang, M.; Li, Y.; Wesdemiotis, C.; Cheng, S. Z. D.; Zhang, W.-B. *Macromolecules* **2012**, *45*, 8126-8134.

72.   Date, R. W.; Bruce, D. W. *J. Am. Chem. Soc.* **2003**, *125*, 9012-9013.

73.   Horsch, M. A.; Zhang, Z.; Glotzer, S. C. *Nano Lett.* **2006**, *6*, 2406-2413.

74.   Iacovella, C. R.; Glotzer, S. C. *Nano Lett.* **2009**, *9*, 1206-1211.

75.   Horsch, M. A.; Zhang, Z. L.; Glotzer, S. C. *Phys. Rev. Lett.* **2005**, *95*.

76.   Iacovella, C. R.; Glotzer, S. C. *Soft Matter* **2009**, *5*, 4492-4498.

77. Wang, C.-L.; Zhang, W.; Yu, X.; Yue, K.; Sun, H.-J.; Hsu, C.-H.; Hsu, C.-S.; Joseph, J.; Modarelli, D. A.; Cheng, S. Z. D. *Chem. Asian J.* **2013**, *8*, 947-955.

78. Wang, C.-L.; Zhang, W.; Sun, H.-J.; Van Horn, R. M.; Kulkarni, R. R.; Tsai, C.-C.; Hsu, C.-S.; Lotz, B.; Gong, X.; Cheng, S. Z. D. *Adv. Energy Mater.* **2012**, *2*, 1375-1382.

79. Sun, H.-J.; Tu, Y.; Wang, C.-L.; Van Horn, R. M.; Tsai, C. C.; Graham, M. J.; Sun, B.; Lotz, B.; Zhang, W.-B.; Cheng, S. Z. D. *J. Mater. Chem.* **2011**, *21*, 14240-14247.

80. Liu, H.; Hsu, C.-H.; Lin, Z.; Shan, W.; Wang, J.; Jiang, J.; Huang, M.; Lotz, B.; Yu, X.; Zhang, W.-B.; Yue, K.; Cheng, S. Z. D. *J. Am. Chem. Soc.* **2014**, *136*, 10691-10699.

81. Teng, F.; Cao, Y.; Qi, Y.; Huang, M.; Han, Z.; Cheng, S. Z. D.; Zhang, W.-B.; Li, H. *Chem. Asian J.* **2013**, *8*, 1223-1231.

82. Cui, L.; Collet, J. P.; Xu, G. Q.; Zhu, L. *Chem. Mater.* **2006**, *18*, 3503-3512.

83. Baffreau, J.; Ordronneau, L.; Leroy-Lhez, S.; Hudhomme, P. *J. Org. Chem.* **2008**, *73*, 6142-6147.

84. Ren, X.; Sun, B.; Tsai, C.-C.; Tu, Y.; Leng, S. W.; Li, K.; Kang, Z.; Van Horn, R. M.; Li, X.; Zhu, M.; Wesdemiotis, C.; Zhang, W.-B.; Cheng, S. Z. D. *J. Phys. Chem. B* **2010**, *114*, 4802-4810.

85. Araki, H.; Naka, K. *J. Polym. Sci. Polym. Chem.* **2012**, *50*, 4170-4181.

86. Wang, C.-L.; Zhang, W.-B.; Van Horn, R. M.; Tu, Y.; Gong, X.; Cheng, S. Z. D.; Sun, Y. M.; Tong, M. H.; Seo, J.; Hsu, B. B. Y.; Heeger, A. J. *Adv. Mater.* **2011**, *23*, 2951-2956.

87. Damasceno, P. F.; Engel, M.; Glotzer, S. C. *Science* **2012**, *337*, 453-457.

88. Huang, M.; Hsu, C.-H.; Wang, J.; Mei, S.; Dong, X.-H.; Li, Y.; Li, M.; Liu, H.; Zhang, W.; Aida, T. Z.; Zhang, W.-B.; Yue, K.; Cheng, S. Z. D. *Science* **2015**, *348*, 424-428.

89. Degennes, P. G. *Angew. Chem. Int. Ed.* **1992**, *31*, 842-845.

90. Granick, S.; Jiang, S.; Chen, Q. *Phys. Today* **2009**, *62*, 68-69.

91. Walther, A.; Muller, A. H. E. *Soft Matter* **2008**, *4*, 663-668.

92. Lattuada, M.; Hatton, T. A. *Nano Today* **2011**, *6*, 286-308.

93. Dendukuri, D.; Pregibon, D. C.; Collins, J.; Hatton, T. A.; Doyle, P. S. *Nat. Mater.* **2006**, *5*, 365-369.

94. Nie, Z. H.; Li, W.; Seo, M.; Xu, S. Q.; Kumacheva, E. *J. Am. Chem. Soc.* **2006**, *128*, 9408-9412.

95. Nisisako, T.; Torii, T.; Takahashi, T.; Takizawa, Y. *Adv. Mater.* **2006**, *18*, 1152-1156.

96. Yu, H.; Chen, M.; Rice, P. M.; Wang, S. X.; White, R. L.; Sun, S. H. *Nano Lett.* **2005**, *5*, 379-382.

97. Percec, V.; Imam, M. R.; Bera, T. K.; Balagurusamy, V. S. K.; Peterca, M.; Heiney, P. A. *Angew. Chem. Int. Ed.* **2005**, *44*, 4739-4745.

98. Percec, V.; Wilson, D. A.; Leowanawat, P.; Wilson, C. J.; Hughes, A. D.; Kaucher, M. S.; Hammer, D. A.; Levine, D. H.; Kim, A. J.; Bates, F. S.; Davis, K. P.; Lodge, T. P.; Klein, M. L.; DeVane, R. H.; Aqad, E.; Rosen, B. M.; Argintaru, A. O.; Sienkowska, M. J.; Rissanen, K.; Nummelin, S.; Ropponen, J. *Science* **2010**, *328*, 1009-1014.

99. Yang, M.; Wang, W.; Yuan, F.; Zhang, X. W.; Li, J. Y.; Liang, F. X.; He, B. L.; Minch, B.; Wegner, G. *J. Am. Chem. Soc.* **2005**, *127*, 15107-15111.

100. Cheng, L.; Hou, G. L.; Miao, J. J.; Chen, D. Y.; Jiang, M.; Zhu, L. *Macromolecules* **2008**, *41*, 8159-8166.

101. Cheng, L.; Zhang, G. Z.; Zhu, L.; Chen, D. Y.; Jiang, M. *Angew. Chem. Int. Ed.* **2008**, *47*, 10171-10174.

102. Nie, L.; Liu, S. Y.; Shen, W. M.; Chen, D. Y.; Jiang, M. *Angew. Chem. Int. Ed.* **2007**, *46*, 6321-6324.

103. Cheng, G. L.; Boker, A.; Zhang, M. F.; Krausch, G.; Muller, A. H. E. *Macromolecules* **2001**, *34*, 6883-6888.

104.   Zhang, M. F.; Muller, A. H. E. *J. Polym. Sci. Polym. Chem.* **2005**, *43*, 3461-3481.

105.   Li, Y. W.; Zhang, W. B.; Hsieh, I. F.; Zhang, G. L.; Cao, Y.; Li, X. P.; Wesdemiotis, C.; Lotz, B.; Xiong, H. M.; Cheng, S. Z. D. *J. Am. Chem. Soc.* **2011**, *133*, 10712-10715.

106.   Hu, M. B.; Hou, Z. Y.; Hao, W. Q.; Xiao, Y.; Yu, W.; Ma, C.; Ren, L. J.; Zheng, P.; Wang, W. *Langmuir* **2013**, *29*, 5714-5722.

107.   Grzelczak, M.; Vermant, J.; Furst, E. M.; Liz-Marzan, L. M. *ACS Nano* **2010**, *4*, 3591-3605.

108.   Hirsch, A. *The Chemistry of the Fullerenes*; Wiley-VCH Verlag GmbH: 1994; p I-XI.

109.   Brettreich, M.; Burghardt, S.; Bottcher, C.; Bayerl, T.; Bayerl, S.; Hirsch, A. *Angew. Chem. Int. Ed.* **2000**, *39*, 1845-1848.

110.   Burghardt, S.; Hirsch, A.; Schade, B.; Ludwig, K.; Bottcher, C. *Angew. Chem. Int. Ed.* **2005**, *44*, 2976-2979.

111.   Charvet, R.; Jiang, D. L.; Aida, T. *Chem. Commun.* **2004**, 2664-2665.

112.   Guldi, D. M.; Zerbetto, F.; Georgakilas, V.; Prato, M. *Acc. Chem. Res.* **2005**, *38*, 38-43.

113.   Homma, T.; Harano, K.; Isobe, H.; Nakamura, E. *Angew. Chem. Int. Ed.* **2010**, *49*, 1665-1668.

114.   Homma, T.; Harano, K.; Isobe, H.; Nakamura, E. *J. Am. Chem. Soc.* **2011**, *133*, 6364-6370.

115.   Zhou, S. Q.; Burger, C.; Chu, B.; Sawamura, M.; Nagahama, N.; Toganoh, M.; Hackler, U. E.; Isobe, H.; Nakamura, E. *Science* **2001**, *291*, 1944-1947.

116.   Wang, Z.; Li, Y. W.; Dong, X. H.; Yu, X. F.; Guo, K.; Su, H.; Yue, K.; Wesdemiotis, C.; Cheng, S. Z. D.; Zhang, W. B. *Chem. Sci.* **2013**, *4*, 1345-1352.

117.   Bingel, C. *Chem. Ber.* **1993**, *126*, 1957-1959.

118. Hirsch, A.; Lamparth, I.; Grosser, T.; Karfunkel, H. R. *J. Am. Chem. Soc.* **1994**, *116*, 9385-9386.

119. Hirsch, A.; Lamparth, I.; Karfunkel, H. R. *Angew. Chem. Int. Ed.* **1994**, *33*, 437-438.

120. Cassell, A. M.; Asplund, C. L.; Tour, J. M. *Angew. Chem. Int. Ed.* **1999**, *38*, 2403-2405.

121. Munoz, A.; Illescas, B. M.; Sanchez-Navarro, M.; Rojo, J.; Martin, N. *J. Am. Chem. Soc.* **2011**, *133*, 16758-16761.

122. Israelachvili, J. N. *Intermolecular and Surface Forces: revised third edition*; Academic press: 2011.

123. Lamparth, I.; Maichlemossmer, C.; Hirsch, A. *Angew. Chem. Int. Ed.* **1995**, *34*, 1607-1609.

124. Whitesides, G. M.; Mathias, J. P.; Seto, C. T. *Science* **1991**, *254*, 1312-1319.

125. Boal, A. K.; Ilhan, F.; DeRouchey, J. E.; Thurn-Albrecht, T.; Russell, T. P.; Rotello, V. M. *Nature* **2000**, *404*, 746-748.

126. Leininger, S.; Olenyuk, B.; Stang, P. J. *Chem. Rev.* **2000**, *100*, 853-907.

127. Philp, D.; Stoddart, J. F. *Angew. Chem. Int. Ed.* **1996**, *35*, 1155-1196.

128. Cui, H.; Chen, Z.; Zhong, S.; Wooley, K. L.; Pochan, D. J. *Science* **2007**, *317*, 647-650.

129. Gröschel, A. H.; Schacher, F. H.; Schmalz, H.; Borisov, O. V.; Zhulina, E. B.; Walther, A.; Müller, A. H. E. *Nat. Commun.* **2012**, *3*, 710.

130. Park, S.; Lim, J. H.; Chung, S. W.; Mirkin, C. A. *Science* **2004**, *303*, 348-351.

131. Iha, R. K.; Wooley, K. L.; Nystrom, A. M.; Burke, D. J.; Kade, M. J.; Hawker, C. J. *Chem. Rev.* **2009**, *109*, 5620-5686.

132. Hoyle, C. E.; Lowe, A. B.; Bowman, C. N. *Chem. Soc. Rev.* **2010**, *39*, 1355-1387.

133. Xi, W.; Scott, T. F.; Kloxin, C. J.; Bowman, C. N. *Adv. Funct. Mater.* **2014**, *24*, 2572-2590.

134. Kade, M. J.; Burke, D. J.; Hawker, C. J. *J. Polym. Sci., Part A: Polym. Chem.* **2010**, *48*, 743-750.

135. Barner-Kowollik, C.; Du Prez, F. E.; Espeel, P.; Hawker, C. J.; Junkers, T.; Schlaad, H.; Van Camp, W. *Angew. Chem. Int. Ed.* **2011**, *50*, 60-62.

136. Zhang, W.-B.; Li, Y.; Li, X.; Dong, X.-H.; Yu, X.; Wang, C.-L.; Wesdemiotis, C.; Quirk, R. P.; Cheng, S. Z. D. *Macromolecules* **2011**, *44*, 2589-2596.

137. He, J.; Yue, K.; Liu, Y.; Yu, X.; Ni, P.; Cavicchi, K. A.; Quirk, R. P.; Chen, E.-Q.; Cheng, S. Z. D.; Zhang, W.-B. *Polym. Chem.* **2012**, *3*, 2112-2120.

138. Yue, K.; Liu, C.; Guo, K.; Wu, K.; Dong, X.-H.; Liu, H.; Huang, M.; Wesdemiotis, C.; Cheng, S. Z. D.; Zhang, W.-B. *Polym. Chem.* **2013**, *4*, 1056-1067.

139. Baney, R. H.; Itoh, M.; Sakakibara, A.; Suzuki, T. *Chem. Rev.* **1995**, *95*, 1409-1430.

140. Laine, R. M. *J. Mater. Chem.* **2005**, *15*, 3725-3744.

141. Loy, D. A.; Shea, K. J. *Chem. Rev.* **1995**, *95*, 1431-1442.

142. Hirsch, A. Frontmatter. In *The Chemistry of the Fullerenes*; Wiley-VCH Verlag GmbH: 2008; pp I-XI.

143. J. Feher, F.; D. Wyndham, K.; K. Baldwin, R.; Soulivong, D.; W. Ziller, J.; D. Lichtenhan, J.; D. Lichtenhan, J. *Chem. Commun.* **1999**, 1289-1290.

144. Li, Y.; Guo, K.; Su, H.; Li, X.; Feng, X.; Wang, Z.; Zhang, W.; Zhu, S.; Wesdemiotis, C.; Cheng, S. Z. D.; Zhang, W.-B. *Chem. Sci.* **2014**, *5*, 1046-1053.

145. Bielawski, C. W.; Benitez, D.; Grubbs, R. H. *Science* **2002**, *297*, 2041-2044.

146. Jia, Z.; Monteiro, M. J. *J. Polym. Sci. Polym. Chem.* **2012**, *50*, 2085-2097.

147. Laurent, B. A.; Grayson, S. M. *Chem. Soc. Rev.* **2009**, *38*, 2202-2213.

148.   Yamamoto, T.; Tezuka, Y. *Polym. Chem.* **2011**, *2*, 1930-1941.

149.   Laurent, B. A.; Grayson, S. M. *J. Am. Chem. Soc.* **2006**, *128*, 4238-4239.

150.   Boydston, A. J.; Xia, Y.; Kornfield, J. A.; Gorodetskaya, I. A.; Grubbs, R. H. *J. Am. Chem. Soc.* **2008**, *130*, 12775-12782.

151.   Binauld, S.; Hawker, C. J.; Fleury, E.; Drockenmuller, E. *Angew. Chem. Int. Ed.* **2009**, *48*, 6654-6658.

152.   Hoskins, J. N.; Grayson, S. M. *Macromolecules* **2009**, *42*, 6406-6413.

153.   Qiu, X. P.; Tanaka, F.; Winnik, F. M. *Macromolecules* **2007**, *40*, 7069-7071.

154.   Shi, G.-Y.; Pan, C.-Y. *Macromol. Rapid Comm.* **2008**, *29*, 1672-1678.

155.   Zhang, K.; Lackey, M. A.; Cui, J.; Tew, G. N. *J. Am. Chem. Soc.* **2011**, *133*, 4140-4148.

156.   Lonsdale, D. E.; Monteiro, M. J. *Chem. Commun.* **2010**, *46*, 7945-7947.

157.   Zhu, X.; Zhou, N.; Zhang, Z.; Sun, B.; Yang, Y.; Zhu, J.; Zhu, X. *Angew. Chem. Int. Ed.* **2011**, *50*, 6615-6618.

158.   Zhu, X.; Zhou, N.; Zhu, J.; Zhang, Z.; Zhang, W.; Cheng, Z.; Tu, Y.; Zhu, X. *Macromol. Rapid Comm.* **2013**, *34*, 1014-1019.

159.   Glassner, M.; Blinco, J. P.; Barner-Kowollik, C. *Macromol. Rapid Comm.* **2011**, *32*, 724-728.

160.   Honda, S.; Yamamoto, T.; Tezuka, Y. *J. Am. Chem. Soc.* **2010**, *132*, 10251-10253.

161.   Eugene, D. M.; Grayson, S. M. *Macromolecules* **2008**, *41*, 5082-5084.

162.   Poelma, J. E.; Ono, K.; Miyajima, D.; Aida, T.; Satoh, K.; Hawker, C. J. *ACS Nano* **2012**, *6*, 10845-10854.

163.   Zhang, B.; Zhang, H.; Li, Y.; Hoskins, J. N.; Grayson, S. M. *ACS Macro Lett.* **2013**, *2*, 845-848.

164. Wan, X.; Liu, T.; Liu, S. *Biomacromolecules* **2011**, *12*, 1146-1154.

165. Zhang, W.-B. S., F.; Tirrell, D. A.; Arnold, F. H. *J. Am. Chem. Soc.* **2013**, *135*, 13988-13997.

166. Zhang, W.-B.; Tu, Y.; Ranjan, R.; Van Horn, R. M.; Leng, S.; Wang, J.; Polce, M. J.; Wesdemiotis, C.; Quirk, R. P.; Newkome, G. R.; Cheng, S. Z. D. *Macromolecules* **2008**, *41*, 515-517.

167. Zhang, S. Y.; Zhao, Y. *J. Am. Chem. Soc.* **2010**, *132*, 10642-10644.

168. Lu, D.; Jia, Z.; Monteiro, M. J. *Polym. Chem.* **2013**, *4*, 2080-2089.

169. Hossain, M. D.; Valade, D.; Jia, Z. F.; Monteiro, M. J. *Polym. Chem.* **2012**, *3*, 2986-2995.

170. Jia, Z.; Lonsdale, D. E.; Kulis, J.; Monteiro, M. J. *ACS Macro Lett.* **2012**, *1*, 780-783.

171. Kulis, J.; Jia, Z.; Monteiro, M. J. *Macromolecules* **2012**, *45*, 5956-5966.

172. Lonsdale, D. E.; Monteiro, M. J. *J. Polym. Sci. Polym. Chem.* **2011**, *49*, 4603-4612.

173. Jiang, X.; Shi, Y.; Zhu, W.; Chen, Y.; Xi, F. *J. Polym. Sci. Polym. Chem.* **2012**, *50*, 4239-4245.

174. Sugai, N.; Heguri, H.; Ohta, K.; Meng, Q. Y.; Yamamoto, T.; Tezuka, Y. *J. Am. Chem. Soc.* **2010**, *132*, 14790-14802.

175. Ko, Y. S.; Yamamoto, T.; Tezuka, Y. *Macromol. Rapid Comm.* **2014**, *35*, 412-416.

176. Lewis, J. K.; Wei, J.; Siuzdak, G. *Encyclopedia of Analytical Chemistry* **2000**.

177. Harth, E.; Van Horn, B.; Lee, V. Y.; Germack, D. S.; Gonzales, C. P.; Miller, R. D.; Hawker, C. J. *J. Am. Chem. Soc.* **2002**, *124*, 8653-8660.

178. Li, Y.; Hoskins, J. N.; Sreerama, S. G.; Grayson, S. M. *Macromolecules* **2010**, *43*, 6225-6228.

216

179. Rubinstein, M.; Colby, R. H. *Polymer Physics*; Oxford Univeristy Press: United Kingdom, 2003.

180. Griffiths, P. C.; Stilbs, P.; Yu, G. E.; Booth, C. *J. Phys. Chem.* **1995**, *99*, 16752-16756.

181. Edwards, C. J. C.; Stepto, R. F. T.; Semlyen, J. A. *Polymer* **1980**, *21*, 781-786.

182. Northrop, B. H.; Coffey, R. N. *J. Am. Chem. Soc.* **2012**, *134*, 13804-13817.

183. Lin, B. J. *J. Micro/Nanolith MEMS MOEMS* **2004**, *3*, 377-395.

184. Tokuyama, H.; Yamago, S.; Nakamura, E.; Shiraki, T.; Sugiura, Y. *J. Am. Chem. Soc.* **1993**, *115*, 7918-7919.

185. Friedman, S. H.; DeCamp, D. L.; Sijbesma, R. P.; Srdanov, G.; Wudl, F.; Kenyon, G. L. *J. Am. Chem. Soc.* **1993**, *115*, 6506-6509.

186. Haryono, A.; Binder, W. H. *Small* **2006**, *2*, 600-611.

187. Sudeep, P. K.; Emrick, T. *ACS Nano* **2009**, *3*, 2870-2875.

188. Almdal, K.; Koppi, K. A.; Bates, F. S.; Mortensen, K. *Macromolecules* **1992**, *25*, 1743-1751.

189. Bates, F. S. *Science* **1991**, *251*, 898-905.

190. Leibler, L. *Macromolecules* **1980**, *13*, 1602-1617.

191. Chiu, J. J.; Kim, B. J.; Kramer, E. J.; Pine, D. J. *J. Am. Chem. Soc.* **2005**, *127*, 5036-5037.

192. Zhao, Y.; Thorkelsson, K.; Mastroianni, A. J.; Schilling, T.; Luther, J. M.; Rancatore, B. J.; Matsunaga, K.; Jinnai, H.; Wu, Y.; Poulsen, D.; Frechet, J. M. J.; Alivisatos, A. P.; Xu, T. *Nat. Mater.* **2009**, *8*, 979-985.

193. Lin, Y.; Boker, A.; He, J.; Sill, K.; Xiang, H. Q.; Abetz, C.; Li, X.; Wang, J.; Emrick, T.; Long, S.; Wang, Q.; Balazs, A.; Russell, T. P. *Nature* **2005**, *434*, 55-59.

194. Li, Q.; He, J.; Glogowski, E.; Li, X.; Wang, J.; Emrick, T.; Russell, T. P. *Adv. Mater.* **2008**, *20*, 1462-1466.

195. Kim, B. J.; Chiu, J. J.; Yi, G.-R.; Pine, D. J.; Kramer, E. J. *Adv. Mater.* **2005**, *17*, 2618-2622.

196. Bockstaller, M. R.; Lapetnikov, Y.; Margel, S.; Thomas, E. L. *J. Am. Chem. Soc.* **2003**, *125*, 5276-5277.

197. Lee, J.-Y.; Thompson, R. B.; Jasnow, D.; Balazs, A. C. *Phys. Rev. Lett.* **2002**, *89*, 155503.

198. Jang, S. G.; Kramer, E. J.; Hawker, C. J. *J. Am. Chem. Soc.* **2011**, *133*, 16986-16996.

199. Warren, S. C.; Messina, L. C.; Slaughter, L. S.; Kamperman, M.; Zhou, Q.; Gruner, S. M.; DiSalvo, F. J.; Wiesner, U. *Science* **2008**, *320*, 1748-1752.

200. Yockell-Lelièvre, H.; Desbiens, J.; Ritcey, A. M. *Langmuir* **2007**, *23*, 2843-2850.

201. Pyun, J.; Matyjaszewski, K.; Kowalewski, T.; Savin, D.; Patterson, G.; Kickelbick, G.; Huesing, N. *J. Am. Chem. Soc.* **2001**, *123*, 9445-9446.

202. Martin, T. B.; Seifpour, A.; Jayaraman, A. *Soft Matter* **2011**, *7*, 5952-5964.

203. Akcora, P.; Liu, H.; Kumar, S. K.; Moll, J.; Li, Y.; Benicewicz, B. C.; Schadler, L. S.; Acehan, D.; Panagiotopoulos, A. Z.; Pryamitsyn, V.; Ganesan, V.; Ilavsky, J.; Thiyagarajan, P.; Colby, R. H.; Douglas, J. F. *Nat. Mater.* **2009**, *8*, 354-359.

204. Keng, P. Y.; Shim, I.; Korth, B. D.; Douglas, J. F.; Pyun, J. *ACS Nano* **2007**, *1*, 279-292.

205. Lin, Z.; Lu, P.; Yu, X.; Zhang, W.-B.; Huang, M.; Wu, K.; Guo, K.; Wesdemiotis, C.; Zhu, X.; Zhang, Z.; Yue, K.; Cheng, S. Z. D. *Macromolecules* **2014**, *47*, 4160-4168.

206. Yu, X.; Li, Y.; Dong, X.-H.; Yue, K.; Lin, Z.; Feng, X.; Huang, M.; Zhang, W.-B.; Cheng, S. Z. D. *J. Polym. Sci. Polym. Phys.* **2014**, *52*, 1309-1325.

207. Wu, K.; Huang, M. J.; Yue, K.; Liu, C.; Lin, Z. W.; Liu, H.; Zhang, W.; Hsu, C. H.; Shi, A. C.; Zhang, W. B.; Cheng, S. Z. D. *Macromolecules* **2014**, *47*, 4622-4633.

208. Ni, B.; Huang, M.; Chen, Z.; Chen, Y.; Hsu, C.-H.; Li, Y.; Pochan, D.; Zhang, W.-B.; Cheng, S. Z. D.; Dong, X.-H. *J. Am. Chem. Soc.* **2015**, *137*, 1392-1395.

209. Aldaye, F. A.; Palmer, A. L.; Sleiman, H. F. *Science* **2008**, *321*, 1795-1799.

210. Balazs, A. C.; Emrick, T.; Russell, T. P. *Science* **2006**, *314*, 1107-1110.

211. Huynh, W. U.; Dittmer, J. J.; Alivisatos, A. P. *Science* **2002**, *295*, 2425-2427.

212. Bockstaller, M. R.; Mickiewicz, R. A.; Thomas, E. L. *Adv. Mater.* **2005**, *17*, 1331-1349.

213. Shenhar, R.; Norsten, T. B.; Rotello, V. M. *Adv. Mater.* **2005**, *17*, 657-669.

214. Zhu, X.; Wang, L.; Lin, J.; Zhang, L. *ACS Nano* **2010**, *4*, 4979-4988.

215. Ma, S.; Qi, D.; Xiao, M.; Wang, R. *Soft Matter* **2014**, *10*, 9090-9097.

216. Zhu, L.; Chen, Y.; Zhang, A.; Calhoun, B. H.; Chun, M.; Quirk, R. P.; Cheng, S. Z. D.; Hsiao, B. S.; Yeh, F.; Hashimoto, T. *Phys. Rev. B* **1999**, *60*, 10022-10031.

217. Dong, X.-H.; Lu, X.; Ni, B.; Chen, Z.; Yue, K.; Li, Y.; Rong, L.; Koga, T.; Hsiao, B. S.; Newkome, G. R.; Shi, A.-C.; Zhang, W.-B.; Cheng, S. Z. D. *Soft Matter* **2014**, *10*, 3200-3208.

218. Zhu, L.; Cheng, S. Z. D.; Calhoun, B. H.; Ge, Q.; Quirk, R. P.; Thomas, E. L.; Hsiao, B. S.; Yeh, F.; Lotz, B. *Polymer* **2001**, *42*, 5829-5839.

219. Kim, D. W.; Hwang, S. S.; Hong, S. M.; Lee, E.-C. *Polym. J.* **2000**, *32*, 531-536.

220. Dong, X.-H.; Zhang, W.-B.; Li, Y.; Huang, M.; Zhang, S.; Quirk, R. P.; Cheng, S. Z. D. *Polym. Chem.* **2012**, *3*, 124-134.

221. Ni, B.; Dong, X.-H.; Chen, Z.; Lin, Z.; Li, Y.; Huang, M.; Fu, Q.; Cheng, S. Z. D.; Zhang, W.-B. *Polym. Chem.* **2014**, *5*, 3588-3597.

222.   Yao, L.; Watkins, J. J. *ACS Nano* **2013**, *7*, 1513-1523.

223.   Thompson, R. B.; Ginzburg, V. V.; Matsen, M. W.; Balazs, A. C. *Science* **2001**, *292*, 2469-2472.

224.   Thompson, R. B.; Ginzburg, V. V.; Matsen, M. W.; Balazs, A. C. *Macromolecules* **2002**, *35*, 1060-1071.

225.   Matsen, M. W.; Bates, F. S. *Macromolecules* **1996**, *29*, 1091-1098.

226.   Huang, P.; Zhu, L.; Cheng, S. Z. D.; Ge, Q.; Quirk, R. P.; Thomas, E. L.; Lotz, B.; Hsiao, B. S.; Liu, L.; Yeh, F. *Macromolecules* **2001**, *34*, 6649-6657.

227.   Zhu, L.; Cheng, S. Z. D.; Calhoun, B. H.; Ge, Q.; Quirk, R. P.; Thomas, E. L.; Hsiao, B. S.; Yeh, F.; Lotz, B. *J. Am. Chem. Soc.* **2000**, *122*, 5957-5967.

228.   Zhu, L.; Huang, P.; Chen, W. Y.; Ge, Q.; Quirk, R. P.; Cheng, S. Z. D.; Thomas, E. L.; Lotz, B.; Hsiao, B. S.; Yeh, F. J.; Liu, L. *Macromolecules* **2002**, *35*, 3553-3562.

229.   Son, J. G.; Hannon, A. F.; Gotrik, K. W.; Alexander-Katz, A.; Ross, C. A. *Adv. Mater.* **2011**, *23*, 634-639.

230.   Cushen, J. D.; Bates, C. M.; Rausch, E. L.; Dean, L. M.; Zhou, S. X.; Willson, C. G.; Ellison, C. J. *Macromolecules* **2012**, *45*, 8722-8728.

231.   Son, J. G.; Chang, J. B.; Berggren, K. K.; Ross, C. A. *Nano Lett.* **2011**, *11*, 5079-5084.

232.   Park, S.; Lee, D. H.; Xu, J.; Kim, B.; Hong, S. W.; Jeong, U.; Xu, T.; Russell, T. P. *Science* **2009**, *323*, 1030-1033.

233.   Bates, C. M.; Seshimo, T.; Maher, M. J.; Durand, W. J.; Cushen, J. D.; Dean, L. M.; Blachut, G.; Ellison, C. J.; Willson, C. G. *Science* **2012**, *338*, 775-779.

234.   Chang, J. B.; Son, J. G.; Hannon, A. F.; Alexander-Katz, A.; Ross, C. A.; Berggren, K. K. *ACS Nano* **2012**, *6*, 2071-2077.

235.   Isono, T.; Otsuka, I.; Kondo, Y.; Halila, S.; Fort, S.; Rochas, C.; Satoh, T.; Borsali, R.; Kakuchi, T. *Macromolecules* **2013**, *46*, 1461-1469.

236. Cushen, J. D.; Otsuka, I.; Bates, C. M.; Halila, S.; Fort, S.; Rochas, C.; Easley, J. A.; Rausch, E. L.; Thio, A.; Borsali, R.; Willson, C. G.; Ellison, C. J. *ACS Nano* **2012**, *6*, 3424-3433.

237. Lin, Y.; Daga, V. K.; Anderson, E. R.; Gido, S. P.; Watkins, J. J. *J. Am. Chem. Soc.* **2011**, *133*, 6513-6516.

238. Tanaka, K.; Yoon, J. S.; Takahara, A.; Kajiyama, T. *Macromolecules* **1995**, *28*, 934-938.

239. Bita, I.; Yang, J. K. W.; Jung, Y. S.; Ross, C. A.; Thomas, E. L.; Berggren, K. K. *Science* **2008**, *321*, 939-943.

240. Hsieh, I.-F.; Sun, H.-J.; Fu, Q.; Lotz, B.; Cavicchi, K. A.; Cheng, S. Z. D. *Soft Matter* **2012**, *8*, 7937-7944.

241. Nose, T. *Polymer* **1995**, *36*, 2243-2248.

242. Jung, Y. S.; Ross, C. A. *Adv. Mater.* **2009**, *21*, 2540-2545.

243. Yue, K.; He, J. L.; Liu, C.; Huang, M.; Dong, X.-H.; Guo, K.; Ni, P.; Wesdemiotis, C.; Quirk, R. P.; Cheng, S. Z. D.; Zhang, W.-B. *Chinese J. Polym. Sci.* **2013**, *31*, 71-82.

244. Hudson, S. D.; Jung, H. T.; Percec, V.; Cho, W. D.; Johansson, G.; Ungar, G.; Balagurusamy, V. S. K. *Science* **1997**, *278*, 449-452.

245. Cho, B. K.; Jain, A.; Gruner, S. M.; Wiesner, U. *Science* **2004**, *305*, 1598-1601.

246. Zeng, X. B.; Ungar, G.; Liu, Y. S.; Percec, V.; Dulcey, S. E.; Hobbs, J. K. *Nature* **2004**, *428*, 157-160.

247. Zhang, X.; Chan, E. R.; Glotzer, S. C. *J. Chem. Phys.* **2005**, *123*, 184718.